Stony Brook University

Structural Change in Impact Altered Phyllosilicates as Detected by Laboratory Spectroscopy and Applied to the Remote Sensing of the Surface of Mars

A Dissertation Presented

by

Lonia Rachael Friedlander

to

The Graduate School

in Partial Fulfillment of the

Requirements

for the Degree of

Doctor of Philosophy

in

Geoscience

Stony Brook University

December 2014

Stony Brook University

The Graduate School

Lonia Rachael Friedlander

We, the dissertation committee for the above candidate for the

Doctor of Philosophy degree, hereby recommend

acceptance of this dissertation.

Timothy D. Glotch
Associate Professor, Department of Geosciences

Scott M. McLennan
Professor, Department of Geosciences

Brian L. Phillips
Professor, Department of Geosciences

Joel A. Hurowitz
Assistant Professor, Department of Geosciences

M. Darby Dyar
Kennedy-Schelkunoff Professor of Astronomy, Mount Holyoke College

This dissertation is accepted by the Graduate School

Charles Taber
Dean of the Graduate School

Abstract of the Dissertation

Structural Change in Impact Altered Phyllosilicates as Detected by Laboratory Spectroscopy and Applied to the Remote Sensing of the Surface of Mars

by

Lonia Rachael Friedlander

Doctor of Philosophy

in

Geoscience

Stony Brook University

2014

Atomic-scale mineral properties directly control detectable macroscopic properties. These include reactivity and stability as well as characteristic vibrational and electronic spectroscopic features. The connection between structure and spectroscopic properties in minerals is of fundamental importance to the interpretation of remote sensing data, especially in planetary science where ground-truth is very difficult. On planets without plate tectonics such as Mars, meteoritic impacts are a fundamental geologic process known to affect the structure of planetary surfaces, as well as their mineralogy. This work uses a wide range of laboratory spectroscopic techniques to detect and investigate structural change in impact-altered phyllosilicates. The analysis of multiple spectroscopic techniques provides a detailed understanding of the structural change induced in phyllosilicates by impacts. These results are then applied to the remote sensing of a geologically complex region on the martian surface.

Dedication Page

For my husband Eitan who pushes me to be the best possible version of myself and whose support made this dissertation possible. You light the fire under my ass.

Table of Contents

List of Tables

List of Figures

Acknowledgments

Writing a dissertation is a grave undertaking. Far too many people have helped me along the way to name them all in these pages. Here are a few.

First and foremost, I am extremely grateful to have had Tim Glotch as my advisor. His guidance has been utterly instrumental in the work I've done to produce this research.

Joseph Michalski, who was primary-investigator on the original project from which the research that became this dissertation grew, provided lots of thoughtful feedback on the submitted manuscripts that became Chapters 1 and 2 of this dissertation. He also provided partial funding through NASA Mars Fundamental Research Grant #NNX10AM83G.

The text of Chapter 1 is an edited pre-print of a manuscript currently in review at *Journal of Geophysical Research: Planets*. I gratefully acknowledge my co-authors on that manuscript, David Bish, M. Darby Dyar, Thomas Sharp, Elizabeth Sklute, and Joseph Michalski, both for their input and guidance on the work, and also for their permission to partially reproduce that work here.

The text of Chapter 2 is an extensively edited pre-print of a manuscript currently in review at *Clays and Clay Minerals*. I gratefully acknowledge my co-authors on that manuscript, Brian Phillips, John Vaughn, and Joseph Michalski, both for their input and guidance on the work, and also for their permission to partially reproduce that work here.

The text of Appendix A is the lightly edited pre-print of a manuscript currently in press at *Journal of Water Health* and expected to be published in the January 2015 issue. I gratefully acknowledge my co-authors on that manuscript, Martin Schoonen, Neha Puri, and A. Wali Karzai, both for their input and guidance on the work (especially Neha), and also for their permission to partially reproduce that work here. The copyright holders, IWA Publishing, have also granted permission to reproduce the text of that manuscript in this dissertation.

I must acknowledge Dr. Patricia Craig and Dr. Janice Bishop, reviewers of Chapter 1 in its manuscript form at *JGR: Planets*, who greatly improved both the style and content of the manuscript (and dissertation chapter).

Perhaps most importantly, I wish to acknowledge my dissertation defense committee for taking the time to read this document, provide comments, and offer feedback. Scott McLennan, Darby Dyar, Joel Hurowitz, and Brian Phillips – many thanks.

Finally, I am grateful to my family, especially my Dad, for making sure that I buckled down when I had to.

Publications (by topic)

The Effect of Impacts on Clay Mineral Structure Spectroscopy

Lonia Friedlander, Timothy D. Glotch, David L. Bish, M. Darby Dyar, Tom G. Sharp, Elizabeth C. Sklute, Joseph R. Michalski. (in review) Structural and spectroscopic changes to natural nontronite induced by experimental impacts between 10 and 40 GPa. *Journal of Geophysical Research: Planets*.

Lonia Friedlander, Timothy D. Glotch, Brian Phillips, Joseph R. Michalski (in review) Comparing structural and related spectral change between iron and magnesium-bearing 2:1 smectites after experimental impacts between 10 - 40 GPa. *Clays and Clay Minerals.*

Reactive and Antibacterial Minerals

L. Friedlander, N. Puri, M. Schoonen, A. Karzai (in press). The effect of pyrite on *E. coli* in water: Proof-of-concept for the elimination of waterborne bacteria by reactive minerals. *Journal of Water and Health.*

Water Resources Management/Drip Irrigation Technology Transfer

Y. Garb and L. Friedlander (2014) From "failed transfer" to fluid translation: Toward a systemic understanding of drip irrigation uptake. *Agricultural Systems,* 128: 13-24.

L. Friedlander, A. Tal and N. Lazarovitch (2013). Technical considerations affecting adoption of drip irrigation in sub-Saharan Africa. *Water Resources Management,* 126: 125-132 .

Chapter 1

Introduction

"The beauty of a…thing is not the atoms that go into it, but the way those atoms are put together" – Carl Sagan

1.1 The role of atomic interactions in crystal structure and mineral properties

Atomic interactions in minerals determine many mineral properties. At the scale of the unit cell, the ionic properties of radius and charge control mineral crystal structures (Pauling, 1927, 1928, 1929). Even smaller, at the atomic scale, electronic orbitals within each atom combine to form the "infinite" energy bands that explain bonding in solids (Hoffmann, 1988). Zooming out slightly, these infinite bands can be broken up based on functional groups into molecular orbitals specific to the patterns of bonding in various parts of complex solids (Pauling and Hendricks, 1925; Pauling, 1930; Bleam and Hoffmann, 1988; Ruiz *et al.*, 1994). Taken together, these interactions produce the measurable properties of minerals. They explain why some minerals are hard and others soft, some soluble and others not, some reactive and others inert. Atomic- and molecular-scale interactions in minerals also produce characteristic nuclear, electronic, and vibrational effects that can be used to identify specific minerals.

The detection of mineral-specific atomic interactions using multiple electromagnetic frequencies is the foundation of solid-state laboratory spectroscopy (Farmer, 1968; Clark, 1999). Laboratory spectroscopic techniques, in turn, have gradually become the basis, over the past two decades, of many new field and orbital remote sensing techniques that non-destructively detect surface mineralogy on planetary bodies. On each new planet, with each new technique, the goal is to understand the geologic processes that produced the detected surface mineral assemblages. This dissertation is an exploration of the effects of one very large-scale process, impacts, on atomic-scale structures in phyllosilicate minerals and the ways in which these effects can be detected in the laboratory. The detection of structural change in minerals, although it is microscopic, has planetary-scale implications. Because the interactions of atoms in minerals are used to spectroscopically identify them on distant planets, even small changes to these interactions can cause big problems for the accurate interpretation of spectroscopic data. To explore this idea thoroughly, I begin this dissertation with a brief overview of mineral spectroscopy.

1.1.1 Mineral spectroscopy

The effects of solid-state interactions with electromagnetic radiation are fundamental mineral properties that depend on the frequency of the light involved and the structure and composition of the mineral. Absorptions in the infrared wavelength region arise from vibrations of the mineral's constituent atoms. The frequency of the absorbed light depends on the masses of the atoms involved, the forces of the bonds that restrain them, and the mineral's overall crystal structure (Farmer, 1968). In different wavelength regions, electromagnetic radiation induces different effects that are indicative of other mineral properties. Light in the ultraviolet and short-wave visible wavelength ranges induces crystal-field electronic transitions that depend on the presence and oxidation states of transition metals in minerals (Burns, 1993). In the case of phyllosilicates, Fe is particularly important. At the very high-energy end of the electromagnetic spectrum, X-rays, with a wavelength on the same order of magnitude as the distance between atoms in a crystal, are diffracted by those atoms in patterns representing the long-range order of

the overall structure (Bragg, 1913). The spectra detected from the interactions of crystals with electromagnetic radiation over a range of wavelengths are characteristic of the minerals that produce them and can be used for non-destructive mineral identification. In addition to providing mineral identification fingerprints, spectroscopy also gives, in favorable conditions, a clear picture of the functional groups of the mineral and can illuminate structural similarities between compositionally different materials.

Mineral spectroscopy can also be used to monitor and characterize structural change in minerals in response to physical and chemical processes, both in the field and in the laboratory. In vibrational (infrared) spectroscopy, band depth directly correlates with the abundance of the absorber. As a result, spectral changes imply either loss of that absorber, or functional group, from the structure, or structural change such that the absorption is no longer associated with the original absorption frequency (Clark, 1999). Vibrational spectroscopy, especially in combination with other techniques, can therefore be used to explore structural change in minerals in detail.

1.1.2 Planetary remote sensing

In addition to providing detailed information on mineral composition and structure, the spectroscopic fingerprints of minerals can be compared to laboratory spectra and applied to the remote sensing of both terrestrial and non-terrestrial planetary surfaces (e.g., Christensen et al., 1998, 2001; Bandfield et al., 2000; Murchie et al., 2007). This allows spectrally dominant minerals on planetary surfaces to be identified, and regional mineralogy to be related to depositional or alteration environments, from which information about climate can be inferred (e.g., Poulet *et al*., 2005; Fairén et al., 2009). However, the dependence of remote sensing on databases of laboratory spectra means that only minerals that have been analyzed in the laboratory can be accurately identified. As a result, the addition of structurally altered minerals to spectral analyses may improve interpretations of remote sensing data (Johnson *et al.*, 2002, 2007; Wright *et al.*, 2006). Some previous work has even suggested that previously identified compositions (e.g., basaltic andesite) have been inaccurately identified and are actually different minerals that have been weathered so that their spectra are no longer characteristic (e.g., weathered basalt) (Wyatt and McSween, 2002). Thus, despite its general robustness, the application of spectroscopy to remote sensing requires detailed analysis and comparisons to carefully characterized and accurately measured laboratory spectra to make robust identifications. Nonetheless, several mineral classes with important implications about past climate and surface environments have been identified by the remote sensing of the martian surface. Phyllosilicates, particularly hydrated smectites, make up one such mineral class.

1.2 Phyllosilicate minerals on Earth and Mars

On Earth, phyllosilicates form in aqueous alteration environments and indicate long-term exposure to water. Smectite group minerals, such as nontronite, saponite, and beidellite, dominate in moderately weathered temperate regions, while rocks in tropical regions are weathered to kaolinite or simple hydroxides. Because local clay mineralogy reflects both regional hydrology and the geochemistry of underlying bedrock, clays can be used as fairly sensitive indicators of both local geology and climate (Allen, 1997). As a result, clay mineral deposits on Mars are often used to infer information about local paleoclimate. For example, early phyllosilicate detections were thought to indicate that Mars was once significantly warmer and

wetter on the surface than it currently is (Poulet *et al.*, 2005; Mustard *et al.*, 2008; Bishop *et al.*, 2013c). Specifically, clay mineralogy has also been investigated for evidence of biological activity and the possible preservation of biosignatures (Bishop *et al*., 2013). More recently, phyllosilicate deposits have been used as indicators of circum-neutral pH in weathering environments and potential indicators of formerly habitable environments (Meslin *et al.*, 2013; Grotzinger *et al.*, 2014). However, the warm-wet early Mars hypothesis has been challenged by alternative hypotheses positing that martian phyllosilicates formed as a result of impact-induced hydrothermal processes on an otherwise cold and dry planet (Marzo *et al.*, 2010; Furukawa *et al.*, 2011), or that Mars was wetter, but not warmer in its early history (Fairén *et al.*, 2009). An additional reason for the importance of accurate phyllosilicate identifications on Mars is that terrestrial processes of phyllosilicate diagenesis (Eberl, 1993) have begun to be associated with martian phyllosilicates and used to infer more specific temperature and pressure regimes for their formation (Bishop *et al.*, 2008b; Ehlmann *et al.*, 2009, 2013; Milliken, 2014; Vaniman *et al.*, 2014). These connections are established based on the relatively straightforward transitions between mineral types that phyllosilicates undergo during physical or chemical alteration on Earth (Hower *et al.*, 1976; Eberl, 1993; Allen, 1997). However, spectroscopic evidence for these identifications is directly related to the crystal structures of both the initial minerals and those produced. Many phyllosilicates are structurally similar and clays can transition from one mineral to another relatively easily by substitution of the loosely-bonded cations in their interlayers and other relatively low-energy processes (Allen, 1997). Because mineral spectroscopy is so intimately related to the structure and chemistry of minerals, the relative instability of clay minerals has important implications for their identification. Before this can be examined in detail, however, a brief overview of clay mineral structure is required.

1.2.1 Phyllosilicate mineral structure

Phyllosilicates have complex and variable structures, but the basic structure is based on six-member rings of SiO_4^{4-} tetrahedra that are joined at their apices and extend outward in infinite sheets. This sheet is superposed on an octahedral sheet made up of Al^{3+} ions (and/or Fe^{2+}, Fe^{3+}, or Mg^{2+}) surrounded by six anions (primarily OH^-) in an octahedral arrangement. Each octahedron shares three edges with neighboring octahedra to also form an infinite sheet (Pauling, 1930). In perfect phyllosilicate structures, every layer is electrically neutral. The structure is built up by a repeated superposition of tetrahedral and octahedral sheets and stacked layers are weakly held together by dispersion forces. However, Al^{3+} can partially substitute into the tetrahedral sites generally dominated by Si and, as a result, negatively charged phyllosilicate layers are produced. This negative charge must be counterbalanced by the addition of positively charged cations, which intercalate into the spaces between the weakly held layers. In some clay minerals, neutral, polar H_2O molecules can then also be held between the negatively charged clay layers and the positively charged interlayer cations (Rich, 1968; Eberl *et al.*, 1978; Laperche *et al.*, 1990; Bishop *et al.*, 1994; Chatterjee *et al.*, 1999; Arab *et al.*, 2003; Boek and Sprik, 2003; Kirkpatrick *et al.*, 2005). In addition to substitution between the tetrahedral and octahedral sheets of clays, there is also variability in the octahedral structure of clays depending on whether the dominant octahedral cation is divalent or trivalent (Bailey, 1966; Rich, 1968; Petit *et al.*, 1999). Divalent cations occupy all available octahedral sites, while trivalent cations (including Al^{3+}) occupy only two of the three symmetrically independent octahedral sites, initially described as "hydrargillite" by *Pauling* (1930). Clay minerals with partially (2/3) occupied octahedral sheets are called dioctahedral clays, while those with fully occupied octahedral sheets are called trioctahedral clays. Generally, dioctahedral clay structures fill both octahedral M2 sites, leaving

the M1 sites vacant (Figure 1.1a). Trioctahedral clay structures always fill all three octahedral cation sheet sites (Figure 1.1b). Dioctahedral clays have been suggested to be more reactive than trioctahedral clays (Sand and Ames, 1957; Ames and Sand, 1958; Yan *et al.*, 2009), which is not surprising given the greater number of vacancies their structures contain. There is additional variability in clay mineral structures due to irregularities, polytypism usually related to stacking defects and rearrangements, and other common structural defects (Bailey, 1966). The complexity and interrelated stability of many clay mineral structures makes definitive identifications difficult. Nonetheless, remote sensing on Mars has identified specific clay mineral species. In general, predictions about the presence of specific clay mineral groups and some species are based on detailed laboratory spectroscopic analyses. However, regional geologic context should also be considered.

1.2.2 Specific phyllosilicate identifications on Mars by remote sensing

Phyllosilicates and other hydrated mineral phases have been identified in many regions of the martian surface, though most identifications cluster together within the heavily bombarded southern highlands (Carter *et al.*, 2013). Fe/Mg phyllosilicates are the most abundant hydrated mineral detections on Mars, found in 89% of all hydrous mineral detections (Carter *et al.,* 2013). Regions where these minerals have been detected include Noctis Labyrinthus, just west of Valles Marineris (Weitz *et al.*, 2011; Thollot *et al.*, 2012), Nili Fossae, northwest of the Isidis Basin (Poulet *et al.*, 2005, 2007; Mangold *et al.*, 2007; Mustard *et al.*, 2008; Ehlmann *et al.*, 2009; Murchie *et al.*, 2009; Michalski *et al.*, 2010; Viviano *et al.*, 2013), and Mawrth Vallis, a central region between the two (Poulet *et al.*, 2005; Loizeau *et al.*, 2007; Michalski and Dobrea, 2007; Bishop *et al.*, 2008b; Mckeown *et al.*, 2009; McKeown *et al.*, 2013). More specifically, nontronite in Mawrth Vallis was one of the first clay minerals ever identified on the martian surface by the Observatoire pour la Minéralogie, l'Eau, les Glaces et l'Activité (OMEGA) spectrometer onboard the Mars Express spacecraft (Poulet *et al.*, 2005). This specific identification was later confirmed by the Compact Reconnaissance Imaging Spectrometer for Mars (CRISM) that flew on the Mars Reconnaissance Orbiter (MRO) (Bishop *et al.*, 2008b). Another smectite, saponite, has been proposed, but never proved as a match for CRISM spectra (Mustard *et al.*, 2008, 2009; Ehlmann *et al.*, 2009). Other specific phyllosilicate identifications proposed as matches for CRISM spectra in diverse regions include chlorite (Mangold *et al.*, 2007; Mustard *et al.*, 2008; Ehlmann *et al.*, 2009; Fairén *et al.*, 2010; Marzo *et al.*, 2010; Thollot *et al.*, 2012; Bishop *et al.*, 2013c; Viviano *et al.*, 2013), serpentine (Ehlmann *et al.*, 2010; Fairén *et al.*, 2010), illite (Mustard *et al.*, 2008; Ehlmann *et al.*, 2009; Mckeown *et al.*, 2009; Milliken *et al.*, 2010; Bishop *et al.*, 2013b; Viviano *et al.*, 2013; Milliken, 2014; Viviano-Beck *et al.*, 2014), kaolinite (Mustard *et al.*, 2008; Murchie *et al.*, 2009; Marzo *et al.*, 2010; Michalski *et al.*, 2010; Weitz *et al.*, 2011; Bishop and Rampe, 2014; Viviano-Beck *et al.*, 2014), and montmorillonite (or its compositional equivalent) in the Colombia Hills and at Endeavor Crater (Clark *et al.*, 2007; Wray *et al.*, 2009; Arvidson *et al.*, 2014). The global distribution and wide variety of clay minerals on Mars has led to many formation hypotheses with as many implications for the geologic history and climate of early Mars. Ehlmann *et al.* (2013) provide an excellent review of these hyphotheses and the remote and *in-situ* measurements that could distinguish between various phyllosilicate formation mechanisms in future missions. Careful analysis of clay mineral assemblages has been used to investigate potential hydrothermal alteration and burial diagenesis in Nili Fossae (Viviano *et al.*, 2013). However, there is one outstanding issue in the detection of clay minerals on Mars that has yet to be satisfactorily addressed. All of the phyllosilicate identifications referenced above were made using visible-near infrared (VNIR) reflectance data.

This same variety and global distribution has yet to be reproduced in thermal infrared (TIR) remote sensing data from the martian surface.

Currently, no unambiguous mineral-specific detections of phyllosilicates have been made on the martian surface using TIR data alone, although some have been made by convolving TIR and VNIR data (e.g., Viviano and Moersch, 2012). There are many potential explanations for the apparent disconnect between robust VNIR phyllosilicate identifications on Mars and the lack of corresponding TIR evidence. Several researchers have proposed that phyllosilicates exist on Mars, but cannot be detected because their abundances are below the detection limits of the Thermal Emission Spectrometer (TES) onboard Mars Global Surveyor (Bandfield, 2002a; Michalski *et al.*, 2006, 2010; Michalski and Fergason, 2008; Mcdowell and Hamilton, 2009; Viviano and Moersch, 2012). However, this directly contradicts estimates of phyllosilicate abundance produced through the application of non-linear spectral unmixing techniques, which place the abundances of phyllosilicate minerals in some regions as high as 55% (Poulet *et al.*, 2008). TES should be able to detect phyllosilicates in such high abundance regions, but has not yet been able to do so. Interestingly, phyllosilicates identified *in-situ* at Gale Crater were also not detected from orbit in the location where they were identified *in-situ* and form the bulk of the amorphous and small grain size fractions of the analyzed sample (Vaniman *et al.,* 2014). Such grain size effects might explain why TES fails to identify phyllosilicates in the TIR, even in high abundance regions. Other explanations include surface roughness, multiple temperatures at sub-pixel scales, or simple difficulty resolving the differences in spectral and spatial resolutions between TES and OMEGA and, especially, CRISM (Michalski and Fergason, 2008). Another potential explanation may be that phyllosilicates are difficult to definitively separate from other high-silica phases at global scales by linear deconvolution. This possibility was suggested even prior to the identification of clays by OMEGA and CRISM (Bandfield, 2002a; Wyatt and McSween, 2002). However, one other possibility, supported by this dissertation, is that impact alteration and related processes have affected the structure and spectroscopic signatures of martian clay minerals such that remote sensing techniques sensitive to structural disorder in different parts of the structure produce different results. Thermal alteration has been demonstrated to be a compelling potential reason for the disconnect between TIR and VNIR phyllosilicate identifications in Nili Fossae (Che and Glotch, 2014). This finding is in contrast with modeling of post-impact temperatures achieved in martian craters that implies that phyllosilicates in these craters will not generally be exposed to temperatures high enough to alter their spectroscopic signatures (Fairén *et al.*, 2010). This thermal stability then becomes one line of evidence cited for the relative age of clay deposits on Mars. However, the fact that clay deposits may be old actually increases the probability that they experienced impact-induced alteration, despite their possible thermal stability. This impact shock may also contribute to the differences between VNIR and TIR phyllosilicate identifications on Mars as discussed in greater detail in the first and second chapters of this dissertation.

The idea that impacts may affect the remote sensing of clay minerals on Mars makes logical sense because clays are thought to be old (Fairén *et al.*, 2010; Arvidson *et al.*, 2014; Vaniman *et al.*, 2014), and are often associated with old, heavily bombarded terrains, as described above. In addition to detections in the older, more heavily bombarded regions of Mars, clays have also been identified in association with impact craters in the comparatively younger, northern lowlands (Carter *et al.,* 2013). For this and other reasons, impact craters have been suggested as places where the ancient crust of Mars is exposed and therefore, martian geologic

history (and past habitability) can be investigated (Schwenzer *et al.*, 2009, 2010). However, impacts do more than simply expose the ancient crust of Mars. They also induce fundamental structural changes in minerals, which can affect their spectroscopic signatures. Here I present a brief review of previous work on the effects of impacts on mineral structure and spectroscopy to introduce impact-induced mineral alteration and previously explored connections to spectroscopy and planetary remote sensing.

1.3 The effects of impact processes on clay mineral spectroscopy

1.3.1 Thermal alteration

Impacts produce waves of both pressure and heat that pass through the materials present at the time of impact inducing structural and related spectroscopic change (French, 1968, 1998; Bischoff and Stöffler, 1992). These effects differ from other metamorphic mineralogical and structural changes (Figure 1.2) and so should be able to be independently detected by laboratory and remote sensing spectroscopic techniques. Experimentally, thermal alteration is easier to study and, as a result, there is relatively more data about its effects on phyllosilicate spectroscopy. Generally, thermal alteration of hydrated phyllosilicates follows a stepwise progression in which the mineral dehydrates, dehydroxylates, collapses, and finally forms new secondary crystalline and amorphous phases (Massiot *et al.*, 1995; Carroll *et al.*, 2005). This has been confirmed by later studies using laboratory spectroscopy to both associate specific thermal alteration steps with spectroscopic change, and to observe the effects of thermal alteration on phyllosilicates (Moskowitz and Hargraves, 1984; Gavin and Chevrier, 2010; Che *et al.*, 2011; Daly *et al.*, 2011; Che and Glotch, 2012). In addition, due to the importance of the ceramics industry, phyllosilicate thermal alteration has been well studied in the laboratory, although many of the techniques used to investigate thermal effects in phyllosilicates in previous studies have not been comparable to those used in planetary remote sensing (Moskowitz and Hargraves, 1984; Drits *et al.*, 1995; Massiot *et al.*, 1995; Fitzgerald *et al.*, 1996; Carroll *et al.*, 2005; Ruff and Hamilton, 2009). In contrast to thermal alteration, the effects of shock on phyllosilicates are less well characterized.

1.3.2 Shock

Shock-recovery experiments are more difficult to carry out than thermal alteration experiments. For this dissertation, the technique of shock reverberation, which is described in greater detail in Chapter 2, was used in a serious of experimental impacts designed by Joseph Michalski and Tom Sharp. Shock reverberation was selected because it partially separates the effects of thermal and shock alteration by controlling the enthalpy gradient across well-packed, finely powdered samples. This is important because many of the mineralogical and structural changes observed in early experiments investigating impact shock effects on phyllosilicates were assumed to be related to impact-induced thermal alteration rather than shock itself as a separate and distinct process (Boslough *et al.*, 1980; Weldon *et al.*, 1982). However, later work showed that shock and thermal alteration produce altered materials with distinct properties (Boslough *et al.*, 1986). Most experimental efforts to understand shock as a process distinct from thermal alteration have been recent. Gavin *et al.* (2013) performed the most detailed work to-date, but they associated spectral and structural changes in their experiments primarily with impactor velocity, rather than pressure. This makes it difficult to directly compare their results with other experiments. Other work on the technical aspects of shock-recovery experiments has thus far

focused on the effects of vented versus unvented sample holders on the laboratory spectra taken after experimental impacts on hydrated samples (Stewart *et al.*, 2010; Kraus *et al.*, 2013). As a result, a detailed investigation of structural change in phyllosilicates exposed to experimental impacts associating structural change directly with spectral features has not yet been performed in the context of planetary science and remote sensing. The results discussed in this dissertation begin to fill this gap. The shock reverberation experiments conducted for this dissertation allowed peak impact pressures to be calculated directly from the measured velocities of the impactors used based on empirical results for impactors of various known compositions (Chapter 2). All experiments were carried out at the Flat Plate Accelerator (FPA) facility at the National Aeronautics and Space Administration's (NASA) Johnson Space Center (JSC). The facility (Figure 1.3a) contains both the FPA and other experimental impact simulators, such as a 5 mm light-gas gun. Motion-sensitive cameras stationed in the flight path monitor each impact to ensure that it approximates 1-dimensional shock (Figure 1.3b). Based on these experiments, the structural and spectroscopic effects of impacts of known peak impact pressures on well-characterized phyllosilicate samples are the primary focus of this dissertation. This is related to spectral change, which is then used to investigate the potential presence of impact-altered phyllosilicates in heavily bombarded regions of the martian surface.

1.4 Other mineral properties

In addition to spectroscopy and susceptibility to structural deformation, atomic interactions also control other mineral properties. In Appendix A of this dissertation, I describe the results of experiments investigating the reactivity and antibacterial efficacy of freshly fractured pyrite and other minerals. These mineral properties and their potential relationship to structural deformation and crystal structure are introduced here.

1.4.1 Reactivity

There is conflicting evidence on the role of long-range structure in mineral-microbe interactions. Anatase was once thought to be more toxic than rutile (Maness *et al.*, 1999), but at nanoscale particle sizes, both polymorphs have been shown to be equally effective at bacterial elimination (Simon-Deckers *et al.*, 2009). Inhalation toxicology experimental results on silicate polymorphs are equally unclear (Meldrum and Howden, 2002). Some studies using amorphous silica show that it is less reactive and toxic than crystalline quartz when inhaled (Rosenbruch *et al.*, 1990), while others show that crystalline quartz is the most toxic form of inhaled silica (Bruch *et al.*, 2000). Asbestiform silica may be more toxic than other silicates (Brunner *et al.*, 2006), but the association of iron with asbestos (Aust *et al.*, 2000) casts doubt on this observation as primarily structural.

Surface defects increase mineral reactivity. In the case of pyrite, surface defects were first theorized (Borda *et al.*, 2003) and then observed driving the formation of reactive oxygen species (ROS), such as hydroxyl radical and hydrogen peroxide, in solution; first by mass-spectrometry (Borda *et al.*, 2003) and again by attenuated total reflectance (ATR) and Fourier transform infrared (FTIR) spectroscopy (Borda *et al.*, 2004). Surface reactivity has also been proposed as a driver of the cytotoxicity of various forms of crystalline silica (Albrecht *et al.*, 2005), and surface defects contribute to the toxicity of inhaled carbon nanotubes (Fenoglio *et al.*, 2008). In the context of mineral-microbe interactions, dissolution features produced by *Shewenella*

putrefaciens on hematite surfaces display crystallographic control and alignment with structural defects (Rosso *et al.*, 2003), implying that certain chemolithoautotrophic bacteria may be able to identify and target these high-energy sites. Freshly fractured quartz is also known to be more reactive than un-fractured quartz and to produce more ROS in solution due to its higher concentration of reactive surface species and high-energy surface sites (Schoonen *et al.*, 2006).

1.4.2 Antibacterial activity

Antibacterial properties have been observed for natural clay minerals in the context of treating antibiotic-resistant flesh-eating bacterial infections (Williams *et al.*, 2004; Haydel *et al.*, 2008; Cunningham *et al.*, 2010). Compositional comparisons between antibacterial clays and non-antibacterial clays have revealed an association between the presence, in clay samples, of reduced iron or reduced iron-bearing phases (i.e. pyrite) and bacterial elimination (Williams *et al.*, 2008, 2011; Cunningham *et al.*, 2010). Additional work has shown that mineral-derived dissolved iron eliminates *E. coli* bacterial cells primarily by infiltrating them, inducing oxidative stress, and producing TEM-observable intracellular iron oxides (Otto *et al.*, 2010; Williams *et al.*, 2011). Natural antibacterial clay mineral samples have complex and varied compositions (Williams et al*.,* 2008). Therefore, experiments with pure minerals are required to connect antibacterial mechanisms with specific mineral-microbe interactions. Recent work on the effect of pyrite (FeS_2) on *E. coli* in water directly confirmed the role of reduced iron in *E. coli* bacterial elimination, but also demonstrated that the effects of iron on bacteria are coupled to and enhanced by mineral-driven ROS production (Friedlander *et al.*, 2014a).

The production of ROS by minerals occurs at both redox-active transition metal sites (Schoonen *et al.*, 2010) and also at surface defect sites (Borda *et al.*, 2003). ROS production by minerals in solution has been directly linked to the quantitative destruction of RNA (Cohn *et al.*, 2004, 2006) and, as a result, is thought to drive bacterial elimination by the disruption of cell function and damage to key proteins (Schoonen *et al.*, 2006). TEM-based morphological studies show no effects on bacterial cell structure after mineral exposure (e.g., Otto *et al.*, 2010; Williams *et al.*, 2008), implying that the antibacterial process occurs inside the cell in the model organisms studied to date. This is consistent with exposure to either ROS or reactive metal cations. In addition, metallic oxide nanoparticles are known to be highly antibacterial and cytotoxic (Jiang et al., 2009; Karlsson et al., 2008; Simon-Deckers et al., 2009), with reduced iron-bearing particles observed to be particularly reactive (Auffan *et al.*, 2008). The importance of iron-driven oxidative stress has been inferred by the increased susceptibility of mutant *E. coli,* devoid of their oxidative stress response enzyme, to Fe(II) oxide nanoparticles. Thus, mineral antibacterial activity, much like mineral spectroscopy, is controlled by a combination of composition and structure.

1.5 The structure of this dissertation

Impact-induced structural change in phyllosilicates as detected by laboratory spectroscopy and related to the remote sensing of the martian surface forms the main subject of this dissertation. However, the topic can more broadly be considered as the detection of changes to atomic-scale interactions in minerals and the relationship between these interactions and mineral properties. This broader topic connects all of the work that I did during the process of

preparing this dissertation, and associates the work that I report in Appendix A with the rest of the dissertation.

Chapter one describes the structural effects of experimental impacts on one well-characterized, iron-rich smectite, nontronite. These effects are detected through laboratory spectroscopic techniques similar to those employed in planetary remote sensing, as well as other techniques, such as Transmission Electron Microscopy (TEM), that are useful for observing structural changes directly and relating these to the laboratory spectroscopy results. This work is also described in a manuscript currently in review at *Journal of Geophysical Research: Planets*. Chapter two compares and contrasts the effects of laboratory impacts on two compositionally different 2:1 smectites. The effects of thermal and shock alteration are also contrasted. This work is also described in a manuscript currently in review at *Clays and Clay Minerals*. Chapter three describes the remote sensing of impact-altered phyllosilicates in heavily bombarded regions of Mars using the data accumulated in chapters one and two. Implications for current understanding of Mars' geologic history and past climate based on clay mineral deposits are also discussed. A manuscript based on this work is currently being prepared for submission to either *Geophysical Research Letters* or *Journal of Geophysical Research: Planets*. Finally, Appendix A describes the effects of pyrite on the waterborne pathogenic bacterium *E. coli* and relates the observed effects to the structure and composition of pyrite. This work is also described in a manuscript currently in press, which will be published in the January 2015 issue of *Journal of Water and Health*. Throughout this dissertation, I highlight the relationship between atomic interactions, crystal structure, spectroscopy, and mineral properties. Although this work is applied in detail to the remote sensing of the martian surface, careful use of mineralogy and crystal structure to understand mineral properties has broad applicability to many questions in geochemistry.

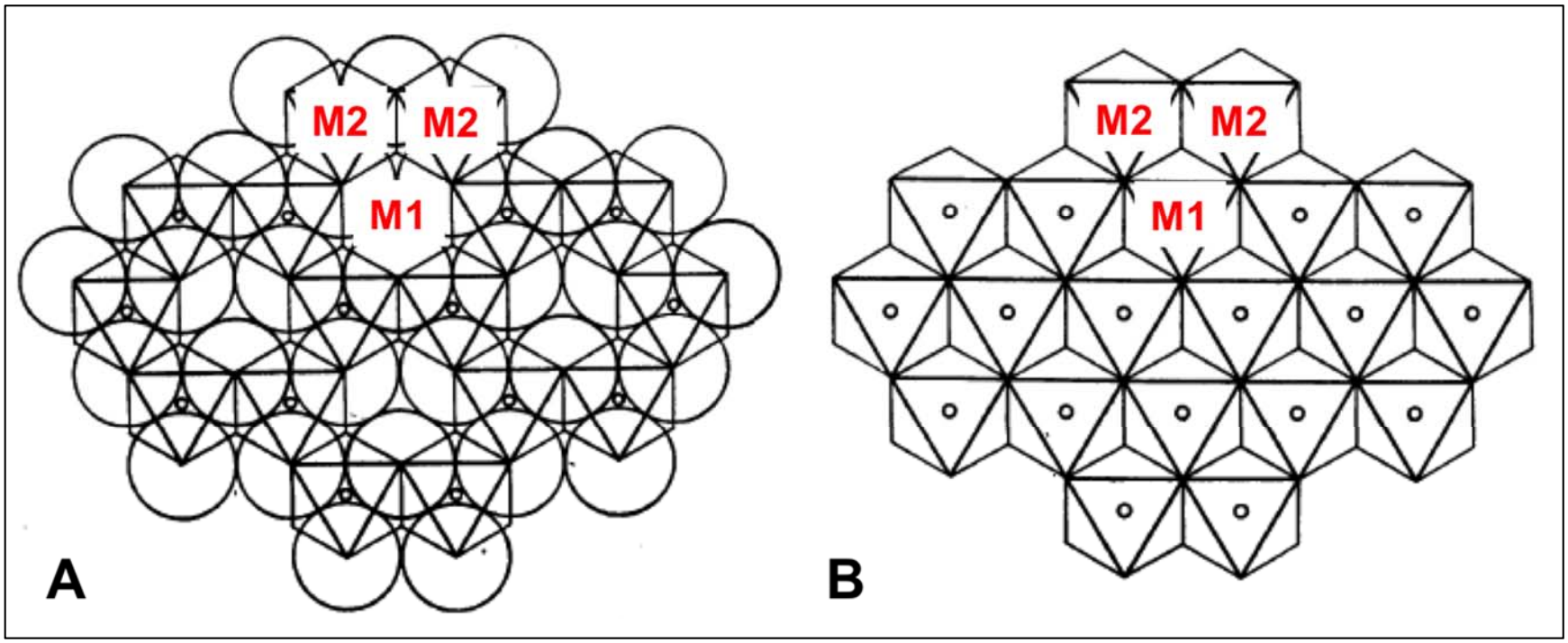

Figure 1.1. Comparison of dioctahedral (A) and trioctahedral (B) phyllosilicate structures based on close-packing of the anions of the mica structure (OH^-, O^{2-}, and F^-), which are explicitly shown in (A) as large circles on which the octahedral cation sites are superposed. Light circles indicate oxygen anions; dark circles indicate hydroxyl or fluorine. The crystallographically non-equivalent cation sites (M2 for the two cis- and M1 for the one trans-site) are labeled in red on both structures. All octahedral sites are filled in the trioctahedral structure (B), while the trans-site (M1) is the cation site most frequently left vacant in dioctahedral structures (A). Figure modified from Pauling (1930).

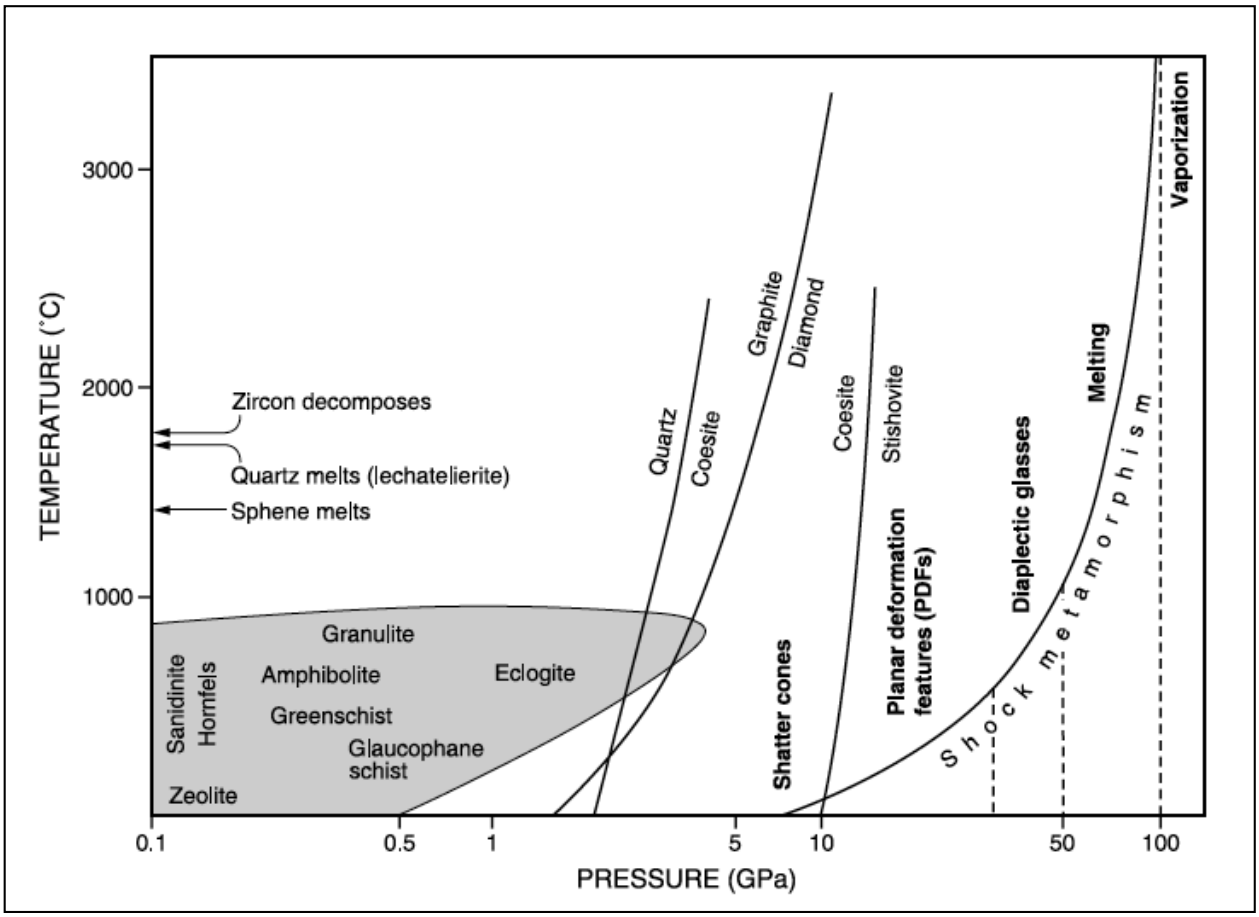

Figure 1.2. The progression of shock metamorphism in silicates demonstrating the differences between shock metamorphism and other types of pressure- and temperature-dependant metamorphism, from French (1998).

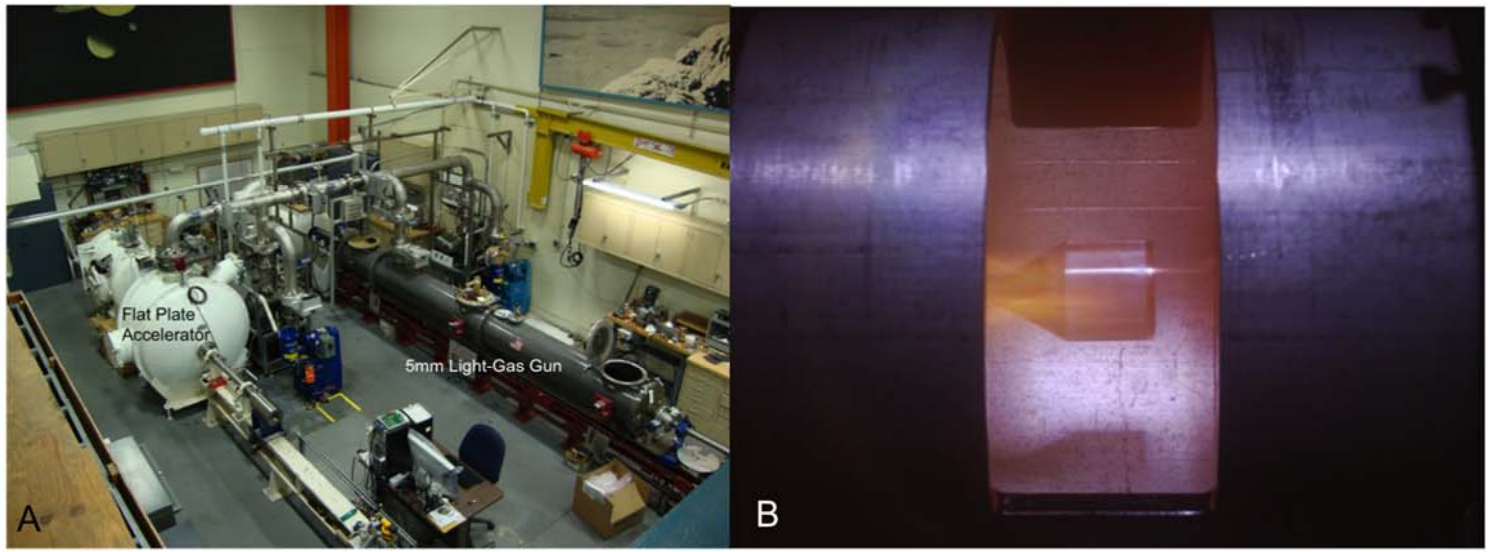

Figure 1.3. The FPA facility at JSC (A) and an example of a photograph taken during the flight of the impactor toward a sample in the FPA (B). Images like those shown in (B) are used to ensure that experimental impacts produced at the FPA approximate 1-dimensional shock.

Chapter 2

Structural and spectroscopic changes to natural nontronite induced by experimental impacts between 10 and 40 GPa

Much of the material presented in this chapter is currently under review in an edited format at *Journal of Geophysical Research: Planets* with co-authors Timothy D. Glotch, David L. Bish, M. Darby Dyar, Thomas G. Sharp, Elizabeth C. Sklute, and Joseph R. Michalski.

Abstract

Many phyllosilicate deposits remotely detected on Mars occur within heavily bombarded terrains. Shock metamorphism from meteor impacts alters mineral structures, which produce mineral spectra. Thus, it is probable that impacts have affected the spectra of remotely sensed martian phyllosilicates. In this chapter, I present spectral analysis results for a natural nontronite sample (Clay Mineral Society Source Clay, NAu-1) before and after laboratory-generated impacts over five peak-pressures between 10 – 40 GPa. I conducted a suite of spectroscopic analyses to characterize the impact-induced structural and spectral changes to the sample.

Nontronite becomes increasingly disordered with increasing peak impact pressure. All of the infrared spectroscopic techniques used showed evidence of structural changes at shock pressures above ~25 GPa. However, the tetrahedral and octahedral sheets of nontronite deform differently. Reflectance spectroscopy in the visible near-infrared (VNIR) region is primarily sensitive to changes in the octahedral sheet of nontronite and detects the OH-group bending and stretching overtone and combination bands, while mid-infrared (MIR) spectroscopic techniques are sensitive to the fundamental stretching and bending vibrations of silicon and oxygen in the nontronite tetrahedral sheet. As a result, impact-driven structural deformation may contribute to difficulties in phyllosilicate detection between remote sensing techniques that are sensitive to different parts of the nontronite structure. The observed spectroscopic changes after laboratory impacts indicate that the nontronite sample's octahedral and tetrahedral sheets were structurally deformed, but not completely dehydroxylated. This finding is an important distinction from previous studies of thermally altered phyllosilicates in which dehydroxylation follows dehydration in a step-wise progression preceding structural deformation.

2.1 Introduction

Phyllosilicates on the martian surface have been identified in early-to-mid Noachian terrains primarily by visible-near infrared (VNIR) reflectance spectroscopy (Bibring *et al.*, 2005, 2006; Poulet *et al.*, 2005; Mustard *et al.*, 2008; Ehlmann *et al.*, 2009; Wray *et al.*, 2009). The occurrence of phyllosilicates in old, heavily bombarded terrains (Mangold *et al.*, 2007; Michalski and Dobrea, 2007; Poulet *et al.*, 2008, 2009; Ehlmann *et al.*, 2009; Fairén *et al.*, 2010) suggests that clay minerals on the martian surface may have experienced shock metamorphism. Shock metamorphism affects the crystal structures of minerals, and thus their spectra (Johnson *et al.*, 2002, 2007; Johnson and Hörz, 2003; Butler and Frost, 2006; Wright *et al.*, 2006), which may explain the ambiguous phyllosilicate identifications on Mars from mid-infrared (MIR) remote sensing data (Friedlander *et al.*, 2012; Sharp *et al.*, 2012).

Recent laboratory work confirms that experimental impacts disrupt MIR phyllosilicate spectra, whereas characteristic smectite VNIR spectral features are retained (Gavin *et al.*, 2013). Previous experiments also demonstrated that thermal alteration causes spectral changes for both phyllosilicates and zeolites, primarily through the processes of dehydration and dehydroxylation (Che *et al.*, 2011; Che and Glotch, 2012). Loizeau *et al.* (2007) hypothesized that dehydration or dehydroxylation may be responsible for the apparent lack of phyllosilicates in one bright outcrop in the western part of Mawrth Vallis. Thus, elevated temperatures or shock-metamorphism may affect the interpretation of remote sensing data from the martian surface. Indeed, it has been demonstrated by laboratory spectroscopy and modeling that pre-existing phyllosilicates can survive post-impact exhumation temperatures (Fairén *et al.*, 2010), but not unaltered, and NIR spectral features from Toro crater ejecta have been found to be consistent with thermally treated nontronite (Gavin and Chevrier, 2010). In addition, a unique spectral feature centered at 450 cm^{-1} in Mars Global Surveyor (MGS) Thermal Emission Spectrometer (TES) data and associated with the detections by the Mars Express/Observatoire pour la Minéralogie, l'Eau, les Glaces et l'Activité (OMEGA) VNIR imaging spectrometer of nontronite-rich deposits around Nili Fossae (Michalski *et al.*, 2010) has been shown to be consistent with nontronite after thermal alteration to 400 °C (Che and Glotch, 2014). Detailed examination of the effects of shock metamorphism on clay mineral spectroscopy may thus provide valuable insights for the analysis and interpretation of martian remote sensing data.

Due to the abundance of nontronite and nontronite-like smectite identifications on the martian surface (Bibring *et al.*, 2005, 2006; Poulet *et al.*, 2005, 2008; Loizeau *et al.*, 2007; Mustard *et al.*, 2008; Mckeown *et al.*, 2009; Carter *et al.*, 2013), this chapter focuses on the spectroscopic effects of experimental impacts on a natural nontronite sample (NAu-1, Clay Minerals Society Source Clay). This work builds on that of Gavin et al. (2013), providing spectroscopic analyses for one clay mineral over a range of impact pressures, using many laboratory and spectral analysis techniques. It also complements the broad spectroscopic analyses performed on thermally altered phyllosilicate and zeolite samples in Che *et al*. (2011) and Che and Glotch (2012).

The use of multiple spectroscopic techniques allowed me to directly investigate the effects of shock pressure on the structure of clay minerals by comparing results from techniques that are sensitive to structural change in different parts of the nontronite structure (Table 1). In particular, spectroscopic techniques in the mid-infrared (MIR) wavelength region, such as emissivity and attenuated total reflectance (ATR) spectroscopy, are sensitive to the Si-O bending

and stretching vibrations of the nontronite tetrahedral sheet (Huang *et al.*, 1999; Bougeard *et al.*, 2000; Bishop *et al.*, 2002a; Palin and Dove, 2004; Michalski *et al.*, 2006), while techniques like VNIR reflectance spectroscopy are sensitive to the overtones and combination bands of metal-OH bonds in the octahedral sheet (Bishop *et al.*, 1999, 2002a; b, 2008a; Frost and Kloprogge, 2000; Petit *et al.*, 2002, 2004; Neumann *et al.*, 2011). The extended visible region (0.3 – 1.0 μm) measures Fe^{3+} crystal-field, electronic transitions that reflect the Fe bonding environment in the octahedral sheet (Burns, 1993) and can be compared to Mössbauer spectroscopic results (Dyar *et al.*, 2008). Thus, by comparing the effects of impacts on the spectral signatures detected by all of these techniques, I can begin to investigate the complex structural changes produced in nontronite by impact alteration. These related structural and spectroscopic effects have important implications for the analysis of remote sensing results from the martian surface and may help explain the differences between ambiguous MIR phyllosilicate detections and definitive VNIR detections.

2.2 Background

2.2.1 Phyllosilicate Identifications on Mars

2.2.1.1 Orbital identifications

In contrast to the detailed and unambiguous identifications of phyllosilicates on the martian surface from VNIR reflectance spectra (Bibring et al., 2005, 2006; Poulet et al., 2005; Bishop et al., 2008a; Ehlmann et al., 2008, 2009; Mustard et al., 2008; Wray et al., 2009), identifications from MIR (5-50 μm) emission spectroscopy have been ambiguous (Bandfield, 2002a; Michalski *et al.*, 2006, 2010; Michalski and Fergason, 2008; Mcdowell and Hamilton, 2009), suggesting low abundances of these minerals. These results contradict the apparently high phyllosilicate abundances estimated by non-linear spectral unmixing (Poulet, 2004; Liu et al., 2014) in regions where strong VNIR absorption features characteristic of phyllosilicates lead to robust identifications (Poulet *et al.*, 2008). For example, Michalski and Fergason (2008) examined TES data for Mawrth Vallis and could not find phyllosilicate detections from TES spectral index mapping comparable to those from OMEGA and CRISM (Compact Reconnaissance Imaging Spectrometer for Mars) data. However, Al-rich phyllosilicate species (and allophane) have been specifically identified by VNIR reflectance (CRISM) spectroscopy and suggested by TES spectral modeling (Rampe *et al.,* 2012; Bishop and Rampe, 2012; Bishop and Rampe*,* 2014a, 2014b). This implies that TES phyllosilicate detections at Mawrth Vallis and elsewhere (e.g., Rampe *et al.,* 2012) may somehow be dominated by Al-rich phyllosilicate spectra, even though Mg/Fe-rich smectites are thought to be one of the most abundant phyllosilicate species on Mars based on VNIR reflectance spectroscopy (Carter *et al.,* 2013). These low nontronite detections thus remain a mystery, despite recent identifications by TES modeling of specific Al- phyllosilicate species. The results presented here demonstrate that impacts can alter the spectral signatures of natural phyllosilicates, providing a mechanism to explain the apparently low abundance of Fe/Mg smectites in TES deconvolution models.

Several hypotheses have been proposed to explain the apparent lack of characteristic phyllosilicate fundamental vibrational bands in MIR spectroscopic data from the martian surface. Michalski and Fergason (2008) suggested three possible explanations: surface roughness, multiple surface temperatures at sub-pixel scales, and low absolute mineral abundances combined with spatial sampling differences. Ruff and Hamilton (2009) also suggested that

phyllosilicates might be present only at or near the TES detection limits of 10 – 20% fractional abundance determined for three smectite clays by Ruff and Christensen (2007). Using spectral linear modeling of the affect of smectite addition in controlled fractional abundances to TES spectra of Arabia Terra, Ruff and Christensen (2007) showed that montmorillonite, nontronite, and Fe-smectite each had to be present at different fractional abundances to alter the generic Arabia Terra TES spectrum in detectable ways. Montmorillonite had to be present in a fractional abundance of at least 15%, nontronite had to be present at an abundance of 20% and Fe-smectite had to present at an abundance of 10% to reach detectable threshold values. Other researchers have found that separating phyllosilicates from other high-silica phases in linear spectral mixture analysis models of TES data at global scales is difficult (Bandfield, 2002a; Wyatt and McSween, 2002; Michalski *et al.*, 2005, 2006). For instance, Bandfield (2002) examined TES data at 1 pixel per degree spatial resolution to determine global mineral distributions, finding a great deal of spectral similarity between phyllosilicates and high-Si glass phases. He also found, however, that certain phyllosilicate species display characteristic vibrational bands in a region of the MIR that is frequently excluded from atmospherically corrected TES spectra. Ruff (2003), however, suggested that recognizing these subtle differences may make MIR phyllosilicate identifications possible at regional to local, rather than global, scales.

Attempts to identify phyllosilicates at regional and local scales using MIR data of the martian surface have been partially successful. Ruff and Christensen (2007) used two spectral indices to differentiate between smectites and TES Surface Type 2 (ST2), a TES average spectrum from 4 – 7 regional locations on Mars, which was originally interpreted as a basaltic-andesite (Bandfield *et al.*, 2000a). They scrutinized the MIR data from regions where phyllosilicate identifications by VNIR reflectance spectroscopy were thought to be unambiguous and found systematic correlations to a spectral index based on long-wavelength phyllosilicate emission features. They did not, however, unambiguously identify phyllosilicates directly using MIR data. More recently, Michalski *et al.* (2010) used VNIR data from OMEGA in combination with TES MIR data to develop a TES spectral index that correlated VNIR reflectance-based phyllosilicate identifications in the Nili Fossae region with spectral signatures from MIR emissivity. However, the TES Nili Fossae phyllosilicate spectra were ambiguous with respect to specific phyllosilicate phases and indicated that phyllosilicates at Nili Fossae were either extremely disordered or were embedded in a matrix of basaltic glass. In later work, Viviano and Moersch (2012) used an approach similar to Michalsk*i et al.* (2010) to map phyllosilicates with the Mars Odyssey Thermal Emission Imaging System (THEMIS). However, they convolved THEMIS with OMEGA and CRISM data and also failed to provide unambiguous phyllosilicate detections from the emissivity spectra alone. Thus, MIR emissivity data from the martian surface have so far offered limited new information to complement robust VNIR identifications, while specific mineral phase identifications directly from MIR spectroscopic data generally remain ambiguous for nontronite-bearing regions. Because impacts have played a role in the geologic history of the martian surface and therefore, martian phyllosilicate mineralogy, and shock metamorphism affects both VNIR and MIR mineral spectra (Johnson *et al.*, 2002, 2007), the effects of shock on phyllosilicate spectra may partially explain this disconnect.

Some recent work using both VNIR and MIR remote sensing techniques has begun to support the hypothesis that martian phyllosilicates may have been structurally disordered by impacts and that this might be affecting their identifications by different remote sensing techniques. First, CRISM phyllosilicate spectra taken at Toro crater and the VNIR reflectance

spectra of nontronite heated to 400 °C were shown to be similar by Gavin and Chevrier (2010). They noted especially that these results implied that Toro crater phyllosilicates predated the impact event, and thus were at least Noachian in age. This supports the hypothesis that phyllosilicates in Nili Fossae are old and might have been structurally disordered by impacts, rather than generated by them (e.g., Michalski et al., 2010). More recently, Che and Glotch (2014) directly matched TES phyllosilicate spectra in the Nili Fossae region with the laboratory emissivity spectra of thermally altered nontronite heated to ~400 °C using a factor analysis and target transformation (FATT) algorithm (Thomas and Bandfield, 2013). These results directly support the hypothesis that impact-induced structural disorder may contribute to the ambiguity of phyllosilicate detections by MIR spectroscopic techniques.

2.2.1.2 Surface identifications

There is only ambiguous Mössbauer evidence for phyllosilicates on the martian surface. In their broad summaries of the results from the Mössbauer spectrometers aboard the Mars Exploration Rovers (MERs) *Spirit* and *Opportunity*, Morris *et al.* (2006a, 2006b) did not identify any specific Mössbauer doublets as representing phyllosilicates. However, one of the Fe^{3+} doublets (Fe3D3) in rocks from the Burns Formation was unassigned, with an isomer shift (δ) of 0.37±0.02 mm/s and quadrupole splitting (Δ) of 0.62±0.03 mm/s. Moreover, rocks at both landing sites contain a doublet assigned by Morris *et al.* (2006a, 2006b) to represent nano-phase ferric oxide (npOx) with $\delta = 0.38\pm0.02$ mm/s and $\Delta = 0.89\pm0.02$ mm/s. Intriguingly, these features closely overlap values reported for various clay minerals, for which there is vast Mössbauer literature (e.g., Dyar, 2002; Dyar et al., 2006, 2008). Consistent with this possibility, Clark *et al.* (2007) presented compelling chemical evidence for the presence of montmorillonite in "Independence class" samples from the Columbia Hills and speculated that "smectite is actually present, but its mineralogical structure has been masked from detection by the MER instrument suite." Thus, it is possible that the mineral assignments made in these Mössbauer papers may be non-unique and so further comparisons of MER results with clay mineral spectra are warranted.

XRD results from the ChemMin instrument aboard the Mars Science Laboratory (MSL) rover *Curiosity* initially failed to directly identify phyllosilicates, but did find an X-ray amorphous, Fe-rich phase that hosts a significant amount of soil volatiles in both the Rocknest aeolian bedform (Bish *et al.*, 2013) and its sand shadow (Blake *et al.*, 2013). More recently, abundant phyllosilicates have been identified by *Curiosity* in the Sheepbed mudstone at Gale Crater (Morris *et al.*, 2014; Rampe *et al.*, 2014; Vaniman *et al.*, 2014). However, specific identifications of individual phyllosilicate species from these XRD patterns have not been possible (Rampe *et al.,* 2014; Vaniman *et al.,* 2014). In addition, some of the phyllosilicates identified by *Curiosity* are associated with an X-ray amorphous phase (Morris *et al.,* 2014) whose formation process(es) is (are) not yet well understood. Thus, results from ChemMin confirm the presence of phyllosilicates on the martian surface, while also leaving open questions about their formation and alteration by later processes including, potentially, impacts.

2.2.2 Previous Laboratory Studies

2.2.2.1 Experimental shock and shock metamorphism

During impacts, intense pressure waves pass through geologic material, initiating processes that cause structural modifications and alteration in the affected rocks and minerals, propagating existing defects and increasing structural disorder (Gault and Heitowit, 1963;

Stöffler, 1972, 1974, 1984; Hanss et al., 1978; Lange and Ahrens, 1982; Bischoff and Stöffler, 1992; Wright et al., 2011). Pressure and associated heating can also induce transitions to entirely new mineral phases (Coes, 1953; Stishov and Popova, 1961), which have been identified in naturally and artificially shocked geologic materials (Chao *et al.*, 1960, 1961, 1962; De Carli and Milton, 1965; Stöffler, 1971). Laboratory shock experiments have contributed to the understanding of shock metamorphism and related processes since impacts were first recognized as important geologic processes (French, 1968; Stöffler, 1974).

In natural samples, determining whether secondary mineral phases resulted from shock or alteration can be difficult (Bruckenthal and Pieters, 1984). Shock experiments reduce this ambiguity. Laboratory shock experiments also provide important sources of spectroscopic data for remote sensing analysis. In one early set of shock experiments, Adams *et al*. (1979) observed distinct changes in the reflectance spectra of shocked versus unshocked plagioclase, pyroxene, and glass, and they noted the pressures at which these changes occurred. Later researchers, using shock experiments to examine the spectra of different minerals after exposure to the same shock pressures, found that shock effects depend dramatically on the mineral involved. In an investigation of the effects of shock on the MIR emissivity and hemispherical reflectance spectra of feldspar and pyroxene, for example, Johnson *et al.* (2002) found that experimental impacts up to 63 GPa produced fewer spectral changes for pyroxene than for feldspar. Later work by Johnson *et al*. (2007) showed that spectra modeled by multiple end-member spectral mixing algorithms using libraries composed of common mineral and glass spectra replicated the emissivity spectra of shocked basalts reasonably well up to pressures of 20-25 GPa. At higher pressures, their reported model errors increased significantly. However, including spectra from shocked feldspars in the spectral libraries improved fits. Thus, understanding the effects of shock on mineral spectroscopy can help improve remote sensing data interpretation. This may be particularly important for understanding and interpreting martian phyllosilicate identifications.

2.2.2.2 Shock metamorphism of phyllosilicates and phyllosilicate spectroscopy

Relative to the large body of work on the structural and spectroscopic effects of shock on rocks and rock-forming minerals, little work has been published about the effects of impacts on the structure and spectra of phyllosilicate minerals. Early work focused on the effects of shock on the dehydration of phyllosilicates, particularly serpentine (Boslough *et al.*, 1980; Lange and Ahrens, 1982; Tyburczy and Ahrens, 1987). Using IR absorption spectroscopy, Boslough *et al.* (1980) confirmed the release of bound hydroxyl and H_2O from the structures of serpentine, nontronite, and kernite after experimental impacts. They also connected decreased absorbance for both the OH-group stretching and H_2O hydrogen bond resonances in the post-shock spectra of all three minerals to this H_2O loss. Using shock-recovery experiments, Lange and Ahrens (1982) determined the amount of shock-induced structural hydroxyl loss from serpentine as a function of shock pressure between 25 and 45 GPa, and they used IR absorption spectroscopy to confirm these structural changes. Tyburczy and Ahrens (1987) later found that shocked serpentine dehydrates 20 to 30 times faster at martian surface conditions than unshocked serpentine does, showing that impacts and related processes may have played an important role in the geologic evolution of planetary surfaces and atmospheres.

Shock effects have also been invoked to explain the color of the martian surface. In particular, Weldon *et al.* (1982) observed that a sample of Riverside nontronite reddened and darkened after experimental impacts between 18 and 30 GPa. Using optical microscopy, X-ray

diffractometry, ^{57}Fe Mössbauer spectroscopy, and IR spectroscopy, they determined that partial dehydroxylation changed the Fe-coordination state and shifted characteristic Fe^{3+}/O^{2-} charge transfer features into the visible wavelength region, producing a redder, darker nontronite sample. Weldon *et al*. (1982) attributed their results primarily to impact-induced heating. However, later work by Boslough *et al.* (1986) showed that the effects of shock differed from those of heat. Boslough *et al.* (1986) contrasted the effects produced on a sample of Riverside nontronite by experimental impacts between 7 – 32 GPa with the effects produced by heating the sample in air (annealing) between 400 – 1000 °C. They found that both shocked and heated samples of Riverside nontronite showed similar increases in magnetization, but that post-shock samples were structurally distinct from annealed samples, as determined by X-ray diffraction. Both processes altered the nontronite sample's color toward redder and darker. Thus, Boslough *et al.* (1986) suggested that repeated impacts might have altered the properties of nontronite to be consistent with those of the fine dust on the surface of Mars.

Despite the early recognition of their potential importance, detailed laboratory spectroscopic studies of the effects of shock and related processes on phyllosilicates have only recently begun. Initial experiments focused on the effects of thermal alteration on phyllosilicate and zeolite structures and spectroscopy. Che *et al.* (2011) conducted extensive laboratory work exploring changes in the MIR spectra of phyllosilicate and zeolite minerals after heating. Che and Glotch (2012) examined the VNIR spectra of the same thermally altered mineral suite. These and other studies (Moskowitz and Hargraves, 1984; Gavin and Chevrier, 2010; Daly et al., 2011) showed that heating fundamentally alters phyllosilicate spectra, mostly through dehydration and dehydroxylation. However, as early impact-shock experiments showed, the effects of elevated temperatures differ from the effects of pressure (e.g., Weldon et al., 1982; Boslough et al., 1986). Thus, additional work to examine shock pressure effects on phyllosilicate spectra is warranted, especially to improve the current understanding of the ways in which impact processes may variably affect the VNIR and MIR spectra of phyllosilicates.

Recent work by Gavin *et al.* (2013) began to address this by providing direct comparisons between pre- and post-shock phyllosilicate spectra for individual shock experiments. However, these results cannot be associated with specific pressures, because Gavin *et al.* (2013) reported primarily impactor velocity, and modeled impact pressures for only two samples (nontronite and montmorillonite). In contrast, the data presented in this work show the progression of structural change in one natural nontronite sample as a result of experimental impacts at peak pressures from 10 – 40 GPa. These experiments are unvented, which previous work suggests may affect sample devolatilization (Kraus *et al.,* 2013) although the exact effects of vented versus unvented shock-recovery experimental setups are, as yet, unclear (Boslough *et al.,* 1980; Kraus *et al.,* 2013). Nonetheless, this work provides additional information about the relationship between pressure and spectroscopically important structural changes in nontronite. In addition to conducting experiments at a range of pressures, I also used an extensive suite of analysis techniques (Table 1) to explore the post-impact structural and spectral changes in nontronite. I selected each of these techniques (Table 1) to be able to examine nontronite's post-impact structural change at various scales (i.e., nuclear, atomic, crystal, bulk), and relative to characteristic parts of the nontronite structure (e.g., OH vs. Si-O vibrational regions). In particular, I collected and analyzed all laboratory vibrational spectroscopic data. My co-authors collected and/or analyzed data from all other analysis techniques as indicated. Based on the

presented results, I offer a hypothesis that may explain the differences between VNIR and MIR phyllosilicate identifications from the remote sensing of Mars.

2.3 Methodology

The shock-recovery impact experiments that form the basis of this entire dissertation were performed at the FPA at NASA's Johnson Space Center (JSC), which provides unique data on the effects of shock pressure. Joseph Michalski and Thomas Sharp designed the experimental plan, which was carried out by Mark Cintala of the FPA laboratory. By attaining peak pressure through the process of shock-reverberation, the FPA achieves lower peak temperatures than would occur in natural impacts of comparable pressure (Gibbons and Ahrens, 1971). Because each is sensitive to different parts of the phyllosilicate structure, a variety of spectroscopic and analytical techniques (Table 1) was used to analyze the starting material and impact products: X-ray diffractometry (XRD), Mössbauer spectroscopy, VNIR reflectance spectroscopy, MIR attenuated total reflectance (ATR) spectroscopy, MIR emission spectroscopy, and transmission electron microscopy (TEM). Using these analyses, I describe the post-impact structural changes in phyllosilicates that produce detectable spectral changes. At the FPA, shock pressures are derived from projectile velocity and the shock impedances of the flyer plate and sample assembly, using the Rankine-Hugoniot equations (Rankine, 1870; Hugoniot, 1889; Gault and Heitowit, 1963). This provides shock pressure estimates for all of the samples and allows me to associate specific spectral and structural changes with known peak shock pressures.

2.3.1 Sample acquisition and preparation

Natural nontronite sample NAu-1 was purchased from the Clay Minerals Society (CMS) Source Clays Repository. Keeling *et al.* (2000) originally reported the chemical composition of this sample in detail. To remove impurities occurring mostly in the >2 μm size fraction (Moore and Reynolds, 1989), Matt Ferrari, Timothy Glotch's lab technician, ground the sample and separated the < 2μm size fraction by first sieving the sample (to separate the <45μm size-fraction), followed by settling using centrifugation (Moore and Reynolds, 1989). In this technique, particles <20 μm are assumed to approximately obey Stoke's Law and, as a result, centrifugation for various lengths of time controls the size of the particles that settle out of suspension. Smaller particles are retained in the supernatant. Moore and Reynolds (1989) describe the complete process in greater detail. After it has been separated by size, the sample can then be washed with acetic acid to remove carbonate impurities. NAu-1 nontronite contains an Al-rich contaminant, which has previously been identified as kaolinite and may also provide a source of octahedral aluminum (Keeling *et al.*, 2000). The processed nontronite sample used in these experiments contains ~16 wt% kaolinite, as determined by David Bish using the reference intensity ratio method (Chung, 1974) from pre-impact XRD analysis (Figure 2.1).

2.3.2 Impact Experiments

Impact experiments were conducted using a shock-reverberation setup at NASA's FPA facility at JSC. Sample powders were pressed into pellets and loaded into stainless steel sample containers that were individually milled to match the dimensions of the pellet. Pressed pellets reduce the initial porosity of the sample, reducing the entropy added to the system by pore collapse. On average, 0.15 g of sample were used in each shock experiment. Stainless steel and fansteel flyer plates were used to produce impacts approximating one-dimensional shock (See *et*

al., 2012). Projectiles were launched horizontally at the mounted sample containers and their velocities were measured directly by lasers in the flight path. Measured impactor velocities ranged from 0.872 km/s (10.2 GPa) to 1.349 km/s (39.1 GPa), just prior to impact. These velocities were converted to pressure by one-dimensional shock-stress calculations after Gault and Heitowit (1963), giving shock stress accuracies of ± 1%. The tilt of the projectile must be less than 3° to approximate one-dimensional shock. Duel cameras stationed along the flight path monitored the projectile tilt. Samples from impacts with tilts great than 3° were not used in this study. Thomas Sharp, Joseph Michalski, and Mark Cintala conducted shock experiments at six peak shock pressures between 10 and 40 GPa, as follows: 10.2, 19.7, 25.2, 30.6, 34.6, and 39.1 GPa. After successful experiments, sample containers were cut open, enabling recovery of nearly the entire (0.15 g) shocked sample. I then analyzed the recovered sample using laboratory spectroscopic techniques in the VNIR and MIR wavelength regions. I also used Raman spectroscopy for additional comparative analysis.

2.3.3 Post-impact spectroscopic analysis technique selection

Each of the selected techniques was chosen for comparison to existing or proposed Mars remote sensing instruments, and for detailed investigation of the many parts of the complex nontronite structure (Table 1). VNIR reflectance spectroscopy probes the Fe-electronic transitions between 0.5 and 1.0 μm (0.65 and 0.92 μm for Fe^{3+} in nontronite) (Burns, 1993; Clark, 1999), metal-OH stretching overtones in combination with both bound H_2O and adsorbed H_2O (1.4 μm) (Bishop *et al.*, 1994, 2002a; Bishop and Pieters, 1995; Petit *et al.*, 1999, 2004), H-O-H structural H_2O bend in combination with adsorbed H_2O vibrations (1.9 μm) (Bishop *et al.*, 1994), and characteristic metal-OH combination and overtone vibrations (2.1 – 2.3 μm) (Petit *et al.*, 1999; Bishop *et al.*, 2002a). Most of the identifications of phyllosilicates on the martian surface from VNIR reflectance remote sensing data are based on characteristic metal-OH combination and overtone bands in the 2.17 – 2.36 μm wavelength region. The 1.4 and 1.9 μm features are sometimes used in association with these bands to strengthen phyllosilicate identifications (Bibring *et al*., 2005; Poulet *et al.*, 2005; Mustard *et al*., 2007). Laboratory VNIR reflectance data are comparable to OMEGA and CRISM data, making this a good technique for direct comparisons with martian remote sensing VNIR reflectance data.

ATR spectroscopy provides useful information on phyllosilicate structures in the MIR frequency region, 4000 – 500 cm^{-1} (2.5 – 20 μm), and can detect changes to the nontronite tetrahedral sheet Si-O bends and stretches (1250 – 850 cm^{-1}), bands related to structural H_2O and adsorbed H_2O (1630 cm^{-1} and 3500-3100 cm^{-1}), as well as octahedral sheet metal-O bends, Fe-FeOH bends, and Fe- and Al-smectite OH stretches (650 cm^{-1}, 820 cm^{-1}, and >3500 cm^{-1}, respectively) (Frost and Kloprogge, 2000; Bishop *et al.*, 2002a; b; Neumann *et al.*, 2011). Because it spans both the fundamental and overtone regions and jointly provides information on both the octahedral and tetrahedral sheets, ATR spectroscopy is particularly useful for examining structural change in impact-altered nontronite, especially differences in the effects of impacts on various parts of the nontronite structure.

Laboratory MIR emissivity spectra are comparable to TES and THEMIS data from the martian surface and are sensitive to changes in the characteristic Si-O bending (400 – 550 cm^{-1}) and stretching (~1000 cm^{-1}) modes of phyllosilicate minerals, as well as diagnostic metal-O-Si bends reflective of changes in both the octahedral and tetrahedral sheets in combination (~500 cm^{-1}) (Michalski *et al.*, 2006; Bishop *et al.*, 2008a).

Raman spectroscopy is sensitive to even small changes in the bonding environments of crystal structures (Frost, 1995; Huang *et al.*, 2007; Gavin *et al.*, 2009). A Raman spectrometer will be on the European ExoMars Rover (European Space Agency, 2013) and another Raman spectrometer was recently selected as a fine-scale mineralogical mapping and organic compound detection experiment onboard NASA's Mars 2020 mission (Mustard *et al.*, 2013). XRD data provide information on the long-range structure and crystallographic order of samples, whereas TEM can be used to visually detect impact-induced structures and structural changes at atomic-scales.

Finally, Mössbauer spectroscopy provides information on the Fe-oxidation and electronic states in the nontronite samples after experimental impacts. Mössbauer results can be compared to the crystal-field transitions detected in the visible wavelength region by VNIR reflectance spectroscopy to investigate changes to the Fe^{3+} cation octahedral sites in nontronite (Burns, 1993; Clark, 1999; Keeling et al*.,* 2000). I acquired all VNIR reflectance, ATR, MIR emissivity, and Raman spectra at the Vibrational Spectroscopy Laboratory at Stony Brook University. David Bish acquired all of the reported XRD data at Indiana University, Thomas Sharp acquired all reported TEM data and images at Arizona State University, and M. Darby Dyar acquired all of the reported Mössbauer spectra at Mount Holyoke College.

2.3.4 VNIR reflectance spectroscopy

I collected VNIR bidirectional reflectance spectra of each sample between 0.35 and 2.5 μm (28571 cm^{-1} – 4000 cm^{-1}) on an ASD Instruments (now PANalytical) Field Spec 3 Max Spectroradiometer fitted with an 8-degree field of view foreoptic. This instrument uses three detectors to cover the relevant VNIR wavelength range. A VNIR 512-element silicon diode array for the 0.35-1.00 μm wavelength region, one shortwave infrared (SWIR) camera with a thermoelectrically (TE) cooled InGaAs photodiode for the 1.00 – 1.83 μm wavelength region, and a second SWIR camera with another TE-cooled InGaAS photodiode for the 1.83 – 2.50 μm wavelength region. As a result, the spectral resolution of the instrument also varies by wavelength region. At 0.70 μm, the full-width-half-maximum (FWHM) spectral resolution is 3 nm, and it is 10 nm at both 1.40 and 2.10 μm. For the spectral region 0.35-1.00 μm, the instrument has a sampling interval of 1.4 nm, and for the region 1.00-2.50 μm, it has a sampling interval of 2 nm (ASD Inc*.,* 2010). Both the spectral resolution and sampling intervals of the ASD Field Spec 3 reflectance spectrometer over the 0.35-2.50 μm wavelength region are comparable to, and slightly better, than the spectral resolutions of either the CRISM (6.55 nm/channel) or OMEGA (7 nm – VNIR, 20 nm – NIR) Mars remote sensing instruments. I used a white fluorescent light source to illuminate the samples (ASD Inc., 2010). The reflectance spectra were referenced to an isotropic Spectralon™ calibration target. I set the incidence and emergence angles to 30±2° and 0°, respectively for all measurements. Samples were held in a matte-black painted sample cup that has no reflectance features in the relevant wavelength region. I acquired all of the VNIR reflectance measurements in a sealed glove bag in the presence of Drierite™ ($CaSO_4$ and $CoCl_2$) desiccant grains with continuous (as-needed) N_2-gas inflow to maintain a relative humidity below 15% for the duration of the spectral measurements.

Prior to taking these measurements, I gently ground all of the samples using a mortar and pestle and placed them in a desiccation cabinet with RH=30% in the presence of a synthetic silica bead desiccant for over 100 hours. In this controlled relative humidity environment,

without heating the samples, I expected to reduce the effect of adsorbed H_2O on the nontronite spectra without inducing layer collapse (Morris *et al.,* 2009; 2010; 2011).

In addition, I also performed a continuum removal (embedded in the ENVI 5.1/IDL 8.3 image processing software package) on all of the laboratory spectra. This process assumes that the continuum of the reflectance spectrum is an ideal convex hull overlying the spectrum itself and divides this ideal continuum out of the spectrum (http://www.exelisvis.com/docs/ContinuumRemoval.html). Continuum removal ensures that individual spectral features are being compared from a common baseline, and is a common spectral processing technique for comparing spectral feature transitions between the spectra of multiple samples (Clark, 1999). I also normalized the spectra to one another using the norm_spec command in Davinci (http://davinci.asu.edu/index.php?title=norm_spec), which further ensured that all spectral features were compared from a common baseline. The same processes were also applied to all of the relevant spectral regions analyzed in the detailed band depth comparisons. To analyze the ATR spectral features, I first converted absorbance to reflectance ($R=1/10^{Abs}$) and then performed the relevant spectra analyses and comparison.

2.3.5 MIR ATR spectroscopy

I collected ATR spectra between 4000 and 500 cm^{-1} on a Nicolet 6700 FTIR spectrometer purged of CO_2 and water vapor and equipped with a Smart Orbit single-bounce ATR accessory with a type-IIA diamond ATR element. The sample is pressed against the ATR element to bring it into intimate optical contact with the diamond. IR radiation passes through the diamond and into the sample where it is totally reflected in the frequency regions over which the sample is non-absorbing and is transmitted in frequency regions where the sample absorbs. ATR spectra thus have high spectral contrast and strongly resemble transmission spectra, which they approximate for quantitative purposes (Fahrenfort, 1961).

2.3.6 MIR emission spectroscopy

Emissivity spectra in the MIR range (2000 – 200 cm^{-1}) were collected on a Nicolet 6700 FTIR purged of CO_2 and water vapor, by switching off the attached Globar IR source and measuring the emitted radiation from the heated samples directly. Prior to heating, I pressed the samples into pellets to increase their emissivity contrast and reduce multiple scattering. Heated samples were maintained at ~80°C to provide adequate emissivity signal. Previous work has shown that clay minerals do not fully dehydrate until exposed to temperatures of 100 °C or higher and that spectral change does not occur until well above 100 °C; as high as 500 °C for some phyllosilicate samples (Harris *et al.*, 1992; Fitzgerald *et al.*, 1996; Roch *et al.*, 1998; Rocha, 1999; Carroll *et al.*, 2005; Gavin and Chevrier, 2010; Che *et al.*, 2011; Che and Glotch, 2012). Therefore, dehydration via heating for emissivity measurements was not a concern. I calibrated my spectra using warm (~70 °C) and hot (~100°C) blackbody standards. I used a CsI beamsplitter and DLaTGS detector with a CsI window to acquire all of the emissivity spectra. Spectra were calibrated in the manner of Ruff *et al.* (1997).

2.3.7 Raman Spectroscopy

I used a WiTEC alpha300R confocal Raman imaging system using both 532 and 785 nm lasers with nominal powers of 50 mW (532 nm laser) and 150 mW (785 nm laser) to collect all of the Raman spectra. Matt Ferrari and I both used the 532 nm laser for the pre-impact Raman spectrum of nontronite, but both also found that after exposure to experimental impacts, even at relatively low pressures, the sample generated considerable fluorescence under the 532 nm laser.

I attempted to reduce this fluorescence and improve the detected signal/noise by using a 785 nm laser, despite the lower overall signal that this laser produces. Due to the low overall signal/noise of the impact-altered samples, I selected a 1200 g/mm grating with a 100X microscope objective, both the highest available on the Raman imaging system. For the laser wavelengths used, this combination gives approximate 700 nm (532 nm laser) and 1008 nm (785 nm laser) spot sizes.

2.3.8 Transmission Electron Microscopy

TEM analyses were carried out by Thomas Sharp at Arizona State University. Samples were prepared for TEM analysis by crushing in clean acetone and dispersing the suspension onto a lacey-carbon film support grid. Grids were then dried under a 100 W incandescent light bulb for several minutes before loading into the TEM sample holder. The clay particles were examined using a Philips CM200FEG S/TEM instrument in the LeRoy-Eyring Center for Solid State Science at Arizona State University. Selected-area electron diffraction (SAED) patterns were collected for each particle to determine crystallinity and disorder. Bright-field images were used to investigate particle size and morphology. High-resolution images of (001) lattice fringes were recorded to investigate thickness and order in the clay crystallites.

2.3.9 X-ray Diffraction

David Bish collected all of the presented XRD patterns at Indiana University. X-ray powder diffraction analyses were conducted using a Bruker D8 Advance instrument with CuKα radiation, incident-and diffracted-beam Soller slits, and a SolX energy-dispersive point detector, using a tube power of 45 kV and 35 mA, over a 2-70° range of 2θ with a 0.02° step size. Starting materials were analyzed both as powders mounted in cavities (i.e., random powder mounts) and as oriented deposits on zero-background quartz plates. All shocked products were analyzed only as deposits on zero-background quartz plates, due to the very small amount of sample available. This small amount of available sample led to increased noise in some patterns, especially after impacts at pressures 19.7 GPa and above. All samples were measured in ambient laboratory conditions of approximately 44% relative humidity.

2.3.10 Mössbauer Spectroscopy

M. Darby Dyar acquired all of the presented Mössbauer spectra, and Elizabeth Sklute performed some of the reported analyses of those spectra. Between 7 and 17 mg of each sample (depending on availability) were mixed with sugar under acetone before mounting in a sample holder confined by Kapton® polyimide film tape. Mössbauer spectra were acquired using a source of ~60 mCi ^{57}Co in Rh on a WEB Research Co. model WT302 spectrometer (Mount Holyoke College) at 295K. Results were calibrated against a 25 mm a-Fe foil. Run times were 2-7 days per spectrum, with baseline counts of up to 30,000 after the Compton correction. Spectra were fit with doublets and sextets using the MEX_FielDD program acquired from the University of Ghent courtesy of E. DeGrave. Values for δ and Δ of the doublets were allowed to vary, and widths (full width at half maximum – Γ, mm/s) of all peaks were coupled to vary in pairs. Errors on isomer shift and quadrupole splitting of well-resolved peaks are usually ±0.02 mm/s in natural samples (e.g., Skogby et al., 1992), while peak area errors are ±1-5% depending on the degree of peak overlap. For absolute site occupancy measurements based on peak areas (%), saturation corrections and recoil-free fraction effects may be considered, but samples in this study were prepared as thin absorbers and proper values of the recoil-free fraction (*f*) for these mixed phases were not known, so the areas were not corrected. In this study, the chief interest is in the changes in δ and Δ that occur with shock.

2.4 Results and Interpretation

2.4.1 VNIR reflectance spectroscopy

Experimental impacts altered the structure of nontronite, producing detectable changes in its VNIR reflectance spectrum (Figure 2.2). To accurately compare observed changes in nontronite's spectral features with shock, the reflectance spectra of impact-altered nontronite samples were continuum removed and normalized (Figure 2.2b). This processing ensured that all features were compared from a common basis (Clark, 1999). Smectites on Mars are primarily identified using VNIR spectroscopy by the presence of characteristic features in the ~2.17 – 2.36 μm region, sometimes in association with the 1.4 μm and 1.9 μm hydrated mineral absorptions (e.g., Poulet *et al.,* 2005*;* Bibring *et al.,* 2006*;* Mustard *et al.,* 2008). Because they are so important for phyllosilicate detection and identification, the shifts observed in the 2.2 – 2.4 μm region of the NAu-1 nontronite VNIR reflectance spectrum after impacts at 39.1 GPa have important implications for the interpretation of remote sensing data from Mars. Because these bands derive from characteristic metal-OH overtones and combination, they are also indicative of changes to the Fe^{3+} bonding environment in the nontronite octahedral sheet. For example, the characteristic ($Fe^{3+}Fe^{3+}$-OH) smectite absorption centered at ~2.29 μm shifted to shorter wavelengths, consistent with the formation of an aluminum-bearing amorphous phase and the breakdown of the nontronite octahedral sheet structure at high peak pressures (Figure 2.3). At intermediate pressures, however, the VNIR reflectance results for impact-altered nontronite are more difficult to interpret. Differing effects of shock on the octahedral and tetrahedral sheets of nontronite, as well as interaction with the kaolinite contaminant, both contribute to the observed VNIR absorptions in this region.

The sharp Fe-OH vibrational feature centered at 2.29 μm changes from an initial full-width-half-minimum (similar to full-width-half-maximum measurements, but applicable to reflectance spectra where features are defined by minima instead of peaks) of 0.23 μm to 0.40 μm after shock pressures of 25.2 GPa or higher. A new, single feature centered at 2.2 μm emerges at 34.6 GPa (FWHM=0.14 μm) and broadens further (FWHM at 39.1 GPa = 0.15 μm) at higher pressures (Figure 2.3), consistent with the formation of a secondary amorphous phase. A weaker Al-OH vibrational feature (associated with the NAu-1 kaolinite contaminant) centered at 2.2 μm is retained up to 19.7 GPa and disappears completely between 19.7 and 25.2 GPa, to be replaced by the single 2.2 μm feature at peak pressures of 34.6 GPa and above (Figure 2.3). These results are consistent with structural deformation in the octahedral sheet that begins quickly (at low pressure), but does not completely deform the structure until relatively high peak pressures are achieved. However, the retention of hydroxyl groups by impact-altered nontronite means that the structurally deformed sample still produces a (spectrally different) VNIR reflectance spectrum with metal-OH overtones in the characteristic phyllosilicate region (2.17 – 2.36 μm). The fact that impact-altered nontronite produces a spectroscopically distinct spectrum and is structural deformed rather than completely dehydroxylated, has important implications for martian remote sensing.

Band center and intensity shifts in the extended visible wavelength region of the impact-altered nontronite VNIR reflectance spectrum provided further evidence for structural change in the nontronite octahedral sheet after impacts. Nontronite has two characteristic Fe^{3+} crystal-field absorptions at 0.65 and 0.87 μm that are attributed to octahedrally coordinated Fe^{3+} cations

(Burns, 1993). At shock pressures of 19.7 GPa and above, a broad, asymmetric feature centered at ~1.0 μm replaces nontronite's two Fe^{3+} crystal-field absorptions (Figure 2.2). This may be explained by partial dehydroxylation or destruction of the Fe^{3+} coordination geometry within the nontronite octahedral sheet (Che *et al.,* 2011*;* Che and Glotch*,* 2012*;* Friedlander *et al.,* 2012), or by the production of nanophase iron oxides (Morris *et al.,* 1985) as a result of impact alteration and shock (Gavin and Chevrier*,* 2010; Gavin et al.*,* 2013). The observed changes in the metal-OH vibrational features between 2.2 and 2.4 μm, however, support a structural change interpretation favoring distorted Fe coordination geometry without complete OH-group loss (metal-OH vibrational bands are still detected). In addition, the Mössbauer data show no evidence for the presence of npOx. It is also possible that the impact-altered nontronite sample has been deprotonated, without significant structural change, but if this were the case, then the intensity of the nontronite crystal field transition (CFT) features should increase because O^{2-} is a higher-field ligand than OH (Burns, 1993) and this is not observed. In addition, no features related to OH-group vibrations would be observed in a completely deprotonated sample.

In addition to mineral-specific identifications, the positions of metal-OH vibrational bands in clay mineral spectra have also been used to identify characteristic cations (Bishop *et al.,* 2002). Changes in the shapes and locations of these bands have been attributed to varying Fe/Mg abundances (Poulet *et al.,* 2005). It is possible, however, that variability in band shape and location might also be due to impact-shock. The changes to the nontronite 2.29 μm Fe-OH vibrational feature that I describe above are similar to the shifts in band-depth and center attributed by Poulet *et al.* (2005) to changes in the Fe/Mg abundance ratios of the phyllosilicate deposits that they identified on Mars. Therefore, I propose impact-shock as a possible alternative explanation for variations in the depths and locations of the 2.2-2.4 μm region bands in martian phyllosilicate spectra. In addition, the presence of Al in the natural nontronite sample used in these experiments has a strong effect on the band center of the broad metal-OH band that emerges after impacts at 39.1 GPa (Figure 2.3). Because the same nontronite sample was used throughout these experiments, I know that the impact-altered, high-pressure samples are still iron rich (and this is confirmed by Mössbauer spectroscopy), but an amorphous, Al-rich phase dominates the VNIR reflectance spectra. This has implications for the identification of Al-rich phyllosilicates in heavily bombarded regions of Mars (Rampe *et al.,* 2012; Bishop and Rampe, 2014a) because it is possible that structurally deformed, iron-rich phases may be present, but not detected in these regions.

2.4.2 MIR ATR spectroscopy

MIR ATR spectroscopy probes both the hydroxyl and silicate parts of the phyllosilicate structure. High-frequency features between 3000 – 3700 cm^{-1} are associated with O-H stretches from structural H_2O or metal-OH stretching (Clark *et al.*, 1990). Lower-frequency features arise from Si-O stretching (1000 cm^{-1}), metal-metal-OH deformations (908 – 742 cm^{-1}), Si-O-metal bends (~500 cm^{-1}), and long-range silicate lattice deformations (~600 – 400 cm^{-1}) (Clark *et al.,* 1990; Bishop *et al.*, 2008b).

The nontronite ATR spectrum changed dramatically above 19.7 GPa shock pressure (Figure 2.4). The broad (structural H_2O) O-H stretching band at 3400 cm^{-1} substantially weakened at pressures above 19.7 GPa, which is consistent with the trend observed for both the 1.4 and 1.9 μm hydration absorption features in the VNIR reflectance spectrum of nontronite. In contrast, the 1630 cm^{-1} H_2O H-O-H bending absorption feature was retained up to 39.1 GPa,

although this was probably due to the presence of adsorbed H_2O on the surfaces of the analyzed phyllosilicate grains. The intensities of the sharp Si-O-Fe bending features (484 cm^{-1}) decreased by nearly 80% after exposure to experimental impacts with the relatively low peak pressure of 19.7 GPa (Figures 2.4 and 2.6), reflecting the combined effects of structural deformation in both the octahedral and tetrahedral sheets of the nontronite structure. The Al-Fe-OH (908 cm^{-1}), Fe-Fe-OH (808 cm^{-1}), and Mg-Fe-OH (742 cm^{-1}) deformation features (second shaded region in Figure 2.4, labeled "dioctahedral OH bending fundamental region") were reduced to a single broad shoulder after impacts at 25.2 GPa or higher. Because all of these spectral changes occurred over a range of peak pressures, I hypothesize that impact shock structurally deformed different parts of the nontronite structure at different rates. However, both the tetrahedral and octahedral sheets are severely deformed by impacts at pressures of 30.6GPa and higher. Thus, I also hypothesize that structural degradation after impacts does not proceed in a completely progressive, step-wise manner (like thermal alteration). Rather, that characteristic components of the structure may be maintained until a high pressure 'tipping point' (>19.7 GPa) is reached, beyond which nontronite becomes spectrally amorphous, but not completely devolatilized.

The ATR spectra of post-shock nontronite also demonstrate spectral differences between clay minerals. Due to the presence of the common Al-rich (kaolinite) contaminant, it is possible to compare the effect of shock pressure on iron in the nontronite structure with that on aluminum in kaolinite. Although the strength of the Fe-OH stretching band at 3550 cm^{-1} progressively declines from a 10.0 GPa shock onward, an Al-FeOH stretching band at 3620 cm^{-1} emerges with increasing contrast from the shoulder of the broad nontronite 3400 cm^{-1} hydration band. Unlike their Fe-OH counterparts, the band depths of Al-OH features do not decrease until after impacts at pressures of 19.7 GPa and above, and they re-emerge as the amorphous Al-rich secondary phase begins to form at peak pressures of ~35 GPa. The Al-Fe-OH deformation feature at 908 cm^{-1} also persists to 19.7 GPa and above (as a weak shoulder on the 1000 cm^{-1} Si-O stretch). Retention of Al-OH features suggests that Al-phyllosilicates may be more structurally resilient after impacts than Fe-rich clays. This result is consistent with previous research on the thermal alteration of clays (e.g., Gavin and Chevrier., 2010), which has shown that the Al-OH bond is stronger than the Fe-OH bond (Haynes and Lide, 2010). Similar effects have also been observed after weathering clay minerals in acidic conditions (Altheide *et al.,* 2010; Craig *et al.,* 2014).

2.4.3 MIR emission spectroscopy

MIR emission spectroscopy is primarily sensitive to structural deformation in the tetrahedral sheet of nontronite. Because it is dominated by silicate bends and stretches, MIR emission spectroscopy provides the most information about changes to the Si bonding environment within the interconnected rings of SiO_4 silicate tetrahedra that make up the nontronite tetrahedral sheet. Initial deformation begins more slowly in the tetrahedral sheet. The MIR emissivity spectrum of nontronite after an impact at 10.2 GPa peak pressure still contains many diagnostic features (Figure 2.5). However, total structural degradation occurs much more rapidly in the tetrahedral than in the octahedral sheet of impact-altered nontronite. After a 19.7 GPa shock, the emission spectrum of nontronite changed substantially, and diagnostic spectral features could no longer be detected. The Si-O stretching band around 1000 cm^{-1} became progressively broader with increasing shock pressure, but could always be detected. This implies that Si-O bonds are retained even as the ordered structure of the silicate tetrahedral begins to break down. This is largely consistent with, if more rapid than, the changes to the nontronite octahedral-sheet observed using ATR and VNIR reflectance spectroscopy, and described in the

preceding sections. There is some evidence from solid-state chemistry that MIR spectroscopic techniques are particularly sensitive to structural disorder (Tarte *et al.*, 1990). More importantly, however, MIR spectroscopic techniques are uniquely sensitive to changes in the bonding environment of a clay mineral's tetrahedral sheet. As a result, the more rapid deformation of the tetrahedral sheet relative to the octahedral sheet (Figure 2.6) produces spectra at intermediate peak pressures that resemble amorphous silicates in the MIR (Figures 2.4 and 2.5), while retaining characteristic Fe-OH nontronite bands in the VNIR (Figures 2.2, 2.3 and 2.4).

2.4.4 Band depth change comparisons between multiple spectroscopic techniques

Impacts induced structural deformations in different parts of the nontronite structure at different rates, producing measurable differences in the changes to band depths and band center for characteristic spectroscopic features, as measured by multiple spectroscopic techniques (Figure 2.6). In particular, deformation of the octahedral sheet begins more quickly (at a lower pressure), but progresses more slowly than deformation of the tetrahedral sheet (Figure 2.6b, c, and d). The effect of adsorbed H_2O on these results is clear (Figure 2.6a), but the changes observed in the 1.4 and 1.9 μm absorption features trend with octahedral sheet and metal-OH interaction deformations (Figure 2.6b, and d). Therefore, it is likely that both hydration state changes and changes to the OH-group bonding environment as a result of impacts may have contributed to the shifts observed for these bands. This result has important implications for detecting the smectite-to-illite transition and diagenesis by remote sensing using the 1.4 and 1.9 μm hydration bands as proxies for relative hydration state (e.g., Milliken, 2014). Such results should be interpreted with caution due both to the complexities of the bands themselves and to the possibility of combined processes, which may produce similar spectroscopic results.

Changes in band depth may also result from increasing grain size (Clark, 1999). This is especially important to note for the nontronite samples described in these experiments because I observed that the finely ground original sample powder was occasionally physically pressed into large flakes by the experimental impacts, especially at high peak pressures. However, comparisons between VNIR reflectance spectra taken separately of these post-impact flakes and spectra of the bulk sample indicated that there were no significant spectral differences between the two. This indicates that the observed differences between the pre- and post-impact VNIR reflectance spectra of the analyzed nontronite sample arise from impact-induced structural changes and not pressure-related physical changes to the sample. These results further indicate that post-impact nontronite may still be identified as either a semi-amorphous phyllosilicate, hydrated amorphous silicate, or a smectite of indeterminate species by VNIR reflectance spectroscopy using the presence of the broad ~2.2 μm band (in combination with 1.4 and 1.9 μm hydration features), even after experimental impacts up to 39.1 GPa. Most importantly, however, at intermediate impact pressures, differing effects of shock on the tetrahedral and octahedral sheets of the nontronite structure produced seemingly contradictory spectral results. In particular, MIR spectra resembled non-specific hydrated amorphous silicates after the tetrahedral sheet deformed, but characteristic nontronite vibrational bands from the more resilient octahedral sheet were still detected by VNIR reflectance spectroscopy.

2.4.5 Raman spectroscopy

With iron-rich minerals (such as nontronite), the sensitivity of Raman spectroscopy to small changes in the bonding environments of samples often results in high fluorescence and low signal/noise. I attempted to mitigate these effects by using a 785 nm laser, but still found that

useful Raman spectra were extremely difficult to collect from samples exposed to impacts above 10 GPa. These results confirm the observations of Gavin *et al.* (2013), who found that many of their samples produced nearly "featureless" Raman spectra. They attributed these results to, "…irregular fracturing, imperfections, amorphous phases, and/or water in the samples." Gavin *et al.* (2013) did not conclude that the changes observed in their Raman spectra were produced by impact-shock, but they suggest that this may be the case. Based on the characteristic pre-impact Raman spectrum and post-impact 'featureless' spectra (Figure 2.7), I find that Raman spectroscopy is extremely sensitive to shock-induced structural change, that post-impact clay minerals do not produce interpretable Raman spectra, and that this is likely a direct result of their exposure to experimental impacts.

2.4.6 Transmission-electron Microscopy

TEM images of both shocked and unshocked nontronite samples were acquired (Figure 2.8). The dispersed particles of unshocked nontronite are poly-crystalline aggregates with complex morphologies and significant structural disorder. These particles are aggregates of (001) flake-like crystallites (Figure 2.8a, d, g) with curled edges that expose packets of clay layers suitable for HRTEM imaging of the (001) lattice fringes (Figure 2.8c, f, i). Selected area electron diffraction (SAED) patterns of the aggregate particles consist of nearly continuous rings corresponding to reflections in the [001] zone axis (Figure 2.8b, e, h), which indicates that the particles are aggregates of oriented (001) flakes. The continuous rings in the [001] patterns indicate turbostratic disorder (rotation about the [001] stacking direction) within and among the clay crystallites that make up the aggregate. HRTEM imaging of some nontronite crystallites show packets of (001) lattice fringes indicating clay crystals up to about 60 nm thick (Figure 2.8c). The complex and disordered structure of these unshocked particles makes documentation of shock–induced deformation difficult.

The onset of shock deformation is visible in samples shocked to 19.7 and 24.6 GPa, but the shock-induced changes are subtle. Morphologically, the particles of nontronite shocked to 19.7 and 24.6 GPa are nearly the same as the unshocked material, but the crystallites are generally smaller and more disordered (Figure 2.8d-i). SAED patterns, like those of the unshocked nontronite, show turbostratic disorder in their (001) zone-axis patterns. The SAED patterns have the same inner rings as the unshocked material (4.4 Å and 2.5 Å), but the diffraction intensity is weaker, and the higher order rings are absent (Figure 2.8e, h). This loss of diffraction intensity indicates loss of structural order. HRTEM images showing (001) lattice fringes indicate that the crystallites are smaller and more deformed than those observed in the unshocked material. Samples shocked to 30.6 and 35.6 GPa have similar morphologies, but the crystallite sizes and the diffracted intensities of higher-order rings are further reduced. Some patterns have only one diffuse ring, indicating nearly complete amorphization. HRTEM imaging shows curved crystallites up to 20-30 nm thick, but they are fewer than in lower pressure samples.

Nontronite shocked to 39.1 GPa is morphologically similar to samples from 35.6 GPa, but SAED indicates that the samples are predominantly amorphous (Figure 2.8g-i). SAED patterns generally show no distinct diffraction rings, indicating that the material is almost completely amorphous. Figure 2.8h shows an example where the ~ 4.4 Å ring is barely visible, indicating some local crystallinity. Many HRTEM images are consistent with a complete loss of long-range order, but some crystallites with visible (001) lattice fringes are present (Figure 2.8i).

As observed in other samples, the shock effects are heterogeneous and the local regions of nano-crystallinity may not be representative of the bulk 39.1-GPa sample. These results are consistent with the progressive onset of structural deformation occurring in different parts of the nontronite structure at different rates.

2.4.7 X-ray Diffraction

XRD data for the pre-impact nontronite sample (Figure 2.1) show features typical of nontronite, with an 001 peak at ~15.2Å (~6° 2θ) and a variety of ***hkl*** bands reflecting turbostratic stacking (e.g., the 02***l***, 11***l*** band beginning at ~19.5° 2θ, and the 06***l***, 33***l*** band at ~60.8° 2θ). The 15.2 Å basal spacing (001) is consistent with two layers of H_2O molecules in the interlayer region (data measured at 44% relative humidity). The data also reveal the presence of kaolinite, whose 001 and 002 reflections are indicated. XRD data for the post-impact samples are compared with those for the pre-impact material in Figure 2.9. These data reveal no significant modifications to the structure after impacts up to 10.0 and 19.7 GPa, as reflected by the persistence of the basal and ***hkl*** features. Data for the samples shocked at 25.2 GPa and above show a gradual intensity decrease and broadening of the 001 reflection, loss of detail for ***hkl*** features, and gradual increase in a broad scattering feature from ~15-40° 2θ. Such a broad feature is generally indicative of the presence of an amorphous phase (Ohashi *et al.*, 2002; Music *et al.*, 2011; Rouff *et al.*, 2012), and this scattering feature probably reflects the increasing, progressive amorphization of the nontronite and kaolinite with increasing peak shock pressure. The minor feature near 44.6° 2θ is from the sample substrate. All samples were analyzed at approximately the same relative humidity (44±4%). The intensity of the 001 reflection gradually decreased as a function of pressure, and Figure 2.9 also illustrates that the width of the 001 reflection increased significantly from 19.7 to 34.6 GPa. The value of d(001) also decreased slightly as a function of pressure, from ~15.3Å in the untreated material to ~14.4Å at 25.2 GPa and 13.9Å at 34.6 GPa, showing that all materials other than the 39.1 GPa sample retained the ability to incorporate interlayer H_2O molecules. Due to the small amounts of available sample, the *y*-axes for some patterns (Figure 2.9) were expanded by a factor of four to increase the contrast in these figures and demonstrate that characteristic peaks are still present.

2.4.8 Mössbauer Spectroscopy

Earlier Mössbauer studies of other ferruginous smectites, including nontronite (Bishop *et al.*, 1999) fit nontronite spectra with four Fe^{3+} doublets, namely two octahedral (~90% of the total Fe) and two tetrahedral (~10%). The presence of tetrahedral Fe^{3+} was also supported by the existence of a band near 22000 cm^{-1} (0.45 μm) in their optical spectra. However, subsequent chemical analyses (Bishop *et al.*, 2002b; c, 2008a; Dyar *et al.*, 2008) showed sufficient Si and Al ions to fill all tetrahedral sites, and Bishop *et al.* (1999) noted some heterogeneity in their nontronite sample. In light of this equivocal evidence for the site occupancy of Fe in nontronite, several different methods were initially used to fit the Mössbauer spectra in this study, using the same methods employed in Dyar *et al.* (2008). As in the 2008 study, attempts to model both octahedral and tetrahedral Fe^{3+} doublets resulted in large values of c^2 and random changes in doublet areas, δ and Δ. Two-doublet models with only octahedral Fe^{3+} doublets produced the lowest values of χ^2 and the most systematic changes in δ with temperature.

Results of the current study therefore reproduce the results of Dyar *et al.* (2008) in the unshocked material (Table 2). A majority (88%) of the Fe^{3+} in this sample is in the doublet with parameters of δ = 0.37 mm/s and Δ = 0.34 mm/s. A smaller doublet initially has 12% of the total

area, with parameters of δ = 0.37 and Δ = 0.69 mm/s. Because Δ generally increases with site distortion (Dyar *et al.*, 2006), this latter doublet is interpreted to be a more distorted local environment in the nontronite six-coordinated sites. As the intensity of the shock increases to 19.7 GPa, Fe^{3+} partitions away from the low-Δ doublet and into the higher-Δ doublet (Figure 2.10). At 25.2 GPa and above, there is no occupancy of an undistorted site with low Δ; instead, a third type of site that is even more distorted occurs with δ = 0.35-0.36 mm/s and Δ = 1.14-1.19 mm/s. These results show that Fe^{3+} in nontronite remains fully oxidized at all shock pressures, but the Fe^{3+} parameters suggest that the octahedral site is increasingly distorted.

2.5 Discussion

2.5.1 Observations from the Use of a Natural Nontronite Sample: Contaminant Effects

The nontronite standard NAu-1 is known to contain kaolinite (Keeling *et al.*, 2000). Contaminant effects are a major drawback of using natural mineral samples in laboratory spectroscopy. Through careful band assignments, however, it is possible to identify the spectroscopic features associated with kaolinite and use them to compare the effects of shock on kaolinite with those observed for nontronite. In general, I found that kaolinite bands were detected more strongly after higher-pressure impacts than nontronite bands were. I interpret this to mean that the kaolinite structure may be better able to withstand the disordering effects of impacts, and that kaolinite is less susceptible to spectral change after experimental impacts, which is consistent with the relative strengths of Fe-OH (weaker) versus Al-OH (stronger) bonds (Lide, 2010). This is in contrast to the results reported in Gavin *et al*. (2013), who found that their nontronite sample partially retained its structure, whereas the structure of their post-impact kaolinite sample was shown by XRD to be completely destroyed. The difference between these and Gavin *et al.*'s (2013) results may be explained by the fact that the nontronite sample in (Gavin *et al.*, 2013) was exposed to an impactor velocity of 3.27 km/s, which they modeled as corresponding to a peak pressure of 17.5 GPa, whereas the kaolinite sample was exposed to a higher impactor velocity of 4.3 km/s, although velocity and stress (i.e. pressure) cannot be directly compared (Kraus *et al*., 2013). I also hypothesize that the presence of Al in the analyzed nontronite sample may be partially responsible for the broad singlet feature centered at ~2.2 μm that emerges in the VNIR reflectance spectra of NAu-1 exposed to impacts at 34.6 GPa or higher (Figure 2.5). The fact that Al-based bands dominate the spectrum of an Fe-rich material after impact at high pressures has important implications for the interpretation of planetary remote-sensing data. In the case of the sample used for these experiments, the altered high-pressure spectrum of nontronite, which is dominated by an amorphous Al-bearing, hydrated silicate, would imply that it is Fe-poor, when it is in fact impact-altered, Fe-rich nontronite in the presence of a potentially Al-rich, amorphous secondary phase.

2.5.2 Comparison of Shock and Thermal Alteration

The effects of thermal alteration on clay mineral structure and spectroscopy have been extensively addressed by previous laboratory spectroscopy work (Boslough et al., 1986; Gavin and Chevrier, 2010; Che et al., 2011; Daly et al., 2011; Che and Glotch, 2012). These results showed that thermal alteration proceeds via the dehydration and dehydroxylation of clay mineral structures, eventually leading to layer collapse and the formation of amorphous phases, followed by the recrystallization of secondary phases, such as cristobalite, hematite, and anorthite (Gavin and Chevrier, 2010; Che *et al*., 2011). In contrast, my results suggest that shock produces

different structural and spectroscopic changes in nontronite than those produced by thermal alteration. This conclusion supports the early findings of Boslough *et al*. (1986), who first observed that color change in shocked nontronite samples differed from that induced by annealing (thermal alteration). It also suggests that the color changes observed in shocked nontronite by Weldon *et al.* (1982) were likely a result of both shock-induced stress and thermal alteration rather than shock-induced thermal alteration alone. It is important to understand the effects of shock and temperature as separate processes because (with the exception of very large impacts), the non-linear relationship between pressure and temperature in impacts makes it unlikely that shocked material would experience temperatures significantly higher than 500 °C for extended time-periods (French, 1998). One important exception to this is localized heating in sample pore-spaces. As Gavin *et al*. (2013) showed, it is possible to reach extremely high, but very spatially localized temperatures in samples exposed to impact shock. For this reason, they concluded that their results showed the combined effects of temperature and pressure. However, in these experiments, peak pressure was achieved by shock-reverberation, which produces less entropy (Kraus *et al.,* 2013) and results in lower peak heating (Gibbons and Ahrens, 1971). Although I could not directly measure the peak temperatures achieved during these impact experiments, previous work has shown that shock-reverberation sample holders only reach temperatures in the range of 130 – 200 °C (Raikes and Ahrens*,* 1979; Boslough *et al.,* 1980), which are not hot enough to devolatilize bound OH from nontronite (Frost *et al.,* 2002). Thus, I suggest that the observed structural (and spectral) changes to the natural samples used in these experiments were generated primarily by shock, and not high temperatures. Further work is warranted to explore the different effects of these two processes on phyllosilicate structure and spectroscopy. However, the distinct spectral changes that I report, and the differences between them and those reported for thermally altered nontronite, demonstrate that shocked and thermally altered phyllosilicates are spectroscopically distinct up to pressures of ~40 GPa and both should be accounted for in future analyses of planetary remote sensing data.

2.5.3 Implications for the Remote and In-Situ Sensing of Mars

The presented results indicate that structural deformation as a result of impact shock occurs in different parts of the nontronite structure at different rates. The onset of deformation in the octahedral sheet is quick, at the relatively low peak pressure of 10.2 GPa, but slow. Characteristic Fe-OH bands are detectable at pressures up to 25.2 GPa. In contrast, deformation of the tetrahedral sheet begins slowly, but progresses quickly. By peak pressures of 19.7 GPa, the intensity of the Si-O-Fe bending feature (500 cm^{-1}) decreased by >70%, while the Si-O-Si bending feature (430 cm^{-1}) was undetectable (Figure 2.6). At these same pressures, characteristic Fe-OH features from the octahedral sheet of nontronite can still be detected in the VNIR wavelength range (Figure 2.6b and d). As a result, impacts of intermediate peak pressures can produce spectrally amorphous MIR detections, which may correspond with characteristic nontronite detections using VNIR reflectance spectroscopic techniques. In addition, impact alteration eventually produces an amorphous secondary phase, an Al-bearing (possibly also Fe-bearing, though this is unclear) amorphous hydroxylated silicate. This secondary phase dominates the spectrum of impact-altered nontronite after experimental impacts at high pressures.

There are two important implications for the remote sensing of the martian surface that can be derived from these observations. First, shocked phyllosilicate spectra should be included in the spectral libraries used to identify minerals from planetary remote sensing data. Shocked

nontronite is spectrally distinct from un-shocked nontronite and should be included as a distinct end-member. It is therefore important to acquire a complete library of laboratory-shocked phyllosilicate spectra. Second, impact-alteration and related processes may explain the challenges experienced by researchers attempting to identify phyllosilicates from TES and THEMIS MIR spectral data. Impact-induced structural disorder, which deforms the octahedral and tetrahedral sheets of nontronite differently, produces different spectral effects in the MIR and the VNIR wavelength detection regions. Because MIR remote sensing techniques are primarily sensitive to the Si-O fundamental bending and stretching vibrations of the tetrahedral sheet, while VNIR reflectance techniques are sensitive to characteristic metal-OH combination and overtone bands, structural deformation in the tetrahedral sheet, but not the octahedral sheet may lead to spectrally amorphous MIR detections, but unambiguous VNIR detections.

These results also have important implications for the specific identification of clay minerals by characteristic cation-OH absorptions (e.g., Poulet *et al.,* 2005*;* Bishop *et al.,* 2008a). They also show that impact-induced structural disorder causes the spectrum of Fe-rich NAu-1 nontronite to become dominated by a secondary Al-bearing amorphous silicate phase. The effects of shock on the sample's kaolinite contaminant produce this phase, demonstrating the complexity of interpreting spectral results from shocked mineral mixtures (and natural samples). This effect may be especially important for heavily bombarded planetary surfaces, which are likely to be made up of mixed mineral components. I thus propose that shock effects may be an alternative interpretation for observed local shifts in metal-OH bands between 2.2-2.4 μm, and I suggest that reconsideration of some mineral specific identifications may be warranted in future remote sensing investigations. The presented results also demonstrate the importance of using multiple techniques (wherever possible) to specifically identify mineral species on remote planetary surfaces. The sensitivity of different remote and *in-situ* sensing techniques to different parts of mineral structures makes comparisons between them particularly important when accounting for the effects of shock and other geologic processes on Mars. IR spectroscopy may not be sufficient to reveal the whole story of martian mineralogy, but should be compared with other techniques, especially as the planetary science community moves closer to missions with sample return capabilities.

The presented Mössbauer results, in combination with the VNIR reflectance spectral results in the extended visible wavelength region, demonstrate that shock changes the coordination polyhedra around the Fe^{3+} cations in nontronite, with site distortion increasing with shock pressure. Parameters of shocked samples must now be recognized to span a broad range of velocities, making unique mineral identifications very difficult. For example, jarosite (δ = 0.37 mm/s and Δ = 1.20 mm/s (Morris *et al.*, 2006a)) has identical parameters to nontronite shocked above 25.2 GPa (δ = 0.35 mm/s and Δ = 1.19-1.23 mm/s). Parameters cited for nanophase Fe oxide at Meridiani and in the Independence Class rocks of Clark *et al.* (2007) (δ = 0.33-0.40 mm/s and Δ = 0.72-1.16 mm/s) span the range of doublet parameters measured in this study from all shock pressures (δ = 0.33-0.37 mm/s and Δ = 0.50-0.75 mm/s). The problem here is that the range of possible Δ values in Fe^{3+}-bearing minerals is relatively small and shock appears to cause even a single mineral to span a large portion of that possible range. If further experiments allow me to generalize this observation and I find that other clay (and silicate) minerals behave similarly, then it greatly complicates (and confuses) the assignment of specific Mössbauer features from the MERs. As with the effects on the VNIR and TIR spectra, an expanded range of parameters associated with shocked samples must now be considered when interpreting martian

remote and *in-situ* sensing data. In addition, the association of MSL-identified phyllosilicates with X-ray amorphous materials (Bish *et al.,* 2013; Blake *et al.,* 2013; Morris *et al.,* 2014; Rampe *et al.,* 2014; Vaniman *et al.,* 2014) raises the possibility of mineral mixtures of altered and unaltered phyllosilicates (and other minerals) on the martian surface. Although the formation mechanisms of these amorphous materials are not yet understood, impact processes should not be ruled out.

2.6 Conclusions

This chapter provides a detailed spectroscopic analysis of the effects of experimental impacts and shock on the structure and spectra of a natural nontronite sample. Both VNIR and MIR spectra show increasing structural disorder with increasing pressure, eventually resembling hydrated amorphous silica (MIR) or an allophane-like phase (VNIR). At intermediate peak pressures, however, VNIR reflectance spectra may still be identified generally as Fe-rich smectite or nontronite. In contrast, MIR spectra much more closely resemble hydrated amorphous silicate phases. This is due to differences between the structural effects of shock on different parts of the nontronite mineral structure. In particular, MIR spectroscopy is sensitive to the more rapid total deformation of the tetrahedral sheet, while VNIR reflectance spectroscopy detects the retention of key features in the more structurally resilient octahedral sheet. TEM imaging, X-ray diffraction, Raman, and Mössbauer spectroscopy all confirm this increasing structural disorder and are consistent with observations implying that shock-induced structural change begins in the octahedral sheet, but proceeds more quickly in the tetrahedral sheet.

These findings provide important additional considerations for future planetary remote sensing and in-situ analyses, although they significantly increase ambiguity and may limit future researchers' ability to make mineral-specific identifications. However, this work advances the ability to distinctly identify shocked versus unshocked nontronite, which may be important to furthering the current understanding of the geologic history of Mars. There are many potential future research directions that arise from these results. I recommend two, in particular. First, more laboratory spectroscopic investigations and analyses are needed to differentiate the spectral and structural effects of shock from the effects of temperature, and to further explore variable effects of shock on different parts of the phyllosilicate structure. Second, detailed remote sensing investigations of heavily cratered regions of the martian surface, particularly locations with strong VNIR phyllosilicate signatures and absent MIR identifications, to look for the spectroscopic signatures of shocked clays may be an important extension of this research. I have already begun investigations of heavily cratered regions using impact-altered phyllosilicate laboratory VNIR spectra, compared to well-described (e.g., Loizeau *et al.,* 2007) CRISM stamps, using FATT and found that some phyllosilicate signatures at Mawrth Vallis are consistent with impact-induced spectral change (Friedlander and Glotch, 2014; Chapter 4 of this dissertation). However, this work is currently undergoing more detailed analyses of the regional geologic context and will be presented in a future paper.

The results of this study build on previous work exploring both thermally and impact-altered phyllosilicates and demonstrate the importance of investigating shock effects in detail, both from the perspective of acquiring data over a range of pressures, and with a wide variety of analytical techniques. I hypothesize that impacts may have altered the structures of martian

phyllosilicates, affecting their spectra in a way that explains the absence of MIR phyllosilicate identifications, even in regions with robust VNIR phyllosilicate spectral signatures.

Chapter 2 – Tables and Figures

Analysis Technique	Wavelength Region	Scale	Sensitive to …	Similar to remote sensing instrument? Y/N (Instrument Name)
Raman Spectroscopy	100-1100 cm^{-1} (100 – 9 μm), 785 nm laser (pre-impact), 532 nm (after)	Atomic	Changes in polarizability, cationic environments	N, but proposed
VNIR reflectance spectroscopy	0.50 – 2.50 μm (20000 – 4000 cm^{-1})	Combined atomic and bulk	Changes in color, hydration state, cation oxidation state or environment, NIR OH and H_2O overtones	Y, OMEGA, CRISM
MIR emissivity spectroscopy	1300 – 200 cm^{-1} (8 – 50.0 μm)	Combined atomic and bulk	Si-O bending and stretching fundamental vibrations	Y, TES, THEMIS
MIR ATR spectroscopy	4000 – 500 cm^{-1} (2.50 – 20.0 μm)	Combined atomic and bulk	OH and H_2O fundamental stretching and bending vibrations, metal-OH fundamental stretches and deformations, Si-O stretch fundamental	N, approximates transmission, good comparison for MIR emissivity results
Mössbauer spectroscopy	N/A (beam energy or counting rate in mm/sec)	Nuclear to atomic	Changes in Fe oxidation state, structural environment	Y, MER Mössbauer spectrometer
TEM	N/A (imaging)	Crystal	Imaging impact-induced deformational features	N
XRD	N/A (counts)	Crystal and bulk identification	Amorphisation, changes in the crystal lattice, mineral identification	Y, Curiosity ChemMin instrument

Table 2.1. Analysis techniques used to investigate the effects of experimental impacts on nontronite structure and spectroscopy and their comparable remote and in-situ sensing instruments for Mars. Commonly used vibrational units are shown; alternative units are listed parenthetically.

		Nontronite Sample:						
Fe^{3+} Doublet	**Mössbauer Parameter**	**Pre-Impact (NAu-1)**	**10.2 GPa**	**19.7 GPa**	**25.2 GPa**	**30.6 GPa**	**34.6 GPa**	**39.1 GPa**
Doublet 1	δ (mm/s)	0.37	0.37	0.36	--	--	--	--
	Δ (mm/s)	0.34	0.34	0.34	--	--	--	--
	Γ (mm/s)	0.46	0.44	0.44	--	--	--	--
	Area (%)	88	85	57	--	--	--	--
Doublet 2	δ	0.37	0.36	0.35	0.33	0.36	0.34	0.35
	Δ	0.69	0.75	0.75	0.67	0.50	0.63	0.71
	Γ	0.23*	0.35	0.43	0.48	0.40	0.38	0.34
	Area	12	15	43	68	55	28	42
Doublet 3	δ	--	--	--	0.36	0.35	0.35	0.35
	Δ	--	--	--	1.14	1.21	1.16	1.23
	Γ	--	--	--	0.36	0.38	0.49	0.46
	Area	--	--	--	32	45	72	58

Table 2.2. Parameters for the 295K Mössbauer spectra of all samples analyzed in these experiments. Not every sample fits iron with every doublet; parameters for doublets that were not needed to fit a given sample's spectrum have been left blank.
*Fixed parameter.

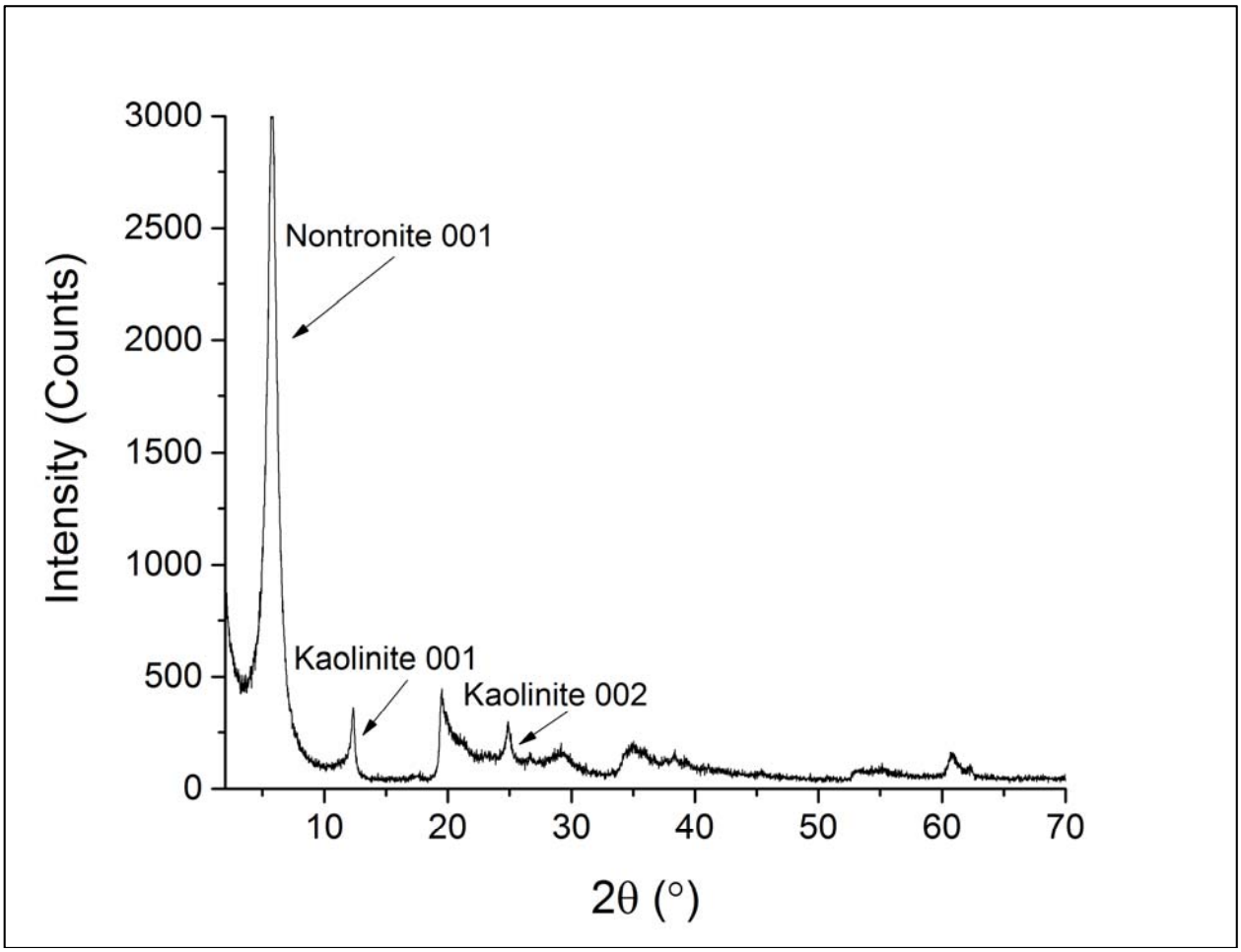

Figure 2.1. XRD pattern of pre-impact, prepared NAu-1 nontronite. The Al-rich contaminant (kaolinite) is identified by characteristic diffraction peaks, the analyzed NAu-1 nontronite sample contains ~16 wt%, as determined using the reference intensity ratio method (Chung, 1974) from the XRD pattern of the prepared, pre-impact NAu-1 nontronite sample.

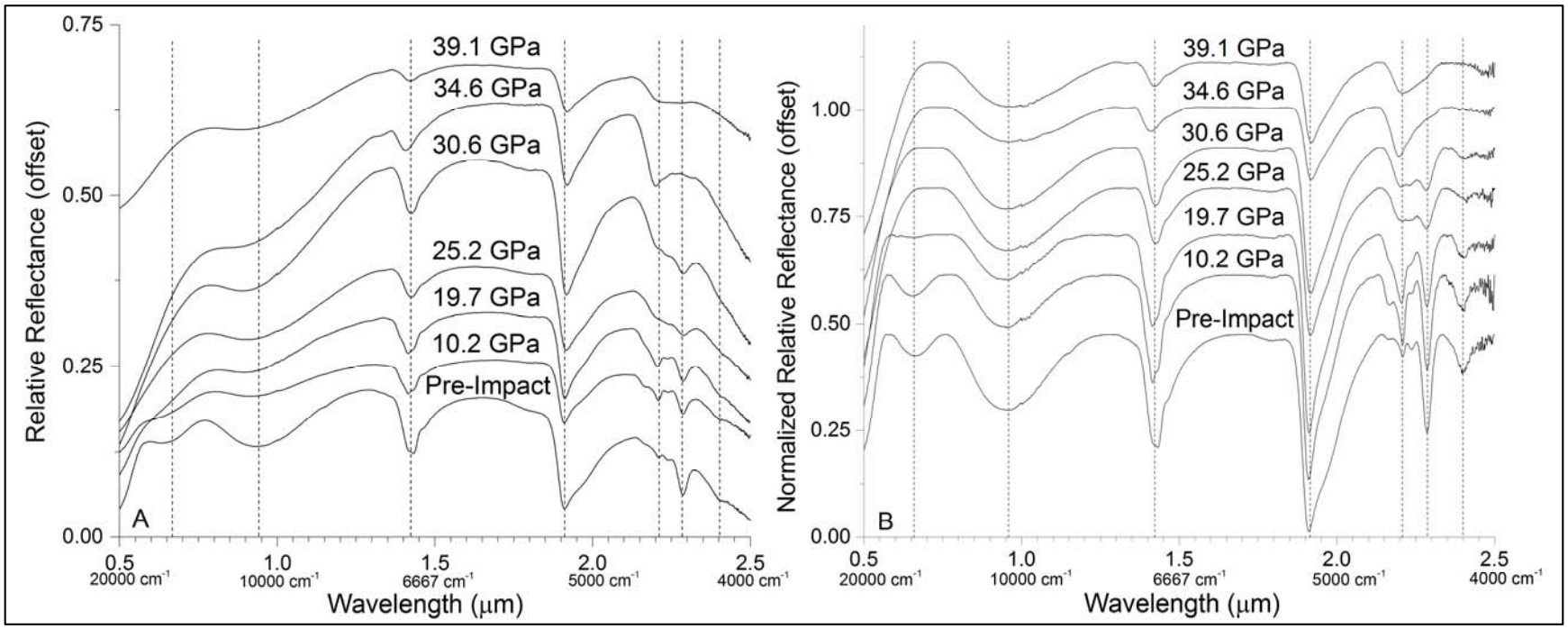

Figure 2.2. VNIR reflectance spectra of NAu-1 nontronite at controlled RH<15% after experimental impacts reaching peak pressures between 10.2 and 39.1 GPa. Raw relative reflectance data (A) are compared to normalized relative reflectance data (B). Continuum-removal (ENVI, IDL) and data normalization (Davinci) improved the spectral contrast of the metal-OH region between 2.2-2.3 μm, which shows increasing disorder in the nontronite octahedral layer with increasing impact pressure. Normalized data also highlight the retention of the HOH bending overtone of structural H2O at 1.9 μm after impacts up to 39.1 GPa. Units in wavenumber (cm^{-1}) have also been provided for secondary reference below the primary X-axis units of μm.

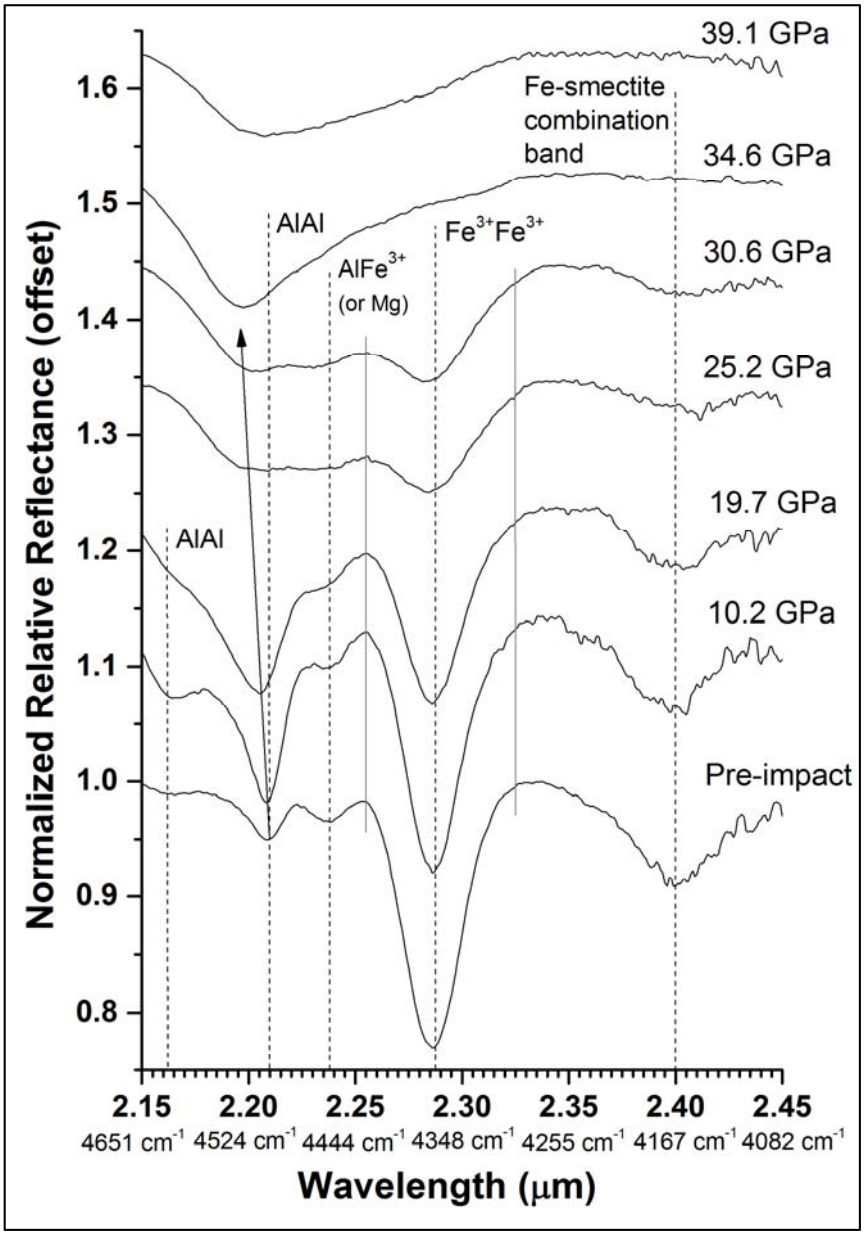

Figure 2.3. Continuum-removed (ENVI, IDL), normalized (Davinci) comparison of characteristic metal-OH vibrational bands in the M-OH vibrational overtone region of the nontronite VNIR reflectance spectrum. Spectra were taken in controlled relative humidity with RH<15%. Band identifications are from (Bishop *et al.*, 2008b; Bishop *et al.*, 2002b). After impacts at or below 30.6 GPa, identifiable metal-OH bands remain; while after impacts 34.6 GPa and above, one broad absorption feature emerges centered at ~2.20 μm. This broad feature is consistent with VNIR reflectance spectrum of allophane, implying that impact-altered ferruginous smectites may appear as hydrated aluminum-rich amorphous silicates to VNIR reflectance remote sensing techniques. Units of frequency (cm^{-1}) are shown for comparison.

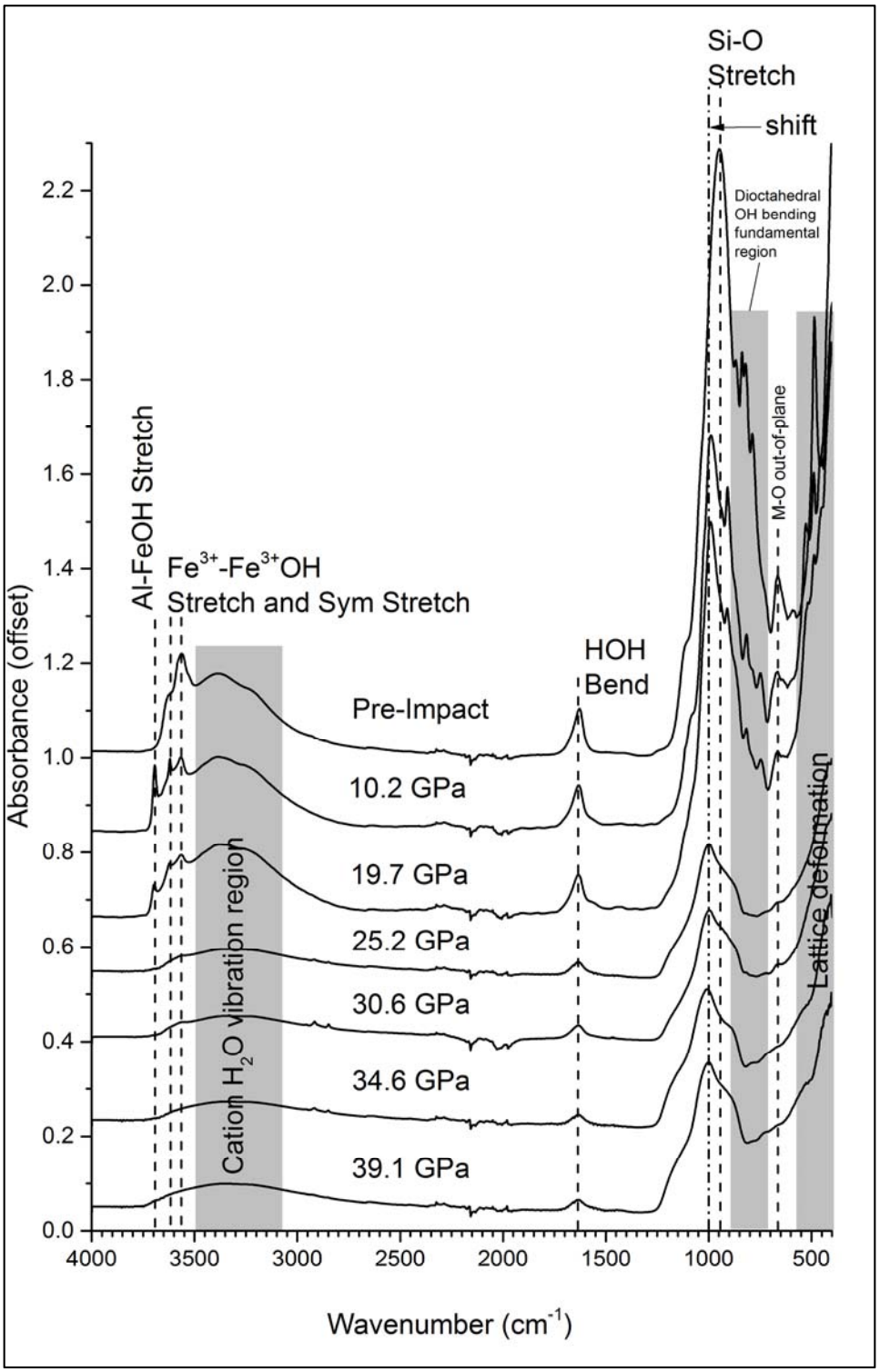

Figure 2.4. MIR ATR spectra of NAu-1 nontronite after experimental impacts reaching peak pressures between 10.2 and 39.1 GPa. Shifts in the Si-O stretching and M-MOH bands are consistent with extensive octahedral layer deformation. Band assignments based on Frost and Kloprogge (2000), Bishop *et al*., (2002a, 2002b), and Neumann *et al.* (2011). The Al-FeOH stretch band (~3700 cm^{-1}) may be related to the NAu-1 kaolinite contaminant (Keeling *et al.,* 2000), but can also arise from tetrahedral Al-substitution in nontronite.

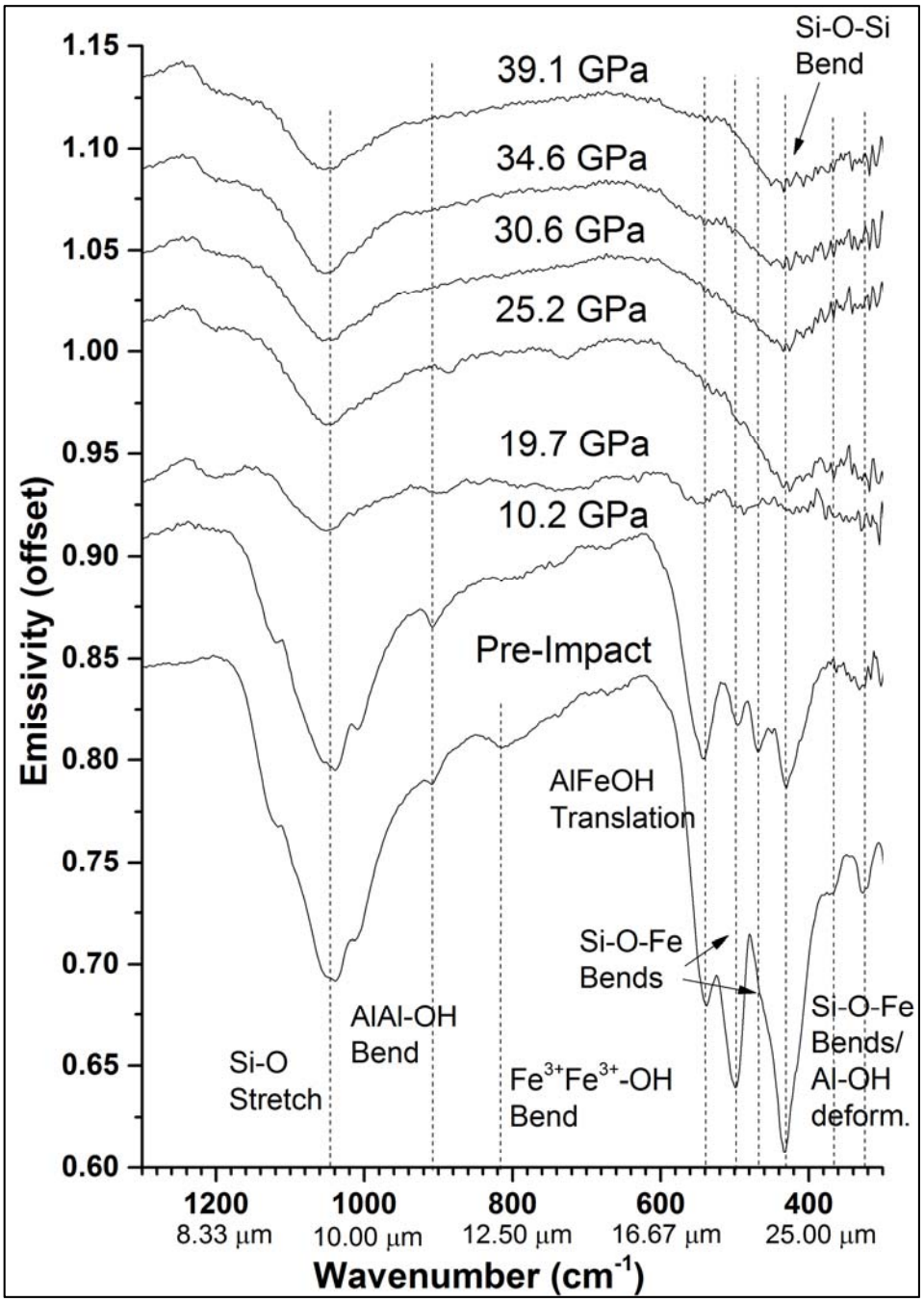

Figure 2.5. MIR emissivity spectra of NAu-1 nontronite after experimental impacts reaching peak pressures between 10.2 and 39.1 GPa. Loss of the characteristics lattice deformation bands of nontronite (600-400 cm^{-1}) and the weak OH bending fundamental bands (950-725 cm^{-1}) supports a hypothesis of increasing octahedral layer disorder with increasing impact pressure. After impacts of 19.7 GPa and higher, the emissivity spectrum of nontronite is indistinguishable from amorphous, hydrated silica. Band assignments were based on (Frost and Kloprogge, 2000; Neumann *et al.,* 2011). Wavelength values (μm) corresponding to standard frequency units (cm^{-1}) have been included for comparison.

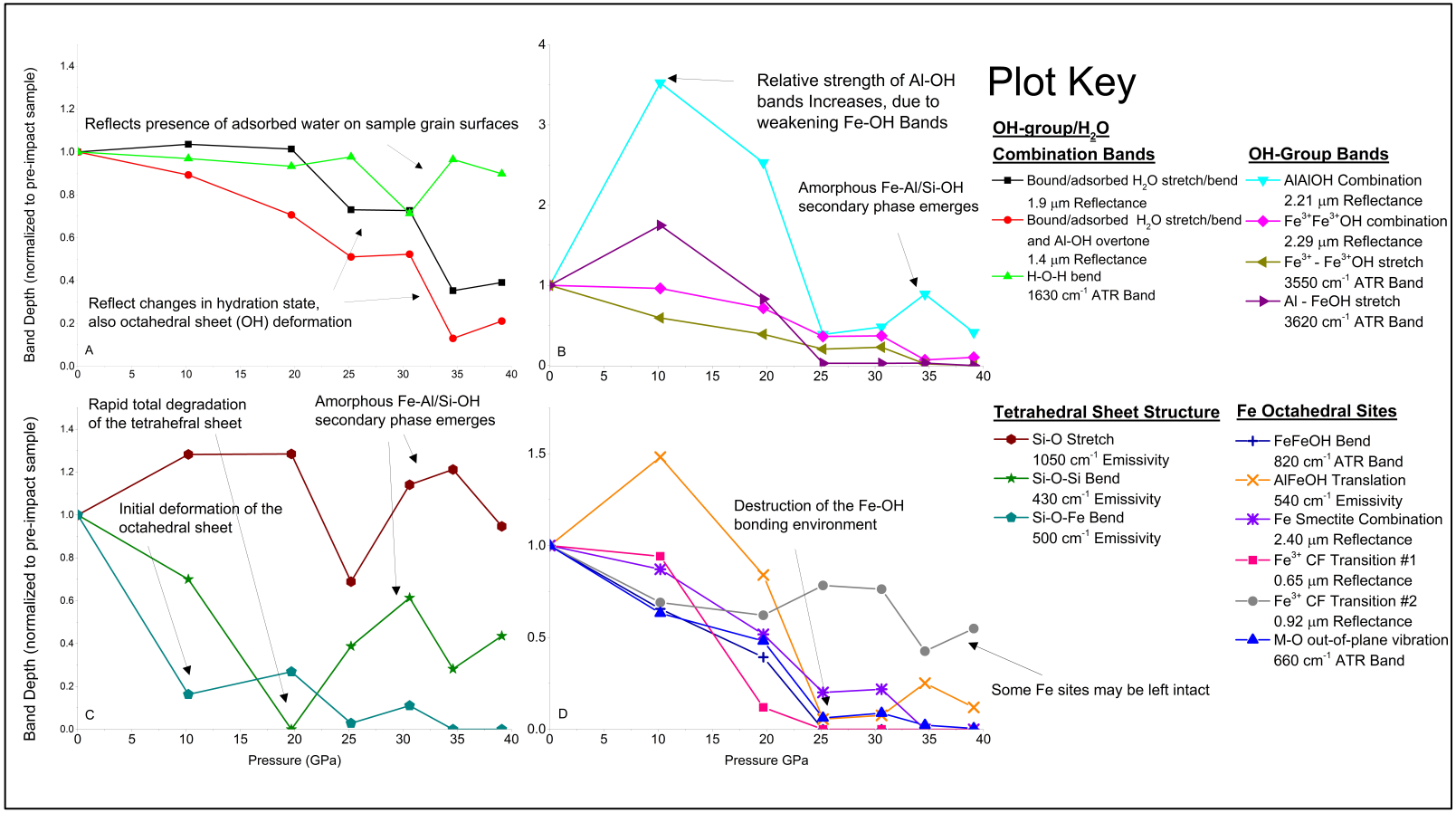

Figure 2.6. Changes in the depths after Pelkey *et al.* (2007) of various characteristic nontronite bands with increasing pressure, reflecting alteration to various parts of the nontronite structure. Bands related to structural H_2O, adsorbed H_2O, and hydroxyl overtone and combination vibrations are shown in (A), bands related to OH-group vibrations characteristic of nearby cations are shown in (B), tetrahedral Si-site vibrations are shown in (C), and bands reflective of the Fe-octahedral environment are shown in (D), although these are also reflected in the changes to the OH-group bands. Because different parts of the structure experience different degrees of alteration with increasing pressure, these band depth changes demonstrate how it is possible to observe seemingly contradictory spectral results from techniques that probe different parts (and length scales) of the nontronite structure. ATR spectra were converted to reflectance before band depths were analyzed by relating reflectance to absorbance ($R=1/10^{Abs}$). All spectra were continuum removed using ENVI/IDL and were normalized in Davinci (excepting the M-O out-of-plane band, which was too noisy to normalize) prior to comparison and analysis.

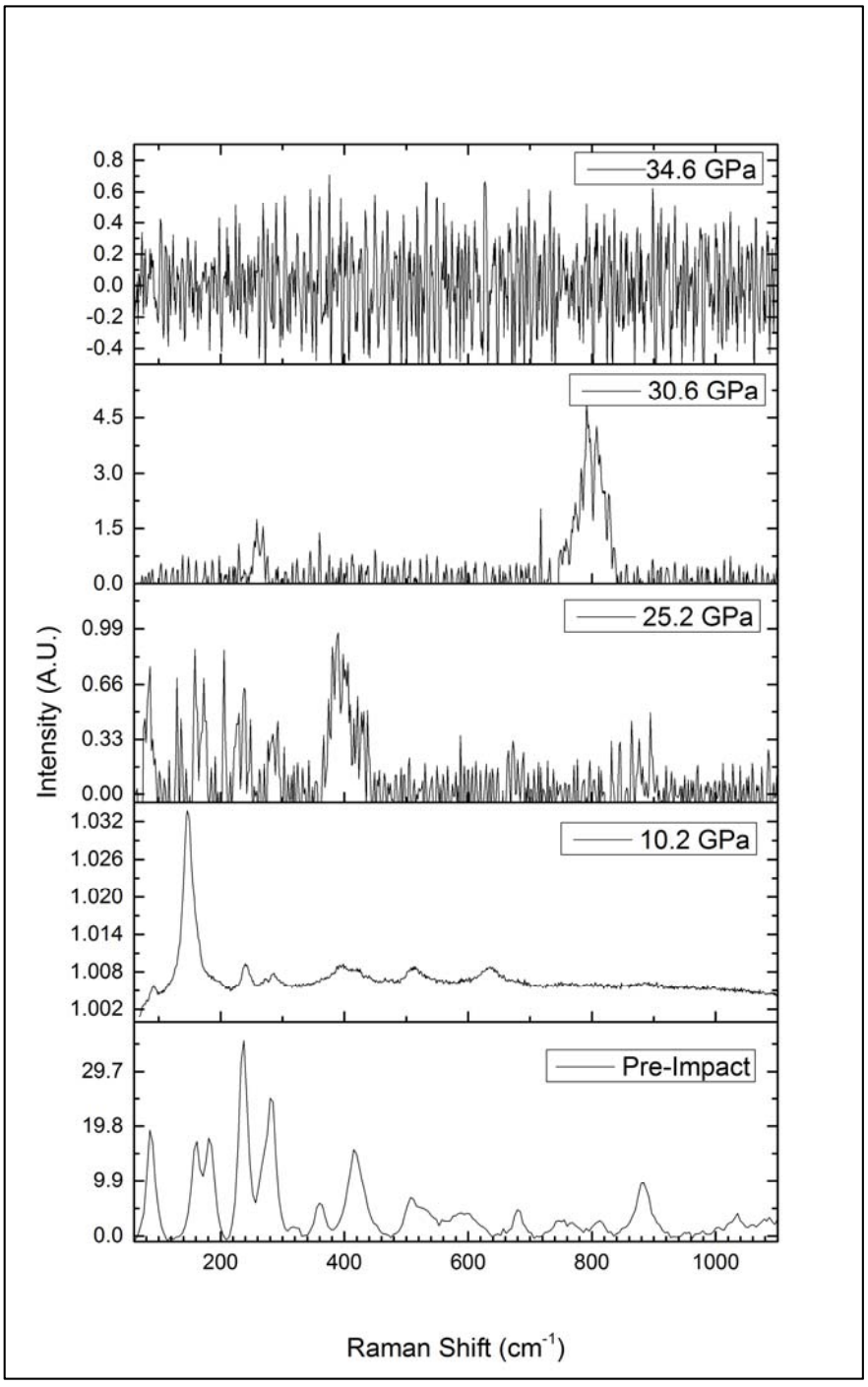

Figure 2.7. Raman spectra of NAu-1 nontronite after experimental impacts between 10.2 and 39.1 GPa, background removal and processing performed in WITec Project Plus software. No signal could be detected for the sample exposed to an experimental impact of peak-pressure 19.7 GPa, so it is not included. The pre-impact spectrum was taken using the 532 nm laser setup, while all post-impact spectra were taken using the 785 nm laser setup to try and reduce fluorescence. Nonetheless, fluorescence increases with increasing pressure, while signal decreases correspondingly.

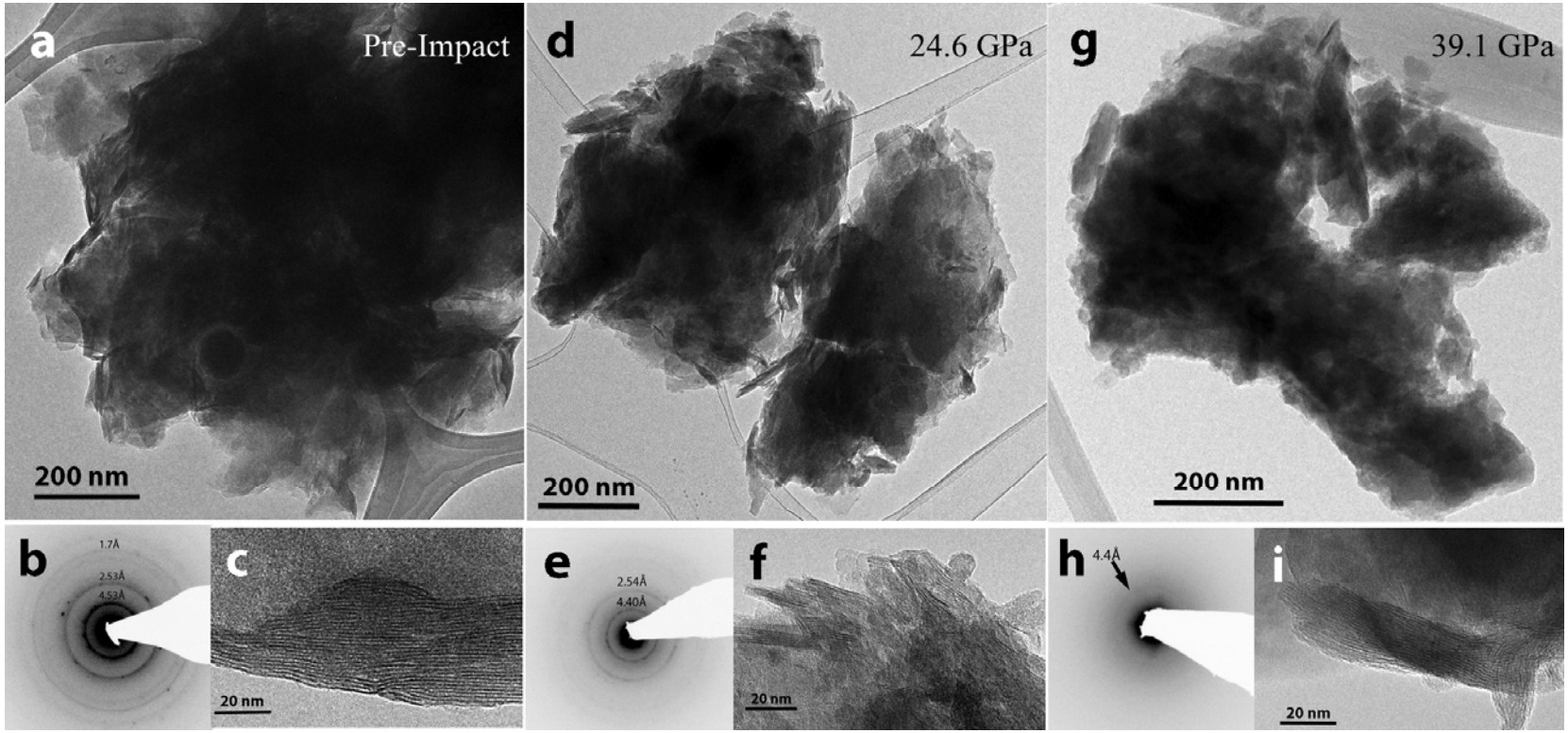

Figure 2.8. Bright field images of aggregate particles of unshocked (a) as well as shocked nontronite after impacts up to 24.6 GPa (d) and 39.1 GPa (g) with associated selected area electron diffraction (SAED) patterns (b, e, h) and HRTEM images of specific crystallites (c, f, i). Both the unshocked and 24.6 GPa samples consist primarily of flat (001) crystallites with curled edges, which appear as fibrous structures around the edges of the flakes in the bright field images (a, d). The unshocked SAED pattern (b) shows rings from reflections in the [001] zone axis with no reflections or rings corresponding to 00l reflections. The continuous rings indicate turbostratic disorder in and between the nontronite crystallites. The ring d-spacings, 4.43, 2.53, and 1.7 Å are illustrated for the unshocked sample (b) for comparison to other SAED patterns (e, h). The HRTEM image of unshocked nontronite (c) shows a 60 nm thick packet of clay (001) layers. The SAED pattern of nontronite shocked up 24.6 GPa shows the same [001] turbostratic ring structure as that produced by unshocked nontronite, but the higher-order ring intensity is somewhat reduced. The HRTEM image (f) shows (001) lattice fringes in smaller and more disrupted crystallites. The SAED pattern of nontronite shocked up to 39.1 GPa on the other hand, has only a trace of the 4.4 Å ring indicating that this aggregate is nearly amorphous. However the HRTEM image of a different particle from this sample (i) shows clear (001) lattice fringes, indicating that some order survives in the clay structure.

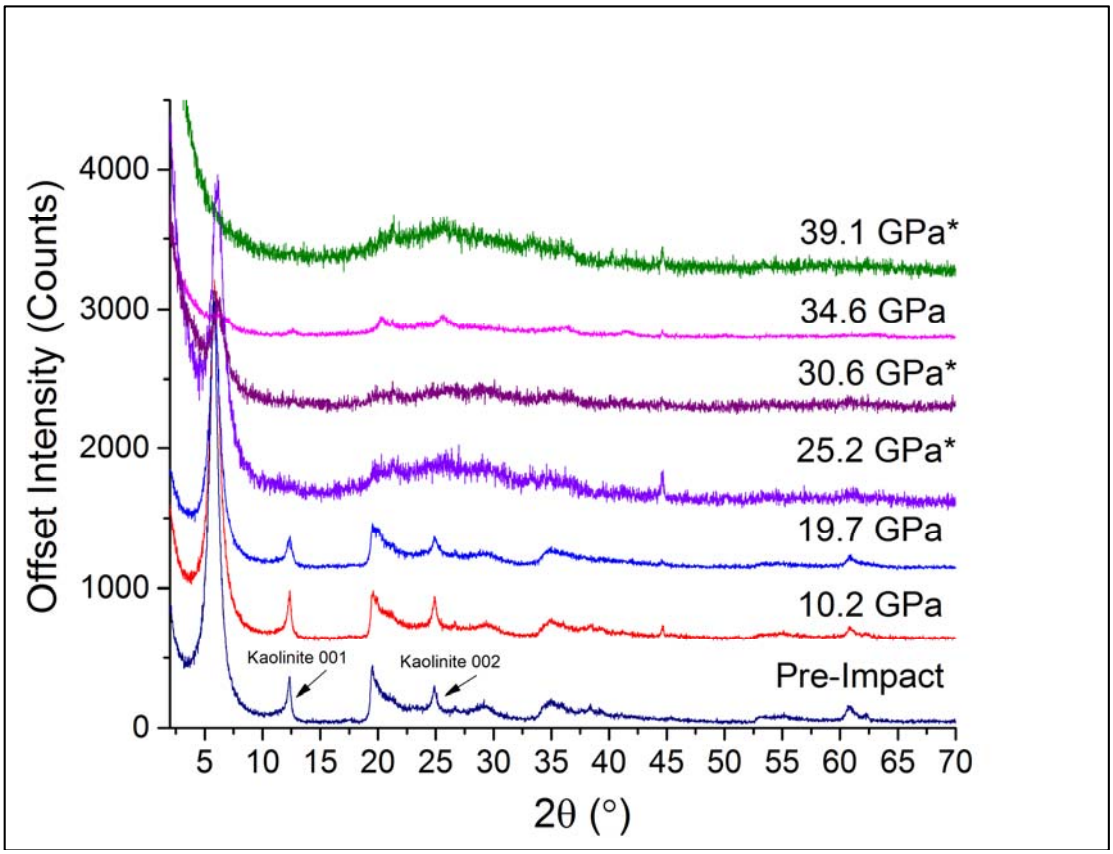

Figure 2.9. X-ray diffraction patterns of NAu-1 nontronite exposed to experimental impacts with peak pressures between 10.2 GPa and 39.1 GPa. Structural disorder, indicated by decreasing peak intensities and peak broadening as well as the emergence of a broad 'amorphous' feature ($20° < 2\theta < 40°$), generally increases with increasing peak impact pressure, but was not observed with XRD below pressures of 25.2 GPa. Small amounts of analyzable sample led to increased noise in some diffraction patterns, especially at impact pressures above 19.7 GPa.
*Intensity expanded by 4.

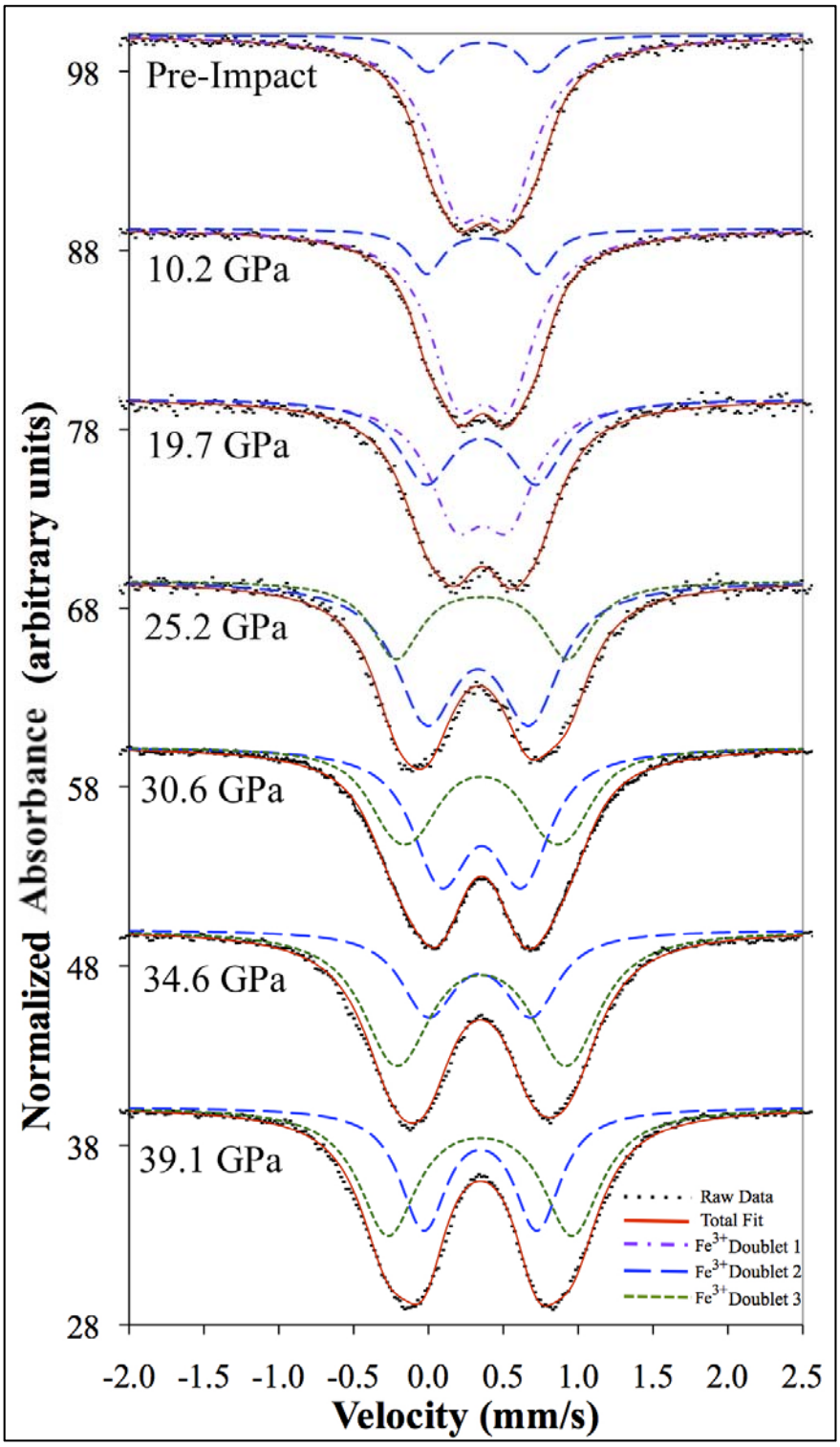

Figure 2.10. Mössbauer spectra of NAu-1 nontronite exposed to experimental impacts between 10.2 and 39.1 GPa. The results indicate that although all iron begins (and remains) in the oxidized, ferric state (Fe^{3+}), the iron coordination geometry in the octahedral sheet becomes increasingly disordered as peak impact pressure increases.

Chapter 3

Comparing structural and related spectral change between iron- and magnesium-rich 2:1 smectites after experimental impacts between 10 - 40 GPa

Much of the material presented in this chapter is currently under review in an edited format at *Clays and Clay Minerals* with co-authors Timothy D. Glotch, Brian L. Phillips, John S. Vaughn and Joseph R. Michalski.

Abstract

Extensive phyllosilicate deposits have been identified on Mars by orbital remote sensing instruments utilizing visible near-infrared (VNIR) reflectance spectroscopy. The detection of clays on Mars may provide clues to past aqueous environments there. Understanding past aqueous activity may be key for understanding martian astrobiological potential. Several lines of evidence suggest that martian clays are ancient (>3.5 Ga) and have been exposed to repeated meteor impacts. In fact, clay minerals are often detected in deposits exhumed by impacts. Impacts alter mineral structures, directly affecting the spectra that are used for mineral identifications on planetary surfaces by remote sensing. This work investigates some of the effects of impact-related shock metamorphism on clay structures and spectroscopy.

The results that I present in this chapter show that the response of 2:1 layered smectites to shock (experimental impacts at 10 GPa ≤ peak pressure ≤ 40 GPa) may depend on composition. Dioctahedral, Fe(III)-rich smectite (nontronite NAu-1) is structurally deformed after impacts at peak pressures of ~40 GPa and its VNIR spectrum ceases resembling that of crystalline, identifiable nontronite. Trioctahedral, Mg-rich smectite (saponite SapCa-2) is structurally resilient and its spectrum remains largely unchanged, even after impacts at peak pressures of ~40 GPa. Results obtained for kaolinite, a 1:1 dioctahedral phyllosilicate, showed that kaolinite is also susceptible to structural and spectral alteration by impacts. This suggests that the dioctahedral sheet may be less resilient than the trioctahedral sheet and, as a result, that dioctahedral clays might be more difficult to accurately detect in heavily bombarded terrains. Spectral changes due to shock and thermal alteration (samples heated stepwise to >900 °C) were also compared. Based on the different spectral changes that each process induces, shock and thermal alteration might proceed via different pathways. The spectral effects of shock and their differences from those of thermal alteration have important implications for the remote sensing of phyllosilicates, especially on planetary bodies where standard methods of comparison between ground-truth and remote sensing data cannot be performed.

3.1 Introduction

Extensive clay mineral deposits have been identified on Mars by orbital visible near-infrared (VNIR) reflectance spectroscopic remote sensing techniques (Poulet *et al.*, 2005, 2009; Clark *et al.*, 2007; Loizeau *et al.*, 2007; Mustard *et al.*, 2008; Mckeown *et al.*, 2009; Wray *et al.*, 2009; Fairén *et al.*, 2010; Michalski *et al.*, 2010; Che and Glotch, 2014). The identification of clays on Mars is exciting because clays may provide evidence for past aqueous environments on the martian surface and/or subsurface, which have potential associations to past or current habitability (Michalski and Dobrea, 2007; Poulet *et al.*, 2009; Grotzinger *et al.*, 2014). Many martian clays are thought to be smectitic because most of the infrared detections of clays on Mars exhibit an absorption near 1.9 μm corresponding to adsorbed and/or interlayer H_2O. Within martian phyllosilicate deposits, one of the most commonly identified phases is an iron-rich smectite similar to nontronite (Carter *et al.*, 2011, 2013). Nontronite has been specifically identified in Nili Fossae (Bibring et al., 2005; Poulet et al., 2005; Che and Glotch, 2014) and Mawrth Vallis (Loizeau *et al.*, 2007). Both of these regions have been heavily bombarded by impacts, and the phyllosilicate identifications in these regions frequently correspond with the evidence of these impacts. For example, Bibring et al. (2006) specifically noted that both in Syrtis Major and Nili Fossae, phyllosilicate-rich rocks are detected within ancient craters, as well as recently excavated ancient terrains. Alone, the association of phyllosilicate deposits with impact craters is not enough to conclusively determine that these deposits are relatively ancient. Indeed, there has been much discussion over whether phyllosilicate deposits associated with impact craters (1) pre- (Fairén *et al.*, 2010) or post-date (Fairén *et al.*, 2010; Marzo *et al.*, 2010) the craters themselves, (2) form as a result of impact-driven (Furukawa *et al.*, 2011) or post-impact alteration (Mangold *et al.*, 2007; Poulet *et al.*, 2008; Fairén *et al.*, 2010), or (3) form as a result of impact-driven hydrothermalism (Tornabene *et al.*, 2013). This debate began with the first identifications of clays on Mars and is ongoing within the planetary science community (Mangold *et al.*, 2007; Poulet *et al.*, 2008; Mustard *et al.*, 2009; Ehlmann *et al.*, 2013; Tornabene *et al.*, 2013). Nonetheless, at the scale of the planetary surface, clays are more common in heavily bombarded terrains on Mars (Carter *et al.*, 2013), and such terrains are though to be ancient (Tanaka, 1986, 2005) as determined through crater counting methods (Hartmann, 1966).

Another line of evidence for the relative age of martian phyllosilicate deposits comes from studies of martian surface geomorphology. Such studies have found that phyllosilicate-bearing units underlie (and therefore pre-date) other hydrated mineral deposits, most of which are thought to have formed in a previous epoch during which the surface of Mars is hypothesized to have been significantly wetter than it is today (Ehlmann *et al.*, 2009; Murchie *et al.*, 2009; Mustard *et al.*, 2009; Wray *et al.*, 2009; Wiseman *et al.*, 2010). It is as yet unclear by how much this epoch may have been warmer than current martian conditions (Fairén *et al.*, 2009; Fairén, 2010).

A third line of evidence for the age of martian clays comes from the technique of crater counting (Fielder, 1963). Comparing martian cratered surfaces to the Moon, where quantitative dates are available (Compston *et al.*, 1970; Tatsumoto, 1970; Tera and Wasserburg, 1972), provides an estimate for the age of heavily cratered terrains on Mars at ~3.5 Ga or older (Hartmann, 1966; Soderblom *et al.*, 1974; Hartmann and Neukum, 2001). Thus, although there is little direct information about the age of clays on Mars, the association of clay minerals with heavily bombarded surfaces marks them as relatively old, and possibly ancient ($\geq$ 3.5 Ga). Further, impacts are a much more important geologic process on Mars than on Earth (Hartmann,

1966; Soderblom *et al.*, 1974). Even if clays are not as ancient as the oldest terrains on Mars, it is still likely that clay mineral deposits experienced alteration as a result of exposure to impacts throughout martian geologic history. Because impact-driven alteration affects the structures and spectroscopic signatures of minerals, impact processes can directly affect the accuracy of clay mineral identifications on the martian surface by remote sensing techniques.

When the intense pressure and heat waves generated by impacts pass through geologic material, they initiate processes that cause structural modifications and alteration. Existing defects may be propagated, and structural disorder increased (Gault and Heitowit, 1963; Stöffler, 1972, 1974, 1984; Hanss *et al.*, 1978; Lange and Ahrens, 1982; Bischoff and Stöffler, 1992). Such structural disorder directly affects mineral spectral signatures (Tarte *et al.*, 1990). To measure these effects, laboratory impact experiments can be used to generate controlled, experimental impacts and associate structural and spectral changes in shocked minerals with known pressures or pressure ranges (De Carli and Jamieson, 1959; Gibbons and Ahrens, 1971; Stöffler, 1972, 1974, 1984; Hanss *et al.*, 1978; Adams *et al.*, 1979; Johnson *et al.*, 2002, 2007; Johnson and Hörz, 2003). Such experiments also provide important sources of spectroscopic data for remote sensing analysis.

Laboratory impact experiments have provided key data on shock effects and processes since impacts were first recognized as a fundamental geologic process (Stöffler, 1972, 1974; Bischoff and Stöffler, 1992). Previous shock experiments have revealed distinct changes in the reflectance spectra of shocked versus unshocked plagioclase, pyroxene, and glass (Adams *et al.*, 1979; Johnson and Hörz, 2003), compared the spectral effects of impacts on pyroxene to those on feldspar (Johnson *et al.*, 2002), and examined the effects of impacts on natural basalt samples, both alone (Johnson *et al.*, 2007) and in comparison to collected samples from impact structures on Earth (Kieffer *et al.*, 1976). Relative to this body of work, very little has been published about the effects of impacts on the structure and spectra of phyllosilicate minerals. This may be due partially to the early belief that layered silicates were largely stable after impacts. Mineralogical comparisons of natural samples from terrestrial impact structures demonstrated that layered silicates showed remarkable stability relative to other minerals, even at shock pressures exceeding 300 kbar (30 GPa). This was explicitly confirmed by investigations of the formation of kinked mica during experimental shock-recovery experiments by Hörz and Ahrens (1969), who showed specifically that, despite large-scale physical deformation, their mica samples remained unchanged at the sub-unit cell scale. Later work on shocked phyllosilicates focused primarily on the role of shock energy and structural deformation on the kinetics and rate of post-shock phyllosilicate dehydration (Boslough *et al.*, 1980; Lange and Ahrens, 1982; Tyburczy and Ahrens, 1987), but not on the potential effects of shock on the structure of the clays themselves.

In planetary science specifically, shock effects have been invoked to explain the color of the martian surface. In particular, Weldon *et al.* (1982) observed that a sample of Riverside nontronite reddened and darkened after experimental impacts between 180 and 300 kbar (18-30 GPa). Using optical microscopy, X-ray diffractometry, ^{57}Fe Mössbauer spectroscopy, and IR spectroscopy, they determined that partial dehydroxylation changed the Fe-coordination state and shifted characteristic Fe^{3+}/O^{2-} charge transfer features into the visible wavelength region, producing a redder, darker nontronite sample. Weldon *et al.* (1982) attributed their results primarily to impact-induced heating. However, later work showed that the effects of shock differed from those of heat. In particular, Boslough *et al.* (1986) showed that post-shock samples

of Riverside nontronite were structurally distinct from samples heated in air for one hour to temperatures 400 – 1000 °C in 100 °C increments, as determined by X-ray diffraction. More recently, work in the planetary science community on both the thermal (Moskowitz and Hargraves, 1984; Gavin and Chevrier, 2010; Che *et al.*, 2011; Daly *et al.*, 2011; Che and Glotch, 2012) and impact (Gavin *et al.*, 2009, 2013; Friedlander *et al.*, 2012, 2014b) alteration of phyllosilicates has revealed intriguing effects on the structure and spectroscopy of impact-altered phyllosilicates that differ between the two processes. In particular, thermal alteration is thought to proceed in a stepwise manner beginning with dehydration (Gavin and Chevrier, 2010; Che *et al.*, 2011; Che and Glotch, 2012), while impact alteration is not. Although the spectral results are consistent with structural deformation in both the octahedral and tetrahedral sheets of impact-altered clays, some vibrational bands associated with OH-groups and structural H_2O are retained. (Friedlander *et al.*, 2012, 2014b; Sharp *et al.*, 2012; Gavin *et al.*, 2013). The responses of phyllosilicates to impact shock have also been shown to depend on the mineral species (Gavin *et al.*, 2009, 2013; Friedlander *et al.*, 2014c). Because impacts have such strong potential effects on mineral structure and spectroscopy, a detailed examination of the responses of different phyllosilicate species to impacts is warranted.

In this chapter, co-authors Brian Phillips and John Vaughn contributed nuclear magnetic resonance (NMR) spectroscopy of shocked and thermally altered phyllosilicates. The addition of NMR spectroscopy, which is a reproducible and extremely sensitive probe of atomic-scale structural disorder in Si-bearing phases, is important for improving my understanding of structural change in silicate phases post-shock. Previously, NMR has been applied primarily to tectosilicates (quartz, feldspar) after experimental impacts (Cygan *et al.*, 1992; Fiske *et al.*, 1998) or as a test of ancient impact hypotheses (e.g., along the K/T boundary) through comparisons of experimental and naturally shocked tectosilicate samples (Boslough *et al.*, 1995). In this chapter, NMR provides unique information about changes to the bonding environments in both the octahedral and tetrahedral sheets of the shocked phyllosilicate species. It is useful especially for comparing between thermal and shock alteration.

The results that I present in this chapter compare and contrast the effects of shock metamorphism on a dioctahedral (nontronite) and a trioctahedral (saponite) smectite. As an added point of comparison, these results are also shown with those for kaolinite, which provides another example of the effect of shock on a dioctahedral clay mineral. I selected these clay minerals to reflect specific detections of clays on the martian surface by remote sensing. Nontronite has been proposed as a best-match for reflectance spectra detected by the Compact Reconnaissance Imaging Spectrometer for Mars (CRISM) from Cape York at Endeavor Crater (Arvidson *et al.*, 2014), and Fe-rich smectite is generally common on the martian surface (Carter *et al.,* 2013). Saponite has been detected in fewer, but still important, regions on Mars such as northern Sinus Meridiani (Wiseman *et al.*, 2010) and, most recently, as a possible component of a martian sedimentary rock from Gale Crater (Archer *et al.*, 2014). Kaolinite has also been identified in several regions of Mars (Murchie *et al.*, 2009; Wray *et al.*, 2009), but primarily provides another reference point, in addition to nontronite, for understanding dioctahedral phyllosilicate alteration after shock.

The selected samples were Clay Minerals Society (CMS) standard clay samples. Such samples are useful for laboratory spectroscopic comparisons because they are well-characterized, representative samples. Comparison to libraries of the laboratory spectra of well-characterized

samples is the most robust method for accurately interpreting remote sensing spectroscopic data, especially from other planets where traditional methods of directly assessing ground-truth, such as sample collection or fieldwork, are impossible (e.g., Bibring et al., 2005; Poulet et al., 2005; Bishop et al., 2008b; Mustard et al., 2008; Arvidson et al., 2014).

Well-characterized, pure materials, however, may not be representative of the martian surface. Despite some results that are consistent with saponite, other X-ray diffraction (XRD) patterns from Gale Crater, Mars, for example, have shown that phyllosilicates in martian mudstones are most-likely poorly crystalline (Rampe *et al.*, 2014; Vaniman *et al.*, 2014). The best available samples to compare to the martian surface are martian (SNC) meteorites, within which there have been many detections of phyllosilicates (Treiman *et al.*, 1993; Brearley, 2000; Thomas-Keprta *et al.*, 2000). The clays identified in martian meteorites, however, often occur as vein-filling or complex matrix components of conglomerate material (Gooding *et al.*, 1990, 1991; Treiman *et al.*, 1993; Thomas-Keprta *et al.*, 2000), making these samples difficult to individually characterize.

Investigating complex processes, such as impacts, using well-characterized materials is much more straightforward than attempting to understand them in complex natural or experimental samples. Studies like that described here provide a better general understanding of the effects of impacts on clay mineral structure and spectroscopy than experiments with more complex samples. For example, this study describes results for multiple phyllosilicate samples, and the impact alteration processes that can be inferred by comparing between them. In addition, NMR and attenuated total reflectance (ATR) spectroscopy were used in combination to directly reveal changes to the clays' cation bonding environments, and to contrast the effects of shock with thermal alteration.

3.2 Materials and methods

All of the phyllosilicate samples used in these experiments were purchased from the CMS Source Clays Repository. Nau-1 was selected as the iron-rich smectite (nontronite) sample. This source clay has previously been described in detail by Keeling et al. (2000). Published compositional data on NAu-1 are also available on the Source Clays Repository website (http://www.clays.org/SOURCE%20CLAYS/SCdata.html). SapCa-2 was selected as the magnesium-rich smectite (saponite) sample, and KGa-1b was selected as the Al-rich, 1:1 phyllosilicate (kaolinite) sample. Compositional data for SapCa-2 and KGa-1b can also be found on the Source Clays Repository website. Samples were selected from the CMS Source Clays Repository because they are well-characterized, generally representative samples of their respective clay mineral species.

3.2.1 Sample Preparation

As described in the previous chapter, Matt Ferrari removed impurities occurring mostly in the >2 μm sample size fraction (Moore and Reynolds, 1989) from all of my phyllosilicate samples by grinding, sieving, and separating them to the <2 μm size fraction after Moore and Reynolds (1989), Che et al. (2011), and Che and Glotch (2012). In a final purification step, he washed the separated clay samples with acetic acid to remove carbonate impurities. As previously discussed, NAu-1 contains detectable amounts of admixed kaolinite and this is one of

the defining characteristics of this nontronite sample. Keeling, *et al.* (2000) estimated the NAu-1 kaolinite abundance at 4 wt%, but Dave Bish estimated that the samples used in these studies contain ~16 wt% kaolinite (Friedlander *et al.* in review; previous chapter). As result, the kaolinite-related spectral features are fairly strong in this material, as described below.

3.2.2 Impact Experiments

The results in this chapter are once again based on impact experiments performed at the Flat Plate Accelerator (FPA) at NASA's (National Aeronautics and Space Administration) Johnson Space Center (JSC), which provides unique data on the effects of shock pressure. By attaining peak pressure through the process of shock-reverberation, the FPA achieves lower peak temperatures (enthalpy) than would occur in natural impacts of comparable pressure (Gibbons and Ahrens, 1971), effectively separating the effects of shock from those of thermal alteration in tested samples. In addition, shock pressures produced by the FPA can be derived using the (known) projectile velocity and the shock impedances of the flyer plate and sample assembly via the Rankine-Hugoniot equations (Rankine, 1870; Hugoniot, 1889; Gault and Heitowit, 1963). This provides shock pressure estimates for all samples, which can be used to associate specific spectral and structural changes with known peak shock pressure values. Peak shock pressures achieved by shock-reverberation, however, differ in both strain-rate and pathway to the Hugoniot from naturally shocked samples, as detailed by Stöffler (1972, 1974), Stöffler and Langenhorst (1994) and Grieve et al. (1996). Despite these differences, shock-recovery experiments remain one of the few methods available to directly investigate shock effects on well-characterized, individual mineral phases. Recent work by Kraus et al. (2013) demonstrated, for example, that deeper understanding of shock-reverberation techniques is required to fully interpret the results of these experiments, while also confirming that the results from variable experimental setups of this kind are likely to be equivalent, especially at low pressures.

Pore space in experimental shock-recovery methods is of great concern due to the high level of variability in both peak temperature and pressure that can be introduced in the pore spaces of an otherwise coherent sample (Kieffer, 1971). For the described experiments, sample powders were pressed into pellets (to minimize pore space) and loaded into stainless steel sample containers that were individually milled to match the dimensions of the pellet. Pressed pellets reduce the initial porosity of the sample, reducing the entropy added to the system by pore collapse. On average, 0.15 g of sample were used in each shock experiment. Stainless steel and fansteel flyer plates were used to produce impacts approximating one-dimensional shock (See *et al.*, 2012). Projectiles were launched horizontally at the mounted sample containers and their velocities were measured directly by lasers in the flight path. Measured impactor velocities ranged from 0.872 km/s (10.2 GPa) to 1.349 km/s (39.1 GPa), just prior to impact for nontronite. Related experimental impactor velocities for saponite ranged from 0.870 km/s (10.2 GPa) to 1.369 km/s (39.8 GPa), and from 0.871 km/s (10.2 GPa) to 1.361km/s (39.6 GPa) for kaolinite. These velocities were converted to pressure by one-dimensional shock-stress calculations after Gault and Heltowit (1963), giving shock stress accuracies of ± 1%. The tilt of the projectile must be less than 3° to approximate one-dimensional shock. Dual cameras stationed along the flight path monitored the projectile tilt. Samples from impacts with tilts great than 3° were not used in this study. Shock experiments were conducted at six peak shock pressures between 10 and 40 GPa for all samples, but specific peak pressures varied by sample and run and are indicated where relevant in all figures and tables. After successful experiments, sample containers were cut open, enabling recovery of nearly the entire ~0.15 g shocked sample.

3.2.3 Thermal Alteration

Thermally altered samples were calcined, or heated under normal atmospheric conditions, in 100 °C increments to temperatures between 100 and 900 °C for 24-hours, then spectroscopically analyzed at the Vibrational Spectroscopy Laboratory at Stony Brook University as described in Che, *et al.* (2011) and Che and Glotch (2012). Data from these experiments are available on the Stony Brook University Vibrational Spectroscopy laboratory website (http://aram.ess.sunysb.edu/tglotch/spectra.html). Spectroscopic results from the calcination of clay and zeolite minerals were previously reported by Che *et al.* (2011) and Che and Glotch (2012), but have been reanalyzed and applied in a different context in the results presented here.

3.2.4 Choice of Analytical Techniques

Impact shocked samples were analyzed using four laboratory spectroscopic techniques. These techniques included VNIR (0.35 – 2.5 μm) reflectance spectroscopy, mid-infrared (MIR; 200-2000 cm^{-1}; 5-50 μm) emissivity spectroscopy, MIR ATR spectroscopy, and NMR spectroscopy. These spectroscopic techniques were used to compare pre- and post-impact samples. Results from experimental impacts were compared to previous work on the effect of thermal alteration on the spectroscopy of clay minerals (Bishop *et al.*, 1994; Gavin and Chevrier, 2010; Che *et al.*, 2011; Daly *et al.*, 2011; Che and Glotch, 2012). Using these techniques, impact-induced structural changes that produced spectral changes were observed directly and described for two 2:1 layered smectites: the iron-bearing smectite nontronite and the magnesium-bearing smectite saponite. The 1:1, dioctahedral phyllosilicate species kaolinite, which contains no interlayer H_2O, provided a comparison to the structural changes observed in the dioctahedral nontronite and was also used in the NMR analyses. XRD results for the effects of shock on both the nontronite sample and saponite sample were presented in prior work (Friedlander *et al.,* 2014b, in review).

3.2.5 VNIR Reflectance, MIR Emissivity, and MIR ATR Spectroscopic Methods

VNIR reflectance, MIR emissivity, and MIR ATR spectra were acquired at the Vibrational Spectroscopy Laboratory at Stony Brook University. VNIR bidirectional reflectance spectra of each sample were collected between 0.35 and 2.5 μm (28571 cm^{-1} – 4000 cm^{-1}) on an ASD Instruments (now PANalytical) Field Spec 3 Max Spectroradiometer fitted with an 8-degree field of view foreoptic. This instrument uses three detectors to cover the relevant VNIR wavelength range. A VNIR 512-element silicon diode array was used for the 0.35-1.00 μm wavelength region, one shortwave infrared (SWIR) camera with a thermoelectrically (TE) cooled InGaAs photodiode for the 1.00 – 1.83 μm wavelength region, and a second SWIR camera with another TE-cooled InGaAS photodiode for the 1.83 – 2.50 μm wavelength region. As a result, the spectral resolution of the instrument varies by wavelength region. At 0.70 μm, the full-width-half-maximum (FWHM) spectral resolution is 3 nm, and it is 10 nm at both 1.40 and 2.10 μm. For the spectral region 0.35-1.00 μm, the instrument has a sampling interval of 1.4 nm, and for the region 1.00-2.50 μm, it has a sampling interval of 2 nm (ASD Inc., 2010). A white fluorescent light source was used in all VNIR reflectance measurements. The instrument produces spectra that are comparable to many orbital reflectance measurements used in remote sensing for data analysis and mineral identification. The collected reflectance spectra were converted to relative reflectance by reference to an isotropic Spectralon™ calibration target. Set incidence and emergence angles of 30±2° and 0°, respectively, were used in all measurements. Samples were held in a matte-black painted sample cup that has no reflectance features in the

relevant wavelength region. All reflectance measurements for a single sample were conducted under ambient laboratory conditions, on a single day with stable RH. The collected reflectance measurements are consistent with fully hydrated samples, but are also stable under dehydrated conditions. Continuum-removal was performed on all collected spectra using ENVI version 5.1 image analysis software for Macintosh and normalized using Davinci version 2.10 (http://davinci.asu.edu) remote sensing data analysis software. These are standard techniques for comparison between reflectance spectra that enable direct comparisons between characteristic spectral features (Clark, 1999) and ensure that comparisons between and among different samples are accurate.

MIR ATR spectra between 4000 and 500 cm^{-1} were collected on a Nicolet 6700 FTIR spectrometer purged of CO_2 and water vapor and equipped with a Smart Orbit single-bounce ATR accessory with a type-IIA diamond ATR element. For this spectroscopic technique, samples are pressed against the ATR element and brought into intimate optical contact with the diamond. IR radiation passes through the diamond and into the sample where it is totally internally reflected in the frequency regions over which the sample is non-absorbing and is partially absorbed in frequency regions where the sample absorbs. As a result, MIR ATR spectra have high spectral contrast and strongly resemble transmission spectra acquired using standard KBr pellet preparation techniques, which they approximate for quantitative purposes (Fahrenfort, 1961).

Emissivity spectra in the MIR range (2000 – 200 cm^{-1}) were collected on a Nicolet 6700 FTIR purged of CO_2 and water vapor, by switching off the attached Globar IR source and measuring the emitted radiation from the heated samples directly. Prior to heating, the samples were pressed into pellets to increase their emissivity contrast and reduce multiple scattering. Heated samples were maintained at ~80°C to provide adequate emissivity signal. Previous work has shown that clay minerals do not begin to dehydrate until exposed to temperatures of 100 °C or higher and that spectral change does not occur until well above 100 °C and as high as 500 °C for some phyllosilicate samples (Harris *et al.*, 1992; Fitzgerald *et al.*, 1996; Roch *et al.*, 1998; Rocha, 1999; Carroll *et al.*, 2005; Gavin and Chevrier, 2010; Che *et al.*, 2011; Che and Glotch, 2012). Dehydration via heating for the purposes of measuring emissivity was therefore not a concern. The collected emissivity spectra were calibrated using both warm (~70 °C) and hot (~100°C) blackbody standards. A CsI beamsplitter and DLaTGS detector with a CsI window were used to acquire all emissivity spectra, which were then calibrated after Ruff *et al.*, (1997).

3.2.6 NMR Spectroscopic Methods

NMR spectroscopic data were collected at Stony Brook University. Data for both ^{29}Si and ^{27}Al were collected for all possible clay samples (excluding iron-rich samples, such as nontronite) and ^{23}Na for the impact shocked saponite. Single-pulse magic angle spinning (SP/MAS) spectra were collected for ^{29}Si with a 400 MHz (9.4 T) Varian Inova spectrometer operating at 79.5 MHz, using Varian/Chemagnetics T3 sample probe assemblies configured for either 7.5 mm or 3.2 mm (o.d.) rotors. Spectra for the heat-treated kaolinite samples were acquired with 8 µs (90°) pulses, 2 s relaxation delays at a spinning rate of 5 kHz. Additional data taken at longer relaxation delay showed no evidence for differential relaxation. For all other samples, the ^{29}Si experiments used 4 µs pulses (90°), relaxation delays of between 2 and 10 s, and 10-12 kHz spinning rates. The ^{27}Al and ^{23}Na SP/MAS NMR spectra were collected using a 500 MHz (11.7 T) Varian Infinity Plus spectrometer operating at 130.3 (^{27}Al) or 132.3 (^{23}Na)

MHz with the sample spinning at 20 kHz in 3.2 mm rotors. The acquisition parameters consisted of 0.5 μs pulses (50 kHz RF field) and 2 s relaxation delays, which correspond to uniform excitation and full relaxation of the central transition. For the shocked kaolinite samples, additional ^{27}Al spectra were acquired with a 700 MHz Bruker spectrometer located in the Stony Brook University Center for Structural Biology. The acquisition parameters included a 0.5 μs single-pulse excitation, 2 s relaxation delay, and 25 kHz spinning rate. Estimated relative abundances of 4-, 5-, and 6-coordinated Al in the impact shocked kaolinite were obtained by fitting both the 500 and 700 MHz spectra with the same set of uncorrelated distributions of NMR parameters (d'Espinose de Lacaillerie *et al.*, 2008).

3.3 Results

3.3.1 Comparison of Spectral Changes Between Post-Impact Nontronite and Saponite

VNIR reflectance measurements of nontronite samples before and after experimental impacts between 10 – 40 GPa (Figure 3.1a) reveal that nontronite is structurally deformed by impacts, producing altered spectra that are distinct from the pre-impact nontronite reflectance spectrum. The acquired spectra also differ as a function of impact pressure. In contrast, VNIR reflectance measurements of saponite after experimental impacts between 10 – 40 GPa (Figure 3.1b) show no change to diagnostic spectral features, and only minor changes overall. As discussed in greater detail in Friedlander, *et al.* (in review) and above, however, nontronite NAu-1 contains a detectable amount of kaolinite contaminant, as well as Al substitution on the octahedral sheet. As a result, characteristic vibrational features associated with the presence of Al-OH groups in the analyzed sample, specifically AlAlOH absorptions at 2.16 (4630 cm^{-1}), 2.21 (4525 cm^{-1}), and 2.23 μm (4484 cm^{-1}), were also observed (Figures 3.1a and 3.2a).

VNIR reflectance spectra cropped to focus on the 2.10 – 2.50 μm (4762 – 4000 cm^{-1}) wavelength region for both nontronite and saponite (Figure 3.2) show the distinct loss of spectral contrast for characteristic nontronite Fe-OH overtone features (2.24 and 2.28 μm; 4464 and 4386 cm^{-1}) and the Fe-smectite combination band (2.40 μm; 4167 cm^{-1}; Figure 3.2a). Al-OH overtone and combination bands related to the NAu-1 kaolinite contaminant weaken, but are retained (Figure 3.2a). In addition, the presence of Al either as a contaminant in the nontronite octahedral sheet, or as an amorphous alluminosilicate phase contributes to the strong, broad band centered at 2.20 μm (4545 cm^{-1}) that emerges in the spectrum of NAu-1 nontronite after experimental impacts up to peak pressures of 39.1 GPa (indicated by the red arrow in Figure 3.2a). In contrast to the changes observed for nontronite, nearly all of the diagnostic Mg-OH combination and overtone bands in the 2.2 – 2.4 μm region of the post-impact saponite VNIR reflectance spectra were retained (Figure 3.2b).

A similar trend was observed for MIR emissivity data compared between post-impact nontronite and saponite (Figure 3.3). At the highest peak pressure of 39.1 GPa, the nontronite emissivity spectra showed a loss of all diagnostic emissivity features (Figure 3.3a), while the saponite spectra retained all diagnostic emissivity features up to peak shock pressures of 39.8 GPa (Figure 3.3b). In contrast to the VNIR reflectance spectroscopic results, even features related to the NAu-1 kaolinite contaminant (<400 cm^{-1}, 540 cm^{-1}, 910 cm^{-1}) are undetected after experimental impacts up to 39.1 GPa.

3.3.2 Comparison of nontronite to another dioctahedral phyllosilicate (kaolinite)

Comparisons between the NIR emissivity and VNIR reflectance spectra of nontronite and kaolinite (Figure 3.4) demonstrated that kaolinite (a dioctahedral phyllosilicate) and nontronite showed similar responses to shock. In particular, kaolinite (KGa-1b), which is a 1:1, unhydrated Al-bearing, dioctahedral phyllosilicate produces emissivity (Figure 4C) and VNIR reflectance (Figure 3.4d) spectra that are consistent with structural deformation similar to that observed for nontronite (Figures 3.4a-b). These results illustrate that other dioctahedral phyllosilicates, in addition to nontronite, are susceptible to shock-induced structural deformation. Impact-induced structural deformation observed in multiple dioctahedral phyllosilicates, but not the trioctahedral smectite saponite, suggests that dioctahedral minerals may be more susceptible to this deformation than trioctahedral minerals, likely due to the high concentration of vacancies in dioctahedral clay minerals. The structural deformation of kaolinite suggested that impact-induced structural deformation is not related to the presence of a hydrated interlayer. Independent kaolinite results are also useful for explaining some of the changes observed in the spectra of NAu-1 nontronite as a result of the kaolinite impurity.

3.3.3 NMR Spectroscopy Revealed Differing Amounts of Deformation Among Clay Minerals

Kaolinite ^{27}Al NMR spectra after impacts up to 40 GPa, compared to saponite ^{27}Al NMR spectra after impacts in the same pressure range (Figure 3.5) showed that each of these clay species experiences different degrees of structural deformation as a result of exposure to experimental impact shock. In particular, unshocked kaolinite had an NMR spectrum consistent with nearly all of the Al in the sample occupying the octahedral sheet. The predominant NMR peak had a chemical shift corresponding to that of 6-coordinated Al, except for a small peak consistent with tetrahedral Al near 71 ppm (0.5%). This may arise either from an impurity phase or a small amount of Al substitution in the tetrahedral sheet. After impacts up to 39.6 GPa, nearly one-half of the Al (47±5%) transitioned to 4- and 5-coordinated sites (Figure 3.5a). In contrast, nearly all of the Al signal from the unaltered saponite sample arises from 4-coordinated Al in the tetrahedral sheet. A small peak for 6-coordinated Al is observed near +5 ppm from Al substitution in the octahedral sheet, representing about 2 percent of the Al in the sample. After experimental impacts up to 39.8 GPa, the width of the tetrahedral Al peak increased slightly and an additional fraction (up to 9±2%) of the total Al transitioned to 6-coordinated Al (Figure 3.5b). For the 29.4 GPa sample, a larger increase in the tetrahedral Al peak width and the appearance of a more prominent shoulder near 55 ppm suggested either that larger structural distortions occurred, or that secondary phases were produced in this experiment. Generally, the ^{27}Al NMR spectrum of post-impact saponite showed much less evidence for structural deformation compared to that observed for kaolinite.

Results for ^{29}Si NMR experiments also show evidence for more deformation of the kaolinite structure compared with saponite (Figure 3.6). For kaolinite, the signal for Si in the tetrahedral sheet becomes broader and its intensity decreased with increasing impact pressure as significant fractions of the Si transitioned to framework-like sites, yielding a broad peak centered near -100 ppm that accounted for 32±5% of the Si at 25.1 GPa and 55±5% at 39.6 GPa (Figure 3.6a). Both the ^{27}Al and ^{29}Si data indicate that about one-half of the sample retained kaolinite-like local structure after being subjected to shock pressures of 39.6 GPa and that the changes approached in a partial manner those observed in previous studies for thermal transformations to

metakaolinite (Rocha and Klinowski, 1990a; b; Massiot *et al.*, 1995; Rocha, 1999). In contrast all of the Si in saponite retains tetrahedral sheet-like polymerization up to 39.8 GPa (Figure 3.6b). The unaltered sample yields peaks at -95.5 and -90.4 ppm for Si in the tetrahedral sheet having, respectively, zero or one Al in adjacent tetrahedral sites. The main effect of increasing shock pressure was an increase in the widths of the main peaks. These peaks remain partially resolved up to 39.8 GPa, although broadened tails extending toward high and low frequency suggest the presence of some sites that were more strongly deformed.

^{23}Na NMR spectra for pre- and post-impact saponite (Figure 3.7) confirmed the structural integrity of saponite after experimental impacts. The primary saponite ^{23}Na NMR peak is consistent with Na^{1+} in a complex with water molecules in the saponite interlayer and this feature remained largely unchanged after impacts up to 39.8 GPa. The main differences among the spectra can be attributed to differences in hydration state (Laperche *et al.*, 1990), which we did not attempt to control during these experiments. (The narrow feature near +7 ppm in the spectrum of the 29.4 GPa sample arises from a contaminant of unknown origin, likely NaCl.)

The NMR spectra of heat-treated kaolinite (Figure 3.8a,c) showed nearly complete transformation at 500°C of the layered Q3 silicate polymerization to Q4 framework-like structure, and of the octahedral Al to principally 4- and 5-coordination. The short-range structural changes brought about by impact at the highest shock pressures appeared qualitatively similar to those caused by thermal alteration (Rocha and Klinowski, 1990b; Massiot *et al.*, 1995; Rocha, 1999), but to a less pervasive extent, retaining some regions of apparent kaolinite-like local structure, more similar to results for flash calcined kaolinite (Slade and Davies, 1991; Slade *et al.*, 1991; Meinhold *et al.*, 1992, 1993). For heat-treated saponite, the NMR spectra (Figure 3.8b,d) showed that thermal alteration initially causes distortion of the tetrahedral sheet, indicated by a small peak shift and broadening of the signals from primary saponite tetrahedral cations (up to 500°C). At higher temperatures (T=800 °C), eventual emergence of a pyroxene-like phase, characterized by primarily Q2 silicate polymerization, and of an amorphous or poorly-crystalline silica-rich phase (broad ^{29}Si peak centered near -101 ppm; Figure 3.8b) distinct from saponite was observed. In contrast, shock processes resulted in mainly modest peak-broadening of the saponite Si and Al Q3 peaks, and did not appear to produce significant amounts of secondary phases, even after experimental impacts at peak pressures of up to 39.8 GPa.

3.3.4 The Spectral Effects of Thermal Alteration Differ from Those of Shock

The MIR ATR spectra of thermally altered nontronite (Figure 3.9), showed that H_2O adsorbed to grain surfaces is driven off first (HOH bend at 1630 cm^{-1}; Che *et al*., 2011), then, at slightly higher temperatures (100 °C<T<300 °C), interlayer H_2O molecules are driven off from the nontronite structure (weakening of the broad cation-H_2O vibration between 3100 – 3500 cm^{-1}). This is followed by dehydroxylation (T=400 °C; loss of all OH-group features >3500 cm^{-1} both Al and Fe(III)-related, as well as much of the spectral contrast of the M-O out of plane vibration), layer collapse (500 °C≤T≤800 °C; shown by the Si-O stretch shift from 900 – 1100 cm^{-1}), and the emergence of completely dehydrated secondary and amorphous phases (T≥800 °C).

The MIR ATR spectra of shocked nontronite samples (Figure 3.10), in contrast, showed retention of the broad cation-H_2O vibrational band (3100 – 3500 cm^{-1}) after experimental

impacts reaching peak pressures of 39.1 GPa, indicating that shocked samples, unlike thermally altered samples, either rehydrate consistently or retain interlayer H_2O molecules. The persistence of the narrow HOH bend feature (1630 cm^{-1}) was most likely due to adsorbed H_2O on grain surfaces as a result of the ambient relative humidity conditions during data collection. Post-impact nontronite showed evidence of structural deformation by the loss of features related to the vibrational bands of iron and hydroxyl groups in the octahedral sheet (900 – 750 cm^{-1}), and the elimination of strong lattice deformation features (~500 cm^{-1}). The Al-FeOH vibrational feature (~3700 cm^{-1}), most likely related to Al-substitution in the nontronite tetrahedral layer, emerged from the shoulder of the broad 3700 – 3000 cm^{-1} interlayer hydration feature as its strength increased relative to the Fe-OH characteristic nontronite features (3550, 3600 cm^{-1}). Fe-OH features weakened after experimental impacts at peak pressures of 10.2 and 19.7 GPa, revealing the relatively stronger Al-FeOH vibration, but this feature too was no longer detected after experimental impacts at peak pressures of 25.2 GPa and above. I note, however, that these spectral changes may also be related to sample heterogeneity (different amounts of tetrahedral Al-substitution between processed samples) and/or changes in the interlayer hydration state of the sample. The intensity of the Al-FeOH vibration is much weaker than the broad hydration feature that overlaps it and I conducted my ATR measurements under ambient conditions. The Si-O stretching vibration shifted to higher frequencies (from ~900 cm^{-1} to 1000 cm^{-1}), even after low-pressure (10.2 GPa) experimental impacts that did not result in significant dehydration or dehydroxylation. As a comparison, the MIR ATR spectra of saponite pre- and post-impact (Figure 3.11) did not show evidence of significant structural deformation. All diagnostic MIR ATR features were detected, even after laboratory impacts up to peak pressures of 39.8 GPa.

3.4 Discussion and conclusion

Thermal and shock alteration effects are associated and, to a large extent, inseparable (French, 1968, 1998; Stöffler, 1972, 1974). By isolating these two processes as much as empirically possible, however, the effects of shock and thermal alteration on clay mineral structure and spectroscopy can be distinguished. Comparisons among different clay mineral species revealed that iron-rich dioctahedral smectite species are more susceptible to shock-induced structural deformation than magnesium-rich trioctahedral smectites. Another dioctahedral phyllosilicate, kaolinite, displayed structural disorder after exposure to shock similar to that observed for nontronite (Fe-rich smectite), so this response to shock may not be specific to iron-bearing smectites. The factors that control structural resilience in phyllosilicates after shock remain unclear. It is possible that the observed differences may be driven by the availability of vacancies in the octahedral sheets of dioctahedral phyllosilicates not present in the octahedral sheets of trioctahedral phyllosilicates. This has been previously suggested as an explanation for observed differences in the hydrothermal reactivity of trioctahedral (less reactive) and dioctahedral (more reactive) smectites (Eberl *et al.*, 1978). Indeed, previous researchers have suggested generally that smectite stability increases when all octahedral sites are fully occupied (Sand and Ames, 1957; Ames and Sand, 1958). Careful comparisons of the shock responses of additional phyllosilicate species may help to prove or disprove this hypothesis.

The most diagnostic changes to the VNIR reflectance spectra of impact-altered NAu-1 nontronite occur in the 2.2 – 2.4 μm (4545 – 4167 cm^{-1}) region, which contains the metal-OH

vibrational combination and overtone bands that are diagnostic of the cations present in the octahedral sheet (Bishop *et al.*, 2002b, 2008a; Petit *et al.*, 2004), Fe(III) (nontronite) or Mg(II) (saponite) in this case. Spectral features in this region have been used for the identification of specific clay mineral species (Petit *et al.*, 1999, 2004; Bishop *et al.*, 2002a; b; Decarreau *et al.*, 2008; Neumann *et al.*, 2011). The pronounced differences between the spectral responses of nontronite and saponite to impacts in this wavelength region are, therefore, particularly important. The pronounced shifts in nontronite's bands in this region (Figure 3.2a) are indicative of structural deformation in the octahedral sheet. In contrast, saponite (Figure 3.2b) retains most of its diagnostic Mg-OH features. The characteristic Mg-OH doublet centered at 2.31 μm (4329 cm^{-1}) and the Mg-OH bending band centered at 2.39 μm (4184 cm^{-1}) did not change either intensity or band center, even after experimental impacts at pressures up to 39.8 GPa. Some variability was observed for bands in the 2.23 – 2.27 μm region (4484 – 4405 cm^{-1}) between samples exposed to experimental impacts at various pressures. The shoulder feature at 2.25 μm (4444 cm^{-1}) and the weak band at 2.23 μm (4484 cm^{-1}) correspond to Al/Mg-OH and Al/Fe-OH combination bands, respectively (Bishop *et al.*, 2002a; b, 2008a) and showed the greatest variability between samples. SapCa-2 contains <1% Fe(III), making it a good contrast for Fe(III)-rich NAu-1. In addition, similar to NAu-1, SapCa-2 also contains Al substituted in the octahedral sheet. Thus variability in the bands between 2.23 – 2.27 μm in the saponite VNIR reflectance spectrum, may be due as much to compositional variability as to any impact-induced structural deformation.

The spectroscopic results indicated that saponite was structurally more resilient to shock than nontronite. After impacts at the highest experimental shock pressure, 39.1 GPa, the diagnostic spectral features of the VNIR reflectance spectrum of nontronite are replaced by a new, broad spectral feature (Figure 3.2a, red arrow) that overlies the wavelength region characteristic of Al-OH combination and overtone bands, ~2.2 μm (Bishop *et al.*, 1999, 2002a; b, 2008a), and may be diagnostic of the presence of a semi-amorphous Al-bearing phase formed as a result of the structural deformation of nontronite. Emissivity spectra for nontronite showed a similar trend, but are indicative of increasing structural disorder in the tetrahedral, rather than octahedral sheet of the dioctahedral smectite structure. The retention of diagnostic emissivity features in the spectra of shocked saponite samples indicates that, in contrast to nontronite, saponite has retained most of the order in the rigid layers of its structure.

These results have important implications for the analysis of remote sensing data, especially in regions that have undergone heavy impact bombardment. They have demonstrated, for example that remote sensing techniques can detect the effects of shock in clay minerals, and it is therefore possible to detect shock metamorphism on Mars from infrared data. Minerals, however, respond to shock differently; two analyzed dioctahedral clays exhibited shock effects at relatively low pressures, whereas the analyzed trioctahedral clay showed almost no effects up to the highest experimental impact peak pressure (~40 GPa). The non-detection of infrared features attributable to shock is, therefore, not evidence that the surface has not been exposed to shock pressures. In other words, the evidence for shock metamorphism on Mars or other terrestrial bodies from IR data must be interpreted with caution. Secondly, shock effects could affect the interpreted ratio of diocthedral to trioctahedral clay on Mars based on IR data. Impact-induced shock metamorphism might have rendered more of the dioctahedral clays undetectable than the trioctahedral, altering the current view of the occurrences of each of these categories of clay.

Kaolinite, also a dioctahedral phyllosilicate, experienced structural alteration to an extent similar to that of nontronite in response to experimental impact shock. This allowed for the comparison of saponite and kaolinite using NMR spectroscopy to explore clay mineral cation bonding environments in detail. In saponite, the structure of the rigid layers is largely unchanged after impact shock, and this was directly confirmed by NMR spectroscopy. In kaolinite, the octahedral sheet becomes increasingly structurally deformed with increasing impact pressure.

NMR spectroscopy provided unique information on the structural deformation induced in dioctahedral (but not trioctahedral) phyllosilicates by impact shock. The ^{27}Al NMR spectrum of unaltered kaolinite was consistent with all structural Al occupying 6-coordinated sites in the octahedral sheet. After experimental impacts up to 39.6 GPa, nearly half (47 ±5%) of the Al has transitioned to 4- and 5-coordinated sites (Figure 3.5a). In contrast, the 4-coordinated ^{27}Al NMR peak of unaltered saponite, consistent with Al substituting for Si in the tetrahedral sheet, is largely unaltered by experimental impacts up to 39.8 GPa. At higher pressures, more intensity is observed for the ^{27}Al NMR peak consistent with 6-coordinated Al in the saponite octahedral sheet. There are three possible interpretations for this result. (1) The saponite tetrahedral sheet was partially structurally deformed, driving some Al into the octahedral sheet. This is unlikely because mobilizing cations requires a large amount of energy. (2) The unaltered saponite sample(s) exposed to experimental impacts at higher peak pressures had larger proportions of aluminum in their octahedral sheets. (3) Impact shock generated secondary phases distinct from saponite. This third interpretation is consistent with NMR spectra from impact altered saponite that showed results similar to those observed for thermal alteration, but on a smaller scale. Localized heating at grain boundaries during the shock-recovery experiments may have produced enough thermally altered saponite to explain these results. Nonetheless, the similarity observed in the ^{23}Na NMR spectra of the pre-impact and high-pressure post-impact saponite (Figure 3.7) indicated that overall shock deformation slightly disrupted the saponite layered structure, without inducing total loss of the sample's long-range structural order.

The NMR results presented here further supported the hypothesis that thermal and shock alteration may proceed via different pathways and produce different structural changes in materials exposed to both processes. The NMR spectra of thermally altered and shocked kaolinite (Figure 3.8) revealed that instead of the gradual change in aluminum coordination that is observed for shocked kaolinite, the aluminum in thermally altered kaolinite passes all-at-once into mostly 4- and 5-coordinated sites characteristic of metakaolinite. The ^{29}Si NMR spectra indicated that transformation of kaolinite to amorphous metakaolinite is complete at T≥500 °C. In contrast, even in the sample shocked up to the highest peak pressure of 39.6 GPa, slightly more than half of the sample retained local kaolinite-like structure. This is consistent with a process that causes irregular, rather than stepwise structural change. These results may also reflect the localized heating that can occur in shock-reverberation experimental samples, or the possibility that shock only imparts enough energy to partially drive mineral transitions to amorphous and/or meta-stable phases. Nonetheless, the non-linear relationship between shock and heat in impact processes (French, 1968, 1998) means that differences between the spectral effects of these two processes are important for remote sensing data analysis, even if the differences themselves are driven by kinetics. The results presented here, however, suggested that kinetics might not entirely explain the observed differences between the spectra of thermally altered and shocked phyllosilicates.

The effects of thermal alteration on clay minerals are well-characterized (Fitzgerald *et al.*, 1996; Carroll *et al.*, 2005; Gavin and Chevrier, 2010; Che *et al.*, 2011; Daly *et al.*, 2011; Che and Glotch, 2012), and these previous works have shown that thermal alteration produces physical and spectral properties in nontronite that differ from those produced by shock (Boslough *et al.*, 1986). The results presented here are consistent with these findings. Because these processes often occur together in natural impacts, it is important to understand their distinct effects on mineral structure and spectroscopy. Such a comparison also illuminates potential explanations for the responses of different smectite species to shock. Nontronite's thermal alteration, for example, follows a stepwise progression beginning with dehydration (T≥100 °C) and ending with layer collapse (T≥800 °C). In contrast, shocked nontronite becomes increasingly structurally disordered without complete devolatilization (Figures 3.9 and 3.10). As a comparison, shocked saponite retains most of its characteristic features (Figure 3.11), while the thermal alteration of saponite follows much the same trend as that of nontronite (Che *et al.*, 2011). This may be due to kinetic differences between shock and thermal alteration. While shock passes nearly instantaneously through a sample (on the order of ~0.1 – 1 μsecond; Stöffler, 1972), Che *et al.* (2011) and Che and Glotch (2012) acquired the thermal alteration results used in this study over a 24-hour experimental period. Therefore, kinetic differences between these two processes are expected. If, however, the observed differences were entirely energetic or kinetic in nature, I would expect the spectral results of impact alteration to more closely resemble those for intermediate thermal alteration and the results presented here do not fully support this. Vibrational spectroscopic features related to metal-hydroxyl group interactions within smectite layers are retained, but disordered for dioctahedral phyllosilicates after impact shock. This shows that shock without thermal alteration does not induce complete dehydroxylation, even in smectites that are not structurally resilient, and contrasts directly with the stepwise progression of thermal phyllosilicate alteration.

The results that I have presented demonstrate the importance of using detailed laboratory work to understand the spectroscopic and structural variability of clays. By comparing between two different smectite species, these results have shown that even structurally similar clay minerals may respond differently to impact alteration. Separating thermal and shock alteration shows that these processes induce structural change in phyllosilicates by distinct alteration pathways that produce spectrally, energetically, and structurally distinct changes. This work confirms the necessity of detailed laboratory spectroscopic analysis for accurate remote sensing and spectroscopic data interpretation.

Chapter 3 – Figures

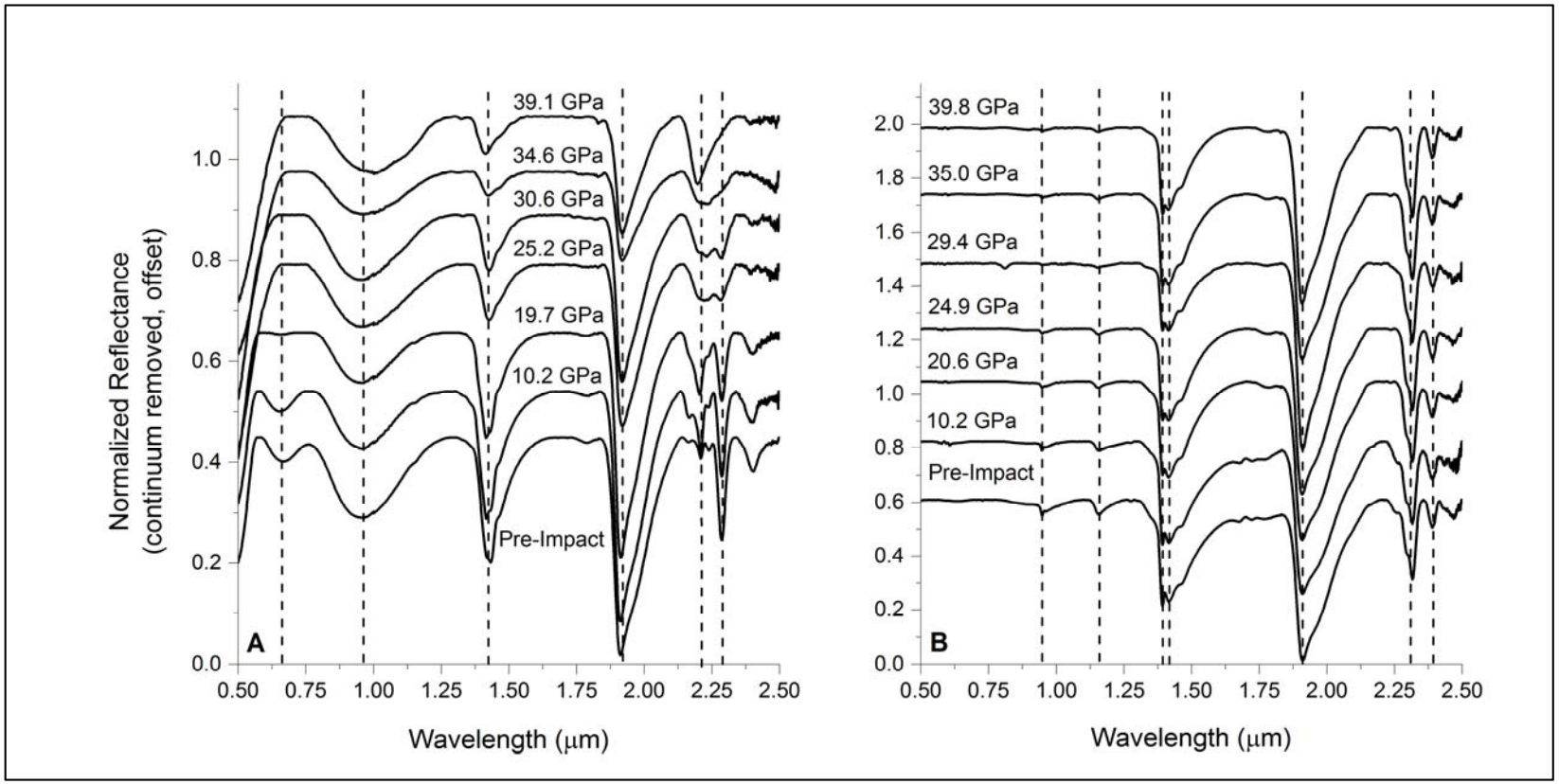

Figure 3.1. Normalized, continuum removed, VNIR reflectance spectra of nontronite (A) compared to saponite (B). Nontronite responds to impact shock by structural deformation, which is reflected in the altered reflectance spectra detected at shock pressures greater-than or equal-to 25.2 GPa. Saponite is more structurally resilient, and its reflectance spectra are largely unchanged even after impacts up to the maximum experimental peak impact pressure that the sample experienced, 39.8 GPa.

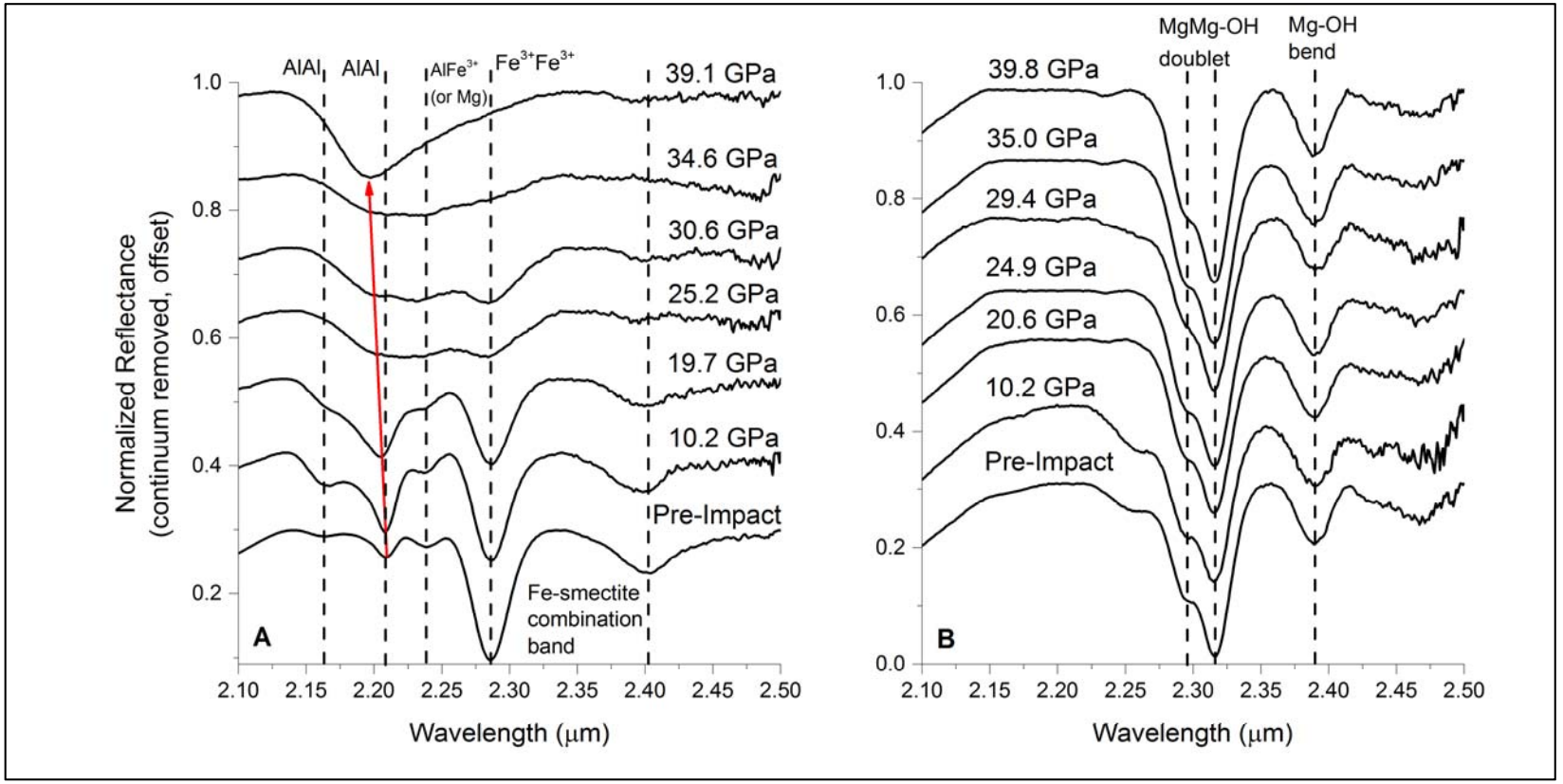

Figure 3.2. Normalized, continuum removed, VNIR reflectance spectra of nontronite (A) and saponite (B) cropped to focus on the 2.2 – 2.4 μm region. This region contains diagnostic features specific to the overtone and combination bands of metal-OH vibrations characteristic of the dominant octahedral cation of the clay. Impact shock induces many structural and related spectroscopic changes in nontronite, while the saponite spectrum is largely unchanged. The red arrow indicates the broad feature centered at ~2.20 μm that dominates the nontronite spectrum after impacts at the highest experimental pressure of 39.1 GPa. This feature overlies the region characteristic of Al-OH vibrations. Specific band assignments are based on previous work reported by Bishop *et al.* (2002a; b, 2008a).

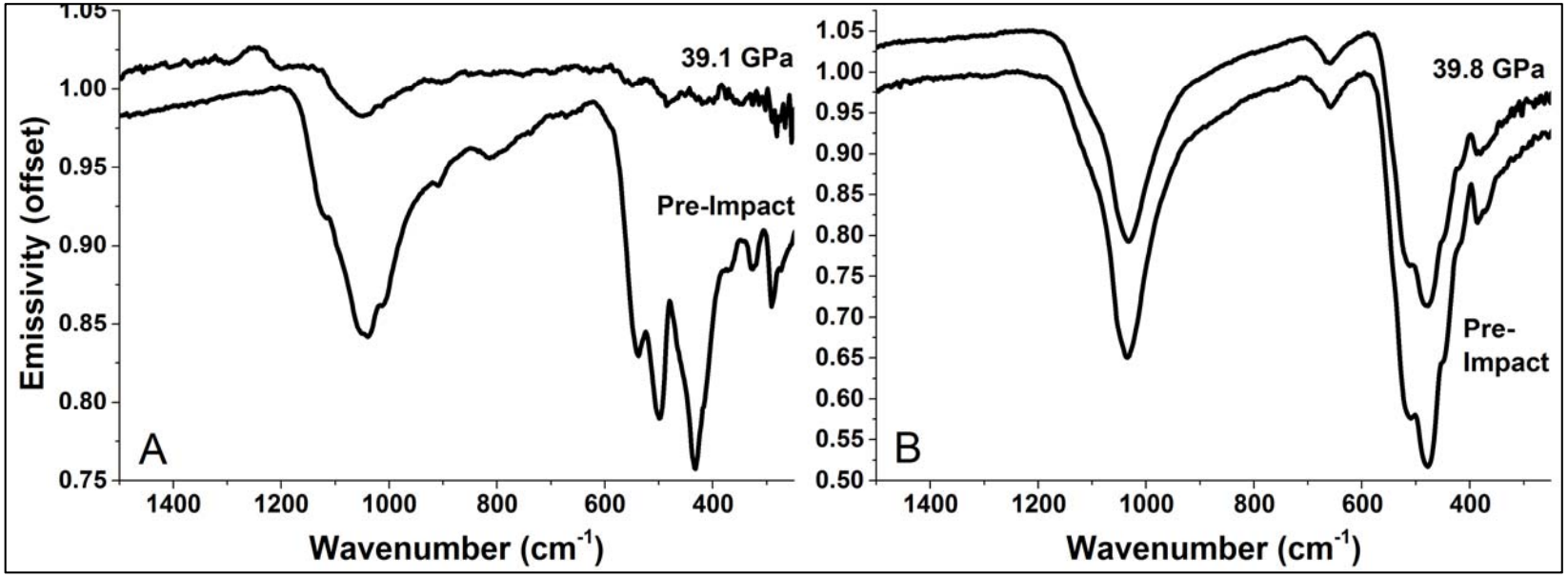

Figure 3.3. Characteristic emissivity spectra of nontronite (A) and saponite (B) showing pre-impact and post-impact spectra from the highest experimental peak impact pressures achieved for both samples. Emissivity confirms the trends in changes to the structure and spectra reported for the reflectance results (Figures 3.1 and 3.2).

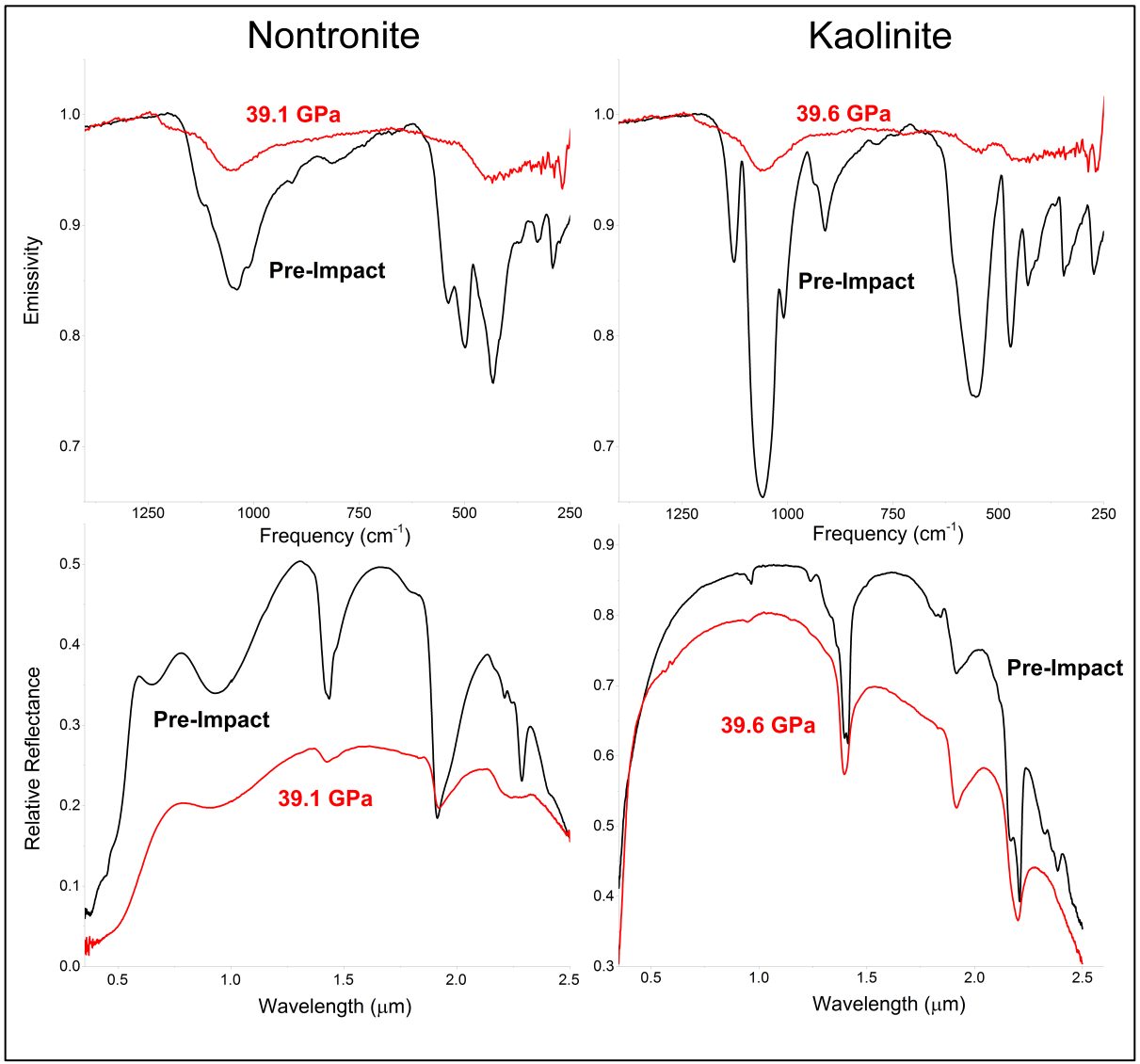

Figure 3.4. Characteristic emissivity (A, C) and reflectance (B, D) spectra, compared between nontronite (A, B) and kaolinite (C, D), showing that both nontronite and kaolinite produce similarly changed spectra after exposure to experimental impacts.

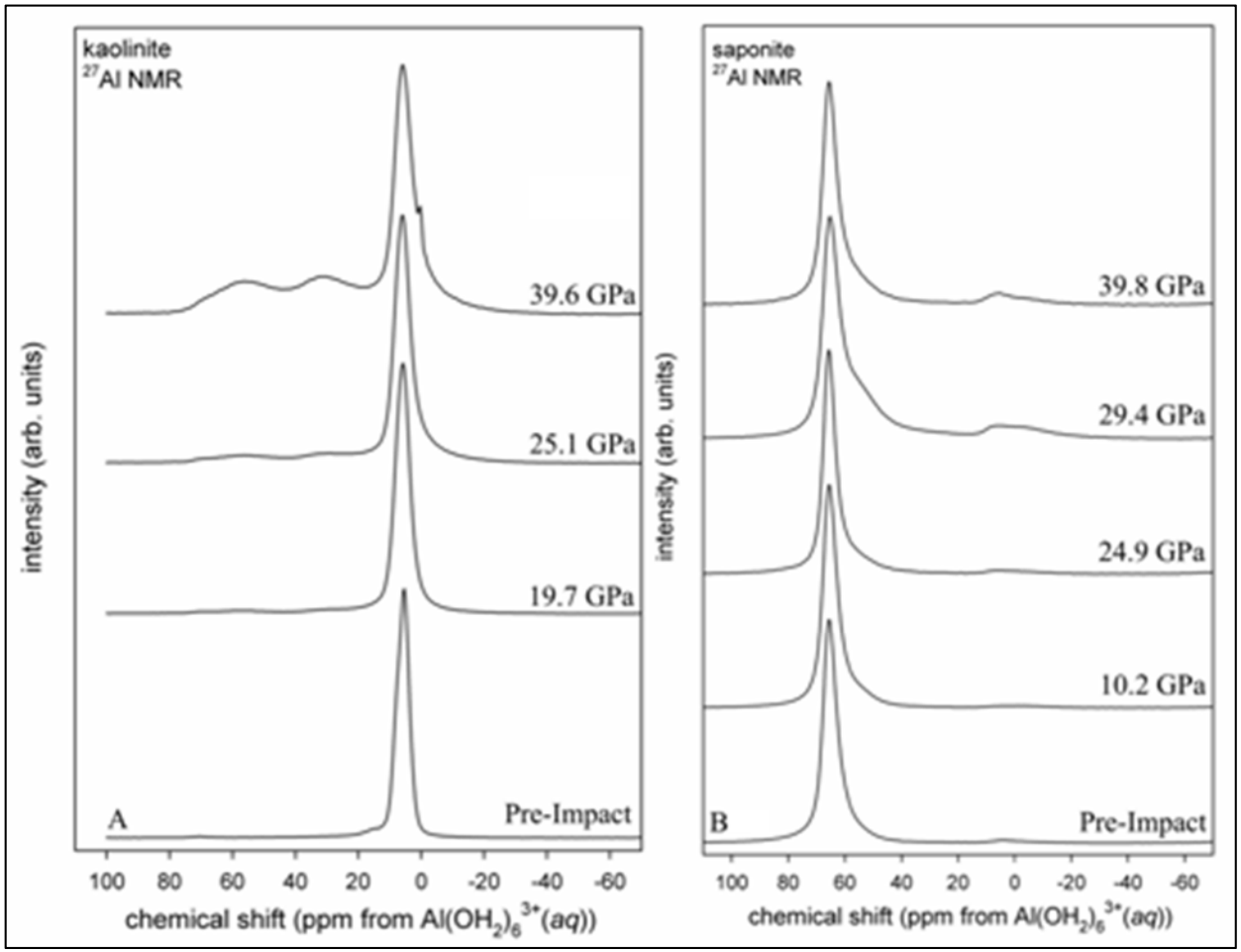

Figure 3.5. Comparison between the ^{27}Al NMR spectra of kaolinite (A) and saponite (B) showing much more structural alteration in impact-altered kaolinite than for the saponite sample, with 47±5 percent of the kaolinite octahedral Al transformed to 5- and 4-coordinated sites at 39.6 GPa.

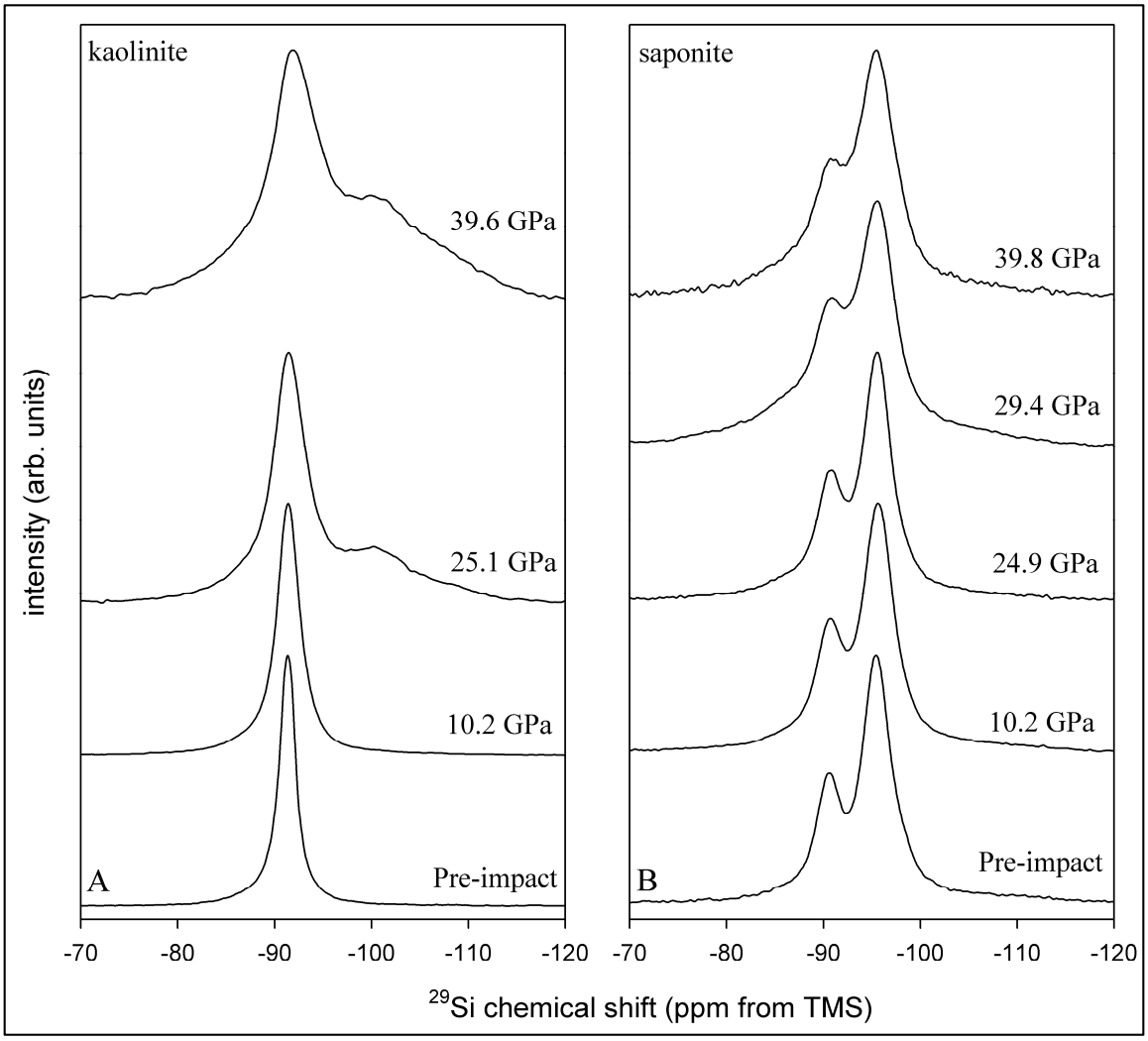

Figure 3.6. Comparison of ^{29}Si NMR spectra of impact-altered kaolinite (A) and saponite (B) showing greater structural deformation of the kaolinite tetrahedral sheet. Exposure of kaolinite to shock pressure of 39.6 GPa results in transformation of 55±5% of the Si to framework-like polymerization, but no change in the polymerization for saponite.

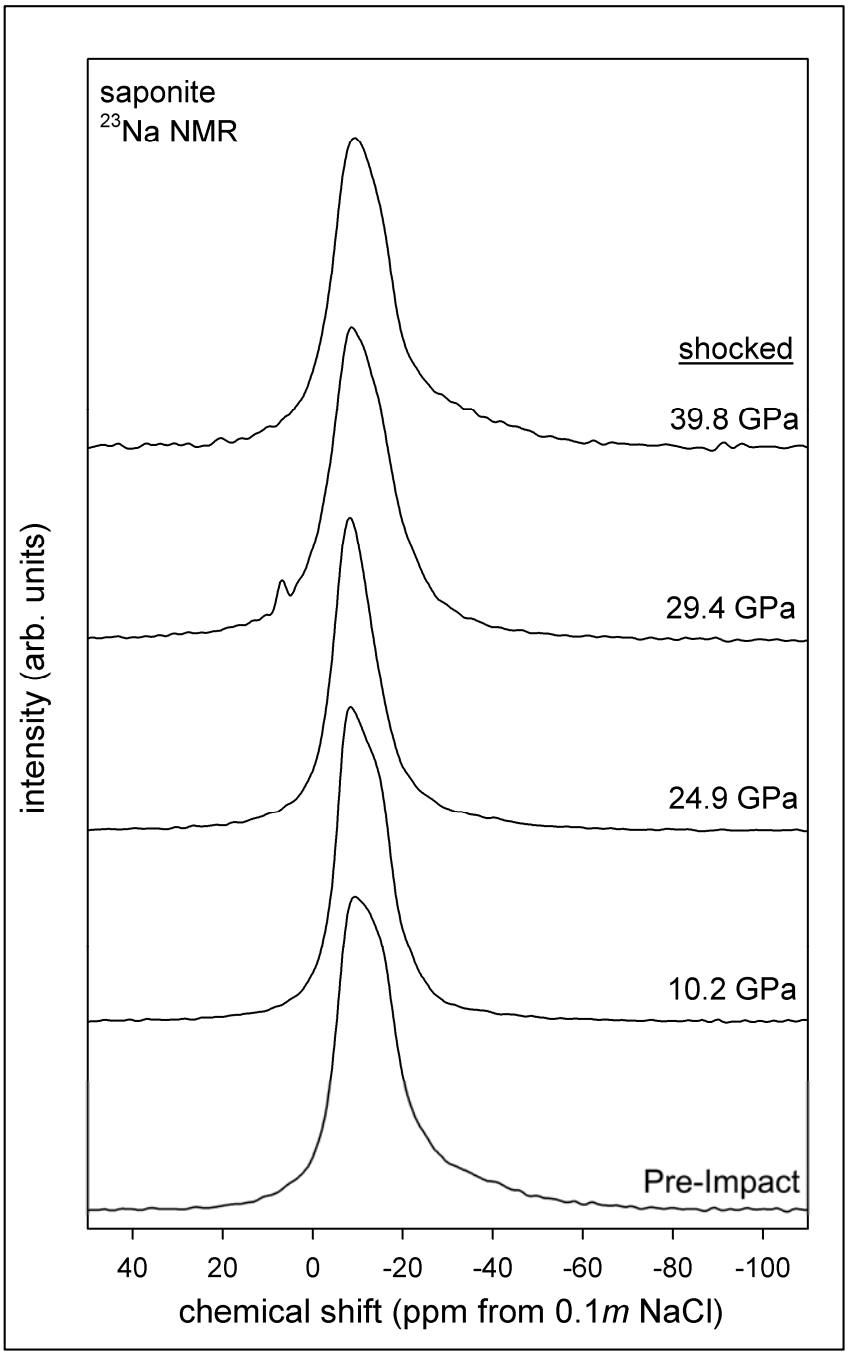

Figure 3.7. The ^{23}Na NMR spectra of saponite after experimental impacts demonstrate that saponite's interlayer order is largely maintained and that Na in the interlayer remains in a similarly coordinated state before and after experimental impacts, even up to the highest peak pressure achieved, 39.8 GPa. The extra peak at 0 ppm chemical shift in the sample exposed to a peak impact pressure of 29.4 GPa arises from a contaminant of unknown origin, likely NaCl.

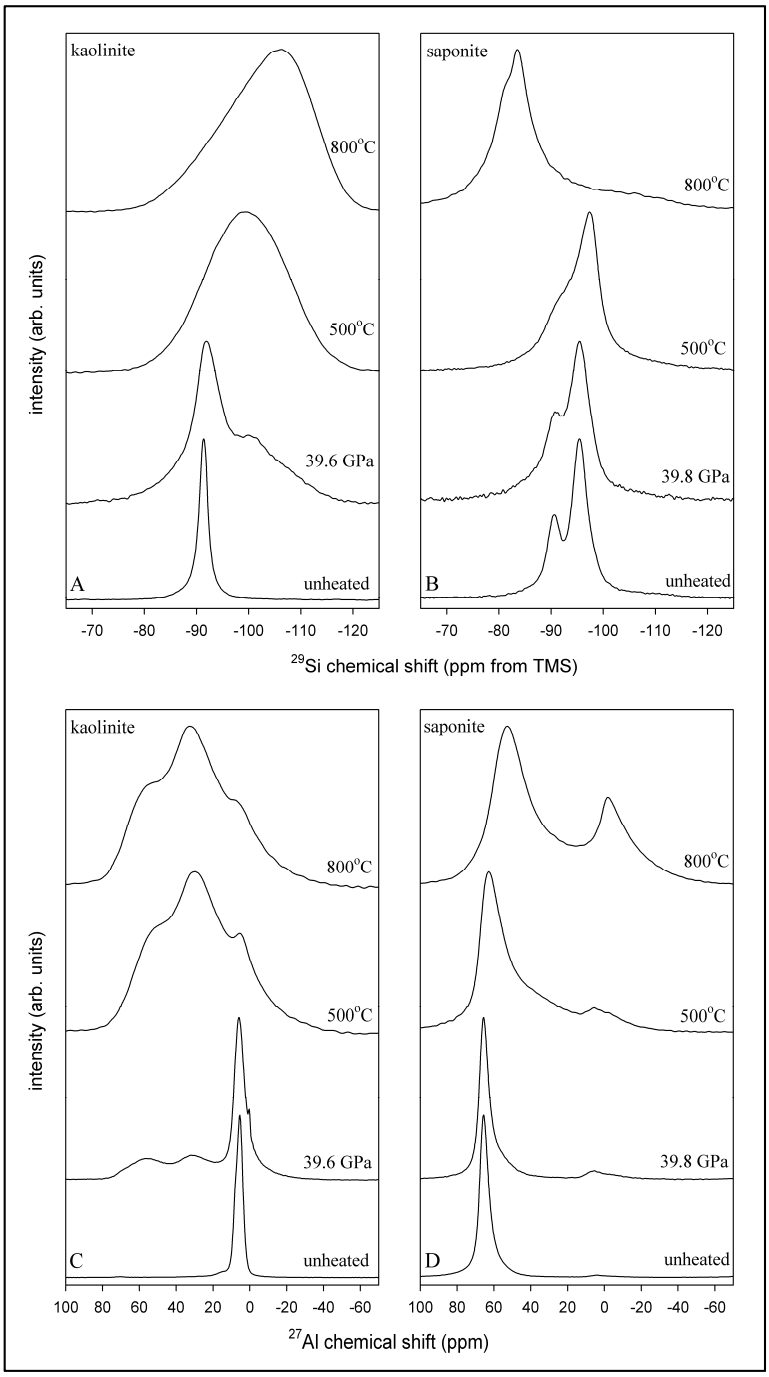

Figure 3.8. Comparison of impact- and thermally altered kaolinite (A,C) and saponite (B,D) from ^{29}Si (A,B) and ^{27}Al (C,D) NMR spectra showing that impacts up to 39.8 GPa do not cause the same changes to the structures as thermal alteration. Heating saponite and kaolinite produces NMR spectra consistent with the formation of secondary phases, which exposure to shock up to 39.8 GPa does not produce in saponite, and only partially in kaolinite.

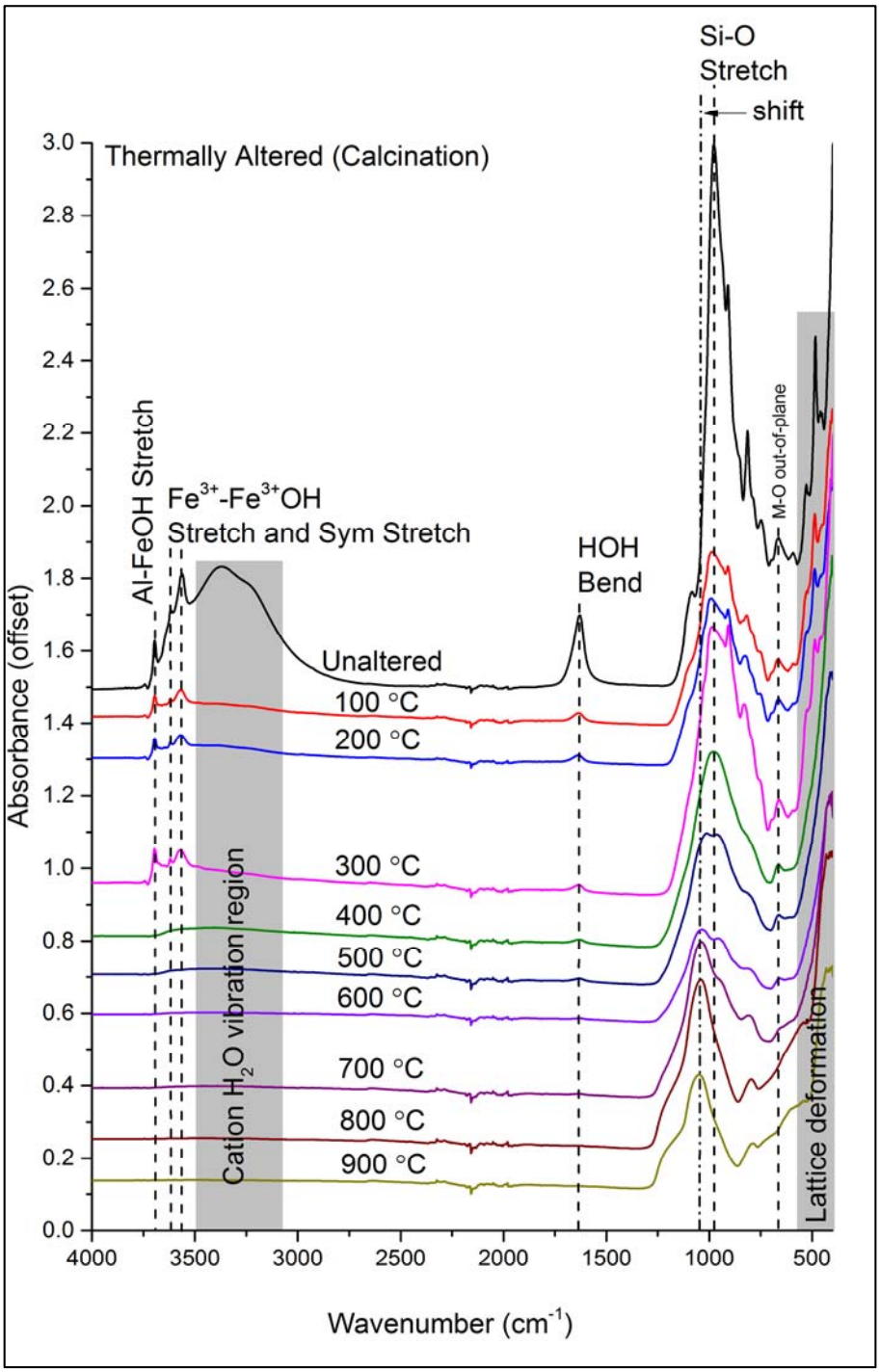

Figure 3.9. MIR ATR spectra of thermally altered nontronite are characteristic of the step-wise nature of thermal alteration of smectites.

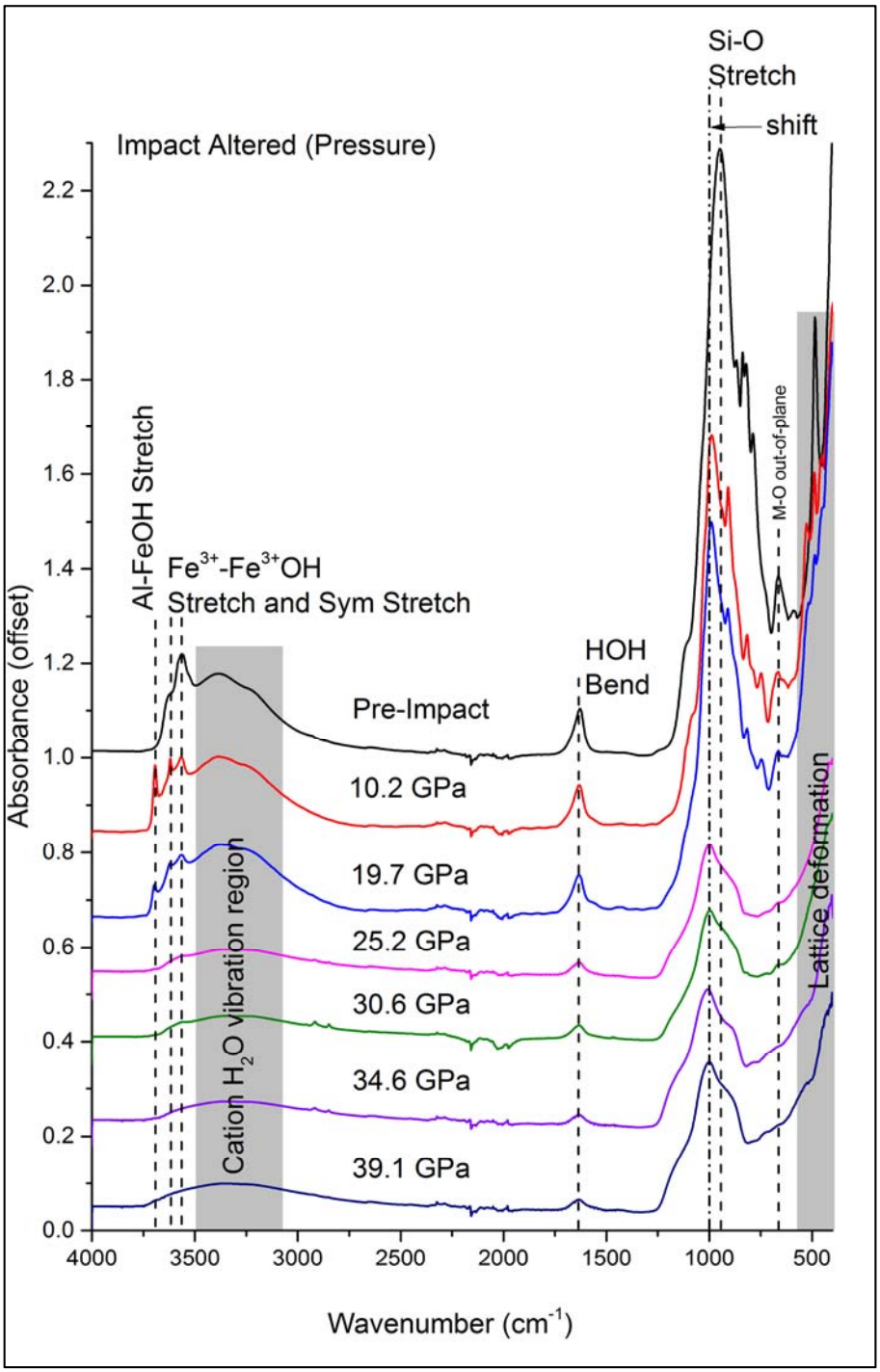

Figure 3.10. MIR ATR spectra of impact-altered nontronite are characteristic of the irregular structural deformation induced by shock in smectites and show increasing disorder in both the octahedral and tetrahedral sheets, with partial retention of some layered structure, interlayer water, and structural OH groups.

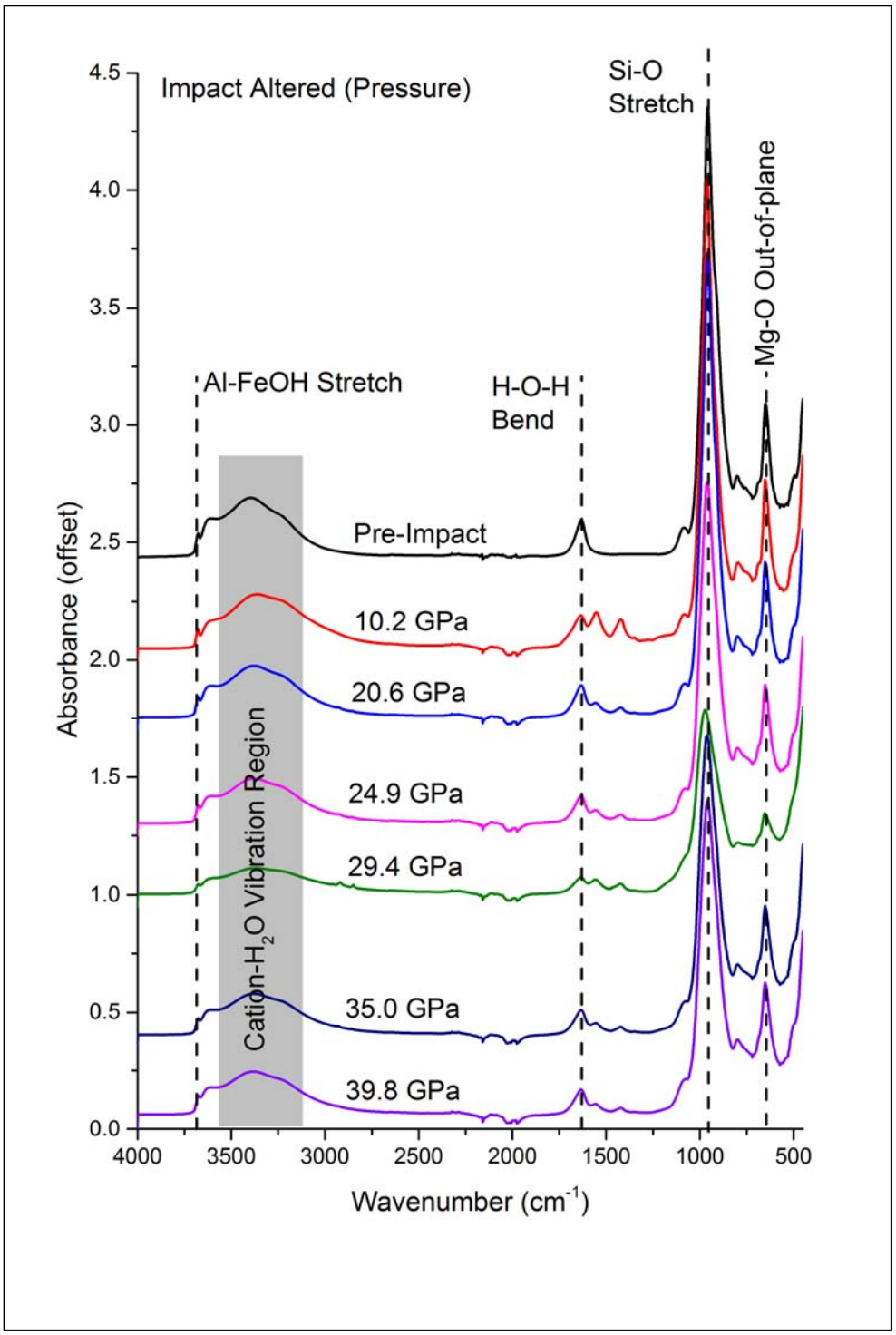

Figure 3.11. MIR ATR spectra of saponite after experimental impacts up to 39.8 GPa show that the saponite structure is largely unchanged, even after experimental impacts up to the highest achieved peak pressure.

Chapter 4

Identification of impact-altered nontronite in geologic context on the martian surface using data from the Compact Reconnaissance Imaging Spectrometer for Mars (CRISM)

Abstract

Craters have been proposed as veritable "windows" into the mineralogy of the martian subsurface, but the impacts that produce them also initiate thermal and geochemical processes that induce structural and related spectral changes to the minerals present at the time of impact. These spectral changes are challenging to interpret in remote sensing data, leading to potential misinterpretations of regional spectral variations, especially within craters themselves and in heavily bombarded regions of the martian surface. I have conducted both preliminary investigations using Factor Analysis and Target Transformation (FATT) of a CRISM scene from the Mawrth Vallis region of Mars, and a more detailed spectral analysis of a CRISM scene from the Nili Fossae region of Mars. Both of these analyses revealed the presence of impact-altered nontronite in nontronite- or Fe-smectite-rich regions. However, the identifications of impact-altered nontronite, especially nearby the Nili Fossae, frequently overlap with other phyllosilicate detections. This ambiguity is especially problematic for the identification of diagenesis on Mars, particularly the smectite-to-illite conversion.

Illite is the dehydrated end product of burial phyllosilicate diagenesis. Mixed-layer illite/smectite clays are therefore thought to be intermediate products and the ratio of smectite/illite indicative of the length of time or depth at which diagenesis has been occurring. Many of the locations in which hypothesized mixed-layer clay deposits have been identified are within the walls, basins, and central peaks of craters. As the identification of impact-altered nontronite in similar locations shows, some of these mixed-layer clay deposits may not be unambiguously distinguishable from impact-generated structural and spectral alteration. As a result, any inferences made about diagenetic environments or the geologic history of Mars based on the identifications of mixed layered clay deposits in craters should be made cautiously and with careful consideration of both local and regional geologic context.

4.1 Introduction

4.1.1 Clay mineral identifications in and around impact craters on Mars

There is evidence for extensive clay mineral deposits on Mars from visible near-infrared (VNIR) remote sensing techniques (Bibring *et al.*, 2005, 2006; Poulet *et al.*, 2007, 2005; Loizeau *et al.*, 2007; Mangold *et al.*, 2007; Bishop *et al.*, 2008b; Mustard *et al.*, 2008; Ehlmann *et al.*, 2009, 2013; Michalski *et al.*, 2010). Most of these identifications have been made in the older, heavily bombarded southern highlands of Mars (Carter *et al.*, 2013). Several are associated directly with impact craters, or with deposits of impact ejecta. For example, Ehlmann *et al.* (2009) specifically described several clay mineral species, or occurrences of characteristic spectral features indicative of specific clay mineral species, that are found within craters surrounding the Nili Fossae. Wray *et al.* (2009) identified phyllosilicate-rich outcrops on the rim of Endeavor Crater using orbital remote sensing data, and saponite has been identified in the center of a crater within the Mawrth Vallis region (Mckeown *et al.*, 2009). As discussed in the previous chapter, the association of phyllosilicates and craters is one of the lines of evidence used to infer the relative ages of phyllosilicate deposits on Mars.

The association of clays with impacts leads naturally to questions about the role of impact processes in clay mineral formation and alteration. Some researchers have suggested that clays on Mars formed as a result of impact-driven hydrothermalism (e.g., Marzo *et al.* 2010). Others believe, based on stratigraphic evidence, that phyllosilicates pre-date most impacts, but that they may also have formed as a result of post-impact weathering, perhaps initiated by the disorder in the underlying rock created by the impact itself (e.g., Fairén *et al.* 2010). It has also been suggested that repeated impact events may provide an energetic and chemical source for extensive hydrated silicates on Mars independent of climate (e.g., Tornabene *et al.* 2013). Nonetheless, efforts to understand the connection between impacts and phyllosilicate diagenesis have recently begun and are ongoing (Viviano *et al.*, 2013; Arvidson *et al.*, 2014; Milliken, 2014). Understanding the diagenesis of martian phyllosilicates may place constraints on the temperature, pressure, and time-scale regimes of phyllosilicate (and other hydrated mineral) formation and deposition (Ehlmann *et al.*, 2009, 2013; Viviano *et al.*, 2013; Milliken, 2014). By comparison with terrestrial phyllosilicate weathering and diagenesis (Hower *et al.*, 1976; Eberl, 1984), associations between mineral assemblages and climate can be established. Understanding the past martian climate is the key to understanding the astrobiological potential of the martian surface. In addition, microbes have been shown to be important for the diagenetic reactions of terrestrial phyllosilicates, particularly the smectite-to-illite transition (Kim *et al.*, 2004). Thus, the identification of phyllosilicate diagenetic reaction products on Mars may directly indicate environments of potential astrobiological activity.

4.1.2 Clay mineral diagenesis on Earth and Mars

Terrestrial clays, as discussed by Eberl (1984), exist in a cycle in which weathering reactions produce neoformed clays, which are then themselves weathered and deposited in burial or hydrothermal environments. In burial or hydrothermal environments, dioctahedral smectite reacts to form the diagenetic products of mixed-layered illite/smectite, which eventually convert entirely to illite. Such metamorphic transitions appear to be associated with specific temperature, pressure, and time constraints. For example, Hower *et al.* (1976) investigated the chemical and mineralogical transitions that occurred in buried argillaceous sediment in a 5,776 m well puncturing an Oligocene-Miocene section of the U.S. Gulf Coast. Over a depth interval from 2,000 to 3,700 m below the surface, they found that illite/smectite, the most abundant mineral in

their sample overall, underwent a mineralogical transition from approximately 20 percent illite at a depth of 2,000 m to 80 percent illite at a depth of 3,700 m. Below 3,700 m they did not observe any change in the proportions of illite/smectite. More important, they found that the stratigraphic interval over which illite layers in illite/smectite or smectite mineral assemblages increased did not relate to the formation boundary or sediment age. Thus, they concluded that increasing illite proportions in illite/smectite are a result of burial metamorphism and depend on burial depth and temperature, rather than variations in the geochemistry or mineralogy of the original sediments. Although they repeatedly mentioned the depth-dependence of their observations, they attributed the extent of the illite conversion in their samples primarily to temperature.

Based on their own observations and previous work, Hower *et al.* (1976) posited that the smectite-to-illite transition proceeded rapidly with increasing temperatures (and correspondingly increasing depths) up to 95 °C. In the temperature range between 95 °C and 175 °C the reaction slowed without reaching completion (their samples retained 20% smectite). They concluded that complete illitization may require temperatures higher than 175 °C and that the temperature range of 95 – 175 °C may therefore represent a stability field for mixed layered illite/smectite assemblages (although they could not rule out the possibility of lower reaction rates due to limited reactants, especially potassium feldspar). Nonetheless, they firmly associated the formation of illite from smectite with burial diagenesis and implied that the relative abundances of illite/smectite could be used as pressure (i.e. burial depth) and temperature indicators. This has been applied in terrestrial environments by later researchers attempting to understand the diagenetic history of complex argillaceous sediments (e.g., Eberl, 1984, 1993). Mineral assemblages of mixed, neoformed phyllosilicates and diagenetic minerals have been equivalently used on Mars to infer the depositional history of detected phyllosilicates (Ehlmann *et al.*, 2009, 2010) or understand their diagenesis (Milliken, 2014). Generally, these analyses rely on regional observations of shifts in the characteristic phyllosilicate bands in the 2.2-2.5 μm wavelength range (Ehlmann *et al.*, 2009; Bishop *et al.*, 2013c; Viviano *et al.*, 2013), although recent efforts have been made to use other characteristic phyllosilicate bands such as the 1.4 μm adsorbed H_2O/metal-OH combination band (Milliken, 2014). In particular, Viviano *et al.* (2013) use band depths and shifts in the 2.31 – 2.35 μm range related to the relative (crater) excavation depths of the identified deposits to propose a relationship on Mars between burial depth and extent of diagenesis similar to that described for burial metamorphosed terrestrial phyllosilicates.

There are, however, important geochemical caveats to the observations I described above. Indeed, Hower *et al.* (1976) specifically mention that their observations may be partly driven by changes in the provenance and geochemistry of the sediments they investigated and not solely by temperature and pressure gradients. In the context of Mars, the geochemical constraints on sediment diagenesis were well explored by Tosca and Knoll (2009). They argue that the fact that phyllosilicate detections on Mars are dominated by Fe/Mg-bearing smectite identifications (Carter *et al.,* 2013) implies that the phyllosilicate deposits on Mars are diagenetically juvenile and that this relative juvenility potentially limits the overall availability of water throughout martian geologic history and that related diagenetic processes must therefore be comparably rare. Smectites on Earth do not persist in ancient sediments. Tosca and Knoll (2009) estimate a ~180 Ma conversion time to produce sediments with 80% illite from smectite at 35 °C. It is unclear whether the persistence of smectites on Mars is due to low surface temperatures (e.g., thermodynamic constraints on the conversion of smectite to illite), the low mobility of K^+ ions on Mars, or a lack of available water. Tosca and Knoll (2009) favor a persistently dry environment

as the reaction-limiting factor. What is clear, however, is that the majority of the phyllosilicate deposits on Mars were not converted from smectite to illite. Based on this, Tosca and Knoll (2009) concluded that burial, hydrothermal alteration, or another process not related to straightforward diagenesis at the martian surface must be responsible for the limited evidence of mature phyllosilicate sediments on Mars. Impacts and related processes should not be discounted as potential drivers of clay mineral diagenesis. Tosca and Knoll (2009) also concluded, however, given the limited mobility of K^+ and its association with the alteration-resistant K-rich feldspar phase on Mars, that chloritization and not illitization is likely to be the preferred phyllosilicate diagenetic pathway on Mars.

This hypothesis is supported by the identification of other diagenetic phyllosilicate minerals, including chlorite, that have been detected by remote sensing on Mars (Mustard *et al.*, 2008; Ehlmann *et al.*, 2009; Poulet *et al.*, 2009; Wiseman *et al.*, 2010; Bishop *et al.*, 2013a; b; c; Tornabene *et al.*, 2013). The widespread identification of diagenetic phyllosilicates may place constraints on the availability of water at the martian surface, thus providing important clues about the past martian climate (Milliken, 2014). Just as primary phyllosilicate identifications are often associated with impact craters, however, diagenetic phyllosilicate identifications are also frequently associated with them. Indeed, craters have been specifically targeted for investigation as self-contained locations where the martian subsurface can be directly probed (Schwenzer *et al.*, 2009, 2010). As the previous chapters of this dissertation have shown, however, impact processes induce structural and related spectral change in phyllosilicates. This chapter investigates the possible convolution of impact-related spectral change with phyllosilicate diagenesis. In this chapter, I also discuss possible implications for inferences about martian climate based on clay mineral diagenesis.

4.2 Datasets and Methods

4.2.1 CRISM data

CRISM is a hyperspectral imaging spectrometer aboard the Mars Reconnaissance Orbiter (MRO) spacecraft that samples the VNIR and IR wavelength regions from 0.4 – 4.0 μm using two detectors with a total of 544 channels (Murchie *et al.*, 2007). The S detector samples wavelengths from 0.4 – 1.0 μm, while the L detector samples wavelengths from 1.0 – 4.0 μm. CRISM has two operational modes. The first, a 72-channel mapping mode provides global coverage of the martian surface at 200m/pixel spatial resolution. The second, a targeted full 544-channel hyperspectral mode provides 10 x 10-20 km hyperspectral image cubes of a limited number of targets of interest on the maritan surface at 15 – 38 m/pixel. In this study, I focused on targeted image cubes from the L detector because the wavelength range and high spatial resolution covered by this data set provided the best probability of accurately identifying impact-altered nontronite. In addition, the spectral range of my laboratory spectra covered only 0.3 – 2.5 μm. To most accurately match my laboratory data, I used a spectral subset of the CRISM image cubes of 1.0 – 2.5 μm for all analyses.

CRISM is a pushbroom-type spectrometer. This means that it uses a row of detectors arranged perpendicular to the flight direction of MRO to collect images of the martian surface. As MRO flies forward, CRISM passively records reflected light images of different parts of the martian surface as they come into view for its various detectors. This design allows CRISM to

produce better quality images because its longer exposure times detect more light than other instrument designs. However, CRISM data is affected by a common artifact of pushbroom-type spectrometers, the so-called "spectral smile," in which the central wavelength and the width of the instrument's spectral response vary with the spatial dimension of the detector array. In other words, the spectral resolution and detection response of CRISM's off-axis detector elements deteriorate relative to the detectors in the center of the array, where spatial distortions are minimal. This artifact produces an overall signal bias affecting all hyperspectral image data, but the magnitude of the effect depends on the column position of the data (i.e. the spatial position of the relevant detector). By ratioing a spectrum of interest with another spectrum from a nearby, spectrally featureless region within the same image column (i.e. from the same detector in the same spatial position), the effect can be mitigated and the spectrum of interest more accurately compared to laboratory spectral standards for identification (Ceamanos and Douté 2010).

4.2.1.1 CRISM context images

I generated all global- to regional-scale context images using the Java Mission-planning and Analysis for Remote Sensing (JMARS) program, which is a geospatial information system (GIS) for Mars developed by ASU's Mars Space Flight Facility. Basic information on JMARS is available through the extensive documentation provided by ASU at (jmars.asu.edu). I also used JMARS to conduct basic searches for relevant CRISM stamps and produce 3D views of the regional geologic context of CRISM stamp FRT000097E2.

4.2.2 Factor analysis and target transformation (FATT) spectral end-member image analysis

Factor analysis derives a unique potential end-member set from complex data (e.g., a spectral image) based on the derivation of orthogonal eigenvectors, using principle components analysis, from a matrix of the original data (Malinowski, 1991). The eigenvectors of a square matrix are those vectors passing through the origin, which, after having been multiplied by the original matrix, remain proportional to themselves. In the case of spectral image data, these vectors can be said to capture the spectral variability in the scene and, thus, can be used to derive the spectral end-members of the scene, although the eigenvectors themselves have no physical meaning (Malinowski, 1991; Bandfield *et al.*, 2000b). The spectral end-members of the scene are derived in the second part of the technique by target transformation, which reconstructs end-member spectra using linear combinations of the derived (non-physical) eigenvectors produced in the first part of the technique (Bandfield *et al.*, 2000b; Thomas and Bandfield, 2013). FATT has been successfully applied to several TIR data sets of the martian surface (Bandfield *et al.*, 2000b; Bandfield, 2002b; Bandfield and Smith, 2003; Glotch and Bandfield, 2006). To apply FATT to CRISM data, which is in the VNIR wavelength range where spectral end-members do not mix linearly, groups of pixels or whole regions of interest (Thomas and Bandfield, 2013) should be analyzed. However, it is important to remember that the end-members are derived from linear combinations of the eigenvectors, which have no physical significance, and not linear combinations of the spectral end-members of the scene. This changes slightly the interpretation of the analysis. Briefly, a good spectral match to laboratory data by a derived spectral end-member indicates that the matched mineral may be present in the analyzed scene, group of pixels, or region of interest. However, mineral identifications based on FATT should be confirmed by additional, direct methods of image analysis.

4.2.3 Preliminary investigations using FATT

In my preliminary analyses, I calculated the band-depth ratio between the 1.4 and 1.9 μm absorption bands in smectite reflectance spectra and compared this with well-characterized nontronite identifications from the surface of Mars. To calculate both band depths and ratios, I used indices, which I developed, based on modified CRISM spectral summary products as originally described by Pelkey *et al.* (2007). The indices that I used represent best fits to the spectra of altered and unaltered nontronite with:

i(1.9 μm) = 1 – (R1912/(0.765*R1844+0.235*R2132)) and

i(1.4 μm) = 1 – (R1433/(0.69*R1366+0.31*R1582)), where all identifying numbers correspond to the reflectance value at relevant wavelength values in nanometers (μm*10^3).

The 1.4 and 1.9 μm bands of smectites reflect the complex interactions and changes to adsorbed and interlayer H_2O (1.9 μm), as well as adsorbed and interlayer H_2O in combination with octahedral metal-OH vibrational overtones (1.4 μm) (Bishop *et al.*, 1994, 2002a; b). Interactions between the overtones and combinations of the fundamental vibrations of all of these functional groups make direct interpretation of changes to these bands difficult (Bishop et al., 1994, 2002a, 2002b). However, the ratio of these two bands can be used as a proxy indicator for dehydroxylation as presented by Che and Glotch (2014) for thermally altered nontronite on Mars. Because dehydroxylation and structural deformation in the octahedral sheet both result in differentiable weakening of OH-group bands separate from the behavior of adsorbed and interlayer H_2O, the 1.4/1.9 μm band ratio may also be used as a proxy indicator for structural deformation in the smectite octahedral sheet. As described in the previous two chapters of this dissertation, this type of structural deformation is indicative of impact-induced structural change in nontronite. To investigate whether impact-altered nontronite might be identifiable on the martian surface, I compared the band depth ratio results from nontronite samples altered by laboratory impacts to well-characterized martian nontronite identifications. All of the nontronite spectra from the regions of the martian surface were taken from CRISM stamps, in which either nontronite- or Fe/Mg smectite-rich regions have previously been identified: Hargrave's Crater (Mustard et al., 2009), another part of the Nili Fossae region (Poulet et al., 2005), and Mawrth Vallis (Loizeau et al., 2007).

I used FATT (Malinowski, 1991; Bandfield *et al.*, 2000b; Bandfield, 2002b; Glotch and Bandfield, 2006; Hamilton and Ruff, 2012; Thomas and Bandfield, 2013) to compare martian nontronite spectra to my laboratory spectra, and analyze CRISM images for the presence of impact altered nontronite. I ran my preliminary analysis using the free data and image processing software Davinci v.2.06 (davinci.asu.edu) developed and distributed by Arizona State University (ASU). The CRISM image FRT00013E49 of a portion of the Mawrth Vallis region (Figure 4.1) provided a good starting point for analyzing the complex and heavily bombarded regions of the martian surface. I used spectral libraries derived from my own laboratory spectroscopic analyses of phyllosilicate samples exposed to experimental impacts (Friedlander et al., 2012, 2014b, 2014c, in review; Sharp et al., 2012), previous laboratory work investigating spectral change in thermally altered phyllosilicates (Che *et al.*, 2011; Che and Glotch, 2012), and standard spectral libraries from the Unites States Geological Survey (USGS) (*http://speclab.cr.usgs.gov/spectral-lib.html*) and NASA Reflectance Experiment Laboratory (RELAB) spectral library databases (*http://www.planetary.brown.edu/relabdocs/relab_disclaimer.htm*).

4.2.4 Detailed investigation of CRISM scene FRT000097E2

To investigate the presence of impact-altered nontronite on the martian surface in detail, I analyzed CRISM scene FRT000097E2, from the Nili Fossae region of Mars, just west of the Isidis Basin (Figure 4.2). I selected this scene because thermally altered nontronite was recently detected in another CRISM scene from this region (FRT0000BEC0) by Che and Glotch (2014), and because it contains two small (0.5 – 1 km) craters in the southwest corner (Figure 4.3), which provide important geologic context for the detection of potentially impact altered clay minerals, both within the scene and the region. Other recent analyses of this scene showed that local mineralogy might be consistent with complex diagenetic environments. Mineral assemblages made up of mixed olivine-carbonate-phyllosilicate detections have been identified, but the regional depositional and potentially diagenetic environments are not yet fully understood (Mustard and Wiseman, 2014). As a false-color IR band composite image, Figure 4.3 provides further context for FRT000097E2. In false-color composite images, bands are assigned primary colors (red, green, and blue) and pixels are individually analyzed to determine which of the assigned spectral bands has the strongest reflectance value. Each pixel is then colored according to the assigned color of the most strongly reflecting band (or combination of bands) within that pixel. In Figure 4.3, red pixels correspond to those that are strongly reflecting at 2.53 μm, green pixels correspond to those that are strongly reflecting at 1.51 μm, and blue pixels correspond to those that are strongly reflecting at 1.08 μm. These are the standard CRISM false-color NIR composite band assignments (Seelos, 2009) and are generally used to accurately represent surface features in the scene using reflected IR radiation, rather than mineralogy. However, this band composite also distinguishes hydrated minerals, which appear cyan to green (Liu and Glotch, 2014). Given both its complexity and the presence of hydrated minerals (Figure 4.3), FRT000097E2 seemed likely to contain impact altered phyllosilicates (possibly nontronite) in addition to complex, possibly diagenetic, aqueous alteration mineral assemblages.

4.2.4.1 Image processing and CRISM data calibration and correction

I carried out the CRISM scene analyses using ENVI/IDL Classic (version 5.1) and the built-in analytical capability of the latest release of the CRISM Analysis Toolkit (CAT: version 7.2.1) (http://pds-geosciences.wustl.edu/missions/mro/crism.htm). FRT000097E2 is in the most up-to-date data format available from the CRISM archive (TRR3) of the NASA Planetary Data System (PDS). The FRT000097E2 data product that I used was also radiometrically calibrated and converted into I/F from a raw CRISM Experiment Data Record (EDR). I/F is defined as the ratio of the spectral radiance of the martian surface as measured by CRISM divided by the solar spectral irradiance of the Sun at Mars's distance divided by π. "I" is intensity or power/area ($I_{measured}$/steradian) and "F" is the solar irradiance at Mars/π. Another way to describe I/F is that it is the ratio of the radiance observed by CRISM at the martian surface to the radiance produced by a perfectly reflecting Lambertian surface illuminated by the same light, but at normal incidence. It is easier to extract surface spectra from I/F data than EDR data because I/F data have been calibrated for variability in solar irradiance on the martian surface by sol and time (http://ode.rsl.wustl.edu/moon/pagehelp/quickstartguide/index.html?crism_product_primer.htm). In addition, TRR3 data formats have also been processed with a custom filtering procedure that removes instrument artifacts generated by variability in the operating temperature of the CRISM IR detector. These artifacts appear as along track column-oriented striping, but have been removed from TRR3 data products prior to their addition to the PDS (Murchie *et al.*, 2012). If Mars had no atmosphere, I/F divided by the cosine of the incidence angle would give the Lambert albedo of a Lambertian surface. However, Mars does have an atmosphere, which must

be accounted for in analysis of the reflectance spectra derived from spectral images of the martian surface. Using the built-in capabilities of CAT, I applied the systematic processing steps required to convert CRISM I/F into apparent surface reflectance. I first corrected the data for photometric effects by dividing by cosine($\theta_{incidence}$) and then atmospherically corrected the data using the most current volcano-scan option available within the CAT. The volcano-scan CRISM atmospheric correction system utilizes a CRISM measurement of martian atmospheric transmission. This is derived by taking the ratio of a nadir-looking I/F spectrum acquired at the summit of Olympus Mons (the largest volcano on Mars – indeed, the largest of all known volcanoes in the Solar System) to a nadir-looking I/F spectrum acquired at the base of Olympus Mons. The volcano-scan technique then automatically rescales this transmission spectrum for other atmospheric pressures in other locations on Mars. It is quick and fairly accurate, though not as robust as other, more computationally intense atmospheric correction techniques. Mcguire *et al.* (2008) provided an excellent description of the volcano-scan method, as well as a comparison of its accuracy relative to their own more robust, but much more computationally intense DIScrete-Ordinate-method Radiative Transfer (DISORT) modeling method.

4.2.4.2 Spectral angle mapping for targeted spectral comparison

To locate potential regions of interest containing impact altered and other phyllosilicate minerals, I used ENVI/IDL's built-in Spectral Angle Mapper (SAM) spectral analysis tool (http://www.exelisvis.com/docs/SpectralAngleMapper.html), which matched spectral data from the CRISM image cube to laboratory and library spectra resampled to CRISM spectral resolution. The SAM method within ENVI/IDL determines the similarity between scene spectra (e.g., unknown material) and library spectra (e.g., potential mineral end-members, known material) by computing the spectral angle between them; treating both spectra as vectors in *n*-dimensional spectral space, where *n* is the number of bands. Because SAM can often be non-intuitive, a simple way to envision the process is to consider the angle between two spectra in a 2-band image as illustrated by the creation of a 2-dimensional scatter plot (Figure 4.4). Each spectrum is defined as a vector passing through the origin that describes the position of each respective spectrum under all possible illumination conditions. Because all possible illumination conditions are represented, the results of SAM analysis are not sensitive to either illumination or albedo effects. ENVI/IDL allows the user to set the spectral angle cutoff (in radians) for defining spectral matches with the end-member spectrum of interest: the smaller the angle, the more robust the match. Pixels are classified based on whether they contain matching spectra and how well those spectra match the known target spectrum. The default setting is 0.100 radians, which is considered a strong match. Pixels containing matching spectral data to the selected end-member spectrum are then classified into regions of interest, which can be mapped or independently analyzed. Using SAM, I was able to focus on and extract spectra from these regions of interest. I then ratioed the extracted spectra to a nearby, spectrally featureless region from the same image column to mitigate spectral smile effects and accentuate relevant spectral features. I then directly compared the extracted, ratioed spectra to resampled laboratory and library spectra to confirm spectral identifications and check my SAM results.

4.3 Results and Interpretation

4.3.1 Preliminary investigations of impact altered phyllosilicates on the martian surface

A comparison of the 1.4/1.9 μm band-depth ratios of the laboratory spectra of nontronite altered by experimental impacts with those of the spectra from nontronite identifications on the martian surface shows that phyllosilicates are likely to have been affected by impact alteration in several regions of Mars (Figure 4.5). Each of the plotted nontronite identifications came from regions in which nontronite has previously been robustly detected: Mawrth Vallis (Loizeau *et al.*, 2007) (FRT00013E49, Figure 4.1), Nili Fossae (Poulet *et al.*, 2005; Ehlmann *et al.*, 2009; Mustard *et al.*, 2009) (FRT000097E2, Figure 4.2), and Hargraves Crater, also in the Nili Fossae region, (Mustard *et al.*, 2009; Michalski *et al.*, 2010) (FRT000088D0, Figure 4.6). The martian band-depth ratios are plotted as horizontal lines, from which hypothetical shock pressures can be inferred based on their intersections with the experimentally derived trend line. Nontronite identified in Mawrth Vallis appears to have experienced little to no shock, or pressures between 0.0 – 10.2 GPa. One of the nontronite identifications from Hargrave's Crater appears to have experienced shock pressures between 19.7 – 25.2 GPa, and a second identification may have experienced shock pressures of 10.2 GPa. The nontronite identifications from other regions nearby the Nili Fossae all have band-depth ratios seeming to correspond to shock pressures between 19.7 – 30.6 GPa. The relatively low pressures predicted for impacts detected in Mawrth Vallis are interesting in light of the more detailed analysis carried out on CRISM image FRT00013E49 from that region, which are discussed below.

Using indices derived from the laboratory spectra of impact-altered phyllosilicates together with standard CRISM spectral summary product indices, I produced a false-color composite image of CRISM scene FRT00013E49 showing the results of spectral analyses produced using the spectral summary products defined in (Pelkey *et al.*, 2007) and my own laboratory spectroscopy results from analyses of impact-altered nontronite. I mapped the LCPINDEX (low-calcium pyroxene index in which LCP appears strongly positive) results in red, the OLINDEX (olivine index, based on fayalite) results in green, and the phyllosilicate detection (based on the D2300 or 2.3 μm slope) in blue. I used SAM to identify pixels that are spectrally similar to impact-altered nontronite over a range of pressures (10.2, 19.7, 25.2, 30.6, and 39.1 GPa) and mapped these to a single, bright red region of interest (Figure 4.7a). I then extracted, ratioed and compared spectra from the shocked nontronite region of interest (red) to spectra from pixels mapped as generic (D2300) phyllosilicate (blue). The generic phyllosilicate spectrum shows the common smectite 2.3 μm absorption feature, while the spectrum extracted from the impact-altered nontronite region-of-interest displays a broad absorption feature at shorter wavelengths, ~2.15 – 2.2 μm (Figure 4.7b). The differences between these two spectral end-members support previous, preliminary work based on FATT analysis of this scene in which shocked nontronite (red) and other phyllosilicates (blue) were detected together in several parts of the scene (Figure 4.8). Detailed analysis by FATT specifically matched CRISM spectra from within the highlighted region of interest (Figure 4.8, orange box) to unaltered nontronite, and impact-altered nontronite exposed to peak pressures of 19.7, 25.2, and 30.6 GPa (Figure 4.9). Because FATT was applied to all of the pixels in the whole of the outlined region, it is impossible to know where exactly these matches occurred within the scene. However, FATT is a principle components-based analysis. Thus, it is possible to identify which altered nontronite spectrum best matched the spectral variability of the pixels from within the region-of-interest based on the root mean square (RMS) error of the fit. RMS error indicates how well the spectral variability of the scene was captured by the linear combination of derived end-member spectra

that resembled a given mineral end-member. Based on this, impact-altered nontronite that experienced peak impact pressures of 25.2 GPa (RMS = 0.0128) and 30.6 GPa (RMS = 0.0114) best matched the spectral variability of the selected region-of-interest.

4.3.2 Detailed analysis of impact altered nontronite in CRISM image FRT000097E2

The geologic context of the Nili Fossae region is complex (Fassett and Head, 2005; Mangold *et al.*, 2007; Mustard *et al.*, 2007, 2008; Ehlmann *et al.*, 2009; Michalski *et al.*, 2010; Saper and Mustard, 2013). The region displays extensive evidence for aqueous alteration through martian geologic history, and it as also been heavily bombarded, making it ideal for studying the impact alteration of phyllosilicates in context. I chose the CRISM stamp FRT000097E2 for my analysis because it shows distinct enrichment of phyllosilicates in and around two small craters in the southwest corner of the scene (Figure 4.10). By overlaying a map-projected, false-color image of this stamp on image PSP006778_1995 from the High Resolution Imaging Science Experiment (HiRISE), the details of the geomorphology of the region can be associated with the regional mineralogy. The false-color composite was produced by assigning the results of the spectral summary products defined by Pelkey *et al.* (2007) as follows: D2300 (red), 2.3 μm band slope (or drop off), identifies hydrated minerals, especially phyllosilicates; OLINDEX (green), based on reflectance at 1.7 μm and surrounding features derived from the fayalite spectrum, olivine is strongly positive; LCPINDEX (blue), based on the difference in reflectance between 1.33 and 1.05 μm bands, pyroxene is strongly positive and low-Ca pyroxene is favored. This figure revealed that phyllosilicate-rich regions surround both craters, and can also be found within them. Figure 4.11 shows a 3D perspective view of the same CRISM scene, with red regions being more phyllosilicate rich based on the D2300 spectral summary parameter (Pelkey *et al.*, 2007), overlaid on Mars Orbiter Laser Altimeter (MOLA) altimetry data (*http://jmars.asu.edu/3d-layer*). This view shows that the two craters in the southwest corner of the scene fall on either side of one of the large concentric grabens (Fossae) that characterize the Nili Fossae region, and that, in addition to other parts of the scene, phyllosilicates appear to be concentrated on the rims and in the ejecta blankets of these craters.

Using the SAM spectral analysis tool in ENVI/IDL, I detected several regions of interest from within FRT000097E2 that are likely to be rich in the minerals of interest namely: impact-altered nontronite and other phyllosilicates including, illite, smectite (BK1JB006, otherwise unspecified in the spectral library provided with CAT), and nontronite (NDJB26, also from the provided CAT resampled CRISM comparison spectral library). The results of this analysis (Figure 4.12) show that the clay minerals detected by SAM by-and-large corresponded with regions that are expected to be clay-rich based on D2300 band parameter mapping (Figures 4.10 and 4.11). In addition, impact altered nontronite, nontronite, smectite, and illite all appear to be present in pixels in or around the two small craters in the southwest corner of the scene (Figure 4.12, outlined in red circles).

Several of the SAM detections shown in Figure 4.12 are more robust than the ENVI-generated automatic spectral angle cut-off of 0.100 radians. The nontronite detection based on an end-member spectrum of nontronite NDJB26 had a SAM cutoff of 0.040 radians, the lowest of all of the detected target spectra. Every other detection was based on a cutoff of 0.055 radians, with the exception of the chlorite and illite detections (Figure 4.12e and f). For these detections, I intentionally used a higher SAM cutoff of 0.100 radians to demonstrate the potential for overlap between remote sensing detections of chlorite, illite, smectite, and impact-altered nontronite.

This overlap is especially noteworthy given that the relative abundance of illite on Mars is likely to be low and controlled by the availability of K^+, which is expected to be limited in waters arising from a basaltic source (Tosca and Knoll, 2009). In addition, K-rich feldspar is one of the mineral species most resistant to erosion on the martian surface. The production of chlorite, however, does not require K^+, making chlorite the more geochemically likely diagenetic product of the conversion of martian smectites, despite the fact that the starting material is likely to be dioctahedral. Given their spectral similarities and close association with impact craters, the geologic and geochemical contexts of potential interstratified smectite/illite deposits should be carefully considered before definitive identification of illite can be claimed.

The SAM analysis detected impact-altered nontronite in several places in this scene, notably in parts of the scene that also have robust smectite or nontronite detections (Figure 4.12b and c), but also in and around the ~1 km crater in the southwest part of the scene. Geologically, it makes sense that impact-altered nontronite would be found around a crater. What is interesting about his detection is that the only impact-altered nontronite sample detected in this scene was nontronite that had experienced a laboratory impact at 39.1 GPa peak pressure. This is a high pressure for a 1 km impact to achieve, although certainly not impossible (Weiss and Head, 2014). This identification is geologically compelling because most of the altered nontronite is detected in the center of the crater, which is where an impact producing a 1 km crater would be expected to also produce its zone of highest pressure (Weiss and Head, 2014). The fact that SAM analysis also detected occurrences of altered nontronite in other parts of the scene may be partially explained by the spectral similarity between altered nontronite, generic smectite and other phyllosilicates. However, the CRISM scene FRT000097E2 sits at the edge of the Isidis basin, which likely formed as a result of a giant impact that is thought to have spread impact ejecta and altered material (including melt) throughout the Nili Fossae region (Mustard *et al.*, 2007). Thus, these detections cannot be completely discounted.

Detections of chlorite and illite with slightly relaxed SAM matching parameters (0.100 radians) shown in Figure 4.12e and 12f, demonstrate the difficulty of unambiguously determining local mineralogy by showing that many phyllosilicate detections can overlap. Characteristic spectra from within each region of interest were extracted from the scene (Figure 4.12, indicated by arrows) and ratioed, then compared to laboratory and library spectra to confirm the SAM results (Figure 4.13). These library spectral comparisons further demonstrate the difficulty in distinguishing between spectrally similar phyllosilicates. Smectite, altered nontronite and illite all possess a characteristic band at ~2.2 μm, which may contribute to their overlapping detections.

4.4 Discussion

4.4.1 Possible overlap between observations of diagenetic clays and impact alteration

Previous chapters of this dissertation described the specific spectral and structural changes that impacts induce (or not) in the phyllosilicates nontronite, kaolinite, and saponite. The purpose of this work is to provide new laboratory data and contribute to the remote sensing analysis of the martian surface. The successful detection of impact-altered nontronite in a CRISM scene from a heavily bombarded region of Mars confirms both that impact alteration produces spectrally distinct changes in phyllosilicates that can be identified by remote sensing,

and also that experimentally impact-altered samples would be useful to include in the libraries used for remote sensing spectral image analysis. This was implied by previous research on the TIR analysis of spectral mixtures using terrestrial impactite samples from Lonar Crater (Wright *et al.*, 2011), and was more recently directly shown to be relevant for thermally altered phyllosilicates (Che and Glotch, 2014). However, the presence of impact-altered phyllosilicates on Mars has not previously been directly shown in an impact-specific geologic context.

Several important implications arise from the detection of impact-altered nontronite in CRISM scene FRT000097E2, especially with respect to the locations of these detections and their proximity to other mineral detections. As previously described, most of the mineral-specific detections made in this scene fall within regions where phyllosilicate detections were expected based on established CRISM spectral summary parameters (e.g., the D2300, 2.3 μm slope) (Pelkey *et al.*, 2007; Viviano-Beck *et al.*, 2014). This means that the altered nontronite that I have detected exists either in a mineral assemblage that also contains unaltered phyllosilicates, or that this detection arises because of the spectral similarities between several minerals that may exist in the region (Figure 4.13c). These spectral similarities are especially important because many of the characteristic band shifts observed for the reflectance spectrum of an experimentally impact-altered natural nontronite sample (NAu-1) occur in the 2.2 – 2.5 μm region. I have described these changes and their importance in detail in the previous two chapters of this dissertation. I revisit this issue here to reiterate that these bands are frequently used as characteristic mineral identification bands in martian remote sensing studies (e.g., Langevin et al., 2005; Poulet et al., 2005, 2009; Mangold et al., 2007]. Under controlled laboratory conditions, it is clear that the location of these band centers can identify the dominant octahedral cation in phyllosilicate structures (Bishop *et al.*, 2002a; b, 2008a), and so their use in mineral specific identifications is logical. However, impact alteration (especially of mineral mixtures such as NAu-1 nontronite, which contains a kaolinite contaminant) induces band shifts in this region that resemble those invoked to determine cation-specific mineral identifications on Mars. This is potentially problematic, especially in heavily bombarded regions.

Another implication of the spectral effects of impact-driven phyllosilicate alteration is potential confusion over remote sensing data interpretation to understand phyllosilicate diagenesis and depositional environments on Mars. This is particularly concerning for smectite-to-illite and smectite-to-chlorite transitions, which are often identified by local or regional-scale spectral transitions also in the 2.2-2.5 μm wavelength range of VNIR reflectance spectra (Ehlmann *et al.*, 2009; Milliken *et al.*, 2010), sometimes in combination with the presence of bands near 1.4 μm (Ehlmann *et al.,* 2009). Comparing the observed shifts in the absorption bands between 2.2 – 2.5 μm for impact-altered nontronite, laboratory spectra of phyllosilicates and related diagenetic species (e.g., chlorite and illite), and spectra from within CRISM scene FRT000097E2 shows how closely these can overlap (Figure 4.14). Ehlmann *et al*. (2009) especially noted that many of their chlorite detections in the Nili Fossae region are associated with craters to the west and south of the Nili Fossae themselves. Chlorite has a strong absorption feature at 2.35 μm and a weaker shoulder at 2.26 μm, neither of which is directly comparable to the spectral features of impact-altered nontronite. However, when investigating the possibility of diagenesis and mixed-layered (smectite/illite or smectite/chlorite interstratified structures) clays on Mars, identifications are more often based on regional spectral variability (e.g., Milliken *et al.,* 2010). In this context, impact-induced spectral change may be very misleading, especially regarding mixed-layered smectite/illite or illitization on Mars, because illite, unlike chlorite, has

a strong absorption band at 2.23 μm, close to the broad 2.21 μm band observed for nontronite after experimental impacts at 39.1 GPa (Figures 4.13c and 4.14).

The potential convolution of these overlapping identifications may be especially prevalent in impact craters, which is important to note because investigating impact crater mineralogy has been proposed as one possible method for understanding the past geologic history of Mars (Schwenzer *et al.*, 2009, 2010). Craters offer "windows (Schwenzer *et al.,* 2009)" into the martian subsurface, but the impacts that made them also induce geologic and thermochemical processes that cause structural and spectral changes in the minerals present. In the case of nontronite, and perhaps other minerals as well, the spectral changes induced by impact processes overlap with the band shifts that are used to identify smectite-to-illite transitions as well as mineral assemblages containing smectite/illite interlayered clays. The processes that produce illite from smectite cannot proceed at the martian surface. Therefore, structures and processes that exhume ancient sediments must be studied to understand them. There are many structures that reveal ancient sediments on Mars. Vallis Marineris exposes rocks 7 km below the surface. However, impacts are the most widespread of these features. As a result, many detections of ancient martian mineral deposits rely on impacts to exhume old material and provide geologic context. As a result, it is difficult to completely decouple mineral diagenesis hypotheses from impact-alteration processes. I suggest that future spectral and remote sensing analyses include impact-altered clay minerals, mapping their detections together with those of proposed diagenetic minerals in an effort to understand the potential interactions and overlap between their detections.

4.4.2 Drawing inferences about martian climate from clay mineral identifications

The presence of clays on Mars implies past availability of liquid water (Poulet *et al.*, 2005). Some clay minerals require circum-neutral pH solutions for formation, which has been interpreted as an indicator of potential habitability (Grotzinger *et al.*, 2014; Rampe *et al.*, 2014; Vaniman *et al.*, 2014). The geochemical constraints of detected martian mineralogy are one of the few tools available to understand martian climate, but they leave open many important aspects of that climate. For example, the fact that liquid water once acted on the martian regolith is clear from the presence of detectable hydrated mineral species at the present-day surface (Mustard *et al.*, 2008; Wiseman *et al.*, 2010; Carter *et al.*, 2013), but the form this water took, its areal extent, and temporal persistence remain key unanswered questions. Was Mars both wetter and warmer (Squyres and Kasting, 1994; Bishop *et al.*, 2013c; Clifford *et al.*, 2014)? Or was it wetter, but cold with solutions at the surface existing primarily in the form of brines (Fairén *et al.*, 2009)? Perhaps impacts themselves provided the energy and liquid water to generate much of the mineralogy currently detected on the martian surface (Marzo *et al.*, 2010; Osinski *et al.*, 2011; Tornabene *et al.*, 2013; Weiss and Head, 2014). Detections of diagenetic minerals can answer some of these questions, which is why any overlap between their detections and the detections of altered minerals from other processes may have such a profound effect on the ability to infer accurate information about paleoclimate on Mars.

There are several potential implications that arise from the possibility that diagenetic clay mineral identifications might be convolved with impact-induced spectral change. The first is that diagenesis on Mars may be significantly less widespread than has been previously suggested. This would imply that extensive water on Mars was either very short-lived, and that water has since been extremely limited, or that liquid water has been primarily confined to the subsurface

throughout Mars's geologic history. Because active diagenetic environments are thought to be more likely to be habitable, or to have been habitable in the past, more limited diagenesis would also limit the number of potentially (or previously) habitable environments on Mars. Another possibility is that the presence of impact-altered phyllosilicates may make detailed inferences based on careful comparison of the smectite/illite ratio inaccurate. This would directly complicate efforts to understand how deeply buried and how long phyllosilicates have been weathered on Mars. However, spectral end-members combine nonlinearly in the VNIR wavelength region, so accurate abundance determinations from VNIR remote sensing data are already difficult and conclusions based on these types of calculations must be carefully considered (Poulet, 2004). Finally, it is possible that impacts themselves induced the processes, or the structural and spectral changes that have been interpreted as diagenesis. If impacts, rather than sedimentation and burial, are the basis for phyllosilicate diagenesis on Mars, then the probability that Mars's paleoclimate contained an epoch with temporally extensive liquid water interactions, and widespread potential habitability, significantly decreases.

4.5 Conclusions

Using new laboratory spectroscopic results investigating structural and spectral change in nontronite after laboratory impacts, I directly investigated the potential presence of impact altered phyllosilicates in several locations on Mars. Analysis of two CRISM scenes from heavily bombarded regions of the martian surface showed that impact altered nontronite could be identified by multiple spectral image analysis techniques. In the analyzed scene from nearby the Nili Fossae, the spectral signature of impact-altered nontronite, in addition to pixels identified as containing that spectral end-member, frequently overlapped with both generic smectite identifications and with illite identifications. The possibility that illite identifications might be convolved with impact altered nontronite (or other impact-altered smectites), especially in and around impact craters, raises important questions about inferences to the past martian climate that have been drawn based on comparison to terrestrial phyllosilicate diagenesis. Such inferences must be considered very carefully. Many important questions about martian climate and the role of phyllosilicates in martian geology remain unanswered. Careful laboratory investigations of key geologic processes and their effect on spectroscopic and remote sensing data are the key to accurate remote sensing data analysis.

Chapter 4 – Figures

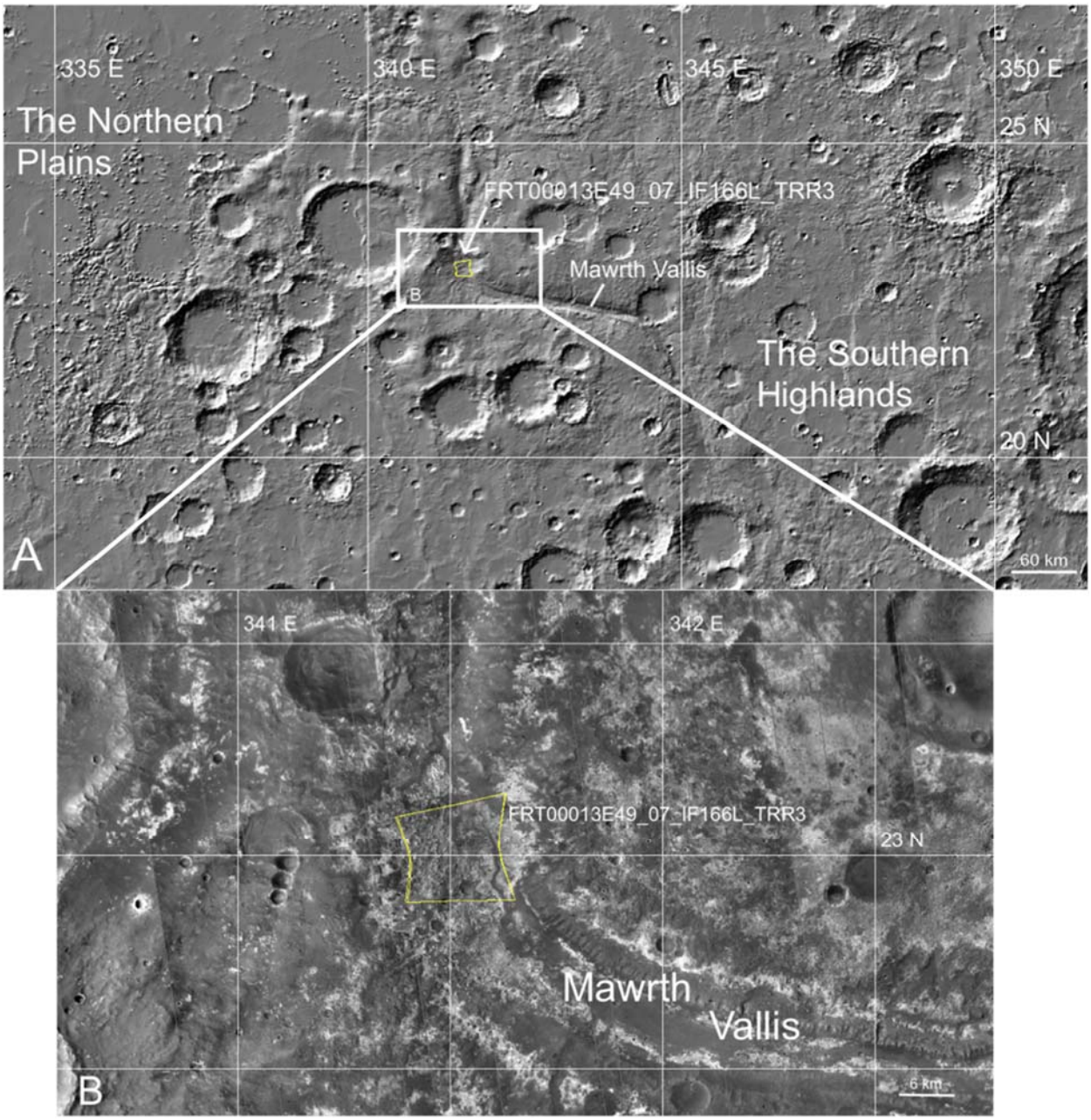

Figure 4.1. JMARS-produced images showing the regional context of CRISM scene FRT00013E49 from the Mawrth Vallis region of Mars. (A) A grayscale map of the scene's broad regional context derived from Mars Orbital Laser Altimeter (MOLA) data in which lower elevations appear darker. (B) A more detailed local context image showing the outline of FRT00013E49 overlain on a mosaic of MRO Context Camera (CTX) grayscale images at 6m/pixel resolution.

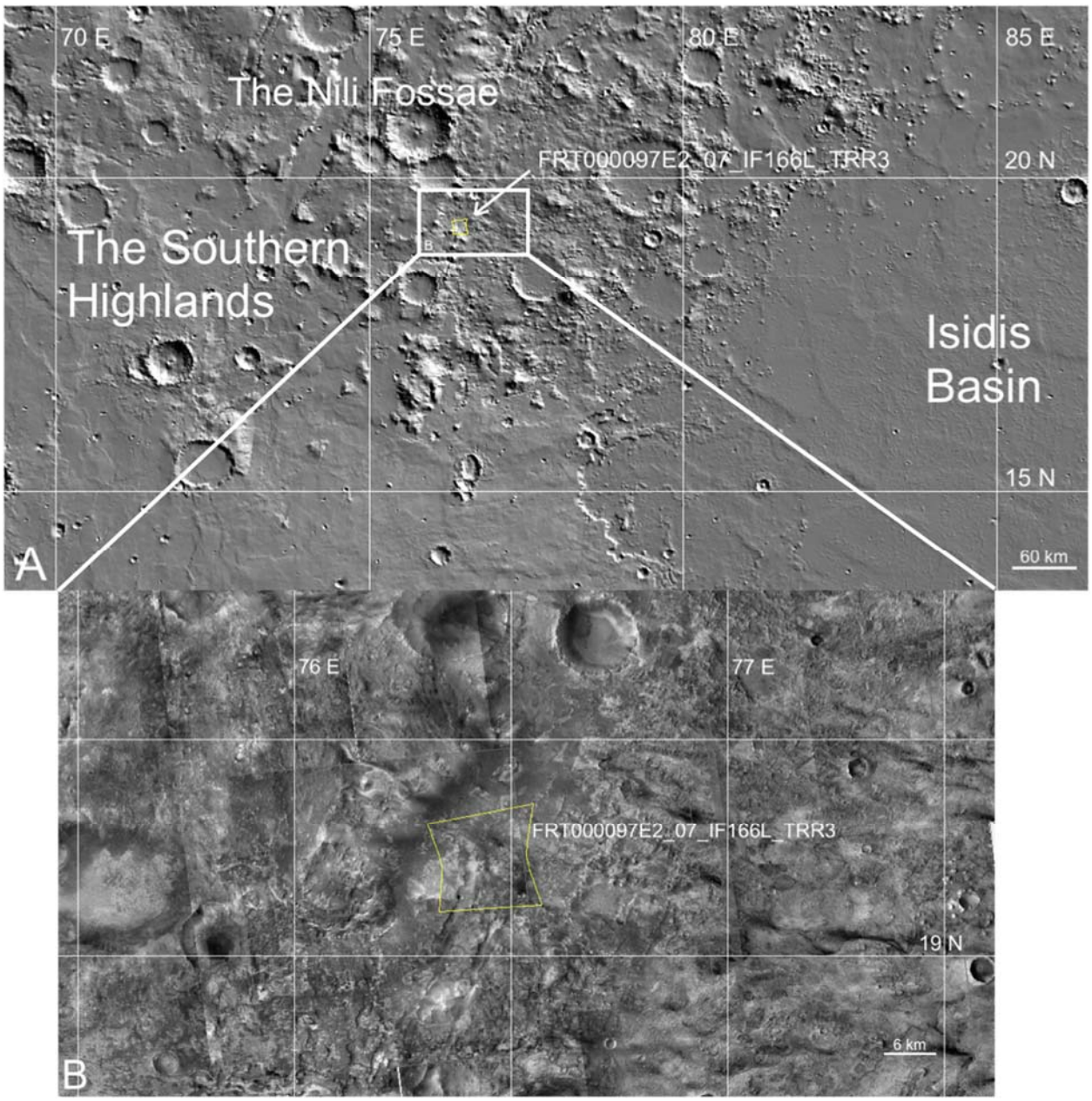

Figure 4.2. JMARS-produced images showing the regional context of CRISM scene FRT000097E2 from the Nili Fossae region of Mars. (A) A grayscale map of the scene's broad regional context derived from MOLA data in which lower elevations appear darker. (B) A more detailed local context image showing the outline of FRT000097E2 overlain on a mosaic of MRO CTX grayscale images at 6m/pixel resolution.

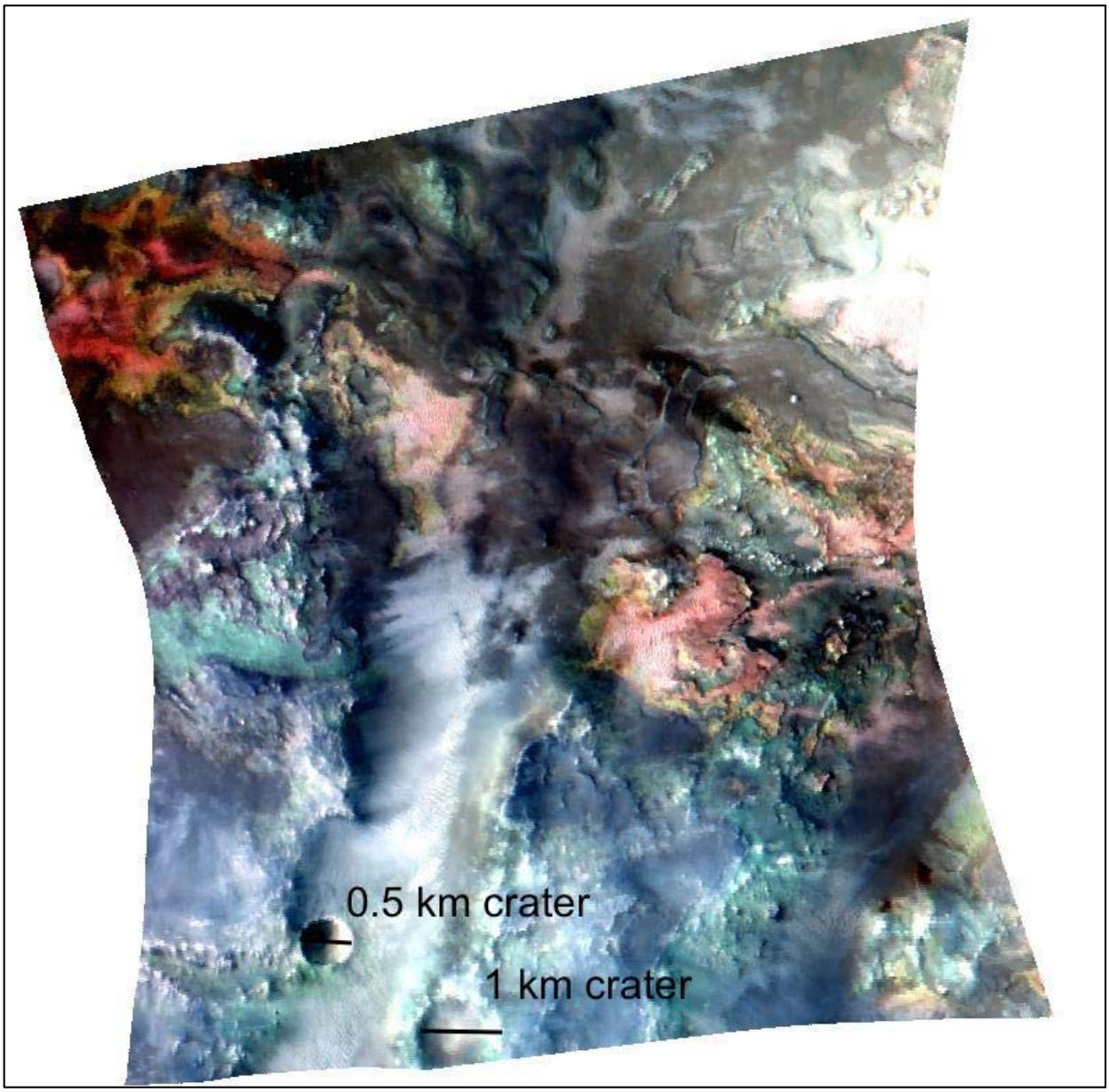

Figure 4.3. False-color composite context image of CRISM scene FRT000097E2 with IR reflectance bands 2.53 μm (red), 1.51 μm (green), and 1.08 μm (blue) mapped. The two small craters in the southwest corner of the image are labeled by size. This IR false-color band combination is commonly used to build CRISM composite images that accurately represent the surface features of the scene, rather than mineralogy. However, this color composite also distinguishes hydrated minerals, which appear cyan to green.

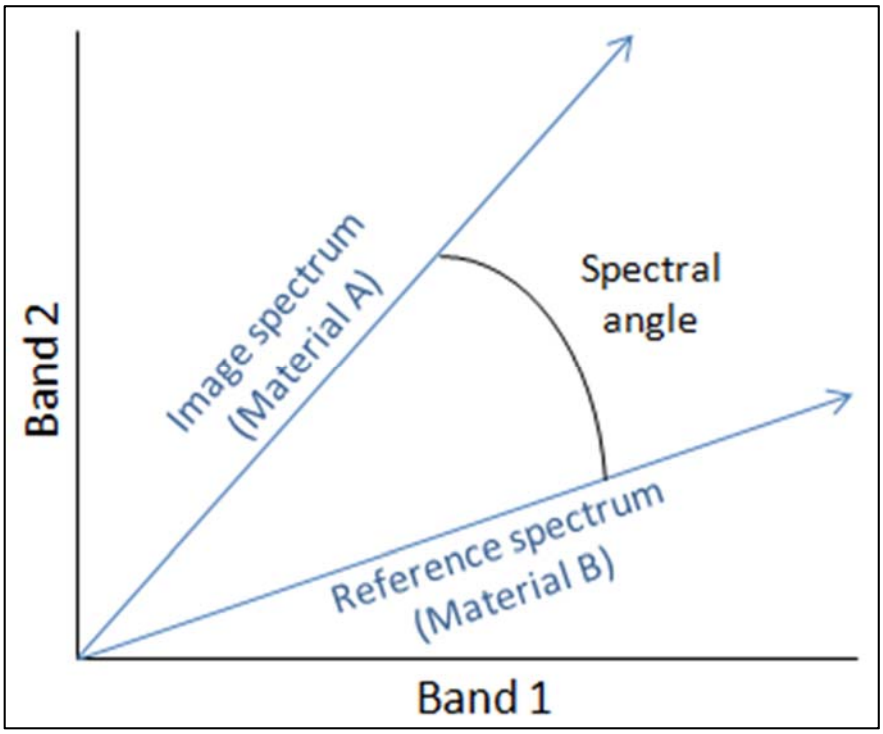

Figure 4.4. Schematic image of the SAM analysis process as described by the comparison of a target and image spectrum in a 2-band image displayed as a 2-dimensional scatter plot. The vector through the origin describes the position of each spectrum under all possible illumination conditions. Because all possible illumination conditions are represented, SAM is not sensitive to either illumination or albedo effects. Reproduced from **(**http://www.exelisvis.com/docs/Whole-Pixel_Hyperspectral_Analysis_Tutorial.html).

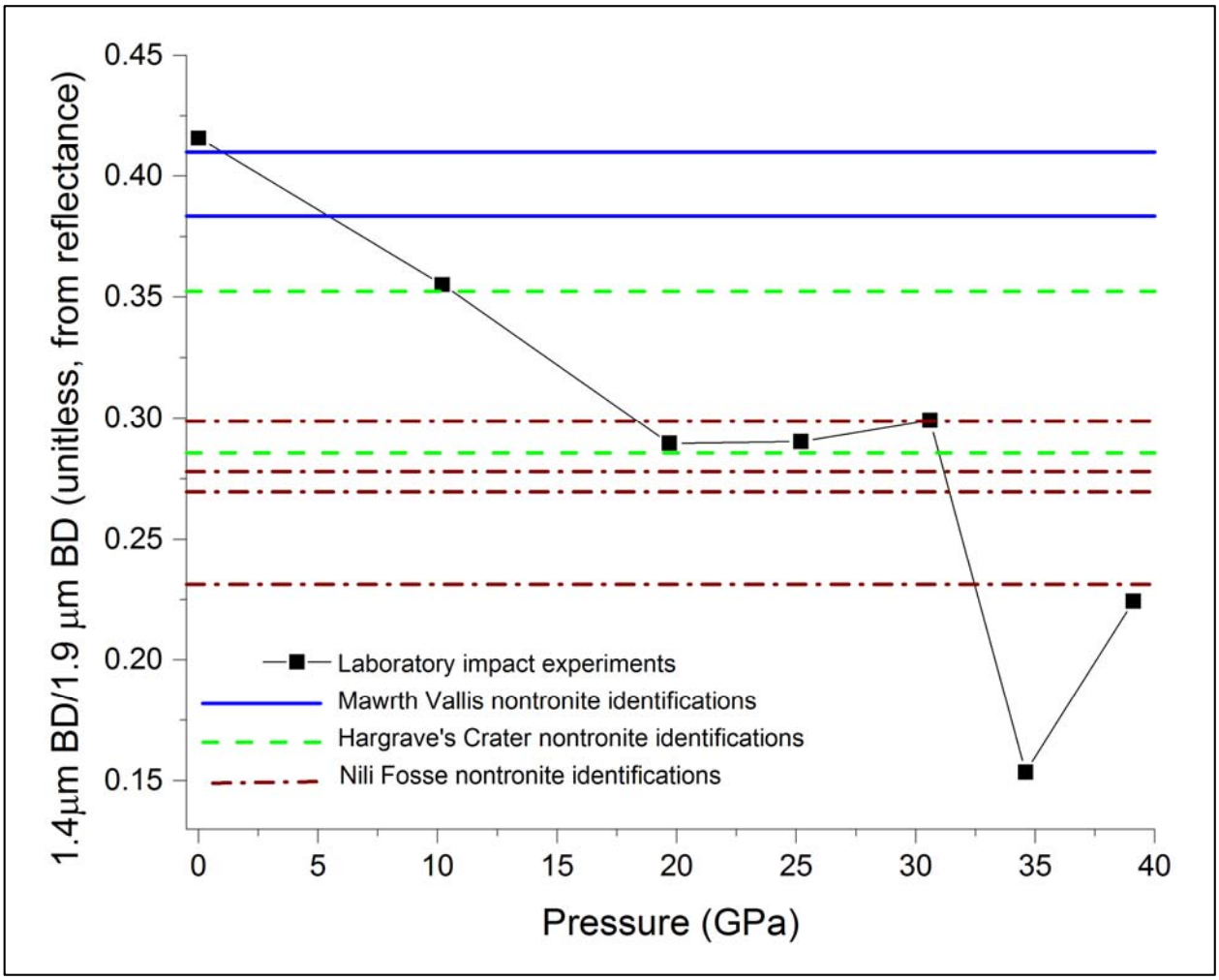

Figure 4.5. 1.4/1.9 micron band depth ratio comparisons between nontronite identifications in various martian locations and band depth changes in the post-impact nontronite VNIR reflectance spectrum. Points of intersection between the two may be indicative of impact alteration pressures experienced at the location of that identification.

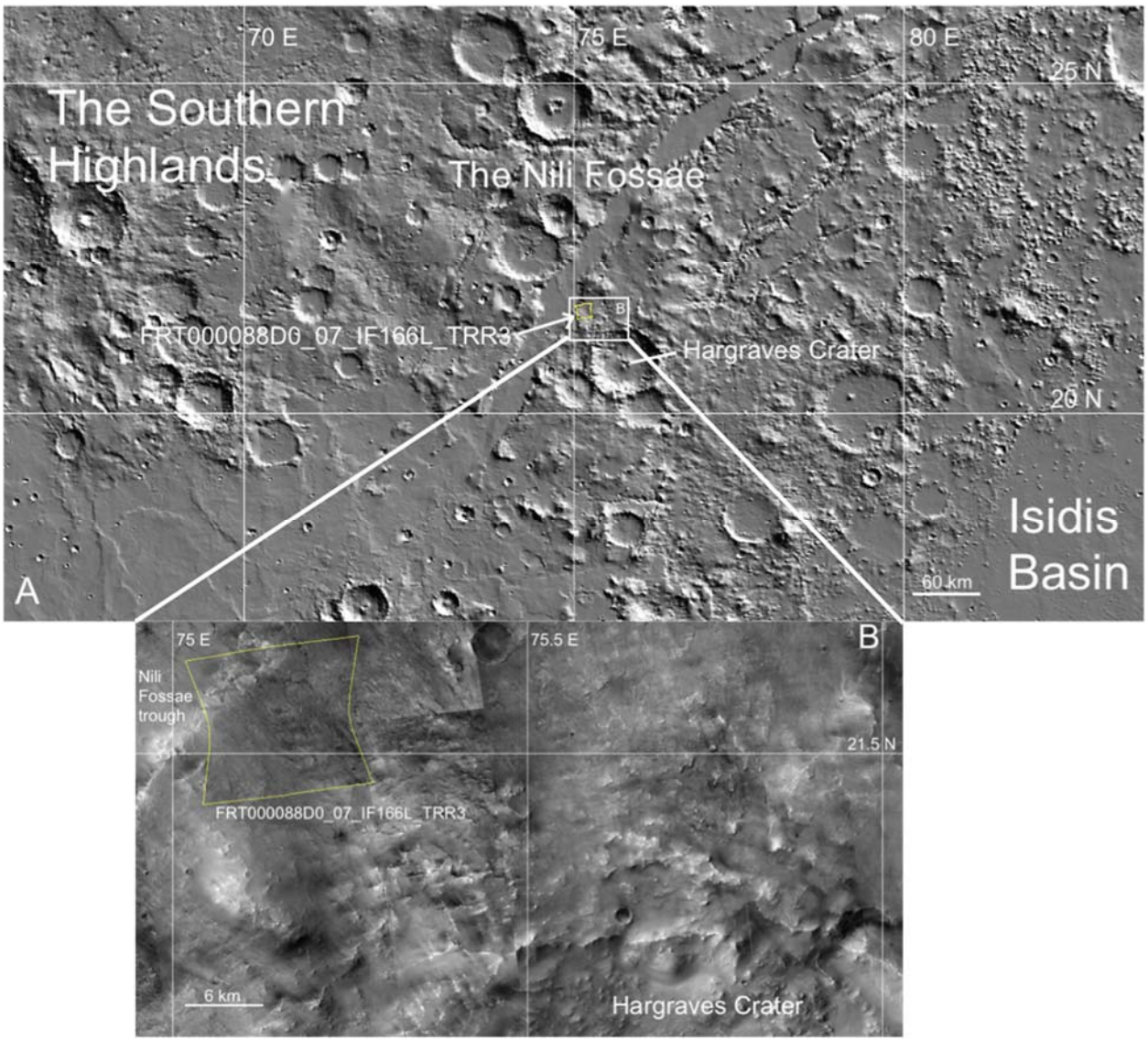

Figure 4.6. JMARS-produced images showing the regional context of CRISM scene FRT000088D0 from the Nili Fossae region of Mars, northwest of Hargraves Crater and within the Hargraves Crater ejecta blanket as described by Mustard *et al.* **(**2009**)** and Michalski *et al.* **(**2010**)**. (A) A grayscale map of the scene's broad regional context derived from MOLA data in which lower elevations appear darker. (B) A more detailed local context image showing the outline of FRT000088D0 overlain on a mosaic of MRO CTX grayscale images at 6m/pixel resolution.

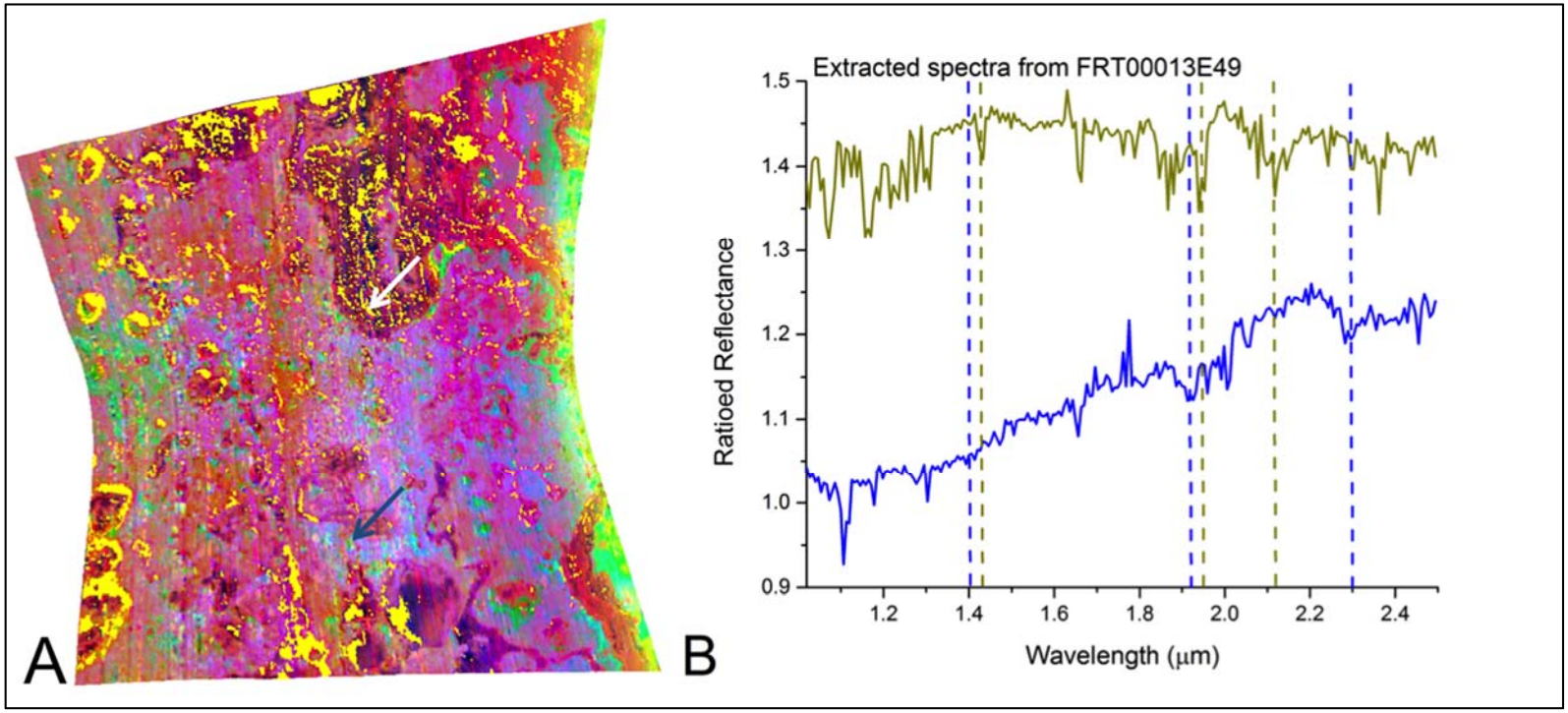

Figure 4.7. False-color composite image of FRT00013E49 with LCPINDEX (red), OLINDEX (green) and phyllosilicates (D2300, blue). Pixels matched to impact-altered nontronite as determined by SAM are shown as a yellow region-of-interest overlay (A). Extracted characteristic spectra from pixels mapped to generic phyllosilicate (D2300) are shown in blue and extracted characteristic spectra from pixels mapped to impact altered nontronite are shown in yellow (B). The white and blue arrows in (A) indicate the locations of the extracted spectra. The white arrow corresponds to the yellow region of interest and yellow spectrum in (B). The blue arrow corresponds to blue generic phyllosilicate regions and the blue spectrum in (B). Compare the mapped phyllosilicate locations in Figure 4.7 to those shown in Figure 4. 8 (produced using Davinci).

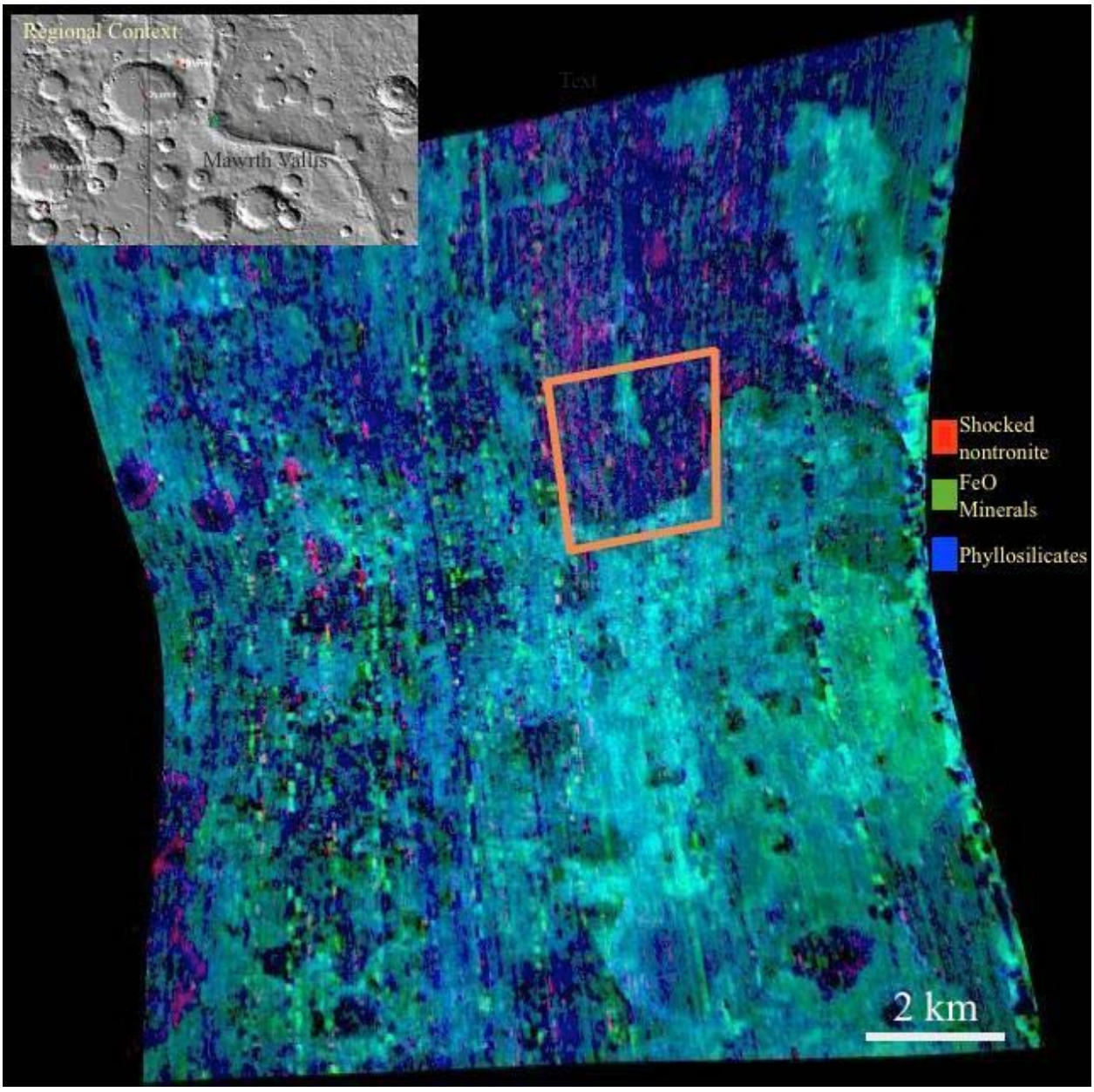

Figure 4.8. CRISM scene FRT00013E49 colorized to reflect end-member identifications of impact-altered nontronite (red), FeO minerals (green), and phyllosilicates (blue). Indices used for spectral mapping were based on Pelkey *et al.* (2007) and modified for the identification of impact altered nontronite. Spectra were extracted by FATT and analyzed from the region of interest outlined in orange.

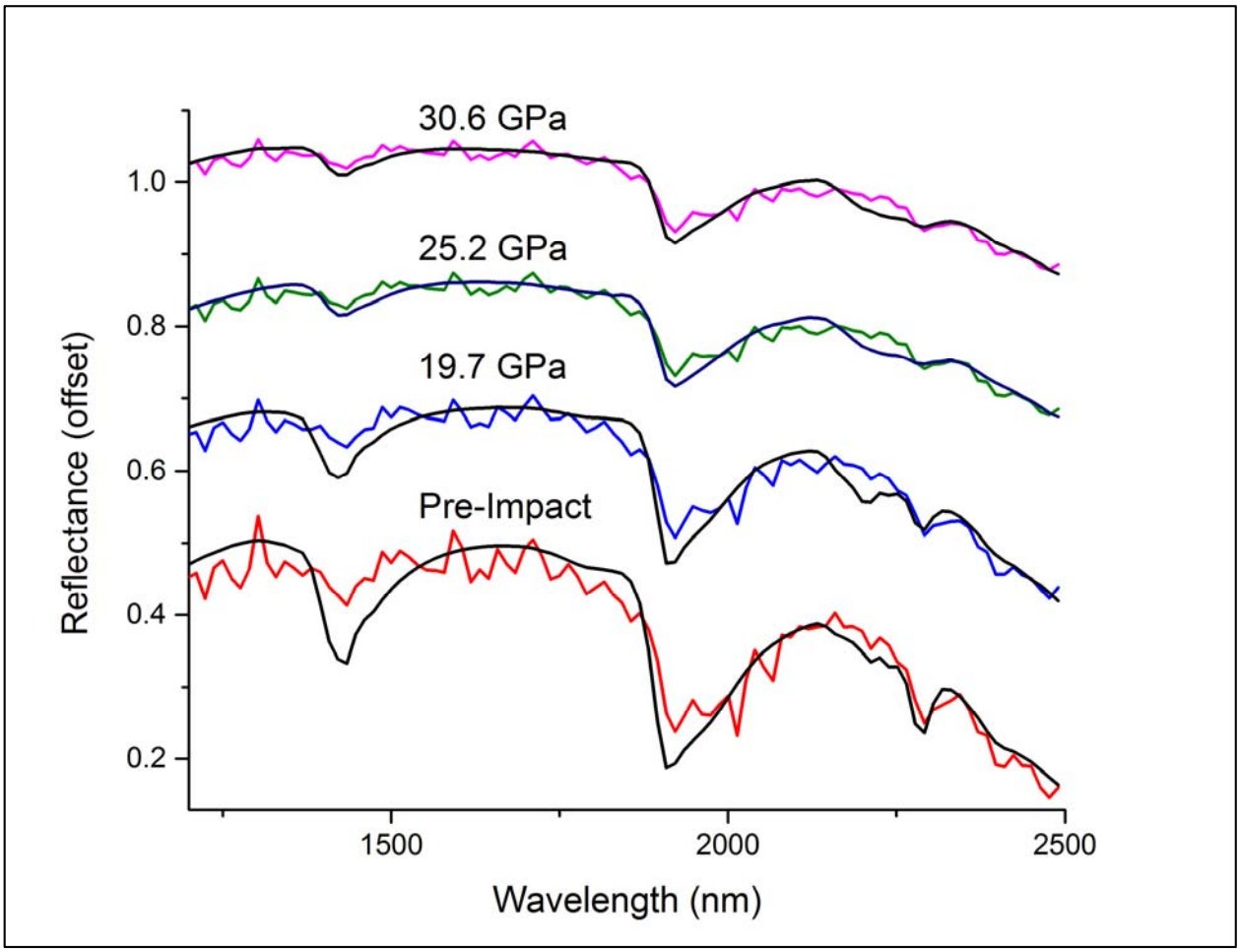

Figure 4.9. FATT-extracted spectra (colored) compared to laboratory spectra of unaltered and impact-altered nontronite samples resampled to CRISM spectral resolution.

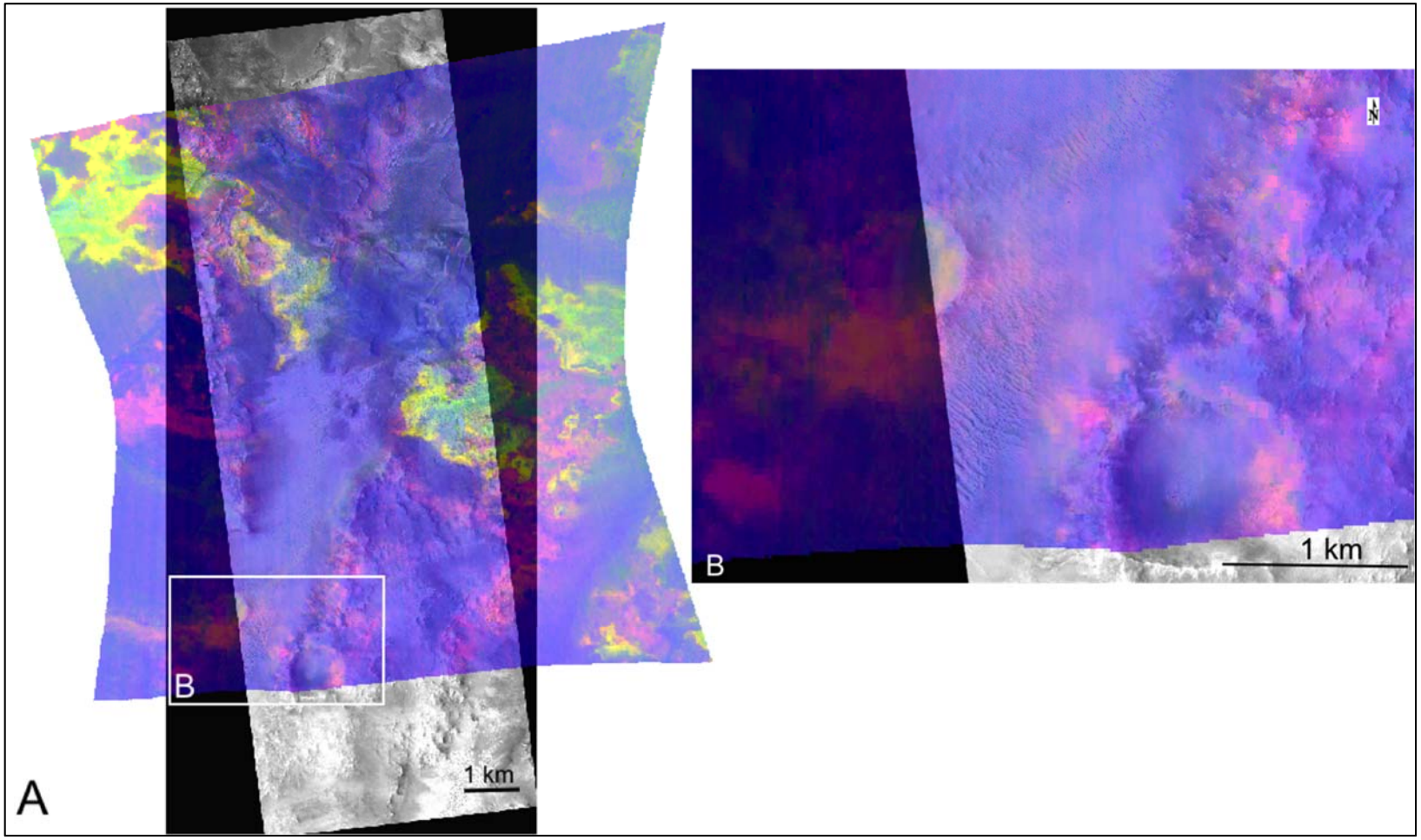

Figure 4.10. False-color CRISM image showing the distribution of phyllosilicates (red), olivine (green) and low-Ca pyroxene (blue) within CRISM scene FRT000097E2. The false-color composite image is overlaid on HiRISE image PSP006778_1995 from the same geographic region (A). The overlay provides context and highlights the relationship between clay mineral deposits and the two small craters in the southwest corner of the CRISM scene (B).

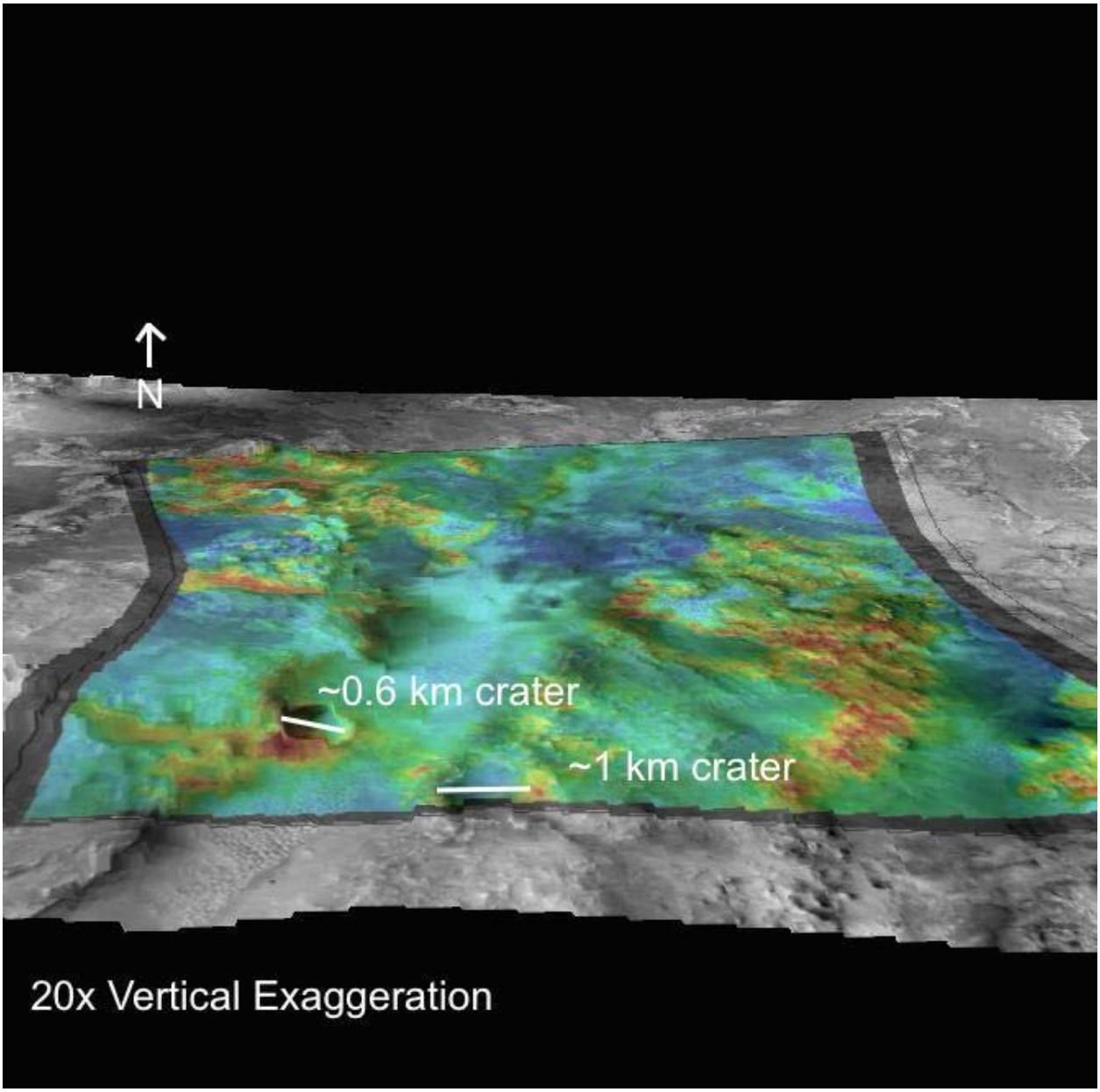

Figure 4.11. Rendered D2300 spectral summary parameter CRISM scene FRT000097E2 (red regions are phyllosilicate-rich) overlain on a CTX-generated 3D contour at 20X vertical exaggeration. The image was produced using JMARS, to highlight regional topography, especially the association of phyllosilicate-rich regions with the two small craters in the southwest corner of the scene.

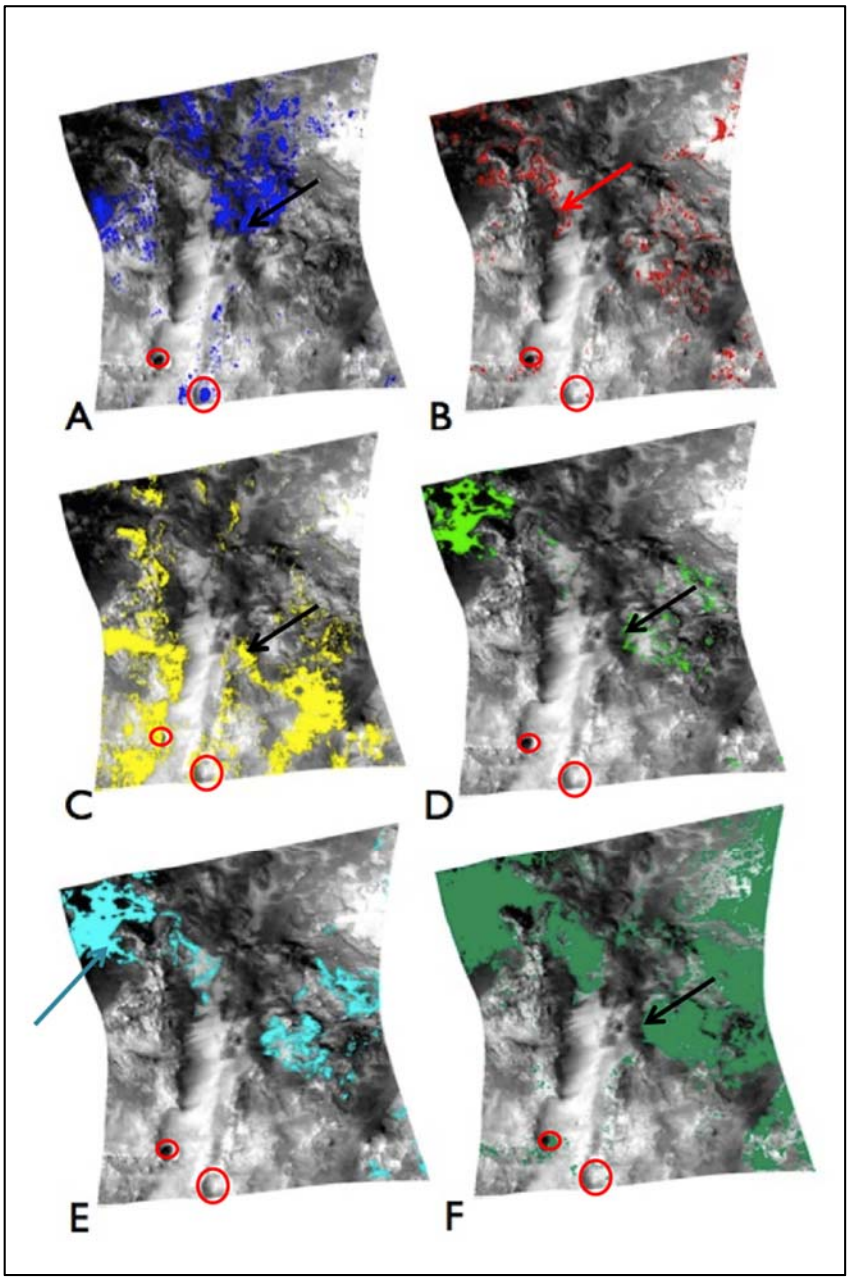

Figure 4.12. Spectral angle mapped (SAM) pixel classifications rendered s regions of interest (ENVI/IDL) and overlain on a single-band 1.3 μm (overall IR albedo) image of CRISM scene FRT000097E2. End-member spectral comparisons were: impact-altered nontronite after impacts at 39.1 GPa (a), CRISM library nontronite NDJB26 (b), CRISM library smectite BKR1JB006 (c), CRISM library illite LAIL01 (d), CRISM library chlorite LACL14 (e), and illite with a relaxed spectral angle differential of 0.100 radians (f). All other classifications used angle differentials of 0.055 radians except for (b), which used a differential of 0.040 radians and (e), which also used a differential of 0.100 radians. The small craters in the southwest of the image are outlined in red circles. Arrows indicate the regions of the scene from which the spectra in Figure 4.13 were extracted. The black arrows correspond to the single spectrum that matched impact altered nontronite (39.1 GPa), smectite, and illite.

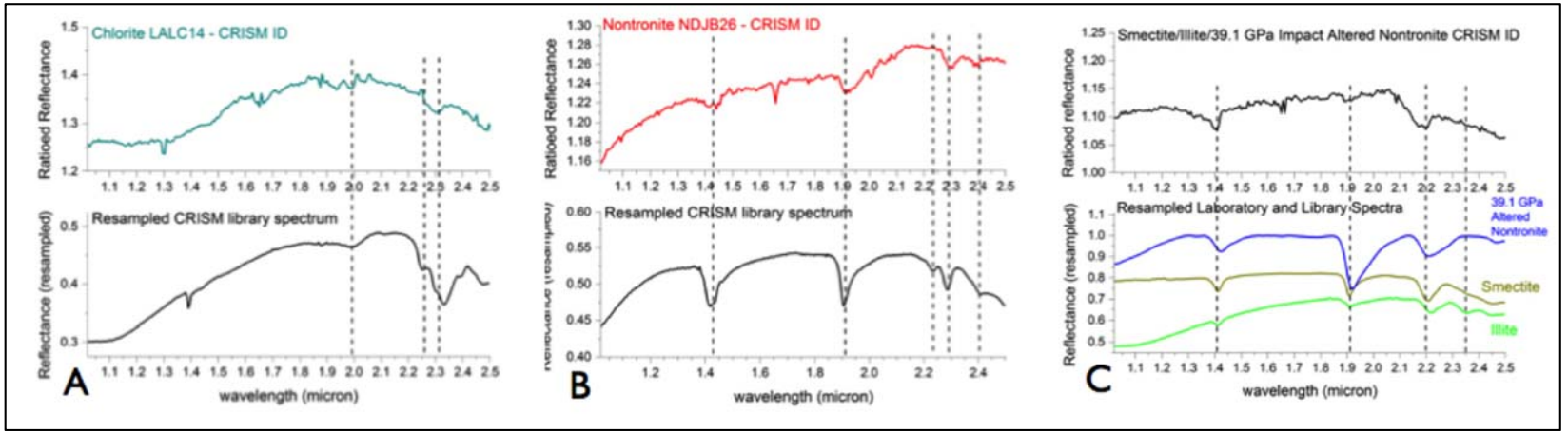

Figure 4.13. Ratioed spectra extracted from CRISM scene FRT000097E2 and compared to laboratory and library spectra of various phyllosilicate minerals, chlorite (a), nontronite (b), and three different altered and unaltered minerals (c). The spectral similarities between smectite, altered nontronite after impacts at 39.1 GPa and illite are highlighted in (c) and compared with a characteristic spectrum from within FRT000097E2 at a location where all of their regions of interest overlap.

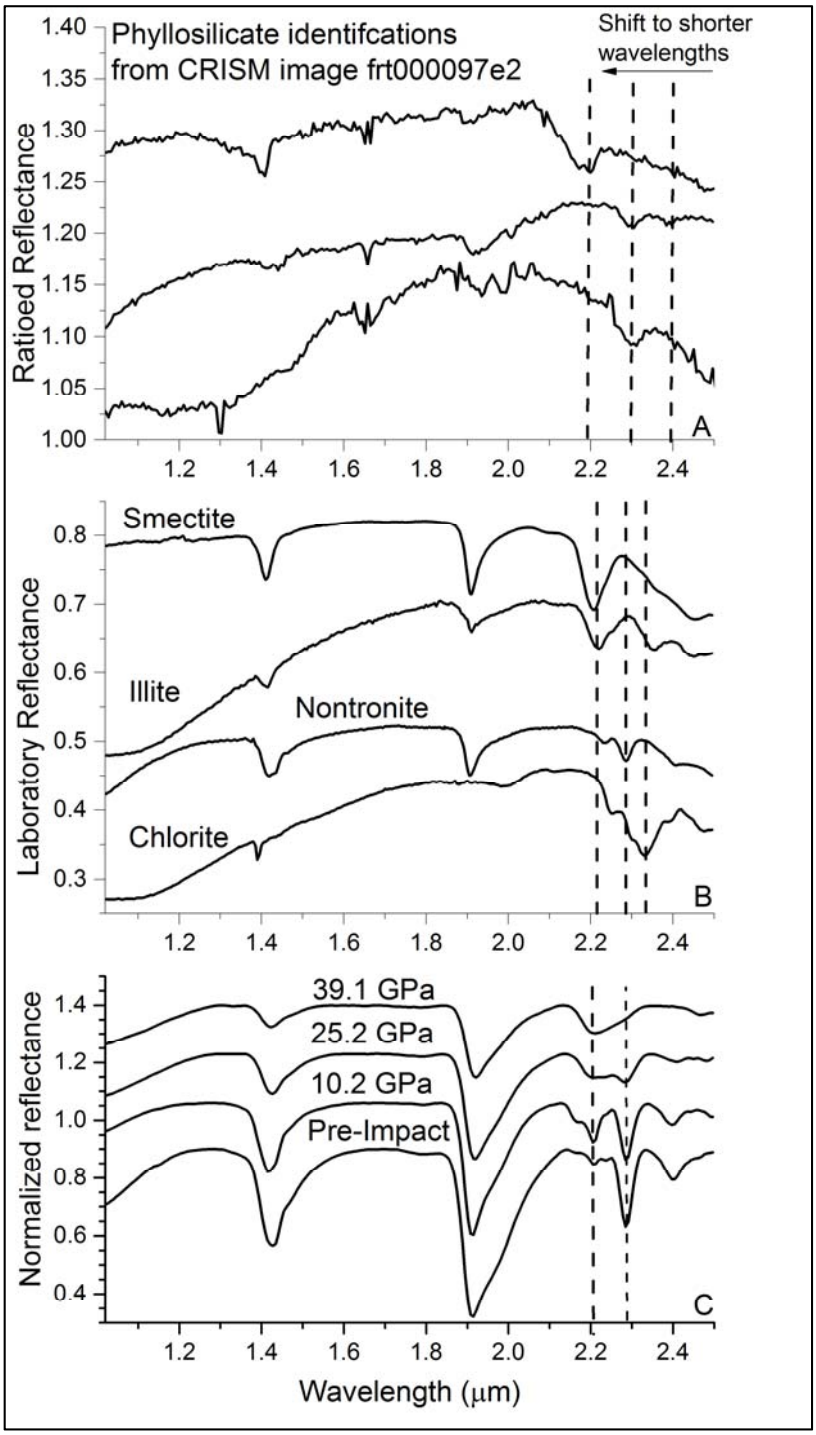

Figure 4.14. A comparison of the shifts in characteristic absorption bands between 2.2-2.5 μm for impact altered nontronite after impacts at various peak pressures, library spectra of common phyllosilicates and minerals formed by phyllosilicate diagenesis, as well as extracted spectra from within CRISM scene FRT000097E2.

Chapter 5

Conclusions

5.1 Impacts induce atomic-scale structural change in phyllosilicate minerals

In the first chapter of this dissertation, I presented results demonstrating that impacts induce structural and spectral changes to the natural nontronite sample NAu-1 (CMS Source Clays Repository). By using complementary spectroscopic techniques, specific information about structural change within the mineral was inferred. In particular, I hypothesized that the octahedral and tetrahedral sheets of the nontronite structure may respond to impact shock differently. Deformation of the silicate tetrahedra severe enough that bands related to Si-O bending vibrations are no longer detected occurs at a lower peak impact pressure (19.7 GPa) than similarly disordered deformation of the octahedral sheet (25.2 GPa). In other words, characteristic VNIR absorption features related to the Fe-OH bending and stretching overtones of the nontronite octahedral sheet are still detected by reflectance spectroscopy after impacts up to 25.2 GPa, while Si-O bending vibrations can only be detected by MIR Emissivity and ATR spectroscopy after impacts up to 19.7 GPa. Interestingly, the Si-O stretching features of the nontronite tetrahedral sheet were detected (at varying intensities) after all impacts. These spectral results implied that the Fe(III) nontronite octahedral sheet was deformed, but not completely devolatilized, while the tetrahedral sheet simply deformed. At very high peak impact pressures amorphous secondary phases emerged. The disordered pathway of nontronite's response to impact shock contrasts with the well-characterized, step-wise pathway of smectite thermal alteration. As a result, the spectral signatures of shocked phyllosilicates are likely to be complex, potentially contradictory, and may contain mixtures of deformed and ordered material. Partial structural deformation without devolatilization is also supported the Mössbauer spectra of post-impact NAu-1 nontronite in which the Fe(III) transitions from the majority of the cations occupying regular octahedral sites, to primarily occupying deformed, but still octahedral, sites. All iron remained fully oxidized.

5.1.1 Structural and spectral change with implications for planetary remote sensing

Mineral spectra are produced by combinations of different atomic-scale transfers of energy that depend on the frequency of the radiation used, the composition, and the crystal structure of the mineral. In the spectroscopic techniques used in this dissertation, the most common processes are electronic transitions in transition metal cations (short wave visible region) and atomic vibrations within the crystal lattice (IR). As nontronite's crystal structure deforms, the spectral signatures detected by the various techniques used change as well. This means that spectroscopy can be used to monitor structural deformation, but also that the spectral signatures used in remote sensing applications of spectroscopy will not be correct. I presented three implications for the remote sensing of Mars that arose from these observations.

1. Spectroscopic techniques that make use of different frequencies of light probe different parts of the nontronite structure. Because each part of the nontronite structure may deform irregularly in response to shock, it is likely that impact shock could produce seemingly contradictory spectral detections. In particular, MIR detections are more likely to resemble amorphous, hydrated silicate phases, while VNIR detections retain detectable characteristic

nontronite absorption features. This may explain currently ambiguous MIR phyllosilicate detections, even in regions with robust VNIR detections.

2. Determinations of composition based on band assignments in the VNIR may be made inaccurate by band shifts related to impact-induced structural deformation. As the nontronite octahedral sheet deforms, characteristic Fe-OH absorption bands related to the Fe-OH bending and stretching overtones lose intensity and are replaced by a broad, ambiguous metal-OH feature centered at ~2.2 μm. Such changes overlap those previously used to determine the relative Mg/Fe abundances of smectites, and make specific mineral identifications, in regions with apparently unambiguous phyllosilicate detections (Bibring *et al.*, 2005; Poulet *et al.*, 2005; Loizeau *et al.*, 2007).

3. In the complex VNIR wavelength range, where spectral mixing is non-linear (Poulet, 2004), the accuracy of calculated mineral abundances may be even more difficult to assess in heavily bombarded regions due to the possibility of atomic-scale mixing between deformed and ordered material.

5.2 Phyllosilicate minerals do not deform equally in response to impact shock

The results presented in the second chapter of this dissertation show that a Mg-rich, 2:1, trioctahedral smectite (saponite, SapCa-2) is less susceptible to structural deformation than an Fe-rich, 2:1, dioctahedral smectite (nontronite, NAu-1), and an Al-rich, 1:1, dioctahedral phyllosilicate (kaolinite, KGa-1b) after impacts at peak pressures up to ~40 GPa. I proposed multiple hypotheses to explain this observation.

1. The observed difference is simply a result of the kinetics of structural deformation in Mg-rich and Fe-rich minerals. Saponite's dehydroxylation energy is higher than nontronite's and a peak impact pressure of ~40 GPa does not impart enough energy to the saponite sample to induce structural deformation. Structural deformation in kaolinite after impacts similar to that observed for flash-calcined kaolinite samples supports the hypothesis that some of the observed differences are due to the time-scale of laboratory impact experiments. Shock passes nearly instantaneously through samples (on the order 1 – 0.1 μseconds), while thermal alteration requires exposure times that are orders of magnitude longer (hours – days).

2. Trioctahedral clays are generally more stable than dioctahedral clays. This is implied in hypothesis 1 and has also been inferred from comparative phyllosilicate weathering experiments (Ames and Sand, 1958; Yan *et al.*, 2009). This hypothesis is also supported by the presented kaolinite results showing structural deformation in kaolinite, a dioctahedral phyllosilicate, which produces spectral changes similar to those observed for nontronite, also a dioctahedral phyllosilicate (although nontronite has a 2:1 tetrahedral-octahedral-tetrahedral layer structure, while kaolinite has a simpler 1:1 tetrahedral-octahedral layer structure and contains no H_2O molecules in its interlayer).

3. The stability of saponite's tri-hydrated interlayer Na^+ cation reduces susceptibility to structural deformation. This is supported by the presented ^{23}Na NMR results, which are unchanged after laboratory impacts up to peak pressures of 39.1 GPa.

Independent of the explanation for the observed differences between the responses of saponite, kaolinite, and nontronite to laboratory impacts, the presented spectral results further complicate martian remote sensing data interpretation. I described one particularly significant implication of these results, which might affect interpretations of clay mineral depositional environments based on detected spectral signatures. Because clay mineral species differ in their susceptibilities to structural deformation after impact shock, it is likely that phyllosilicate

detections in heavily bombarded regions of the martian surface will contain mixtures of impact-altered and unaltered spectral signatures. Thus, the absence of spectral evidence for impact-alteration does not prove that no impact-induced alteration has taken place. Phyllosilicate detections need to be carefully considered in light of the regional geologic and morphologic contexts.

5.3 Detections of impact-altered phyllosilicates and diagenetic phyllosilicates can overlap

Careful consideration of the contexts of phyllosilicate detections on Mars is especially important when attempting to infer environmental, diagenetic, or paleoclimatic constraints based on the specific mineralogy of phyllosilicate detections. The burial/hydrothermal and low-grade metamorphic smectite-to-illite transition is particularly concerning because the long-short 2.17 – 2.35 μm band shifts used to detect diagenetic phyllosilicate deposits is similar to the shifts induced in impact-altered nontronite spectra, in particular. In addition, the heavily deformed nontronite sample after laboratory impacts up to peak pressures of 39.6 GPa produces a spectrum that strongly resembles generic "smectite" spectra from the CRISM RELAB spectral library, making it difficult to distinguish the two species.

Impacts are a widespread process on the martian surface that exhumes and exposes ancient sediments. As a result, many phyllosilicate, and other relatively old mineral, detections are associated with craters. Given the increasing interest in understanding the depositional and (potentially) metamorphic history of martian phyllosilicates, impact processes and their structural and spectral effects must be carefully taken into account.

5.4 Mineral reactivity as an extension of atomic interactions in crystals

The overarching theme of this dissertation associates atomic-scale interactions in crystals with planetary geology and paleoclimatology. Similarly, mineral properties that are observed at the macro-scale also relate to atomic-scale interactions either within or between crystals and the environment. In Appendix A, I describe a series of experiments used to measure the reactivity of pyrite (FeS_2) as observed by the elimination of *E. coli* bacteria from water. Pyrite eliminates *E. coli* through the combined effects of Fe^{2+} dissolution and the production of ROS, both of which are driven by surface defects on pyrite crystals. Because these reactions are driven by atomic-scale interactions, they can be chemically controlled. Indeed, in Appendix A I also describe how to chemically mitigate the effects of pyrite on *E. coli* and I compare pyrite's bactericidal properties in water to those of anatase (TiO_2). Anatase eliminates bacteria in the presence of ultraviolet (UV) light, but in its absence is not antibacterial. Without UV light, the electronic transitions induced in photoactive Ti that produce ROS in solution do not occur, the suspended TiO_2 particles remain inert, and *E. coli* bacteria survive.

One final concluding thought; in my work on this dissertation, I have come to view the chemical properties of minerals as a continuum connecting atomic-scale interactions to macro-scale properties. By examining challenging problems at both scales, my goal was to understand both the reported observations and the interactions that produced them. Of course, reality is always more complex than anticipated and seemingly straightforward macro-scale observations may require complicated atomic-scale interactions for their explanations. I can't claim to have achieved fluency in moving from the micro to the macro, but I think these results are a good beginning.

Bibliography

Adams, J.B., Hörz, F., and Gibbons, R.V. (1979) Effects of shock-loading on the reflectance spectra of plagioclase, pyroxene, and glass. Pp. 5–7 in: *Proceedings of the 10th Lunar and Planetary Science Conference*. Lunar and Planetary Institute, Houston, TX.

Albrecht, C., Knaapen, A.M., Becker, A., Höhr, D., Haberzettl, P., van Schooten, F.J., Borm, P.J.A., and Schins, R.P.F. (2005) The crucial role of particle surface reactivity in respirable quartz-induced reactive oxygen/nitrogen species formation and APE/Ref-1 induction in rat lung. *Respiratory Research*, **6**.

Allen, P.A. (1997) *Earth Surface Processes*. John Wiley & Sons, Hoboken, N. J.

Ames, L.L. and Sand, L.B. (1958) Factors effecting maximum hydrothermal stability in montmorillonites. *The American Mineralogist*, **43**, 641–648.

Arab, M., Bougeard, D., and Smirnov, K.S. (2003) Structure and dynamics of the interlayer water in an uncharged 2 : 1 clay. *Physical Chemistry and Chemical Physics*, **5**, 4699–4707.

Archer, P.D.J., Franz, H.B., Sutter, B., Arevalo, R.D.J., Coll, P., Eigenbrode, J.L., Glavin, D.P., Jones, J.J., Leshin, L.A., Mahaffy, P.R., McAdam, A.C., McKay, C.P., Ming, D.W., Morris, R. V., Navarro-González, R., Niles, P.B., Pavlov, A., Squyres, S.W., Stern, J.C., Steele, A., and Wray, J.J. (2014) Abundances and implications of volatile-bearing species from evolved gas analysis of the Rocknest aeolian deposit, Gale Crater, Mars. *Journal of Geophysical Research: Planets*, **119**, 237–254.

Arvidson, R.E., Squyres, S.W., Bell, J.F., Catalano, J.G., Clark, B.C., Crumpler, L.S., de Souza, P. a, Fairén, a G., Farrand, W.H., Fox, V.K., Gellert, R., Ghosh, A., Golombek, M.P., Grotzinger, J.P., Guinness, E. a, Herkenhoff, K.E., Jolliff, B.L., Knoll, a H., Li, R., McLennan, S.M., Ming, D.W., Mittlefehldt, D.W., Moore, J.M., Morris, R. V, Murchie, S.L., Parker, T.J., Paulsen, G., Rice, J.W., Ruff, S.W., Smith, M.D., and Wolff, M.J. (2014) Ancient aqueous environments at Endeavour crater, Mars. *Science*, **343**, 1248097.

Auffan, M., Achouak, W., Rose, J., Roncato, M.-A., Chanéac, C., Waite, D.T., Masion, A., Woicik, J.C., Wiesner, M.R., and Bottero, J.-Y. (2008) Relation between the Redox State of Iron-Based Nanoparticles and Their Cytotoxicity toward Escherichia coli. *Environmental Science and Technology*, **42**, 6730–6735.

Aust, A.E., Lund, L.G., Chao, C., Park, S., and Fang, R. (2000) ROLE OF IRON IN THE CELLULAR EFFECTS OF ASBESTOS. *Inhalation Toxicology*, **12**, 75–80.

Bailey, S.W. (1966) The Status of Clay Mineral Structures. Pp. 1–23 in: *Clays and Clay Minerals*. Pergamon Press, New York, New York.

Bandfield, J. (2002a) Global mineral distribution on Mars. *Journal of Geophysical Research*, **107**, 1–21.

Bandfield, J.L. (2002b) Spectroscopic study of the Moses Lake dune field, Washington: Determination of compositional distributions and source lithologies. *Journal of Geophysical Research*, **107**, 5092.

Bandfield, J.L. and Smith, M.D. (2003) Multiple emission angle surface–atmosphere separations of thermal emission spectrometer data. *Icarus*, **161**, 47–65.

Bandfield, J.L., Hamilton, V.E., and Christensen, P.R. (2000a) A global view of martian surface compositions from MGS-TES. *Science*, **287**, 1626–1630.

Bandfield, J.L., Christensen, P.R., and Smith, M.D. (2000b) Spectral data set factor analysis and end-member recovery : Application to analysis of Martian atmospheric particulates. *Journal of Geophysical Research*, **105**, 9573–9587.

Bibring, J., Langevin, Y., Gendrin, A., Gondet, B., Poulet, F., Berthé, M., Soufflot, A., Arvidson, R., Mangold, N., Mustard, J., Drossart, P., and Team, T.O. (2005) Mars surface diversity as revealed by the OMEGA/Mars Express observations. *Science*, **307**, 1576–1581.

Bibring, J., Langevin, Y., Mustard, J., Poulet, F., Arvidson, R., Gendrin, A., Gondet, B., Mangold, N., Pinet, P., Forget, F., and Team, T.O. (2006) Global mineralogical and aqueous mars history derived from OMEGA/Mars Express data. *Science*, **312**, 400–404.

Bischoff, A. and Stöffler, D. (1992) Shock metamorphism as a fundamental process in the evolution of planetary bodies: information from meteorites. *European Journal of Mineralogy*, **4**, 707–755.

Bish, D.L., Blake, D.F., Vaniman, D.T., Chipera, S.J., Morris, R. V, Ming, D.W., Treiman, a H., Sarrazin, P., Morrison, S.M., Downs, R.T., Achilles, C.N., Yen, a S., Bristow, T.F., Crisp, J. a, Morookian, J.M., Farmer, J.D., Rampe, E.B., Stolper, E.M., and Spanovich, N. (2013) X-ray diffraction results from Mars Science Laboratory: mineralogy of Rocknest at Gale crater. *Science*, **341**, 1238932.

Bishop, J., Murad, E., and Dyar, M.D. (2002a) The influence of octahedral and tetrahedral cation substitution on the structure of smectites and serpentines as observed through infrared spectroscopy. *Clay Minerals*, **37**, 617–628.

Bishop, J., Madejová, J., Komadel, P., and Fröschl, H. (2002b) The influence of structural Fe, Al and Mg on the infrared OH bands in spectra of dioctahedral smectites. *Clay Minerals*, **37**, 607–616.

Bishop, J., Lane, M., Dyar, M., and Brown, A. (2008a) Reflectance and emission spectroscopy study of four groups of phyllosilicates: smectites, kaolinite-serpentines, chlorites and micas. *Clay Minerals*, **43**, 35–54.

Bishop, J.L. and Pieters, C.M. (1995) Low-temperature and low atmospheric pressure infrared reflectance spectroscopy of Mars soil analog materials. *Journal of Geophysical Research*, **100**, 5369.

Bishop, J.L. and Rampe, E.B. (2014) The importance of nanophase aluminosilicates at Mawrth Vallis. P. 2068 in: *Lunar and Planetary Institute Science Conference Abstracts*. Lunar and Planetary Institute, Houston, TX.

Bishop, J.L., Pieters, C.M., and Edwards, J.O. (1994) Infrared spectroscopic analyses on the nature of water in montmorillonite. *Clays and Clay Minerals*, **42**, 702–716.

Bishop, J.L., Murad, E., Madejová, J., Komadel, P., Wagner, U., and Scheinost, A.C. (1999) Visible, Mössbauer and infrared spectroscopy of dioctahedral smectites: Structural analyses of the Fe-bearing smectites Sampor, SWy-1 and SWa-1. Pp. 413–419 in: *Proceedings of the 11th International Clay Conference, 1997*. Bahia, Argentina.

Bishop, J.L., Schiffman, P., and Southard, R. (2002c) Geochemical and mineralogical analyses of palagonitic tufts and altered rinds of pillow basalts in Iceland and applications to Mars. Pp. 371–392 in: *Volcano-Ice Interaction on Earth and Mars* (J.L. Smellie and M.G. Chapman, editors). The Geological Society of London, London, UK.

Bishop, J.L., Dobrea, E.Z.N., McKeown, N.K., Parente, M., Ehlmann, B.L., Michalski, J.R., Milliken, R.E., Poulet, F., Swayze, G.A., Mustard, J.F., Murchie, S.L., and Bibring, J.-P. (2008b) Phyllosilicate diversity and past aqueous activity revealed at Mawrth Vallis, Mars. *Science*, **321**, 830–833.

Bishop, J.L., Perry, K. a., Darby Dyar, M., Bristow, T.F., Blake, D.F., Brown, A.J., and Peel, S.E. (2013a) Coordinated spectral and XRD analyses of magnesite-nontronite-forsterite mixtures and implications for carbonates on Mars. *Journal of Geophysical Research: Planets*, **118**, 635–650.

Bishop, J.L., Tirsch, D., Tornabene, L.L., Jaumann, R., McEwen, A.S., McGuire, P.C., Ody, A., Poulet, F., Clark, R.N., Parente, M., McKeown, N.K., Mustard, J.F., Murchie, S.L., Voigt, J., Aydin, Z., Bamberg, M., Petau, A., Michael, G., Seelos, F.P., Hash, C.D., Swayze, G. a., and Neukum, G. (2013b) Mineralogy and morphology of geologic units at Libya Montes, Mars: Ancient aqueously derived outcrops, mafic flows, fluvial features, and impacts. *Journal of Geophysical Research: Planets*, **118**, 487–513.

Bishop, J.L., Loizeau, D., McKeown, N.K., Saper, L., Dyar, M.D., Des Marais, D.J., Parente, M., and Murchie, S.L. (2013c) What the ancient phyllosilicates at Mawrth Vallis can tell us about possible habitability on early Mars. *Planetary and Space Science*, **86**, 130–149. Elsevier.

Blake, D.F., Morris, R. V, Kocurek, G., Morrison, S.M., Downs, R.T., Bish, D., Ming, D.W., Edgett, K.S., Rubin, D., Goetz, W., Madsen, M.B., Sullivan, R., Gellert, R., Campbell, I., Treiman, a H., McLennan, S.M., Yen, a S., Grotzinger, J., Vaniman, D.T., Chipera, S.J., Achilles, C.N., Rampe, E.B., Sumner, D., Meslin, P.-Y., Maurice, S., Forni, O., Gasnault, O., Fisk, M., Schmidt, M., Mahaffy, P., Leshin, L. a, Glavin, D., Steele, A., Freissinet, C., Navarro-González, R., Yingst, R. a, Kah, L.C., Bridges, N., Lewis, K.W., Bristow, T.F., Farmer, J.D., Crisp, J. a, Stolper, E.M., Des Marais, D.J., and Sarrazin, P. (2013) Curiosity at Gale crater, Mars: characterization and analysis of the Rocknest sand shadow. *Science*, **341**, 1239505.

Bleam, W.F. and Hoffmann, R. (1988) Isomorphous Substitution in Phyllosilicates as an Electronegativity Perturbation: Its Effect on Bonding and Charge Distribution. *Inorganic Chemistry*, **27**, 3180–3186.

Boek, E.S. and Sprik, M. (2003) Ab Initio Molecular Dynamics Study of the Hydration of a Sodium Smectite Clay. *Journal of Physical Chemistry B*, **107**, 3251–3256.

Borda, M.J., Elsetinow, A.R., Strongin, D.R., and Schoonen, M.A. (2003) A mechanism for the production of hydroxyl radical at surface defect sites on pyrite. *Geochimica et Cosmochimica Acta*, **67**, 935–939.

Borda, M.J., Strongin, D.R., and Schoonen, M.A. (2004) A vibrational spectroscopic study of the oxidation of pyrite by molecular oxygen. *Geochimica et Cosmochimica Acta*, **68**, 1807–1813.

Boslough, M., Venturini, E., Morosin, B., Graham, R., and Williamson, D. (1986) Physical properties of shocked and thermally altered nontronite: Implications for the Martian surface. *Journal of Geophysical Research*, **91**, E207–E214.

Boslough, M.B., Weldon, R.J., and Ahrens, T.J. (1980) Impact-induced water loss from serpentine, nontronite and kernite. Pp. 2145–2158 in: *Proceedings of the Lunar and Planetary Sciences Conference, 11th*.

Boslough, M.B., Cygan, R.T., and Izett, G.A. (1995) NMR Spectroscopy of quartz from the K/T Boundary: Shock-induced peak broadening, dense glass, and coesite. Pp. 149–150 in: *Lunar and Planetary Science Conference XXVI*. Lunar and Planetary Institute, Houston, TX.

Bougeard, D., Smirnov, K.S., and Geidel, E. (2000) Vibrational Spectra and Structure of Kaolinite : A Computer Simulation Study. *Journal of Physical Chemistry B*, **104**, 9210–9217.

Bragg, W.H. (1913) The structure of some crystals as indicated by their diffraction of X-rays. *Proceedings of the Royal Society of London*, 248–277.

Brearley, A.J. (2000) Hydrous phses in ALH84001: Further evidence for preterrestrial alteration and a shock-induced thermal overprint. P. Abstract# 1203 in: *Proceedings of the 31st Lunar and Planetary Science Conference*. Lunar and Planetary Institute, Houston, TX.

Bruch, J., Seiler, F., and Rehn, B. (2000) DNA damage and Inflammation in the Rat Quartz Model: Differences in Inflammatory Response and Formation of Oxidative DNA Adducts to High and Low Dose of DQ12 Quartz. *Inhalation Toxicology*, **12**, 205–213.

Bruckenthal, E.A. and Pieters, C.M. (1984) Spectral effects of natural shock on plagioclase feldspar. Pp. 96–97 in: *Proceedings of the 15th Lunar and Planetary Science Conference*. Lunar and Planetary Institute, Houston, TX.

Brunner, T.J., Wick, P., Manser, P., Spohn, P., Grass, R.N., Limbach, L.K., Bruinink, A., and Stark, W.J. (2006) In vitro cytotoxicity of oxide nanoparticles: comparison to asbestos, silica, and the effect of particle solubility. *Environmental science & technology*, **40**, 4374–81.

Burns, R.G. (1993) *Mineralogical Applications of Crystal Field Theory*. 2nd Editio. Cambridge University Press, New York, NY.

Butler, I. and Frost, R. (2006) An overview of the high□pressure vibrational spectra of clays and related minerals. *Applied Spectroscopy Reviews*, **41**, 449–471.

De Carli, P.S. and Jamieson, J.C. (1959) Formation of an amorphous form of quartz under shock conditions. *The Journal of Chemical Physics*, **31**, 1675.

De Carli, P.S. and Milton, D.J. (1965) Stishovite: Synthesis by shock wave. *Science*, **147**, 144–145.

Carroll, D.L., Kemp, T.F., Bastow, T.J., and Smith, M.E. (2005) Solid-state NMR characterisation of the thermal transformation of a Hungarian white illite. *Solid State Nuclear Magnetic Resonance*, **28**, 31–43.

Carter, J., Poulet, F., Ody, A., Bibring, J., and Murchie, S. (2011) Global distribution, composition and setting of hydrous minerals on Mars: A reappraisal. *42nd Lunar and Planetary Sciences Conference*, **Abstract #**, 1–2.

Carter, J., Poulet, F., Bibring, J.-P., Mangold, N., and Murchie, S. (2013) Hydrous minerals on Mars as seen by the CRISM and OMEGA imaging spectrometers: Updated global view. *Journal of Geophysical Research: Planets*, **118**, 831–858.

Ceamanos, X. and Douté, S. (2010) Spectral Smile Correction of CRISM/MRO Hyperspectral Images. *IEEE Transactions on Geoscience and Remote Sensing*, **48**, 3951–3959.

Chao, E.C.T., Shoemaker, E.M., and Madsen, B.M. (1960) First natural occurrence of coesite. *Science*, **132**, 220–222.

Chao, E.C.T., Fahey, J.J., and Littler, J. (1961) Coesite from Wabar Crater, near Al Hadida, Arabia. *Science*, **133**, 882–883.

Chao, E.C.T., Fahey, J.J., and Littler, J. (1962) Stishovite, SiO2, a very high pressure new mineral from Meteor Crater, Arizona. *Journal of Geophysical Research*, **67**, 419–421.

Chatterjee, a., Iwasaki, T., Ebina, T., and Miyamoto, a. (1999) A DFT study on clay–cation–water interaction in montmorillonite and beidellite. *Computational Materials Science*, **14**, 119–124.

Che, C. and Glotch, T.D. (2012) The effect of high temperatures on the mid-to-far-infrared emission and near-infrared reflectance spectra of phyllosilicates and natural zeolites: Implications for martian exploration. *ICARUS*, **218**, 585–601. Elsevier Inc.

Che, C. and Glotch, T.D. (2014) Thermal alteration: A possible reason for the inconsistency between OMEGA/CRISM and TES detections of phyllosilicates on Mars? *Geophysical Research Letters*, **41**, 321–327.

Che, C., Glotch, T., Bish, D., Michalski, J.R., and Xu, W. (2011) Spectroscopic study of the dehydration and/or dehydroxylation of phyllosilicate and zeolite minerals. *Journal of Geophysical Research*, **116**, E05007.

Christensen, P.R., Anderson, D.L., Chase, S.C., Clancy, R.T., Clark, R.N., Conrath, B.J., Kieffer, H.H., Kuzmin, R.O., Malin, M.C., Pearl, J.C., Roush, T.L., and Smith, M.D. (1998) Results from the Mars Global Surveyor Thermal Emission Spectrometer. *Science*, **279**, 1692–1698.

Christensen, P.R., Bandfield, J.L., Hamilton, V.E., Ruff, S.W., Kieffer, H.H., Titus, T.N., Malin, M.C., Morris, R. V, Lane, M.D., Clark, R.L., Jakosky, B.M., Mellon, M.T., Pearl, J.C., Conrath, B.J., Smith, M.D., Clancy, R.T., Kuzmin, R.O., Roush, T., Mehall, G.L., Gorelick, N., Bender, K., Murray, K., Dason, S., Greene, E., Silverman, S., and Greenfield, M. (2001) Mars Global Surveyor Thermal Emission Spectrometer experiment : Investigation description and surface science results. *Journal of Geophysical Research*, **106**, 23823–23871.

Clark, B.C., Arvidson, R.E., Gellert, R., Morris, R. V., Ming, D.W., Richter, L., Ruff, S.W., Michalski, J.R., Farrand, W.H., Yen, a., Herkenhoff, K.E., Li, R., Squyres, S.W., Schröder, C., Klingelhöfer, G., and Bell, J.F. (2007) Evidence for montmorillonite or its compositional equivalent in Columbia Hills, Mars. *Journal of Geophysical Research*, **112**, E06S01.

Clark, R.N. (1999) Chapter 1: Spectroscopy of Rocks and Minerals, and Principles of Spectroscopy. Pp. 3–58 in: *Manual of Remote Sensing, Volume 3, Remote Sensing for the Earth Sciences* (A.N. Rencz, editor). John Wiley and Sons, New York, NY.

Clark, R.N., King, T.V. V, Klejwa, M., and Swayze, G.A. (1990) High Spectral Resolution Reflectance Spectroscopy of Minerals. *Journal of Geophysical Research*, **95**, 12653–12680.

Clifford, S.M., Farmer, J., Carr, M.H., Des Marais, D., Bibring, J.-P., Craddock, R., and Newsom, H. (2014) Introduction to the Early Mars III Special Section and Key Questions from the Third International Conference on Early Mars. *Journal of Geophysical Research: Planets*, 1892–1894.

Coes, L. (1953) A new dense crystalline silica. *Science*, **118**, 131–132.

Cohn, C.A., Borda, M.J., and Schoonen, M.A. (2004) RNA decomposition by pyrite-induced radicals and possible role of lipids during the emergence of life. *Earth and Planetary Science Letters*, **225**, 271–278.

Cohn, C.A., Laffers, R., and Schoonen, M.A. (2006) Using yeast RNA as a probe for generation of hydroxyl radicals by earth materials. *Environmental Science and Technology*, **40**, 2838–2843.

Compston, W., Chappell, B.W., Arriens, P.A., and Vernon, M.J. (1970) The chemistry and age of Apollo 11 lunar material. *Proceedings of the Apollo 11 Lunar Science Conference*, **2**, 1007–1027.

Cunningham, T.M., Koehl, J.L., Summers, J.S., and Haydel, S.E. (2010) pH-dependent metal ion toxicity influences the antibacterial activity of two natural mineral mixtures. *Plos One*, **5**, e9456.

Cygan, R.T., Boslough, M.B., and Kirkpatrick, R.J. (1992) NMR spectroscopy of experimentall shocked quartz and plagioclase feldspar powders. *Proceedings of Lunar and Planetary Science*, **22**, 127–136.

d'Espinose de Lacaillerie, J.-B., Fretigny, C., and Massiot, D. (2008) MAS NMR spectra of quadrupolar nuclei in disordered solids: the Czjzek model. *Journal of Magnetic Resonance*, **192**, 244–51.

Daly, T., Gavin, P., and Chevrier, V. (2011) Effects of Thermal Alteration on the Near-Infrared and Mid-Infrared Spectra of Martian Phyllosilicates. P. 1164 in: *42nd Lunar and Planetary Science Conference*. The Woodlands, TX.

Decarreau, A., Petit, S., Martin, F., Farges, F., Vieillard, P., and Joussein, E. (2008) Hydrothermal Synthesis, Between 75 and 150ºC, of High-Charge, Ferric Nontronites. *Clays and Clay Minerals*, **56**, 322–337.

Drits, V.A., Besson, G., and Muller, F. (1995) An improved model for structural transformations of heat-treated aluminous dioctahedral 2:1 layer silicates. *Clays and Clay Minerals*, **43**, 718–731.

Dyar, M.D. (2002) Optical and Mössbauer Spectroscopy of Iron in Micas. *Reviews in Mineralogy and Geochemistry*, **46**, 313–349.

Dyar, M.D., Agresti, D.G., Schaefer, M.W., Grant, C. a., and Sklute, E.C. (2006) Mössbauer Spectroscopy of Earth and Planetary Materials. *Annual Review of Earth and Planetary Sciences*, **34**, 83–125.

Dyar, M.D., Schaefer, M.W., Sklute, E.C., and Bishop, J.L. (2008) Mössbauer spectroscopy of phyllosilicates: effects of fitting models on recoil-free fractions and redox ratios. *Clay Minerals*, **43**, 3–33.

Eberl, D., Whitney, G., and Khoury, H. (1978) Hydrothermal reactivity of smectite. *American Mineralogist*, **63**, 401–409.

Eberl, D.D. (1984) Clay mineral formation and transformation in rocks and soils. *Philosophical Transactions of the Royal Society London A*, **311**, 241–257.

Eberl, D.D. (1993) Three zones for illite formation during burial diagenesis and metamorphism. *Clays and Clay Minerals*, **41**, 26–37.

Ehlmann, B.L., Mustard, J.F., Fassett, C.I., Schon, S.C., Head III, J.W., Des Marais, D.J., Grant, J.A., and Murchie, S.L. (2008) Clay minerals in delta deposits and organic preservation potential on Mars. *Nature Geoscience*, **1**, 355–358.

Ehlmann, B.L., Mustard, J.F., Swayze, G. a., Clark, R.N., Bishop, J.L., Poulet, F., Des Marais, D.J., Roach, L.H., Milliken, R.E., Wray, J.J., Barnouin-Jha, O., and Murchie, S.L. (2009)

Identification of hydrated silicate minerals on Mars using MRO-CRISM: Geologic context near Nili Fossae and implications for aqueous alteration. *Journal of Geophysical Research*, **114**, E00D08.

Ehlmann, B.L., Mustard, J.F., and Murchie, S.L. (2010) Geologic setting of serpentine deposits on Mars. *Geophysical Research Letters*, **37**, n/a–n/a.

Ehlmann, B.L., Berger, G., Mangold, N., Michalski, J.R., Catling, D.C., Ruff, S.W., Chassefière, E., Niles, P.B., Chevrier, V., and Poulet, F. (2013) Geochemical Consequences of Widespread Clay Mineral Formation in Mars' Ancient Crust. *Space Science Reviews*, **174**, 329–364.

European Space Agency. (2013) ESA: The ExoMars rover instrument suite. <http://exploration.esa.int/mars/45103-rover-instruments/> (10 December 2013).

Fahrenfort, J. (1961) Attenuated total reflection: A new principle for the production of useful infra-red reflection spectra of organic compounds. *Spectrochimica Acta*, **17**, 698–709.

Fairén, A.G. (2010) A cold and wet Mars. *Icarus*, **208**, 165–175. Elsevier Inc.

Fairén, A.G., Davila, A.F., Gago-Duport, L., Amils, R., and McKay, C.P. (2009) Stability against freezing of aqueous solutions on early Mars. *Nature*, **459**, 401–4.

Fairén, A.G., Chevrier, V., Abramov, O., Marzo, G. a, Gavin, P., Davila, A.F., Tornabene, L.L., Bishop, J.L., Roush, T.L., Gross, C., Kneissl, T., Uceda, E.R., Dohm, J.M., Schulze-Makuch, D., Rodríguez, J.A.P., Amils, R., and McKay, C.P. (2010) Noachian and more recent phyllosilicates in impact craters on Mars. *Proceedings of the National Academy of Sciences of the United States of America*, **107**, 12095–100.

Farmer, V.C. (1968) Invited Review: Infrared Spectroscopy in Clay Mineral Studies. *Clay Minerals*, **7**, 373–387.

Fassett, C.I. and Head, J.W. (2005) Fluvial sedimentary deposits on Mars: Ancient deltas in a crater lake in the Nili Fossae region. *Geophysical Research Letters*, **32**, n/a–n/a.

Fenoglio, I., Greco, G., Tomatis, M., Muller, J., Raymundo-Piñero, E., Béguin, F., Fonseca, A., Nagy, J.B., Lison, D., and Fubini, B. (2008) Structural defects play a major role in the acute lung toxicity of multiwall carbon nanotubes: physicochemical aspects. *Chemical research in toxicology*, **21**, 1690–7.

Fielder, G. (1963) Nature of the Lunar Maria. *Nature*, **198**, 1256–1260.

Fiske, P.S., Nellis, W.J., Xu, Z., and Stebbins, J.F. (1998) Shocked quartz : A 29 Si magic-angle-spinning nuclear magnetic resonance study. *American Mineralogist*, **83**, 1285–1292.

Fitzgerald, J.J., Hamza, A.I., Dec, S.F., and Bronnimann, C.E. (1996) Solid-atate 27Al and 29Si NMR and 1H CRAMPS studies of the thermal transformations of the 2:1 phyllosilicate pyrophyllite. *Journal of Physical Chemistry*, **3654**, 17351–17360.

French, B.M. (1968) Shock metamorphism as a geologic process. Pp. 1–17 in: *Shock Metamorphism of Natural Materials: Proceedings of the First Conference Held at NASA, Goddard Space Flight Center, Greenbelt, Maryland, April 14-16, 1966* (B.M. French and N.M. Short, editors). Mono Book Corp., Baltimore, MD.

French, B.M. (1998) *Traces of Catastrophe: A Handbook of Shock-Metamoprhic Effects in Terrestrial Meteorite Impact Structures*. LPI Contri. Lunar and Planetary Institute, Houston, TX.

Friedlander, L.R., Glotch, T., Michalski, J.R., Sharp, T.G., Dyar, M.D., and Bish, D.L. (2012) Spectroscopic studies of nontronite after impacts at 3 pressures. in: *43rd Lunar and Planetary Science Conference*.

Friedlander, L. R. and Glotch, T. (2014) Phyllosilicate spectra identified at Mawrth Vallis by factor analysis and targer transformation are consistent with impact-related spectral change. *Lunar and Planetary Science Conference XLV*, Abstract #2001, The Woodlands, TX.

Friedlander, Lonia R., Puri, Neha, Schoonen, Martin A. A., Karzai, Wali A. (2014a) The effect of pyrite on *Escherichia coli* in water: Proof-of-concept for the elimination of waterborne bacteria by reactive minerals. *Journal of Water and Health*, in press and available online.

Friedlander, L.R., Glotch, Timothy, D., Bish, D.L., Sharp, Thomas, G., Dyar, M.D., and Michalski, J.R. (2014b) Impact-Induced Structural Changes Differ Between Two Smectite Species, Nontonite (NAu-1) and Saponite (SapCa-2): Possible Implications for the Remote Sensing of the Martian Surface. Pp. 92–92 in: *51st Annual Meeting of the Clay Minerals Society*.

Friedlander, L.R., Glotch, T.D., Bish, D.L., Sharp, T.G., and Dyar, M.D. (2014c) The impact of impacts on martian phyllosilicates. P. 1034 in: *Lunar and Planetary Institute Science Conference Abstracts*. Lunar and Planetary Institute, 8th International Conference on Mars.

Friedlander, L.R., Glotch, T. D., Bish, D. L., Dyar, M. D., Sharp, T. G., Sklute, E. C. Michalski., J. R. (in review) Structural and spectroscopic changes to natural nontronite induced by experimental impacts between 10 and 40 GPa. *Journal of Geophysical Research: Planets*.

Frost, R.L. (1995) Fourier Transform Raman Spectroscopy of Kaolinite, Dickite and Halloysite. *Clays and Clay Minerals*, **43**, 191–195.

Frost, R.L. and Kloprogge, J.T. (2000) Vibrational spectroscopy of ferruginous smectite and nontronite. *Spectrochimica Acta Part A*, **56**, 2177–2189.

Furukawa, Y., Sekine, T., Kakegawa, T., and Nakazawa, H. (2011) Impact-induced phyllosilicate formation from olivine and water. *Geochimica et Cosmochimica Acta*, **75**, 6461–6472. Elsevier Ltd.

Gault, D.E. and Heitowit, E.D. (1963) The partition of energy for hypervelocity impact craters formed in rock. Pp. 1–38 in: *Proceedings of the 6th Hypervelocity Impact Symposium*. National Aeronautics and Space Administration, Cleveland, Ohio/Moffett Field, California.

Gavin, P. and Chevrier, V. (2010) Thermal alteration of nontronite and montmorillonite: Implications for the martian surface. *Icarus*, **208**, 721–734. Elsevier Inc.

Gavin, P., Chevrier, V., Ninagawa, K., Gucsik, A., and Hasegawa, S. (2009) Experimental investigation of the effect of meteoritic impacts on clays on Mars. Pp. 10–11 in: *Proceedings of the 40th Lunar and Planetary Science Conference*. Lunar and Planetary Institute, Houston, TX.

Gavin, P., Chevrier, V., Ninagawa, K., Gucsik, A., and Hasagawa, S. (2013) Experimental investigation into the effects of meteoritic impacts on the spectral properties of phyllosilicates on Mars. *Journal of Geophysical Research*, **118**, 1–16.

Gibbons, R. V. and Ahrens, T.J. (1971) Shock metamorphism of silicate glasses. *Journal of Geophysical Research*, **76**, 5489–5498.

Glotch, T.D. and Bandfield, J.L. (2006) Determination and interpretation of surface and atmospheric Miniature Thermal Emission Spectrometer spectral end-members at the Meridiani Planum landing site. *Journal of Geophysical Research*, **111**, E12S06.

Gooding, J.L., Aggrey, K.E., and Muenow, D.W. (1990) Volatile compounds in shergottite and nakhlite meteorites. *Meteoritics & Planetary Science*, **25**, 281–289.

Gooding, J.L., Wentworth, S.J., and Zolensky, M.E. (1991) Aqueous alteration of the Nakhla meteorite. *Meteoritics & Planetary Science*, **26**, 135–143.

Grieve, R.A.F., Langenhorst, F., and Stöffler, D. (1996) Invited Review: Shock metamorphism of quartz in nature and experiment: II. Significance in geoscience. *Meteoritics & Planetary Science*, **31**, 6–35.

Grotzinger, J.P., Sumner, D.Y., Kah, L.C., Stack, K., Gupta, S., Edgar, L., Rubin, D., Lewis, K., Schieber, J., Mangold, N., Milliken, R., Conrad, P.G., DesMarais, D., Farmer, J., Siebach, K., Calef, F., Hurowitz, J., McLennan, S.M., Ming, D., Vaniman, D., Crisp, J., Vasavada, A., Edgett, K.S., Malin, M., Blake, D., Gellert, R., Mahaffy, P., Wiens, R.C., Maurice, S., Grant, J. a, Wilson, S., Anderson, R.C., Beegle, L., Arvidson, R., Hallet, B., Sletten, R.S., Rice, M., Bell, J., Griffes, J., Ehlmann, B., Anderson, R.B., Bristow, T.F., Dietrich, W.E., Dromart, G., Eigenbrode, J., Fraeman, A., Hardgrove, C., Herkenhoff, K., Jandura, L., Kocurek, G., Lee, S., Leshin, L. a, Leveille, R., Limonadi, D., Maki, J., McCloskey, S., Meyer, M., Minitti, M., Newsom, H., Oehler, D., Okon, A., Palucis, M., Parker, T., Rowland, S., Schmidt, M., Squyres, S., Steele, A., Stolper, E., Summons, R., Treiman, A., Williams, R., and Yingst, A. (2014) A habitable fluvio-lacustrine environment at Yellowknife Bay, Gale Crater, Mars. *Science*, **343**, 1242777.

Hamilton, V.E. and Ruff, S.W. (2012) Distribution and characteristics of Adirondack-class basalt as observed by Mini-TES in Gusev crater, Mars and its possible volcanic source. *Icarus*, **218**, 917–949. Elsevier Inc.

Hanss, R.E., Montague, M.K., Davis, C., and Galindo, C. (1978) X-ray diffractometer studies of shocked materials. Pp. 2773–2787 in: *Proceedings of the Lunar and Planetary Sciences Conference 9th*. Lunar and Planetary Institute, NASA Astrophysics Data System.

Harris, W.G., Hollien, K.A., Bates, S.R., and Acree, W.A. (1992) Dehydration of hydroxy-interlayered vermiculite as a function of time and temperature. *Clays and Clay Minerals*, **40**, 335–340.

Hartmann, W.K. (1966) Martian cratering. *Icarus*, **5**, 565–576.

Hartmann, W.K. and Neukum, G. (2001) Cratering chronology and the evolution of Mars. *Space Science Reviews*, **96**, 165–194.

Haydel, S.E., Remenih, C.M., and Williams, L.B. (2008) Broad-spectrum in vitro antibacterial activities of clay minerals against antibiotic-susceptible and antibiotic-resistant bacterial pathogens. *Journal of Antimicrobial Chemotherapy*, **61**, 353–361.

Hoffmann, R. (1988) *Solids and Surfaces: A Chemist's View of Bonding in Extended Structures*. VCH Publishers, Inc., New York, New York.

Hörz, F. and Ahrens, T.J. (1969) Deformation of experimental shocked biotite. *American Journal of Science*, **267**, 1213–1229.

Hower, J., Eslinger, E. V., Hower, M.E., and Perry, E. a. (1976) Mechanism of burial metamorphism of argillaceous sediment: 1. Mineralogical and chemical evidence. *Geological Society of America Bulletin*, **87**, 725.

Huang, E., Li, A., Xu, J., Chen, R., and Yamanaka, T. (2007) High-pressure phase transition in Al(OH)3: Raman and X-ray observations. *Geophysical Research Letters*, **23**, 3083–3086.

Huang, Y., Jiang, Z., and Schwieger, W. (1999) Vibrational Spectroscopic Studies of Layered Silicates. *Chemistry of Materials*, **11**, 1210–1217.

Hugoniot, H. (1889) Sur la propagation du movement dans les corps et spécialement dans les gaz parfaits. *Journal Ecole Polytechnique*, **58**, 1–125.

Jiang, W., Mashayekhi, H., and Xing, B. (2009) Bacterial toxicity comparison between nano- and micro-scaled oxide particles. *Environmental pollution*, **157**, 1619–25. Elsevier Ltd.

Johnson, J., Hörs, F., Lucey, P.G., and Christensen, P.R. (2002) Thermal infrared spectroscopy of experimentally shocked anorthosite and pyroxenite: Implications for remote sensing of Mars. *Journal of Geophysical Research*, **107**, 5073.

Johnson, J.R. and Hörz, F. (2003) Visible/near-infrared spectra of experimentally shocked plagioclase feldspars. *Journal of Geophysical Research*, **108**, 5120.

Johnson, J.R., Staid, M.I., and Kraft, M.D. (2007) Thermal infrared spectroscopy and modeling of experimentally shocked basalts. *American Mineralogist*, **92**, 1148–1157.

Karlsson, H.L., Cronholm, P., Gustafsson, J., and Möller, L. (2008) Copper oxide nanoparticles are highly toxic: a comparison between metal oxide nanoparticles and carbon nanotubes. *Chemical research in toxicology*, **21**, 1726–32.

Keeling, J.L., Raven, M.D., and Gates, W.P. (2000) Geology and characterization of two hydrothermal nontronites from weathered metamorphic rocks at the Uley graphite mine, south Australia. *Clays and clay minerals*, **48**, 537–548.

Kieffer, S.W. (1971) Shock metamorphism of the Coconino Sandstone at Meteor Crater, Arizona. *Journal of Geophysical Research*, **76**, 5449–5473.

Kieffer, S.W., Schaal, R.B., Gibbons, R., Hörz, F., Milton, D.J., and Dube, A. (1976) Shocked basalt from Lonar Impact Crater, India and experimental analogues. *Proceedings of the Lunar Science Conference*, **7th**, 1391–1412.

Kim, J., Dong, H., Seabaugh, J., Newell, S.W., and Eberl, D.D. (2004) Role of microbes in the smectite-to-illite reaction. *Science*, **303**, 830–2.

Kirkpatrick, R.J., Kalinichev, A.G., Wang, J., Hou, X., and Amonette, J.E. (2005) Molecular modeling of the vibrational spectra of interlayer and surface species of layered double hydroxides. Pp. 239–285 in: *The Application of Vibrational Spectroscopy to Clay Minerals and Layered Double Hydroxides* (J.T. Kloprogge, editor). CMS Worksh. The Clay Minerals Society, Aurora, CO.

Kraus, R.G., Stewart, S.T., Newman, M.G., Milliken, R.E., and Tosca, N.J. (2013) Uncertainties in the shock devolatilization of hydrated minerals: A nontronite case study. *Journal of Geophysical Research: Planets*, **118**, 2137–2145.

Lange, M.A. and Ahrens, T.J. (1982) Impact induced dehydration of serpentine and the evolution of planetary atmospheres. *Journal of Geophysical Research*, **87**, A451–A456.

Langevin, Y., Poulet, F., Bibring, J.-P., and Gondet, B. (2005) Sulfates in the north polar region of Mars detected by OMEGA/Mars Express. *Science*, **307**, 1584–6.

Laperche, V., Lambert, J.F., Prost, R., and Fripiat, J.J. (1990) High-Resolution Solid-state NMR of Exchangeable Cations in the Interlayer Surface of a Swelling Mica: 23Na, 111Cd, and 133 Cs Vermiculites. *Journal of Physical Chemistry*, **94**, 8821–8831.

Liu, Y. and Glotch, T. (2014) Spectral mixture analysis of hydrated minerals in southwest Melas Chasma. P. Abstract# 2443 in: *Proceedings of the 45th Lunar and Planetary Science Conference*. Lunar and Planetary Institute, The Woodlands, TX.

Loizeau, D., Mangold, N., Poulet, F., Bibring, J., Gendrin, A., Ansan, V., Gomez, C., Gondet, B., Langevin, Y., Masson, P., and Neukum, G. (2007) Phyllosilicates in the Mawrth Vallis region of Mars. *Journal of Geophysical Research*, **112**, E08S08.

Malinowski, E.R. (1991) *Factor Analysis in Chemistry*. 2nd Ed. John Wiley, New York, NY.

Maness, P.C., Smolinksi, S., Blake, D.M., Huang, Z., Wolfrum, E.J., and Jacoby, W.A. (1999) Bactericidal activity of photocatalyitc TiO(2) reaction: Toward an understanding of its killing mechanism. *Applied and Environmental Microbiology*, **65**, 4094–4098.

Mangold, N., Poulet, F., Mustard, J., Bibring, J., Gondet, B., Langevin, Y., Ansan, V., Masson, P., Fassett, C., Head, J., Hoffmann, H., and Neukum, G. (2007) Mineralogy of the Nili

Fossae region with OMEGA/Mars Express data: 2. Aqueous alteration of the crust. *Journal of Geophysical Research*, **112**, E08S04.

Marzo, G. a., Davila, A.F., Tornabene, L.L., Dohm, J.M., Fairén, A.G., Gross, C., Kneissl, T., Bishop, J.L., Roush, T.L., and McKay, C.P. (2010) Evidence for Hesperian impact-induced hydrothermalism on Mars. *Icarus*, **208**, 667–683. Elsevier Inc.

Massiot, D., Dion, P., Alcover, J.F., and Bergaya, F. (1995) 27Al and 29Si MAS NMR study of kaolinite thermal decomposition by controlled rate thermal analysis. *Journal of the American Ceramic Society*, **78**, 2940–2944.

Mcdowell, M. and Hamilton, V. (2009) Seeking phyllosilicates in thermal infrared data: A laboratory and Martian data case study. *Journal of Geophysical Research*, **114**, E06007.

Mcguire, P.C., Wolff, M.J., Smith, M.D., Arvidson, R.E., Murchie, S.L., Clancy, R.T., Roush, T.L., Cull, S.C., Lichtenberg, K.A., Wiseman, S.M., Green, R.O., Martin, T.Z., Milliken, R.E., Cavender, P.J., Humm, D.C., Seelos, F.P., Seelos, K.D., Taylor, H.W., Ehlmann, B.L., Mustard, J.F., Pelkey, S.M., Titus, T.N., Hash, C.D., Malaret, E.R., and Team, C. (2008) MRO/CRISM Retrieval of Surface Lambert Albedos for Multispectral Mapping of Mars With DISORT-Based Radiative Transfer Modeling : Phase 1 — Using Historical Climatology for Temperatures , Aerosol Optical Depths, and Atmospheric Pressures. *IEEE Transactions on Geoscience and Remote Sensing*, **46**, 4020–4040.

Mckeown, N., Bishop, J., Noe Dobrea, E., Ehlmann, B., Parente, M., Mustard, J., Murchie, S., Swayze, G., Bibring, J., and Silver, E. (2009) Characterization of phyllosilicates observed in the central Mawrth Vallis region, Mars, their potential formational processes, and implications for past climate. *Journal of Geophysical Research*, **114**, E00D10.

McKeown, N.K., Bishop, J.L., and Silver, E. a. (2013) Variability of rock texture and morphology correlated with the clay-bearing units at Mawrth Vallis, Mars. *Journal of Geophysical Research: Planets*, **118**, 1245–1256.

Meinhold, R.H., Atakul, H., Davies, T.W., and Slade, R.C.T. (1992) Flash Calcines of Kaolinite : Kinetics of Isothermal Dehydroxylation of Partially Dehydroxylated Flash Calcines and of Flash Calcination Itself. *Journal of Materials Chemistry*, **2**, 913–921.

Meinhold, R.H., Slade, R.C.T., and Davies, T.W. (1993) High-field (27)Al MAS NMR studies of the formation of metakaolinite by flash calcination of kaolinite. *Applied Magnetic Resonance*, **4**, 141–155.

Meldrum, M. and Howden, P. (2002) Crystalline Silica: Variability in Fibrogenic Potency. *Annals of Occupational Hygiene*, **46**, 27–30.

Meslin, P., Gasnault, O., Forni, O., Schröder, S., Cousin, A., Berger, G., Clegg, S.M., Lasue, J., Maurice, S., Sautter, V., Mouélic, S. Le, Wiens, R.C., Fabre, C., Goetz, W., Bish, D., Mangold, N., Ehlmann, B., Lanza, N., Harri, A., Anderson, R., and Rampe, E. (2013) Soil Diversity and Hydration at Gale Crater , Mars. *Science*, **341**, 1238670.

Michalski, J., Kraft, M., Sharp, T., Williams, L., and Christensen, P. (2006) Emission spectroscopy of clay minerals and evidence for poorly crystalline aluminosilicates on Mars from Thermal Emission Spectrometer data. *Journal of Geophysical Research*, **111**, 1–14.

Michalski, J., Poulet, F., Bibring, J.-P., and Mangold, N. (2010) Analysis of phyllosilicate deposits in the Nili Fossae region of Mars: Comparison of TES and OMEGA data. *Icarus*, **206**, 269–289. Elsevier Inc.

Michalski, J.R. and Dobrea, E.Z.N. (2007) Evidence for a sedimentary origin of clay minerals in the Mawrth Vallis region, Mars. *Geology*, **35**, 951.

Michalski, J.R. and Fergason, R.L. (2008) Composition and thermal inertia of the Mawrth Vallis region of Mars from TES and THEMIS data. *Icarus*, **199**, 25–48. Elsevier Inc.

Michalski, J.R., Kraft, M.D., Sharp, T.G., Williams, L.B., and Christensen, P.R. (2005) Mineralogical constraints on the high-silica martian surface component observed by TES. *Icarus*, **174**, 161–177.

Milliken, R.E. (2014) Widespread diagenesis on Mars and implications for crustal fluids. in: *Proceedings of the 8th International Conference on Mars*. Lunar and Planetary Institute, Pasadena, CA.

Milliken, R.E., Bish, D.L., Bristow, T., and Mustard, J.F. (2010) The case for mixed-layered clays on Mars. P. Abstract #2030 in: *Proceedings of the 41st Lunar and Planetary Science Conference*. Lunar and Planetary Institute, The Woodlands, TX.

Moore, D.M. and Reynolds, R.C.J. (1989) X-Ray Diffraction and the Identification and Analysis of Clay Minerals. Pp. 187–190 in: *X-Ray Diffraction and the Identification and Analysis of Clay Minerals*. Oxford University Press, Oxford UK.

Morris, R. V., Klingelhöfer, G., Schröder, C., Rodionov, D.S., Yen, a., Ming, D.W., de Souza, P. a., Fleischer, I., Wdowiak, T., Gellert, R., Bernhardt, B., Evlanov, E.N., Zubkov, B., Foh, J., Bonnes, U., Kankeleit, E., Gütlich, P., Renz, F., Squyres, S.W., and Arvidson, R.E. (2006a) Mössbauer mineralogy of rock, soil, and dust at Gusev crater, Mars: Spirit's journey through weakly altered olivine basalt on the plains and pervasively altered basalt in the Columbia Hills. *Journal of Geophysical Research*, **111**, E02S13.

Morris, R. V., Klingelhöfer, G., Schröder, C., Rodionov, D.S., Yen, a., Ming, D.W., de Souza, P. a., Wdowiak, T., Fleischer, I., Gellert, R., Bernhardt, B., Bonnes, U., Cohen, B. a., Evlanov, E.N., Foh, J., Gütlich, P., Kankeleit, E., McCoy, T., Mittlefehldt, D.W., Renz, F., Schmidt, M.E., Zubkov, B., Squyres, S.W., and Arvidson, R.E. (2006b) Mössbauer mineralogy of rock, soil, and dust at Meridiani Planum, Mars: Opportunity's journey across sulfate-rich outcrop, basaltic sand and dust, and hematite lag deposits. *Journal of Geophysical Research*, **111**, E12S15.

Morris, R.V., Ming, D.W., Gellert, R., Vaniman, D.T., Bish, D.L., Blake, D.F., Chipera, S.J., Downs, R.T., Treiman, A.H., Yen, A.S., Achilles, C.N., Archer, P.D., Bristow, T.F., Crisp, J.A., Des Marais, D.J., Farmer, J.D., Grotzinger, J.P., Mahaffy, P.R., McAdam, A.C., Morookian, J.M., Morrison, S.M., Rampe, E.B., and Science Team, M. (2014) Chemical

composition of crystalline, smectite, and amorphous components for Rocknest soil and John Klein and Cumberland mudstone drill fines using APXS, ChemMIn, and SAM datasets from Gale Crater, Mars. Pp. 1–2 in: *45th Lunar and Planetary Science Conference*. The Woodlands, TX.

Moskowitz, B.M. and Hargraves, R.B. (1984) Magnetic Cristobalite (?): A Possible New Magnetic Phase Produced by the Thermal Decomposition of Nontronite. *Science*, **255**, 1152–1154.

Murchie, S., Arvidson, R., Bedini, P., Beisser, K., Bibring, J.-P., Bishop, J., Boldt, J., Cavender, P., Choo, T., Clancy, R.T., Darlington, E.H., Des Marais, D., Espiritu, R., Fort, D., Green, R., Guinness, E., Hayes, J., Hash, C., Heffernan, K., Hemmler, J., Heyler, G., Humm, D., Hutcheson, J., Izenberg, N., Lee, R., Lees, J., Lohr, D., Malaret, E., Martin, T., McGovern, J. a., McGuire, P., Morris, R., Mustard, J., Pelkey, S., Rhodes, E., Robinson, M., Roush, T., Schaefer, E., Seagrave, G., Seelos, F., Silverglate, P., Slavney, S., Smith, M., Shyong, W.-J., Strohbehn, K., Taylor, H., Thompson, P., Tossman, B., Wirzburger, M., and Wolff, M. (2007) Compact Reconnaissance Imaging Spectrometer for Mars (CRISM) on Mars Reconnaissance Orbiter (MRO). *Journal of Geophysical Research*, **112**, E05S03.

Murchie, S., Guinness, E., and Slavney, S. (2012) *Mars Reconnaissance Orbiter CRISM Data Product Software Interface Specification Version 1.3.7.1*. St. Louis, MO.

Murchie, S.L., Mustard, J.F., Ehlmann, B.L., Milliken, R.E., Bishop, J.L., McKeown, N.K., Noe Dobrea, E.Z., Seelos, F.P., Buczkowski, D.L., Wiseman, S.M., Arvidson, R.E., Wray, J.J., Swayze, G., Clark, R.N., Des Marais, D.J., McEwen, A.S., and Bibring, J.-P. (2009) A synthesis of Martian aqueous mineralogy after 1 Mars year of observations from the Mars Reconnaissance Orbiter. *Journal of Geophysical Research*, **114**, E00D06.

Music, S., Filipovic-Vincekovic, N., and Sekovanic, L. (2011) Precipitation of amorphous SiO2 particles and their properties. *Brazilian Journal of Chemical Engineering*, **28**, 89–94.

Mustard, J.F. and Wiseman, S.M. (2014) Carbonate-olivine-phyllosilicate associations across the Noachian-Hesperian boundary. *45th Lunar and Planetary Science Conference*, Abstract #2583.

Mustard, J.F., Poulet, F., Head, J.W., Mangold, N., Bibring, J.-P., Pelkey, S.M., Fassett, C.I., Langevin, Y., and Neukum, G. (2007) Mineralogy of the Nili Fossae region with OMEGA/Mars Express data: 1. Ancient impact melt in the Isidis Basin and implications for the transition from the Noachian to Hesperian. *Journal of Geophysical Research*, **112**, E08S03.

Mustard, J.F., Murchie, S.L., Pelkey, S.M., Ehlmann, B.L., Milliken, R.E., Grant, J. a, Bibring, J.-P., Poulet, F., Bishop, J., Dobrea, E.N., Roach, L., Seelos, F., Arvidson, R.E., Wiseman, S., Green, R., Hash, C., Humm, D., Malaret, E., McGovern, J. a, Seelos, K., Clancy, T., Clark, R., Marais, D.D., Izenberg, N., Knudson, A., Langevin, Y., Martin, T., Mcguire, P., Morris, R., Robinson, M., Roush, T., Smith, M., Swayze, G., Taylor, H., Titus, T., and Wolff, M. (2008) Hydrated silicate minerals on Mars observed by the Mars Reconnaissance Orbiter CRISM instrument. *Nature*, **454**, 305–309.

Mustard, J.F., Ehlmann, B.L., Murchie, S.L., Poulet, F., Mangold, N., Head, J.W., Bibring, J.-P., and Roach, L.H. (2009) Composition, Morphology, and Stratigraphy of Noachian Crust around the Isidis basin. *Journal of Geophysical Research*, **114**, E00D12.

Mustard, J.F., Adler, M., Allwood, A., Bass, D.S., Beaty, D.W., Bell, J.F.I., Brinckerhoff, W.B., Carr, M., Des Marais, D.J., Drake, B., Edgett, K.S., Eigenbrode, J., Elkins-Tanton, L.T., Grant, J.A., Milkovich, S.M., Ming, D., Moore, C., Murchie, S., Onstott, T.C., Ruff, S.W., Sephton, M.A., Steele, A., and Treiman, A. (2013) *Report of the Mars 2020 science definition team*.

Neumann, A., Petit, S., and Hofstetter, T. (2011) Evaluation of redox-active iron sites in smectites using middle and near infrared spectroscopy. *Geochimica et Cosmochimic Acta*, **75**, 2336–2355.

Ohashi, F., Wada, S.-I., Suzuki, M., Maeda, M., and Tomura, S. (2002) Synthetic allophane from high-concentration solutions: nanoengineering of the porous solid. *Clay Minerals*, **37**, 451–456.

Osinski, G.R., Tornabene, L.L., and Grieve, R. a. F. (2011) Impact ejecta emplacement on terrestrial planets. *Earth and Planetary Science Letters*, **310**, 167–181. Elsevier B.V.

Otto, C.C., Cunningham, T.M., Hansen, M.R., and Haydel, S.E. (2010) Effects of antibacterial mineral leachates on the cellular ultrastructure, morphology, and membrane integrity of Escherichia coli and methicillin-resistant Staphylococcus aureus. *Annals of Clinical Microbiology and Antimicrobials*, **9**, 26.

Palin, E.J. and Dove, M.T. (2004) Investigation of Al/Si ordering in tetrahedral phyllosilicate sheets by Monte Carlo simulation. *American Mineralogist*, **89**, 176–184.

Pauling, L. (1927) The sizes of ions and the structure of ionic crystals. *Journal of American Chemical Society*, **49**, 765–790.

Pauling, L. (1928) The influence of relative ionic sizes on the properties of ionic compounds. *Journal of the American Chemical Society*, **50**, 1036–1045.

Pauling, L. (1929) The principles determining the structure of complex ionic crystals. *Journal of the American Chemical Society*, **51**, 1010–1026.

Pauling, L. (1930) The structure of the micas and related minerals. *Proceedings of the National Academy of Sciences*, **16**, 123–129.

Pauling, L. and Hendricks, S.B. (1925) The crystal structures of hematite and corundum. *Journal of the American Chemical Society*, **47**, 781–790.

Pelkey, S.M., Mustard, J.F., Murchie, S., Clancy, R.T., Wolff, M., Smith, M., Milliken, R., Bibring, J.-P., Gendrin, a., Poulet, F., Langevin, Y., and Gondet, B. (2007) CRISM multispectral summary products: Parameterizing mineral diversity on Mars from reflectance. *Journal of Geophysical Research*, **112**, E08S14.

Petit, S., Madejova, J., Decarreau, A., and Martin, F. (1999) Characterization of octahedral substitutions in kaolinites using near infrared spectroscopy. *Clays and Clay Minerals*, **47**, 103–108.

Petit, S., Caillaud, J., Righi, D., Madejová, J., Elsass, F., and Köster, H. (2002) Characterization and crystal chemistry of an Fe-rich montmorillonite from Ölberg; Germany. *Clay Minerals*, **37**, 283–297.

Petit, S., Decarreau, A., Martin, F., and Buchet, R. (2004) Refined relationship between the position of the fundamental OH stretching and the first overtones for clays. *Physics and Chemistry of Minerals*, **31**, 585–592.

Poulet, F. (2004) Nonlinear spectral mixing: Quantitative analysis of laboratory mineral mixtures. *Journal of Geophysical Research*, **109**, E02009.

Poulet, F., Bibring, J., Mustard, J., Gendrin, A., Mangold, N., Langevin, Y., Arvidson, R., Gondet, B., Gomez, C., Berthé, M., Erard, S., Forni, O., Manaud, N., Poulleau, G., Soufflot, A., Combes, M., Drossart, P., Encrenaz, T., Fouchet, T., Melchiorri, R., Bellucci, G., Altieri, F., Formisano, V., Fonti, S., Capaccioni, F., Cerroni, P., Coradini, A., Korablev, O., Kottsov, V., Ignatiev, N., Titov, D., Zasova, L., Pinet, P., Schmitt, B., Sotin, C., Hauber, E., Hoffmann, H., Jaumann, R., Keller, U., and Forget, F. (2005) Phyllosilicates on Mars and implications for early martian climate. *Nature*, **438**, 623–627.

Poulet, F., Gomez, C., Bibring, J., Langevin, Y., Gondet, B., Pinet, P., Belluci, G., and Mustard, J. (2007) Martian surface mineralogy from Observatoire pour la Minéralogie, l'Eau, les Glaces et l'Activité on board the Mars Express spacecraft (OMEGA/MEx): Global mineral maps. *Journal of Geophysical Research*, **112**, E08S02.

Poulet, F., Mangold, N., Loizeau, D., Bibring, J., Langevin, Y., Michalski, J., and Gondet, B. (2008) Abundance of minerals in the phyllosilicate-rich units on Mars. *Astronomy and Astrophysics*, **487**, L41–L44.

Poulet, F., Beaty, D., Bibring, J., Bish, D., Bishop, J., Dobrea, E., Mustard, J., Petit, S., and Roach, L. (2009) Key scientific questions and key investigations from the first international conference on martian phyllosilicates. *Astrobiology*, **9**, 257–267.

Rampe, E.B., Morris, R.V., Ming, D.W., Archer, P.D., Bish, D.L., Chipera, S.J., Vaniman, D.T., Blake, D.F., Bristow, T.F., Sutter, B., Farmer, J.D., Downs, R.T., Leveille, R., Achilles, C.A., Crisp, J.A., Des Marais, D.J., Morookian, J.M., Morrison, S.M., Sarrazin, P.C., Spanovich, N., Treiman, A.H., Yen, A.S., and Science Team, M. (2014) Characterizing the phyllosilicate component of the Sheepbed mudstone in Gale Crater, Mars using laboratory XRD and EGA. Pp. 2–3 in: *45th Lunar and Planetary Science Conference*. The Woodlands, TX.

Rankine, W.J.M. (1870) On the thermodynamic theory of waves of finite longitudinal disturbance. *Proceedings of the Royal Society of London*, **18**, 80–83.

Rich, C.I. (1968) Hydroxy interlayers in expansible layer silicates. *Clays and Clay Minerals*, **16**, 15–30.

Roch, G.E., Smith, M.E., and Drachman, S.R. (1998) Solid state NMR characterization of the thermal transformation of an illite-rich clay. *Clays and Clay Minerals*, **46**, 694–704.

Rocha, J. (1999) Single- and triple-quantum 27Al MAS NMR study of the thermal transformation of kaolinite. *Journal of Physical Chemistry B*, **103**, 9801–9804.

Rocha, J. and Klinowski, J. (1990a) 29Si and 27Al magic-angle-spinning NMR studies of the thermal transformation of kaolinite. *Physics and Chemistry of Minerals*, **17**, 179–186.

Rocha, J. and Klinowski, J. (1990b) Solid-state NMR studies of the structure and reactivity of metakaolinite. *Angewandte Chemie International Edition in English*, **29**, 553–554.

Rosenbruch, M., Idel, H., Friedrichs, K.H., Reiffer, F.J., and Brockhaus, A. (1990) Comparative studies of the effect of quartz glass and quartz DQ-12 in inhalation tests in rats. *Zentralbl Hyg Umweltmed*, **189**, 419–40.

Rouff, A., Phillips, B.L., Cochiara, S.G., and Nagy, K.L. (2012) The effect of dissolved humic acids on alluminosilicate formation and associated carbon sequestration. *Applied Environmental Science*.

Ruff, S. (2003) Basaltic andesite or weathered basalt: A new assessment. *Sixth International Conference on Mars*, **Abstract #**.

Ruff, S. and Christensen, P. (2007) Basaltic andesite, altered basalt, and a TES-based search for smectite clay minerals on Mars. *Geophysical Research Letters*, **34**, L10204.

Ruff, S. and Hamilton, V. (2009) New insights into the nature of mineralogic alteration on Mars from orbiter, rover, and laboratory data. *40th Lunar and Planetary Sciences Conference*, **Abstract #**.

Ruff, S.W., Christensen, P.R., Barbera, P.W., and Anderson, D.L. (1997) Quantitative thermal emission spectroscopy of minerals: A laboratory technique for measurement and calibration. *Journal of Geophysical Research*, **102**, 14,899–14,913.

Ruiz, E., Alvarez, S., Hoffmann, R., and Bernsteid, J. (1994) Crystal Orbital Displacement Analysis of Interactions in the Solid State. Application to the Study of Host-Guest Interactions in the Hofmann Clathrates. *Journal of the American*, **116**, 8207–8221.

Sand, L.B. and Ames, L.L. (1957) Stability and decomposition products of hectorite. *Clays and Clay Minerals*, **6**, 392–398.

Saper, L. and Mustard, J.F. (2013) Extensive linear ridge networks in Nili Fossae and Nilosyrtis, Mars: implications for fluid flow in the ancient crust. *Geophysical Research Letters*, **40**, 245–249.

Schoonen, M.A.A., Cohn, C.A., Roemer, E., Laffers, R., Simon, S.R., and O'Riordan, T. (2006) Mineral-induced formation of reactive oxygen species. *Reviews in Mineralogy and Geochemistry*, **64**.

Schoonen, M.A.A., Harrington, A.D., Laffers, R., and Strongin, D.R. (2010) Role of hydrogen peroxide and hydroxyl radical in pyrite oxidation by molecular oxygen. *Geochimica et Cosmochimica Acta*, **74**, 4971–4987. Elsevier Ltd.

Schwenzer, S.P., Abramov, O., Allen, O., Clifford, C.C., Filiberto, S., Kring, J., Lasue, D.A., McGovern, P.J., Newsom, H.E., Treiman, A.H., and Wittman, A. (2009) *The importance of (Noachian) impact craters as windows to the sub-surface and as potential hosts of life*. Pasadena, CA.

Schwenzer, S.P., Abramov, O., Allen, C.C., Clifford, S., Filiberto, J., Kring, D.A., Lasue, J., McGovern, P.J., Newsom, H.E., Treiman, A., Vaniman, D.T., Wiens, R.C., and Wittman, A. (2010) Exploring martian impact craters: What they can reveal about the subsurface and why they are important in the search for life. P. Abstract# 1589 in: *Proceedings of the 41st Lunar and Planetary Science Conference*. Lunar and Planetary Institute, The Woodlands, TX.

Seelos, F. (2009) *Nili Fossae Data Processing Walkthrough*. CRISM Data Users' Workshop.

Sharp, T.G., Michalski, J.R., Dyar, M.D., Bish, D.L., Friedlander, L.R., and Glotch, T. (2012) Effects of shock metamorphism on phylloscilicate structures and spectroscopy. Pp. 3–4 in: *43rd Lunar and Planetary Science Conference*.

Simon-Deckers, A., Loo, S., Mayne-L'Hermite, M., Herlin-Boime, N., Menguy, N., Reynaud, C., Gouget, B., and Carriere, M. (2009) Size-, Composition- and Shape-Dependent Toxicological Impact of Metal Oxide Nanoparticles and Carbon Nanotubes toward Bacteria. *Environmental Science and Technology*, **43**, 8423–8429.

Skogby, H., Annersten, H., Domeneghetti, M.C., Molin, G.M., and Tazzoli, V. (1992) Iron distribution in orthopyroxene: A comparison of Mössbauer spectroscopy and X-ray refinement results. *European Journal of Mineralogy*, **4**, 441–452.

Slade, R.C.T. and Davies, T.W. (1991) Evolution of Structural Changes during Flash Calcination of Kaolinite: A (29)Si and (27)Al nuclear magnetic resonance spectroscopy study. *Journal of Materials Chemistry*, **1**, 361–364.

Slade, R.C.T., Davies, T.W., and Atakul, H. (1991) Flash Calcination of Kaolinite: Mechanistic Information from Thermogravimetry. *Journal of Materials Chemistry*, **1**, 751–756.

Soderblom, L.A., Condit, C.D., West, R.A., Herman, B.M., and Kreidler, T.J. (1974) Martian planetwide crater distributions: Implications for geologic mistory and surface processes. *Icarus*, **22**, 239–263.

Squyres, S.W. and Kasting, J.F. (1994) Early Mars: how warm and how wet? *Science*, **265**, 744.

Stewart, S.T., Kraus, R.G., Milliken, R.E., and Tosca, N.J. (2010) Uncertainties in the shock devolatilization of hydrated minerals. Pp. 2–3 in: *The Proceedings of the 41st Lunar and Planetary Science Conference*. Houston, TX.

Stishov, S.M. and Popova, S.V. (1961) A new modification of silica. *Geokhimiya*, **10**, 923–926.

Stöffler, D. (1971) Coesite and stishovite in shocked crystalline rocks. *Journal of Geophysical Research*, **76**, 5474–5488.

Stöffler, D. (1972) Deformation and transformation of rock-forming minerals by natural and experimental shock processes: I. Behavior of minerals under shock compression. *Fortschritte der Mineralogie*, **49**, 50–113.

Stöffler, D. (1974) Deformation and transformation of rock-forming minerals by natural and experimental shock processes: II. Physical properties of shocked minerals. *Fortschritte der Mineralogie*, **51**, 256–289.

Stöffler, D. (1984) Glasses formed by hypervelocity impact. *Journal of Non-Crystalline Solids*, **67**, 465–502.

Stöffler, D. and Langenhorst, F. (1994) Shock metamorphism of quartz in nature and experiment: I. Basic observation and theory. *Meteoritics*, **29**, 155–181.

Tanaka, K.L. (1986) The stratigraphy of Mars. *Proceedings of the 17th Lunar and Planetary Science Conference, Part I*, **91**, E139–E158.

Tanaka, K.L. (2005) Geology and insolation-driven climatic history of Amazonian north polar materials on Mars. *Nature*, **437**, 991–4.

Tarte, P., Rulmont, A., Liégeois-Duyckaerts, M., Cahay, R., and Winand, J.M. (1990) Vibrational spectroscopy and solid state chemistry. *Solid State Ionics*, **42**, 177–196.

Tatsumoto, M. (1970) Afe of the moon: An isotopic study of U-Th-Pb systematics of Apollo 11 lunar samples-II*. *Proceedings of the Apollo 11 Lunar Science Conference*, **2**, 1595–1612.

Tera, F. and Wasserburg, G.J. (1972) U-Th_Pb systematics in three Apollo 14 basalts and the problem of initial Pb in lunar rocks. *Earth and Planetary Science Letters*, **14**, 281–304.

Thollot, P., Mangold, N., Ansan, V., Le Mouélic, S., Milliken, R.E., Bishop, J.L., Weitz, C.M., Roach, L.H., Mustard, J.F., and Murchie, S.L. (2012) Most Mars minerals in a nutshell: Various alteration phases formed in a single environment in Noctis Labyrinthus. *Journal of Geophysical Research*, **117**, E00J06.

Thomas, N.H. and Bandfield, J.L. (2013) Identification of spectral endmembers in CRISM data using factor analysis and target transformation. in: *44th Lunar and Planetary Science Conference (2013)*.

Thomas-Keprta, K.L., Wentworth, S.J., Mckay, D.S., and Gibson, E.K. (2000) Field emission gun scanning electron (FEGSEM) and transmission electron (TEM) microscopy of phyllosilicates in martian meteorites ALH84001, Nakhla, and Shergotty. P. Abstract# 1690 in: *Proceedings of the 31st Lunar and Planetary Science Conference*. Lunar and Planetary Institute, Houston, TX.

Tornabene, L.L., Osinski, G.R., McEwen, A.S., Wray, J.J., Craig, M. a., Sapers, H.M., and Christensen, P.R. (2013) An impact origin for hydrated silicates on Mars: A synthesis. *Journal of Geophysical Research: Planets*, **118**, 994–1012.

Tosca, Nicholas J., and Knoll, Andrew Herbert (2009) Juvenile chemical sediments and the long-term persistence of water at the surface of Mars. *Earth and Planetary Science Letters*, **286**(3-4), 379-386.

Treiman, A.H., Barrett, R.A., and Gooding, J.L. (1993) Preterrestrial aqueous alteration of the Lafayette (SNC) meteorite. *Meteoritics & Planetary Science*, **28**, 86–97.

Tyburczy, J.A. and Ahrens, T.J. (1987) Dehydration kinetics of shocked serpentine. Pp. 435–441 in: *Proceedings of the Lunar and Planetary Sciences Conference, 18th*. Cambridge University Press/Lunar and Planetary Institute, Cambridge and New York/Houston, TX.

Vaniman, D.T., Bish, D.L., Ming, D.W., Bristow, T.F., Morris, R. V, Blake, D.F., Chipera, S.J., Morrison, S.M., Treiman, a H., Rampe, E.B., Rice, M., Achilles, C.N., Grotzinger, J.P., McLennan, S.M., Williams, J., Bell, J.F., Newsom, H.E., Downs, R.T., Maurice, S., Sarrazin, P., Yen, a S., Morookian, J.M., Farmer, J.D., Stack, K., Milliken, R.E., Ehlmann, B.L., Sumner, D.Y., Berger, G., Crisp, J. a, Hurowitz, J. a, Anderson, R., Des Marais, D.J., Stolper, E.M., Edgett, K.S., Gupta, S., and Spanovich, N. (2014) Mineralogy of a mudstone at Yellowknife Bay, Gale crater, Mars. *Science*, **343**, 1243480.

Viviano, C.E. and Moersch, J.E. (2012) A technique for mapping Fe/Mg-rich phyllosilicates on Mars using THEMIS multispectral thermal infrared images. *Journal of Geophysical Research*, **117**, E07007.

Viviano, C.E., Moersch, J.E., and McSween, H.Y. (2013) Implications for early hydrothermal environments on Mars through the spectral evidence for carbonation and chloritization reactions in the Nili Fossae region. *Journal of Geophysical Research: Planets*, **118**, n/a–n/a.

Viviano-Beck, C.E., Seelos, F.P., Murchie, S.L., Kahn, E.G., Seelos, K.D., Taylor, H.W., Taylor, K., Ehlmann, B.L., Wisemann, S.M., Mustard, J.F., and Morgan, M.F. (2014) Revised CRISM spectral parameters and summary products based on the currently detected mineral diversity on Mars. *Journal of Geophysical Research: Planets*, **119**, 1403–1431.

Weiss, D.K. and Head, J.W. (2014) Ejecta mobility of layered ejecta craters on Mars: Assessing the influence of snow and ice deposits. *Icarus*, **233**, 131–146. Elsevier Inc.

Weitz, C.M., Bishop, J.L., Thollot, P., Mangold, N., and Roach, L.H. (2011) Diverse mineralogies in two troughs of Noctis Labyrinthus, Mars. *Geology*, **39**, 899–902.

Weldon, R.J., Thomas, W.M., Boslough, M.B., and Ahrens, T.J. (1982) Shock-Induced color changes in nontronite: Implications for the martian fines. *Journal of Geophysical Research*, **87**, 10,102–10,114.

Williams, L.B., Holland, M., Eberl, D.D., Brunet, T., and De Courrsou, L.B. (2004) Killer clays! Natural antibacterial clay minerals. *Mineralogical Society Bulletin*, 3–8.

Williams, L.B., Haydel, S.E., Giese, R.F., and Eberl, D.D. (2008) Chemical and Mineralogical Characteristics of French Green Clays Used for Healing. *Clays and Clay Minerals*, **56**, 437–452.

Williams, L.B., Metge, D.W., Eberl, D.D., Harvey, R.W., Turner, A.G., Prapaipong, P., and Poret-Peterson, A.T. (2011) What makes a natural clay antibacterial? *Environmental Science and Technology*, **45**, 3768–3773.

Wiseman, S.M., Arvidson, R.E., Morris, R. V., Poulet, F., Andrews-Hanna, J.C., Bishop, J.L., Murchie, S.L., Seelos, F.P., Des Marais, D., and Griffes, J.L. (2010) Spectral and stratigraphic mapping of hydrated sulfate and phyllosilicate-bearing deposits in northern Sinus Meridiani, Mars. *Journal of Geophysical Research*, **115**, E00D18.

Wray, J., Noe Dobrea, E., Arvidson, R., Wiseman, S., Squyres, S., Mcewen, A., Mustard, J., and Murchie, S. (2009) Phyllosilicates and sulfates at Endeavour Crater, Meridiani Planum, Mars. *Geophysical Research Letters*, **36**, L21201.

Wright, S.P., Christensen, P.R., and Sharp, T.G. (2006) Thermal emission spectroscopy of shocked basalt from the Earth and Mars: A review plus new insights. P. Abstract #1786 in: *Proceedings of the Lunar and Planetary Science Conference XXXVII*. Lunar and Planetary Institute, The Woodlands, TX.

Wright, S.P., Christensen, P.R., and Sharp, T.G. (2011) Laboratory thermal emission spectroscopy of shocked basalt from Lonar Crater, India, and implications for Mars orbital and sample data. *Journal of Geophysical Research*, **116**, E09006.

Wyatt, M. and McSween, H. (2002) Spectral evidence for weathered basalt as an alternative to andesite in the northern lowlands of Mars. *Nature*, **417**, 263–266.

Yan, H., Wei, M., Ma, J., Li, F., Evans, D.G., and Duan, X. (2009) Theoretical study on the structural properties and relative stability of M(II)-Al layered double hydroxides based on a cluster model. *The journal of physical chemistry. A*, **113**, 6133–41.

Appendix A

The effect of pyrite on *E. coli* in water: Proof-of-concept for the elimination of waterborne bacteria by reactive minerals

This section of the dissertation is a pre-print of a manuscript currently in press at *Journal of Water and Health* with co-authors Martin A. A. Schoonen, Neha Puri, and A. Wali Karza. The article is expected to be published in the January 2015 issue of *Journal of Water and Health*.

Abstract

In this appendix, I present proof-of-concept results for the elimination of waterborne bacteria by reactive minerals. I exposed *E.coli* MG1655 suspended in water to the reactive mineral pyrite (FeS_2) at room temperature and ambient light. This slurry eliminates 99.9% of bacteria in fewer than 4 hours. I also exposed *E. coli* to pyrite leachate (supernatant liquid from slurry after 24-hours), which eliminates 99.99% of bacteria over the same time-scale. Unlike SOlar water DISinfection (SODIS) these results do not depend on the presence of ultraviolet (UV) light. I confirmed this by testing proposed SODIS additive and known photo-catalyst anatase (TiO_2) for antibacterial properties and found that, in contrast to pyrite, it does not eliminate *E. coli* under the reported experimental conditions. Previous investigations of naturally antibiotic minerals have focused on the medical applications of antibiotic clays, and thus have not been conducted under experimental conditions resembling those found in water purification. In my examination of the relevant literature, I have not found previously reported evidence for the use of reactive minerals in water sanitization. The results from this proof-of-concept experiment may have important implications for future directions in household water purification research.

Keywords: Antibacterial minerals, household water treatment, sanitation, sustainable development

A. 1 Introduction

Worldwide, diarrheal diseases are the second-most common cause of death for children under five years old (Bhutta *et al.* 2013). Exposure to the four pathogens (rotavirus, *Cryptosporidium*, enterotoxigenic *E. coli* and *Shigella*) most often responsible for moderate-to-severe diarrhea (MDS) in children (Kotloff *et al.* 2013), is preventable, and generally stems from the consumption of unsanitary or faecally contaminated water (Bhutta *et al.* 2013). A complete response to diarrheal disease requires improvements in the availability of medical treatment, water provision, and sanitation (Bhutta *et al.* 2013). However, research shows that interventions addressing water quality (protection or treatment at the source or point-of-use) are significantly more effective at reducing childhood morbidity from MDS than those that improve water supply (improved source or distribution) (Waddington *et al.* 2009). One methodology for point-of-use water treatment involves treating water in the home, instead of centrally or at the source. Such techniques, known as household water treatment and safe storage (HWTS), may provide cost effective interim approaches for improving water quality and have become an important part of the joint WHO/UNICEF strategy to control diarrhea (WHO & Unicef 2013)**.** Many currently available HWTS devices have already been shown to provide effective, low-cost methods for improving drinking water quality (Lantagne, Quick & Mintz 2011) in the homes of the more than 768 million people who lack access to improved water sources (WHO & Unicef 2013), and the estimated 1.2 billion additional people who use water from sources with significant sanitary risks (Onda, LoBuglio & Bartram 2012).

Common, currently available HWTS options include: boiling, filtration (biosand and ceramic), chlorination, combinations of filtration or flocculation with chlorination, and SODIS. Although these technologies are effective, they are not without their drawbacks. Because SODIS involves exposing water to sunlight in clear plastic or glass bottles, its only associated cost is that of acquiring an appropriate bottle, therefore it is an essentially no-cost intervention (Lantagne *et al.* 2011). However, the efficacy of SODIS depends on highly variable solar intensity (Berney *et al.* 2006), which makes sustained use difficult to encourage and reduces its overall efficacy (Mäusezahl *et al.* 2009). In contrast to SODIS, initial cost is a major drawback of biosand filters (CDC & USAID 2008d), while chlorination (with and without flocculation) and ceramic filtration both require continued investment or replacement (CDC & USAID 2008a b, 2010). In addition, many ceramic filters contain colloidal silver, which is both expensive and potentially dangerous, as an antibacterial agent. HWTS techniques based on chlorination have the added environmental costs associated with chlorine manufacture (Stringer & Johnston 2001). Chlorination also faces safety concerns about the potential long-term carcinogenic effects of chlorine by-products (CDC & USAID 2008c). Boiling has low monetary costs and has been traditionally practiced for hundreds of years, but it has high fuel, environmental, and human health costs (Gadgil 2008; CDC & USAID 2009). Thus, a novel HWTS technique that addresses some of the drawbacks of the currently available HWTS options may be more effective and attractive to users, saving additional lives.

Efforts to improve existing HWTS options can be found throughout the water treatment and sustainable development literatures. In particular, research to speed up or mitigate the solar dependence of SODIS has revealed both the mechanisms of SODIS (Acra *et al.* 1980; Malato *et al.* 2007), and many possibilities for improving the speed or efficacy of these mechanisms through chemical additives (e.g., Gelover et al. 2006; Berney et al. 2006; Fisher et al. 2008;

Sciacca et al. 2010; Spuhler, Andrés Rengifo-Herrera & Pulgarin 2010; Heaselgrave & Kilvington 2010; Harding & Schwab 2012). Unfortunately, many of these experiments assume extensive UV-exposure (Gelover *et al.* 2006; Malato *et al.* 2007; Spuhler *et al.* 2010) and thus continue to depend on solar radiation. Several other proposed improvements involve pure chemicals (e.g., Fisher et al. 2008; Sciacca et al. 2010; Spuhler et al. 2010) not readily available in developing countries. Many proposed SODIS additives are chosen based on the hypothesis that UV-produced ROS drive bacterial cell death in SODIS (Malato *et al.* 2007; Spuhler *et al.* 2010). This is very similar to the products observed for reactive minerals in solution in the geochemical literature (Schoonen *et al.* 2000, 2006; Borda *et al.* 2001, 2003; Borda, Strongin & Schoonen 2004; Cohn, Borda & Schoonen 2004; Cohn *et al.* 2006b; Harrington, Hylton & Schoonen 2012a). Thus, I hypothesized that minerals might provide effective, natural water sanitization that acts via a mechanism similar to that of SODIS, and may address some of its drawbacks.

Recent results from experiments on the efficacy and composition of naturally occurring antibiotic clays (Williams *et al.* 2004, 2008, 2011) further support the potential of minerals as water sanitizers. Clay minerals, however, are impractical for use in water sanitization as they are fine-grained and difficult to remove from water. Further, natural variation in clay mineral deposits makes the identification of potentially antibacterial clays difficult, and hinders the understanding of the drivers of their antibacterial properties (Haydel, Remenih & Williams 2008; Williams *et al.* 2008).

I tested the effectiveness of a natural (Huanzala, Peru) pyrite sample of high purity (Harrington *et al.* 2012a) at culturable *E. coli* reduction in water as a proof-of-concept experiment demonstrating the potential of the elimination of waterborne bacteria by minerals. I chose pyrite based on observations of ROS production by pyrite in solution in the geochemical literature (Schoonen *et al.* 2000; Borda *et al.* 2001, 2003; Cohn *et al.* 2004, 2006c b; Harrington *et al.* 2012a), the presence of pyrite in one particularly effective antibiotic natural clay (Williams *et al.* 2011), and compelling results that iron-based additives significantly improve the speed and efficacy of SODIS (Sciacca *et al.* 2010; Spuhler *et al.* 2010). As a comparison, I also tested the ability of pure, synthetic anatase (TiO_2), a previously proposed SODIS additive (Gelover *et al.* 2006) to reduce culturable *E. coli* bacteria in water in the absence of UV-light. Finally, I combined pyrite leachate with the iron-chelator ethylenediamenetetraacetic acid (EDTA) to reduce the reactivity of the dissolved iron, as well as the enzyme catalase to remove hydrogen peroxide, a precursor to other ROS. The results of these experiments confirmed that cell death is driven by a combination of dissolved iron and ROS, a mechanism similar to that hypothesized for SODIS.

Our experiments involved exposing exponential phase *E. coli* MG1655 bacteria to one pure mineral, thus ensuring that any observed bactericidal effects would be attributable only to the tested mineral (or leachate). I conducted my experiments in conditions similar to actual water purification: bacteria suspended in water, room temperature, and ambient light. This contrasts with previous research on antibiotic clays, in which cells are usually incubated with the mineral slurry or leachate and retained (at least partially) in growth media (Williams *et al.* 2004, 2008, 2011; Haydel *et al.* 2008; Cunningham *et al.* 2010; Otto *et al.* 2010); and also with previous research on SODIS additives (Gelover *et al.* 2006; Fisher *et al.* 2008; Sciacca *et al.* 2010; Spuhler *et al.* 2010; Heaselgrave & Kilvington 2010; Harding & Schwab 2012), which usually

involves UV-exposure. I also present time-dependent bacterial survival, which has not been extensively studied in mineral slurries.

A. 2 Materials and Methods

A. 2. 1 Tested anti-bacterial minerals and materials

I tested the anti-bacterial properties of the reactive mineral pyrite (FeS_2) in comparison with the photo-catalyst anatase (TiO_2) by exposing *E. coli* MG1655 bacteria to slurries of these minerals. To understand the chemical drivers of cell death in pyrite slurry and to eliminate physical bacteria-mineral interactions as a potential cause of cell death, I also tested bacterial survival in pyrite leachate. I then used the iron-chelator EDTA and enzyme catalase to chemically modify pyrite slurry and test potential chemical drivers of cell death. Finally, I tested the survival of *E. coli* in acid solution to confirm that acidity was not a factor in bacterial elimination by pyrite.

A. 2. 1. 1 Pyrite (FeS_2)

Natural pyrite from Huanzala, Peru was purchased from Wards Natural Science and prepared for use in my experiments according to methods previously described by Harrington et al. (2012a). Two batches of pyrite were prepared, one for use during the slurry exposure experiments and a later, additional batch used in my leachate exposure experiments. The specific surface areas (SSA) of both samples were determined by analysis with a Quantachrome NOVA 5-point BET analyzer. The SSA of the pyrite used in the slurry experiments was found to be 2.434 m^2/g, while that for the pyrite used in the leachate exposure experiments was 4.354 m^2/g. I added appropriate amounts of pyrite from each batch to achieve mineral loadings of 0.10 m^2/mL in all experiments. Mineral loadings were normalized to SSA based on previous mineral toxicity research that showed that toxicity between materials is most easily compared when normalized with respect to exposed surface area (e.g., Harrington 2012a, and citations therein).

A. 2. 1. 2 Anatase (TiO_2)

Reagent-grade (99%) synthetic anatase powder was purchased from Fisher Scientific and used it as received in my anatase slurry exposure experiments. The SSA was again analyzed using a Quantachrome NOVA 5-point BET analyzer and found to be 9.471 m^2/g. To allow for direct comparisons between my pyrite and anatase experiments, I maintained a surface area-normalized mineral loading of 0.10 m^2/mL.

A. 2. 2 Mineral slurry preparation

I added 0.26 g of the <38μm size-fraction (specific surface area = 2.434 m^2/g) of my prepared pyrite sample to 5 mL bacterial solution, for a total surface-area normalized pyrite loading of 0.10 m^2/mL. I used the same surface area-normalized loading for my anatase exposure experiments; 0.0106 g of anatase at specific surface area = 9.471 m^2/g added to 1 mL bacterial solution gives a 0.10 m^2/mL TiO_2 loading.

A. 2. 2. 1 Pyrite leachate preparation

My pyrite leachate consisted of 0.11 g of the <38μm size-fraction (specific surface area = 4.354 m^2/g) of my second prepared pyrite sample added to 5 mL deionized water at a surface area-normalized loading of 0.10 m^2/mL. I left this slurry on a shaker for 24 hours, and then filtered it through a 0.2μm filter to remove any suspended mineral particles. This leachate can be considered representative of the most extreme amounts of potentially bactericidal chemicals released by pyrite in my mineral slurry experiments.

A. 2. 2. 2. Stock ethylenediamenetetraacetic acid (EDTA) solution preparation

I used reagent-grade disodium ethylenediameneteraacetate dihydrate (Sigma-Aldrich) to make a stock solution of 0.5 M EDTA, which I diluted to a 250 mM concentration. I then treated the pyrite leachate with 20 μL of EDTA solution per 1 mL leachate, based on my measurements of dissolved Fe_{total}.

A. 2. 2. 3 Catalase treatment

To remove hydrogen peroxide, a precursor to OH radical, from my pyrite leachate, I added 10 mg of culture-suitable solid catalase (Sigma-Aldrich) directly to 1 mL leachate, based on my measurements of the total ROS production in pyrite leachate after 24 hours.

A. 2. 3. 4 Chemical analysis of pyrite leachate

I measured the dissolved Fe_{total} (both ferrous and ferric) of the leachate using Ferrozine reagent (Schoonen *et al.* 2006). I also measured the production of ROS with an OH-detection protocol using 3'-(p-Aminophenyl) fluorescein (APF), which converts to a fluorescent species in the presence of OH-radical. I measured the fluorescence of APF after 24 hours of exposure to my mineral slurries using a HACH4000 bench-top spectrophotometer equipped with a fluorometer setting and compared my measured values to empirical calibration curves to determine the OH-radical concentration in pyrite slurry after 24 hours. This method has previously been shown to effectively determine the concentrations of ROS in mineral slurries (Cohn *et al.* 2009).

A. 2. 3. 5 Acid solution

I diluted stock 12 M HCl (Sigma-Aldrich) to a 1 mM concentration with de-ionized water to produce a solution at pH=3.0, which I used to test *E. coli* MG1655 survival in acid. pH=3.0 was the lowest pH value I observed in either my pyrite leachates or slurries over 24 hours.

A. 2. 3 Bacterial culture

I performed all of my experiments using *E. coli* MG1655 bacteria obtained from the laboratory of Dr. Wali Karzai in the Department of Biochemistry and Cell Biology and Center for Infectious Diseases at Stony Brook University. Fresh cultures were prepared in advance of each replicate by subculturing from a liquid culture incubated overnight in Luria-Bertrani (LB) broth at 37 °C. Subcultures were incubated in LB at 37°C to approximately log-phase, an optical density at 600 nm (OD_{600}) of about 1, or 4-5 hours. The bacteria were collected by centrifugation, rinsed twice in de-ionized water by centrifugation and suspended in de-ionized water. The bacterial suspension was diluted to produce a 10 mL bacterial solution at an OD_{600} of 0.05. This dilute bacterial solution was then separated into two 5 mL samples, one of which received treatment (pyrite or anatase) and the other served as control. For leachate exposure, the

test bacterial population was collected by centrifugation after the final rinse and re-suspended in pyrite leachate, chemically modified (by the addition of either EDTA or catalase) pyrite leachate or HCl. The control population again remained in water.

A. 2. 4 Pyrite and anatase slurry exposure

Both the mineral-treated and control bacterial solutions were maintained in suspension on a bench-top shaker at room temperature for 24 hours. Aliquots were taken immediately after mineral addition, after 1 hour, 4 hours, and 24 hours to measure time-dependent bacterial elimination. Each of these experiments was repeated in triplicate with independent replicates.

A .2. 5 Pyrite leachate exposure experiments

Both the test *E. coli* bacterial population (suspended in pyrite leachate), and the control population (suspended in water) were retained in suspension on a bench-top shaker at room temperature for 24 hours. Aliquots were taken immediately before treatment, immediately after treatment, at 30 minutes (leachate only), 1 hour, 2 hours (leachate only) and 4 hours. I replicated these experiments in triplicate.

A. 2. 6 Acid exposure experiments

The test *E. coli* population (suspended in acid) and the control population (suspended in water) were retained in suspension on a bench-top shaker at room temperature for 24 hours. Aliquots were taken immediately before treatment, at 2 and 24 hours after exposure. The experiment was triply replicated.

A. 2. 7 Mitigation of pyrite leachate to understand the drivers of bacterial elimination

Based on my measurements of Fe_{total}, I added 20 μL of stock EDTA solution to 1.0 mL total leachate. In a separate experiment, I added 10 mg catalase to 1.0 mL total leachate. I then exposed exponential phase *E. coli* MG1655 to either water (control), untreated leachate (positive control), EDTA-treated, or catalase-treated leachate. I measured viable bacterial populations (CFU/mL) immediately before the final suspension in leachate (pre-treatment), at 0 minutes (immediately after treatment with leachate) and at 2 hours. Cell death at these time-points was then compared to that observed in slurry and unmodified leachate. Each of these experiments was independently replicated in triplicate.

A. 2. 8 Quantifying *E. coli* elimination

To measure time-dependent bacterial survival, aliquots of each bacterial suspension were taken at the specified time-points throughout each experiment. These aliquots were then serially diluted 10^{-2} – 10^{-4} fold and 10 μL spots were placed on dry LB agar plates, which were incubated for 12 hours. For each time-point, I spotted each dilution twice, on two separate dry LB agar plates to account for variability in the dilute bacterial suspensions. I used standard colony counting techniques to detect viable bacteria (CFU/mL) after the techniques described in (Zuberer 1994). Colony counts were first estimated by using the 10 μL spots and accounting for serial dilution. These were confirmed in later replicates by plating 1 mL of the lowest dilution in which visible colonies occurred.

A.3 Results

A. 3. 1 Bactericidal effects of pyrite slurry

I found pyrite to be extremely detrimental to bacterial viability (Figure A-1a), and observed a steady decrease in viability over the 24-hour slurry exposure period. Four hours of pyrite slurry exposure eliminate 99.9% of the original viable bacteria. This is two hours faster than the recommended SODIS exposure time (CDC & USAID 2008e). However, *E. coli* bacteria are not completely eliminated until after four hours. Thus, exposure to pyrite slurry will not make drinking water EPA compliant (US EPA 2012) until after exposures longer than 4 hours. However, 3-fold viable *E. coli* reduction after only 4 hours is a large reduction of bacterial load. With fewer active bacteria, the risk of exposure to diarrheal disease may be reduced.

I observed an inconsistent initial reduction in bacterial viability immediately after the addition of pyrite. Viability is not consistently reduced to below 10% until after 1 hour of exposure. These results are consistent with previous experiments exposing live epithelial lung cells to reactive earth materials (Harrington, Tsirka & Schoonen 2012b; Harrington *et al.* 2012a), although the rate of cell death is significantly slower for bacteria. A similar trend has been observed for bacteria exposed to bactericidal clay and clay leachates (Cunningham *et al.* 2010; Williams *et al.* 2011). The quick and effective sanitization of water by pyrite demonstrates the potential of mineral water sanitization. After 24-hours, culturable *E. coli* is reduced to zero in pyrite slurry. No colonies form, even after plating a full 100 μL of slurry. Bacterial elimination by pyrite proceeds in the absence of UV light.

A. 3. 2 In the absence of UV light anatase is not anti-bacterial

In contrast to previous experiments on anatase in the presence of a UV-light source, I found only a minimal difference between bacterial survival in water (control) and anatase slurry (Figure A-1b). These results reinforce the known dependence of photoactive bactericides on UV light. Although such additives make SODIS faster and more effective (Gelover *et al.* 2006; Fisher *et al.* 2008; Sciacca *et al.* 2010; Spuhler *et al.* 2010; Heaselgrave & Kilvington 2010; Harding & Schwab 2012), their dependence on photo-activation means end-user results will still be weather dependent and potentially inconsistent.

A. 3. 4 Bactericidal effects of pyrite leachate

I then conducted a series of experiments to understand the interactions between *E. coli* MG1655 and pyrite. Understanding the factors that lead to the elimination of *E. coli* by pyrite is necessary for determining which minerals may be used to replace pyrite, which cannot be applied to water treatment directly, in future water sanitization aids. *E. coli* bacterial elimination occurs more quickly in 24-hour pyrite leachate than in pyrite slurry (Figure A-2). These results eliminate physical grain-bacteria interactions as the driver of pyrite's bactericidal properties.

A. 3. 5 Chemical analysis of pyrite leachate

The 24-hour pyrite leachate contains 100 ± 10 (SD) mg/L total Fe and produces 4.39 ± 0.2 (SD) μmol/mL OH-radical. Based on these observations, I surmised that the dissolution of iron into solution drives both bacterial elimination and a steady production of ROS. This hypothesis is supported by previous work on the oxidation of pyrite and its production of OH-

radical in solution (Borda *et al.* 2003, 2004). The pyrite-produced ROS may disrupt the cell membrane while $Fe_{(aq)}$ infiltrates and overwhelms the cell. A lag between mineral addition and dissolution in slurry might explain the quicker bacterial elimination observed in leachate. The greater importance of chemical, rather than physical, interactions in bacterial elimination by pyrite reinforces the potential for using these findings as a starting point to find and test other mineral bactericides. It may be possible to find commonly available rocks and/or minerals that will be more appropriate for use in HWTS techniques than pyrite. For example, laterite, a soil type rich in iron oxides that is common in the tropics and is an effective arsenite adsorbent (Maiti *et al.* 2007), may also be an effective treatment for bacterially contaminated water, but has not yet been specifically tested for antibacterial properties. However, a laterite-based constructed soil filter was reported to reduce culturable fecal coliform bacteria by a factor of 3-log over the course of a season at an Indian water treatment plant, which is encouraging (Kadam *et al.* 2009).

A. 3. 6 Chemical drivers of pyrite leachate's reduction of culturable *E. coli* in water

To better understand the drivers of pyrite's bactericidal properties, I systematically blocked or tested the chemical interactions of the three major products of pyrite dissolution: dissolved iron, ROS, and acidity. I first added the iron-chelator EDTA to pyrite leachate to reduce the reactivity of the dissolved iron. I then added the enzyme catalase to remove hydrogen peroxide, a precursor to OH radical. Finally, I compared bacterial survival in acid to that observed in acidic pyrite leachate. The addition of EDTA (Figure A-3a) and catalase (Figure A-3b) both significantly reduced pyrite leachate's bactericidal efficacy. Bacterial survival is higher after EDTA addition than catalase addition (Figure A-3). However, iron chelation also reduces the capacity for ROS production (Cohn, Laffers & Schoonen 2006a), so there may be combined effects between ROS and dissolved iron for which these experiments cannot account. To address these combination effects, I attempted to test bacterial survival in leachate to which I simultaneously added both EDTA and catalase. However, this produces an unidentified precipitate and does not prevent bacterial elimination (SI Figures A-S1 and A-S2). Despite this, results showing increased *E. coli* CFUs in pyrite leachate after either dissolved iron, or ROS have been mitigated indicate that ROS and dissolved iron may act in combination to eliminate *E. coli* cells in water. Such a mechanism is similar to that proposed for bactericidal natural clays (Williams *et al.* 2008, 2011), and has also been suggested as an explanation of the enhanced bacterial reduction of SODIS in the presence of a natural, iron-rich clay from Burkina Faso (Sciacca *et al.* 2010).

Pyrite dissolution in the presence of oxygen produces sulfuric acid via reaction 1.

$$2FeS_2 + 7O_2 + 2H_2O \rightarrow 2Fe^{2+}_{(aq)} + 4SO_4^{2-}{}_{(aq)} + 4H^+_{(aq)} \quad (1)$$

Dissolving pyrite rapidly achieves pH=3 and then stabilizes. To test whether low solution pH drives cell death, I exposed *E. coli* MG1655 to 1 mM HCl (pH = 3.09). After 24 hours of exposure, *E. coli* MG1655 viability is slightly reduced (Figure 4), but this reduction is not at all comparable to the bacterial elimination observed in either leachate or slurry. This implies that pH is not the driving factor of pyrite's bactericidal properties. This finding is consistent with previous research on *E. coli* survival in acidic solutions (Small *et al.* 1994; Cunningham *et al.* 2010).

These results confirm that the major drivers of pyrite's bactericidal properties are chemical and result from the release of ROS and dissolved ferrous iron into solution.

A. 4 Discussion

In this study, I investigated the ability of one highly reactive mineral, pyrite, to reduce culturable *E. coli* in water in order to understand the potential of reactive minerals to eliminate waterborne bacteria for use in possible HWTS techniques. These experiments demonstrate the hitherto untapped potential of minerals as sustainable point-of-use techniques to eliminate common waterborne pathogens in the water of people who lack access to appropriate water treatment and sanitation. Worldwide, 1.2 billion people lack access to clean water and must use compromised water sources with high sanitary risks (Onda *et al.* 2012; WHO & Unicef 2013). Effective methods for addressing this global problem must be low-cost, simple to implement, locally available and involve familiar materials (Lantagne & Clasen 2012). Ideally, such methods will also be environmentally responsible and themselves sustainable. The use of inexpensive and readily available minerals as a water sanitation tool may be a promising approach. However, all HWTS technologies require ongoing operation and maintenance efforts in addition to community investment and behavioral change to promote sustained use (Figueroa & Kincaid 2010). Thus, developing mineral-based water treatment options is only a start and must be followed by engagement with the social and cultural issues surrounding sanitation as well.

A. 4. 1 Possible implementation options for mineral water sanitization

HWTS interventions with the highest rates of effective use target high-risk households, offer an effective technique, present this technique to a population familiar with it, and provide appropriate materials for use (Lantagne & Clasen 2012). Minerals and earth materials are ubiquitous, cheaper than metals and pure chemicals, and already in use globally as homeopathic remedies for infection (Williams *et al.* 2011). Therefore, minerals may make appropriate materials for HWTS options because they are familiar, can be provided sustainably and may be available locally (depending on regional geology).

I envision two possible approaches for implementing mineral water sanitization. The first involves identifying safe, effective bactericidal minerals and distributing them in a form optimized for water purification, with relevant instructions. This approach is similar to that practiced by providers of dilute sodium hypochlorite and PUR Purifier of Water™ sachets for household chlorination. Thus, I anticipate that this implementation may suffer from similar drawbacks including: distribution and supply-chain issues, continuous costs to users to replace and replenish their chemicals, and risks of negative user experiences through improperly used sachets. However, mineral-based interventions would have the advantage of being naturally derived and would not incur the environmental costs of either manufacturing pure chemicals or exposing people to the risks associated with prolonged chlorine exposure (U.S. EPA 1999; Stringer & Johnston 2001). An alternative approach may be to distribute a guide for identifying local bactericidal minerals, along with information on possible ways to use them for water purification. With training and technical assistance, local leaders could then teach mineral water purification to their communities. This approach is most similar to that taken by SODIS promoters, but is otherwise a radical departure from previous HWTS interventions because it relies on enhanced behavior modification; all HWTS interventions require some level of behavioral change. One possible drawback of this approach is that it will require significant

investment in follow-up and ongoing technical assistance. However, the availability of technical assistance has been shown to be important for the success of nearly all HWTS interventions (Lantagne *et al.* 2011). In this way mineral-based HWTS interventions do not differ from currently available options. To ensure that water treated by mineral-based HWTS interventions is of a reliable quality, users will need to be trained and supported in the proper use of antibacterial minerals. However, like chemical-based HWTS interventions, the reported results indicate that reactive minerals eliminate bacteria in a consistent and predictable way. This is an important advantage over SODIS whose efficacy changes significantly with solar flux and weather (Berney *et al.* 2006; du Preez *et al.* 2011; McGuigan *et al.* 2011).

A. 4. 2 Mineral-based modifications for current HWTS options

Research on mineral water sanitization, might help address barriers to adoption for other HWTS options. For example, replacing the colloidal silver currently used in ceramic filters with an antibacterial mineral may significantly reduce initial costs of the filters, and simplify their manufacture. With appropriate research to optimize and implement it, mineral water sanitization may provide a lower-cost alternative to chemical HWTS interventions (e.g., chlorination, PUR Purifier of Water™ sachets) that does not require the manufacture (Stringer & Johnston 2001) and transport of pure chemicals (CDC & USAID 2008b c). The addition of a bactericidal mineral to the sand column in biosand filters (CDC & USAID 2008d) may improve their bacterial elimination. As I have previously discussed, mineral water purification may be appropriate for replacing SODIS because it works via a similar mechanism.

A. 4. 3 Potential drawbacks and further research

Although these initial results are encouraging, more research is needed to address existing and potential drawbacks to mineral water purification, as well as determine the best methods for implementation. One primary drawback to mineral water sanitization is the four-hour wait time. This is still prohibitively long (although faster than SODIS), and may limit future adoption of mineral-based HWTS techniques. However, I have not yet optimized mineral water sanitization techniques for implementation. My ultimate goal is to find the optimal mineral, or combination of minerals, that can provide safe drinking water on-demand, without having to wait hours. Thus, future research to optimize bacterial elimination by mineral exposure should be conducted. In addition, future research may discover other minerals with more rapid bacterial elimination than pyrite. The methods I have outlined here can be used to test their efficacy.

I selected pyrite as a proof-of-concept mineral because of its well-established reactivity and the extensive geochemical research on its production of ROS in solution. As these results show, pyrite is a highly effective bactericide. I do not, however, recommend that pyrite itself be used for water sanitization. Pyrite acidifies water, may contain heavy metals and other dangerous contaminants, and pyrite dust is dangerous if repeatedly inhaled (Harrington *et al.* 2012b a). Thus, I do not propose pyrite itself for use in HWTS techniques and I present it here only as a demonstration of the potential of mineral-based water sanitization. Previous research has shown that other iron-bearing minerals may be similarly (if less) reactive in solution (Schoonen *et al.* 2006). Future research should focus on the bactericidal potential of these minerals in particular. I intend to build on these results, conducting further research to identify other minerals and geologic materials better suited than pyrite for use in implemented HWTS techniques. Finally, *E. coli* is only one of four pathogens commonly associated with MDS in children under five

(Kotloff *et al.* 2013). Further research is needed to test the efficacy of mineral water sanitization on rotavirus, *Shigella* and *Cryptosporidium*.

Despite these drawbacks, water purification with minerals presents a compelling research direction for the development of future HWTS techniques. In addition, several barriers to implementation and adoption that currently limit the efficacy of HWTS options (Schmidt & Cairncross 2009; Lantagne & Clasen 2012) might be addressed by mineral-based modifications. Additional research on mineral water purification is necessary to know which of these might be effective and to optimize mineral use as a stand-alone HWTS option.

To arrive at the concept of mineral bactericides as a low-cost HWTS technology, I applied previous research from three disciplines to a seemingly unrelated challenge. Not only do these results support the potential of mineral water purification, they also emphasize the possibilities of interdisciplinary approaches to sustainable development. This manuscript is intended as a base, providing new research directions that may eventually lead to innovative solutions for the ongoing global challenge of sustainably providing equitable access to clean water and sanitation.

Lack of access to improved sanitation and clean drinking water is a global crisis. The most effective methods for addressing this crisis must be low-cost, quickly effective, and simple to implement. The use of cheaply available minerals and earth materials as water sanitation aids is based on decades of previous research in complementary fields that have not previously been considered in concert or applied in this context.

References

Acra, A., Karahagopian, Y., Raffoul, Z. & Dajani, R. 1980 Disinfection of oral rehydration solutions by sunlight. *Lancet*. **2**, 1257–8.

Berney, M., Weilenmann, H.-U., Simonetti, A. & Egli, T. 2006 Efficacy of solar disinfection of Escherichia coli, Shigella flexneri, Salmonella Typhimurium and Vibrio cholerae. *J. Appl. Microbiol.* **101**, 828–36.

Bhutta, Z.A., Das, J.K., Walker, N., Rizvi, A., Campbell, H., Rudan, I., *et al.* 2013 Interventions to address deaths from childhood pneumonia and diarrhoea equitably: what works and at what cost? *Lancet*. **381**, 1417–29.

Borda, M.J., Elsetinow, A.R., Schoonen, M.A. & Strongin, D.R. 2001 Pyrite-induced hydrogen peroxide formation as a driving force in the evolution of photosynthetic organisms on an early earth. *Astrobiology*. **1**, 283–8.

Borda, M.J., Elsetinow, A.R., Strongin, D.R. & Schoonen, M.A. 2003 A mechanism for the production of hydroxyl radical at surface defect sites on pyrite. *Geochim. Cosmochim. Acta*. **67**, 935–939.

Borda, M.J., Strongin, D.R. & Schoonen, M.A. 2004 A vibrational spectroscopic study of the oxidation of pyrite by molecular oxygen. *Geochim. Cosmochim. Acta*. **68**, 1807–1813.

CDC & USAID 2009 *Household Water Treatment Options in Developing Countries : Boiling*. Washington D.C.,.

CDC & USAID 2008a *Household Water Treatment Options in Developing Countries : Ceramic Filtration*. Washington D.C.,.

CDC & USAID 2008b *Household Water Treatment Options in Developing Countries : Flocculant/Disinfectant Powder*. Washington D.C.,.
CDC & USAID 2008c *Household Water Treatment Options in Developing Countries : Household Chlorination*. Washington D.C.,.
CDC & USAID 2008d *Household Water Treatment Options in Developing Countries : Slow Sand Filtration*. Washington D.C.,.
CDC & USAID 2008e *Household Water Treatment Options in Developing Countries : Solar Disinfection (SODIS)*. Washington D.C.,.
CDC & USAID 2010 *Preventing Diarrheal Disease in Developing Countries : Proven Household Water Treatment Options*. Washington D.C.,.
Cohn, C.A., Borda, M.J. & Schoonen, M.A. 2004 RNA decomposition by pyrite-induced radicals and possible role of lipids during the emergence of life. *Earth Planet. Sci. Lett.* **225**, 271–278.
Cohn, C.A., Laffers, R. & Schoonen, M.A. 2006a Using yeast RNA as a probe for generation of hydroxyl radicals by earth materials. *Environ. Sci. Technol.* **40**, 2838–2843.
Cohn, C.A., Laffers, R., Simon, S.R., O'Riordan, T. & Schoonen, M.A.A. 2006b Role of pyrite in formation of hydroxyl radicals in coal: possible implications for human health. *Part. Fibre Toxicol.* **3**, 16.
Cohn, C.A., Mueller, S., Wimmer, E., Leifer, N., Greenbaum, S., Strongin, D.R., *et al.* 2006c Pyrite-induced hydroxyl radical formation and its effect on nucleic acids. *Geochem. Trans.* **7**, .
Cohn, C.A., Pedigo, C.E., Hylton, S.N., Simon, S.R. & Schoonen, M.A.A. 2009 Evaluating the use of 3'-(p-Aminophenyl) fluorescein for determining the formation of highly reactive oxygen species in particle suspensions. *Geochem. Trans.* **10**, .
Cunningham, T.M., Koehl, J.L., Summers, J.S. & Haydel, S.E. 2010 pH-dependent metal ion toxicity influences the antibacterial activity of two natural mineral mixtures. *PLoS One*. **5**, e9456.
Figueroa, M.E. & Kincaid, D.L. 2010 *Social, Cultural and Behavioral Correlates of Household Water Treatment and Storage*, Center Pub. Johns Hopkins Bloomberg School of Public Health, Center for Communication Programs, Baltimore, MD,.
Fisher, M.B., Keenan, C.R., Nelson, K.L. & Voelker, B.M. 2008 Speeding up solar disinfection (SODIS): effects of hydrogen peroxide, temperature, pH, and copper plus ascorbate on the photoinactivation of E. coli. *J. Water Health*. **6**, 35–51.
Gadgil, A. 2008 Safe and Affordable Drinking Water for Developing Countries. In: *Phys. Sustain. Energy* (D. Hafemeister, B. Levi, M.D. Levine & P. Schwartz, Eds.). American Institute of Physics, Melville, NY, pp. 176–191.
Gelover, S., Gómez, L. a, Reyes, K. & Teresa Leal, M. 2006 A practical demonstration of water disinfection using TiO2 films and sunlight. *Water Res.* **40**, 3274–80.
Harding, A.S. & Schwab, K.J. 2012 Using limes and synthetic psoralens to enhance solar disinfection of water (SODIS): A laboratory evaluation with Norovirus, Eschericia coli, and MS2. *Am. J. Trop. Med. Hyg.* **86**, 566–572.
Harrington, A.D., Hylton, S.N. & Schoonen, M.A.A. 2012a Pyrite-driven reactive oxygen species formation in simulated lung fluid: implications for coal workers' pneumoconiosis. *Environ. Geochem. Health*. **34**, 527–38.

Harrington, A.D., Tsirka, S.E. & Schoonen, M.A.A. 2012b Quantification of particle-induced inflammatory stress response: a novel approach for toxicity testing of earth materials. *Geochem. Trans.* **13**, .

Haydel, S.E., Remenih, C.M. & Williams, L.B. 2008 Broad-spectrum in vitro antibacterial activities of clay minerals against antibiotic-susceptible and antibiotic-resistant bacterial pathogens. *J. Antimicrob. Chemother.* **61**, 353–361.

Heaselgrave, W. & Kilvington, S. 2010 Antimicrobial activity of simulated solar disinfection against bacterial, fungal, and protozoan pathogens and its enhancement by riboflavin. *Appl. Environ. Microbiol.* **76**, 6010–2.

Kadam, A.M., Nemade, P.D., Oza, G.H. & Shankar, H.S. 2009 Treatment of municipal wastewater using laterite-based constructed soil filter. *Ecol. Eng.* **35**, 1051–1061.

Kotloff, K.L., Nataro, J.P., Blackwelder, W.C., Nasrin, D., Farag, T.H., Panchalingam, S., *et al.* 2013 Burden and aetiology of diarrhoeal disease in infants and young children in developing countries (the Global Enteric Multicenter Study, GEMS): a prospective, case-control study. *Lancet*. **6736**, 1–14.

Lantagne, D.S. & Clasen, T.F. 2012 Use of household water treatment and safe storage methods in acute emergency response: case study results from Nepal, Indonesia, Kenya, and Haiti. *Environ. Sci. Technol.* **46**, 11352–60.

Lantagne, D.S., Quick, R. & Mintz, E.D. 2011 *Household Water Treatment and Safe Storage Options in Developing Countries : A Review of Current Implementation Practices*. Washington D.C.,.

Maiti, A., Dasgupta, S., Basu, J. & De, S. 2007 Adsorption of arsenite using natural laterite as adsorbent. *Sep. Purif. Technol.* **55**, 350–359.

Malato, S., Blanco, J., Alarcón, D.C., Maldonado, M.I., Fernández-Ibáñez, P. & Gernjak, W. 2007 Photocatalytic decontamination and disinfection of water with solar collectors. *Catal. Today*. **122**, 137–149.

Mäusezahl, D., Christen, A., Pacheco, G.D., Tellez, F.A., Iriarte, M., Zapata, M.E., *et al.* 2009 Solar drinking water disinfection (SODIS) to reduce childhood diarrhoea in rural Bolivia: a cluster-randomized, controlled trial. *PLoS Med.* **6**, e1000125.

McGuigan, K.G., Samaiyar, P., du Preez, M. & Conroy, R.M. 2011 High compliance randomized controlled field trial of solar disinfection of drinking water and its impact on childhood diarrhea in rural Cambodia. *Environ. Sci. Technol.* **45**, 7862–7.

Onda, K., LoBuglio, J. & Bartram, J. 2012 Global access to safe water: accounting for water quality and the resulting impact on MDG progress. *Int. J. Environ. Res. Public Health*. **9**, 880–94.

Otto, C.C., Cunningham, T.M., Hansen, M.R. & Haydel, S.E. 2010 Effects of antibacterial mineral leachates on the cellular ultrastructure, morphology, and membrane integrity of Escherichia coli and methicillin-resistant Staphylococcus aureus. *Ann. Clin. Microbiol. Antimicrob.* **9**, 26.

Du Preez, M., Conroy, R.M., Ligondo, S., Hennessy, J., Elmore-Meegan, Mi., Soita, A., *et al.* 2011 Randomized intervention study of solar disinfection of drinking water in the prevention of dysentery in Kenyan children aged under 5 years. *Environ. Sci. andTechnology*. **45**, 9315–9323.

Schmidt, W.-P. & Cairncross, S. 2009 Household Water Treatment in Poor Populations: Is There Enough Evidence for Scaling up Now? *Environ. Sci. Technol.* **43**, 986–992.

Schoonen, M., Elsetinow, A., Borda, M. & Strongin, D. 2000 Effect of temperature and illumination on pyrite oxidation between pH 2 and 6. *Geochem. Trans.* **4**, .

Schoonen, M.A.A., Cohn, C.A., Roemer, E., Laffers, R., Simon, S.R. & O'Riordan, T. 2006 Mineral-induced formation of reactive oxygen species. *Rev. Mineral. Geochemistry*. **64**, .

Sciacca, F., Rengifo-Herrera, J. a, Wéthé, J. & Pulgarin, C. 2010 Dramatic enhancement of solar disinfection (SODIS) of wild Salmonella sp. in PET bottles by H2O2 addition on natural water of Burkina Faso containing dissolved iron. *Chemosphere*. **78**, 1186–91.

Small, P., Blankenhorn, D., Welty, D., Zinser, E. & Slonczewski, J.L. 1994 Acid and base resistance in Escherichia coli and Shigella flexneri: role of rpoS and growth pH. *J. Bacteriol.* **176**, 1729–37.

Spuhler, D., Andrés Rengifo-Herrera, J. & Pulgarin, C. 2010 The effect of Fe2+, Fe3+, H2O2 and the photo-Fenton reagent at near neutral pH on the solar disinfection (SODIS) at low temperatures of water containing Escherichia coli K12. *Appl. Catal. B Environ.* **96**, 126–141.

Stringer, R. & Johnston, P. 2001 *Chlorine and the Environment*, 1st edn. Kluwer Academic Publishers, Dordrecht, The Netherlands,.

United States Environmental Protection Agency 1999 *Wastewater Technology Fact Sheet: Chlorine Disinfection*. Washington D.C.

United States Environmental Protection Agency 2012 EPA Water: Drinking Water Standards & Risk Management. Washington D.C.

Waddington, H., Snilstveit, B., White, H. & Fewtrell, L. 2009 *Water, sanitation and hygiene interventions to combat childhood diarrhoea in developing countries*. New Delhi,.

WHO & Unicef 2013 WHO/UNICEF Joint Monitoring Program (JMP) for Water Supply and Sanitation. *JMP*.

Williams, L.B., Haydel, S.E., Giese, R.F. & Eberl, D.D. 2008 Chemical and Mineralogical Characteristics of French Green Clays Used for Healing. *Clays Clay Miner.* **56**, 437–452.

Williams, L.B., Holland, M., Eberl, D.D., Brunet, T. & De Courrsou, L.B. 2004 Killer clays! Natural antibacterial clay minerals. *Mineral. Soc. Bull.* 3–8.

Williams, L.B., Metge, D.W., Eberl, D.D., Harvey, R.W., Turner, A.G., Prapaipong, P., *et al.* 2011 What makes a natural clay antibacterial? *Environ. Sci. Technol.* **45**, 3768–3773.

Zuberer, D.A. 1994 Recovery and Enumeration of Viable Bacteria. In: *Methods Soil Anal. Part 2 - Microbiol. Biochem. Prop.*, SSSA Book (P.S. Bottomley, J.S. Angle & R.W. Weaver, Eds.). Soil Science Society of America pp. 119–144.

Appendix A – Figures

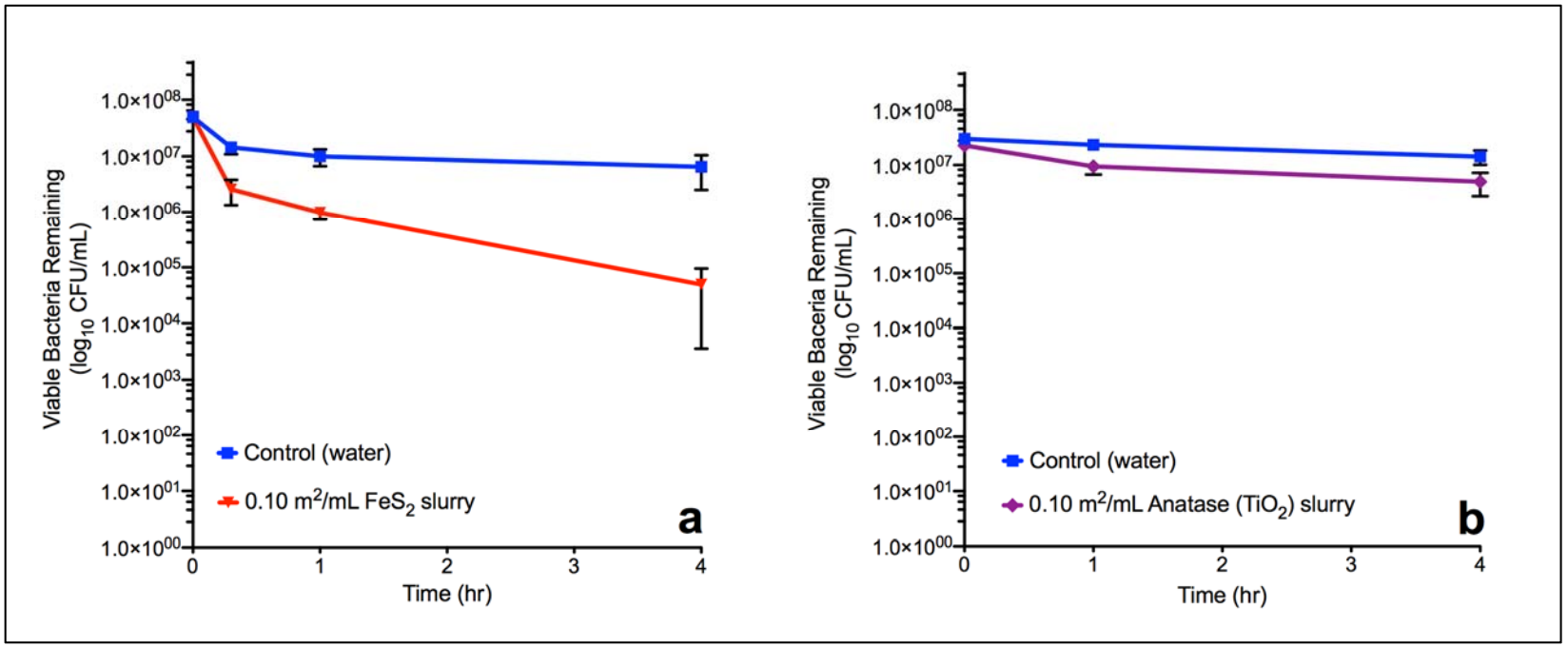

Figure A-1. *E. coli* MG1655 cell death in pyrite (FeS_2) and anatase (TiO_2) slurry. Pyrite slurry causes rapid cell death in water with 99.9% of original bacteria eliminated after 4 hours (a). In contrast, anatase slurry does not cause significant culturable *E. coli* bacterial reduction after 4 hours (b). Both pyrite and anatase exposures were conducted in the absence of UV light. Displayed values represent mean CFU (N=3, SEM) of viable bacteria at each time point.

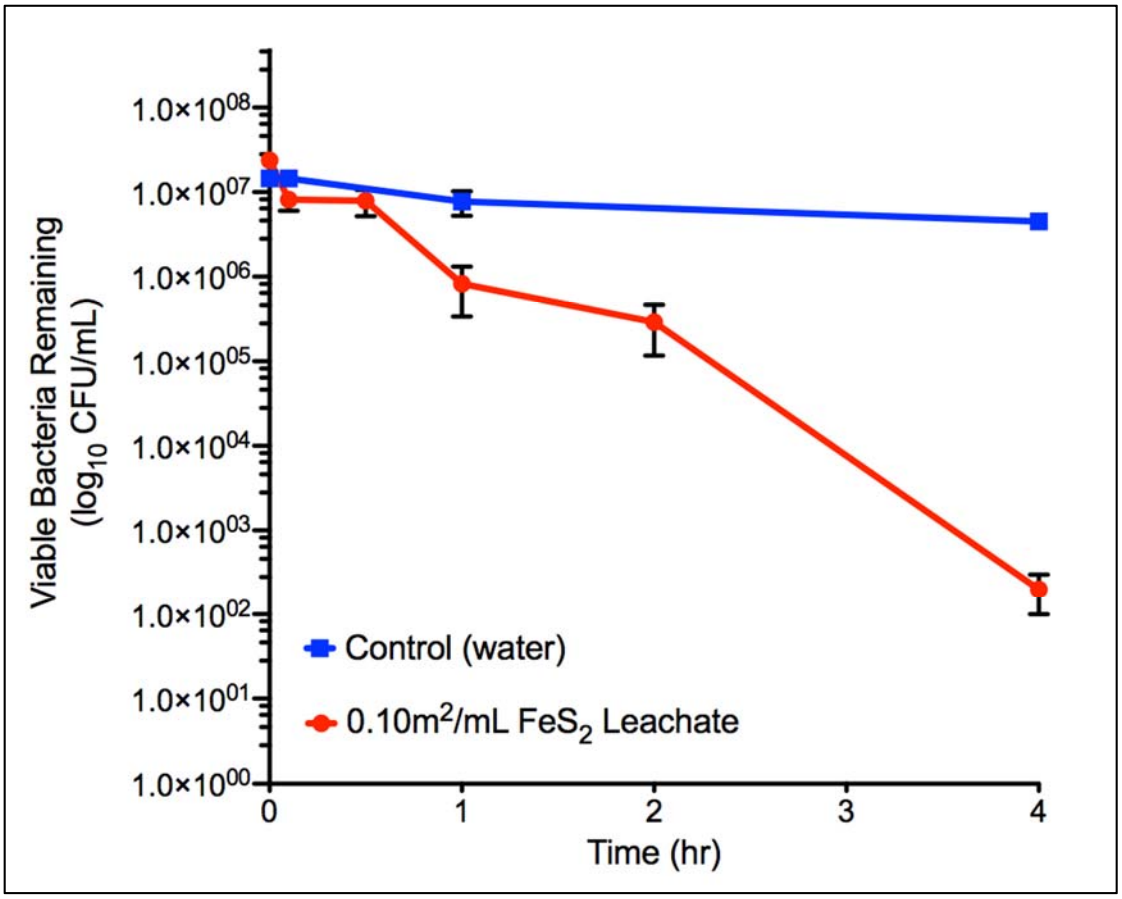

Figure A-2. *E. coli* MG1655 cell death in 24-hour pyrite leachate. *E. coli* bacteria die more rapidly in pyrite leachate than slurry. Leachate eliminates 99.99% of original bacteria after 4 hours. Displayed values represent mean CFU (N=3, SEM) of viable bacteria at each time point.

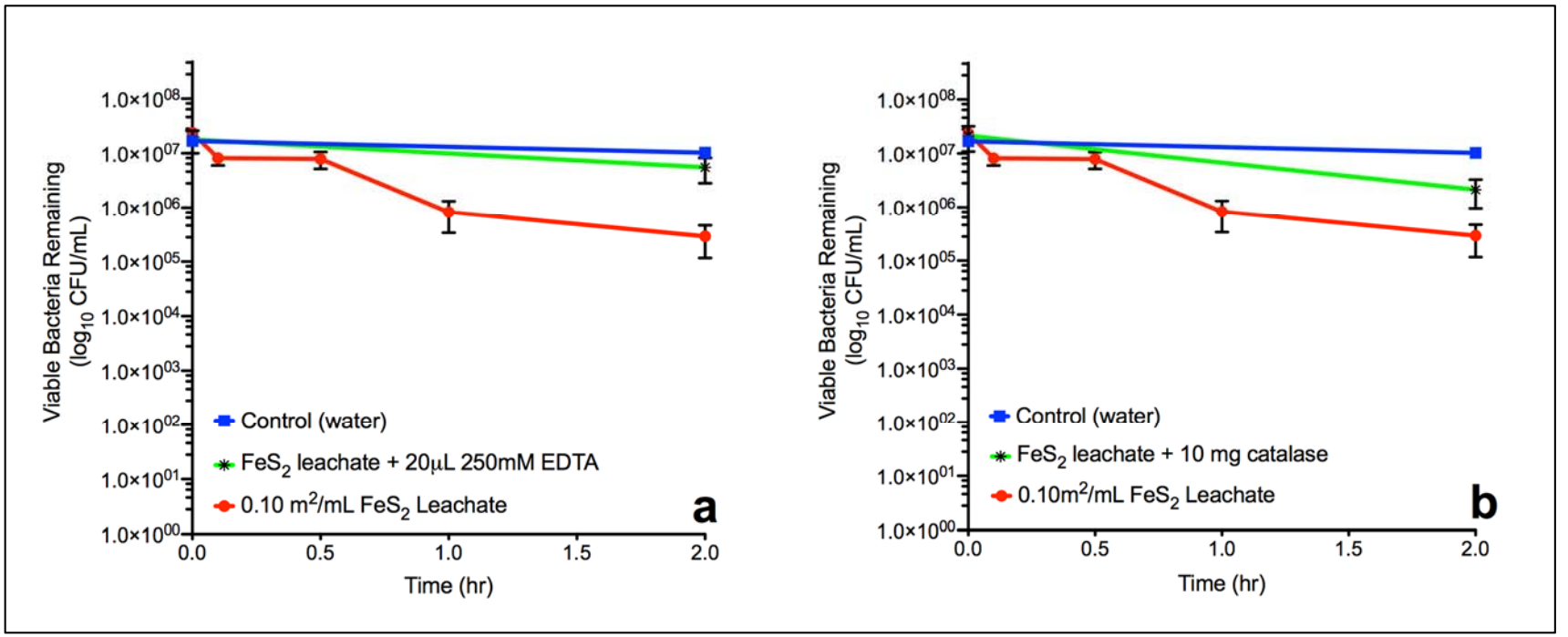

Figure A-3. Comparison of *E. coli* MG1655 survival in pyrite leachate with added EDTA versus added catalase. (a) Bacterial survival in 24-hour pyrite leachate with added EDTA. (b) Bacterial survival in 24-hour pyrite leachate with added catalase. EDTA more effectively prevents bacterial cell death, confirming $Fe_{(aq)}$ as a driver of pyrite's bactericidal properties. Plots display mean CFU (N=3, SEM) of viable bacteria at each time point.

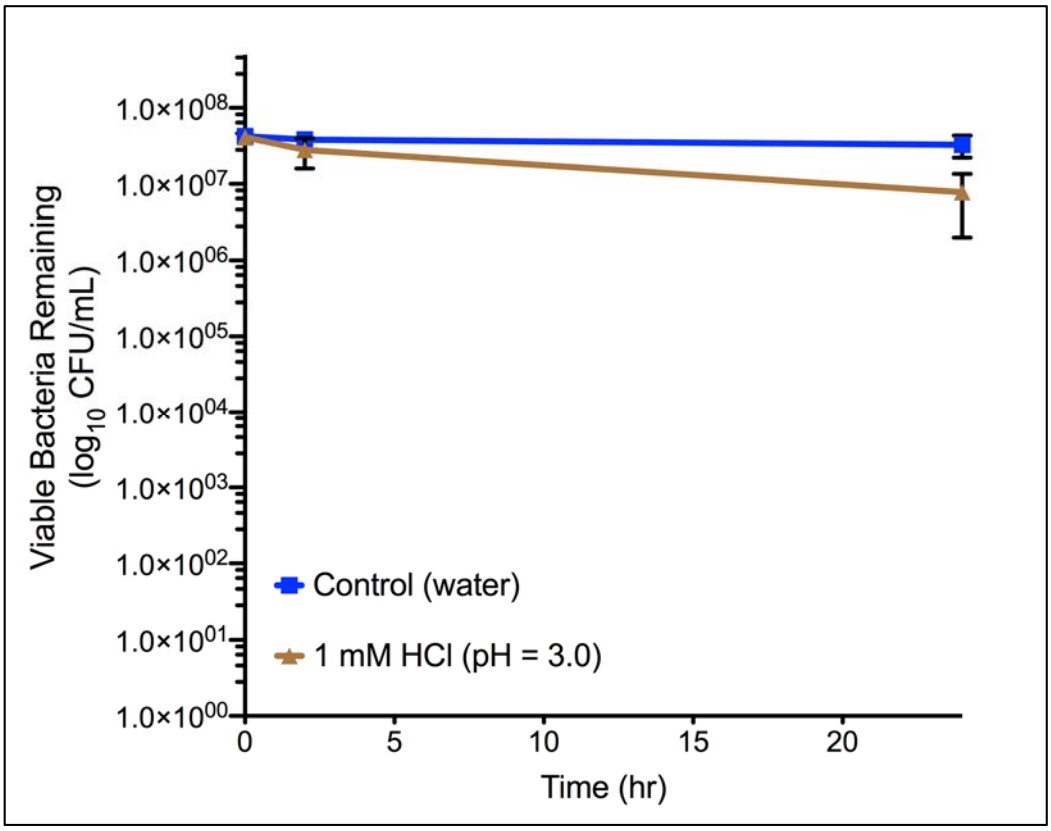

Figure A-4. *E. coli* MG1655 survival in 1 mM HCl (pH = 3.0) after 24 hours. *E. coli* MG1655 cell death in 1 mM HCl is not comparable to that in pyrite leachate or slurry. Plot displays mean CFU (N=4, SEM) of viable bacteria at each time point.

Supplemental Information for the manuscript in Appendix A

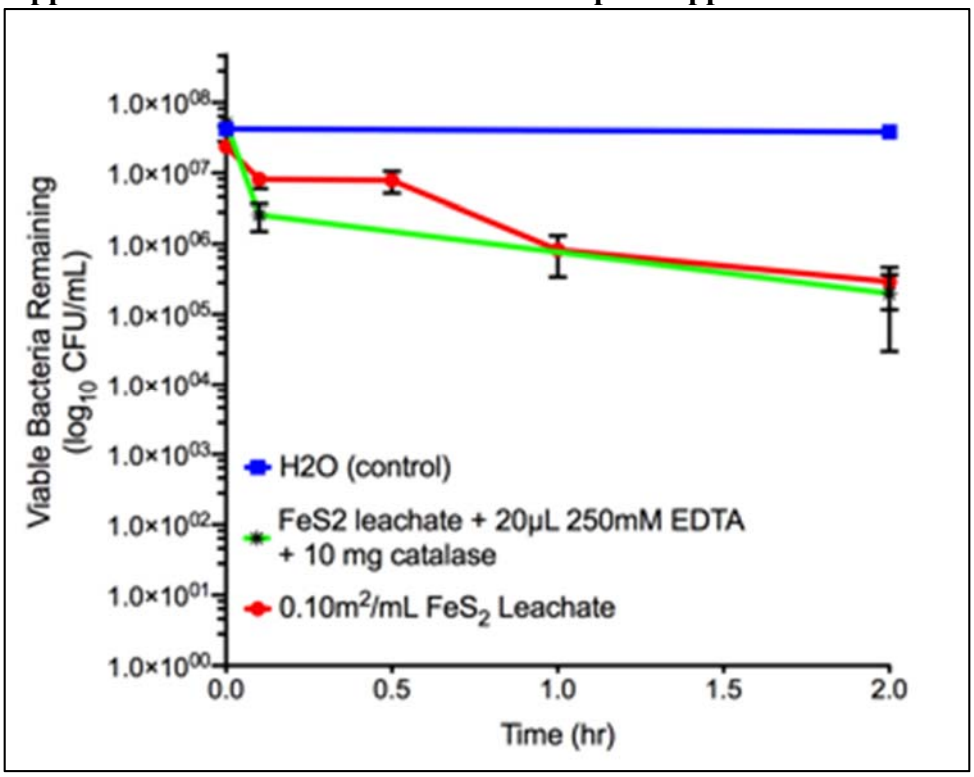

Figure A-S1. *E. coli* MG1655 cell death in 24-hour pyrite leachate with both catalase and EDTA added. When added together EDTA and catalase do not decrease the bactericidal efficacy of pyrite leachate. Displayed values represent mean CFU (N=4, SEM) of viable bacteria at each time point.

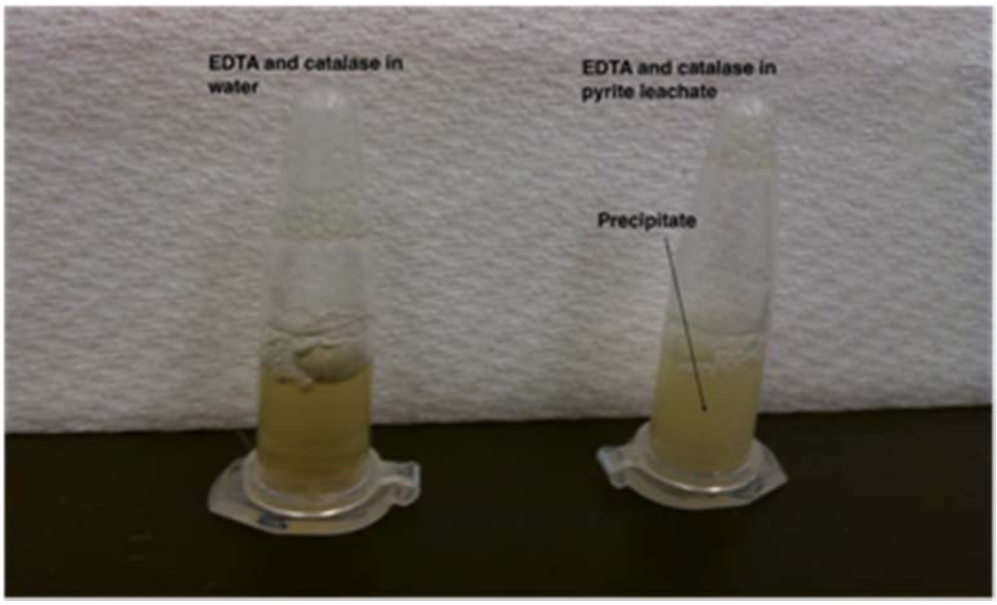

Figure A-S2. Photo showing precipitate formation in pyrite leachate after the combined addition of EDTA and catalase. When EDTA and catalase are added together to distilled water (left), the precipitate does not form. The formation of the precipitate in pyrite leachate (right) may be a low-pH reaction between EDTA and catalase that disrupts the chemistry of both and leads to continued leachate bactericidal efficacy (S1).